OBSERVATIONAL SIGNATURES OF MASSIVE STAR FORMATION: AN INVESTIGATION OF THE ENVIRONMENTS IN WHICH THEY FORM AND THE APPLICABILITY OF THE PARADIGM OF LOW-MASS STAR FORMATION

Katharine Grace Johnston

A Thesis Submitted for the Degree of PhD
at the
University of St. Andrews

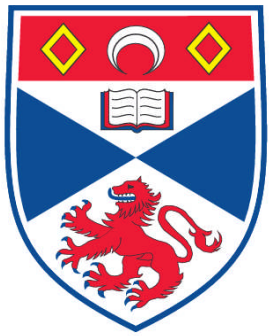

2011

Full metadata for this item is available in
Research@StAndrews:FullText
at:
http://research-repository.st-andrews.ac.uk/

Please use this identifier to cite or link to this item:
http://hdl.handle.net/10023/1895

This item is protected by original copyright

This item is licensed under a
Creative Commons License

Observational Signatures of Massive Star Formation

an investigation of the environments in which they form, and the applicability of the paradigm of low-mass star formation

by

Katharine Grace Johnston

Submitted for the degree of Doctor of Philosophy in Astrophysics

15th October 2010

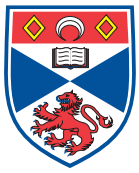

University of St Andrews

Declaration

I, Katharine Johnston, hereby certify that this thesis, which is approximately 50,000 words in length, has been written by me, that it is the record of work carried out by me and that it has not been submitted in any previous application for a higher degree.

I was admitted as a research student in September 2006 and as a candidate for the degree of PhD in September 2006; the higher study for which this is a record was carried out in the University of St Andrews between 2006 and 2009, and at the Harvard-Smithsonian Center for Astrophysics during 2010.

Date Signature of candidate

I hereby certify that the candidate has fulfilled the conditions of the Resolution and Regulations appropriate for the degree of PhD in the University of St Andrews and that the candidate is qualified to submit this thesis in application for that degree.

Date Signature of supervisor

Copyright Agreement

In submitting this thesis to the University of St Andrews I understand that I am giving permission for it to be made available for use in accordance with the regulations of the University Library for the time being in force, subject to any copyright vested in the work not being affected thereby. I also understand that the title and the abstract will be published, and that a copy of the work may be made and supplied to any bona fide library or research worker, that my thesis will be electronically accessible for personal or research use unless exempt by award of an embargo as requested below, and that the library has the right to migrate my thesis into new electronic forms as required to ensure continued access to the thesis. I have obtained any third-party copyright permissions that may be required in order to allow such access and migration, or have requested the appropriate embargo below.

The following is an agreed request by candidate and supervisor regarding the electronic publication of this thesis: access to printed copy and electronic publication of thesis through the University of St Andrews.

Date Signature of candidate

Date Signature of supervisor

Abstract

This thesis presents both a study of the cluster-scale environments in which massive stars form, investigating in particular how the ionized gas in these regions relates to the molecular star-forming material, as well as detailed studies of two luminous forming stars, AFGL 2591 and IRAS 20126+4104, to determine whether they are forming similarly to their low-mass counterparts.

The results of this work include the identification of 35 HII regions (20 newly discovered) via a radio continuum survey of ionized gas towards 31 molecular cluster-forming clumps. The observed ionized gas was found to be preferentially associated with the clumps, which were shown to have a range of evolutionary stages. The massive star formation efficiency was determined for the clumps with associated ionized gas, and a relationship was found between the mass of the clumps and the mass of their embedded massive stars.

By modeling the SEDs and images of AFGL 2591 and IRAS 20126+4104, it was found that the geometry of their circumstellar material was generally consistent with an envelope plus disk, similar to that expected for low-mass protostars. However, within the central $\sim$1800 AU, the mid-IR images of IRAS 20126+4104 were better described by only a flattened envelope, suggesting that the radiation from IRAS 20126+4104 may be affecting the regions closest to the star.

Observations of the ionized and molecular gas towards AFGL 2591 were carried out, and a photoionization code was developed to interpret these observations. The results showed that the observed 3.6 cm emission is likely to be produced by both a shock-ionized jet and a hypercompact HII region that does not appear to have disrupted the jet or the large-scale circumstellar environment. In addition, the $C^{18}O$(1-0) emission observed towards AFGL 2591 traces the densest parts of the outflow, with the blue-shifted emission exhibiting many of the properties of the outflows from low-mass protostars.

Acknowledgements

There are several people without which this thesis would not have been possible. First and foremost, I want to thank my supervisors. I appear to have a habit of collecting them, but I am proud of my collection! First, there's Kenny Wood. Thank you Kenny for being such an enthusiastic supervisor! I really enjoyed working with the Monte Carlo code later on in my PhD. Second there's Deb Shepherd. Thank you Deb for teaching me the ways of radio interferometry, and for investing so much time to patiently teach me data reduction, give me a thesis topic, and to keep me going in the right direction. I want you to know I am really grateful. Third, a late addition, there is Eric Keto. Thank you Eric for being forthright in your comments and criticisms, from them I can safely say that I learnt something while at Harvard.

In addition to STFC, who sponsored my PhD studentship, thanks also to NRAO and CfA for having me as a Graduate Intern and a predoc during my PhD. Although completely different places, I thoroughly enjoyed my time in both Socorro and Cambridge, and meeting and working with the people there.

One thing a PhD student needs is sustenance. Thank you to all the students and postdocs at NRAO and CfA who made the marvelous coffee (and even sometimes cakes!) so we could take a break to have a chat. Also, rainy Mondays in St Andrews were always made bearable by the weekly pilgrimage of the PhD students and postdocs to the Whey Pat Tavern, to feed our addiction to bacon and brie sandwiches and quiz machines.

Thank you Mum, Dad, Lou and Rich, for always cheering me on. Finally, thank you Tom for always believing I could do it, for supporting me through it all, and for agreeing to proof read it too. So here it is.

Contents

List of Figures

List of Tables

1

Introduction

Although far fewer in number than their low-mass siblings, massive stars ($M_\star > 8\,M_\odot$) dominate the evolution of our Galaxy. During their short ($\lesssim$15 Myr) lifetimes, these brilliant stars shape and inject vast amounts of energy into their surroundings via the production of H II regions and stellar winds. In death, their dramatic supernova explosions enrich the surrounding interstellar medium with the heavier elements required to synthesise planets and ultimately life. However, their energy production can also eventually destroy the molecular clouds in which they, and lower mass stars, form. Hence they are the linchpin in the cycle of star and planet formation in the Galaxy.

Historically, massive stars have also played an important role in the first steps taken towards an understanding of star formation. Just over 60 years ago, they provided one of the first pieces of evidence that star formation was an ongoing, and hence observable, process in the Milky Way. In 1948 Spitzer commented, that the “similarity of the distribution between [high luminosity] stars and interstellar matter suggests that such stars have been formed from interstellar matter, and may even be forming at the present time" (Herbig, 2002). This

was inferred from the then recent finding that early-type stars had short lifetimes, due to the fact they rapidly consume their nuclear energy supplies, and therefore must exist close to their birthplaces.

He was surely right, as in the following decades astronomers went on to discover and observe thousands of forming stars throughout the Galaxy. The first of these young stellar objects to be observed, in the constellation of Taurus (Joy, 1945), had masses similar to that of the Sun, and in addition many of the subsequently studied nearby star formation regions were dominated in number by low-mass objects. Due to this fact, much of the theory and observation of forming stars was geared towards stars of these masses (as noted by Shu et al., 1987).

In contrast, due to the rarity of massive stars, the regions in which they form lie at much farther distances. In addition, it appears that the majority of their formation has already occurred once they become optically visible. Therefore, although massive stars provided the first clue to the origin of stars, it was not until more recently, with the advent of high resolution observations at infrared through centimetre wavelengths, that we have been able to observe them in detail, and hence begin to construct the theory of their formation.

This thesis concerns the formation of massive stars, and whether their formation bears resemblance to that of their low-mass counterparts. Therefore, in the following two introductory sections I will firstly give an outline of the paradigm of low-mass star formation, which will provide a framework for the latter section concerning the observations and current theory of the formation of massive stars.

1.1 The Paradigm of Low-Mass Star Formation

1.1.1 The Collapse of a Star-Forming Core

Stars form in dense clouds mostly composed of molecular hydrogen. Structurally, these giant molecular clouds are highly hierarchical, with sizes of up to 100 pc and masses of $10^6\,M_\odot$, down to the densest cores of approximately 0.1 pc and $\sim$1 $M_\odot$. In their quiescent state, they are also very cold, being opaque to external radiation and cooled to temperatures of $\sim$10 K by a range of molecular, atomic and thermal emission processes.

When considering only the gravitational and thermal pressures in these roughly isother-

mal clouds, it is possible to calculate a length scale over which a small density enhancement in the cloud becomes unstable to collapse, the Jeans length:

$$\lambda_J = c_s \sqrt{\frac{\pi}{G\rho}}, \tag{1.1}$$

where c_s is the isothermal sound speed $c_s = \sqrt{kT/m}$, ρ is the characteristic density of the original enhancement, and m is the average particle mass. This length scale also corresponds to a minimum mass (the 'Jeans mass') defined as $M_J \sim \rho \lambda_J^3$, giving $M_J \propto T^{3/2}/\rho^{1/2}$. Therefore, within the densest regions of the cloud where $\rho \sim 10^{-18} \mathrm{g\,cm^{-3}}$, the smallest scale on which the gas will be unstable to collapse is on the order of 0.1 pc, and has a mass of approximately $1\,\mathrm{M}_\odot$.

In the absence of any additional forces, the high densities and low temperatures of these clouds should therefore allow them to quickly and efficiently collapse to form stars. However, the star-forming efficiencies of giant molecular clouds are observed to be on order of only a few percent (e.g. Myers et al., 1986). Therefore there must be further forces at work within molecular clouds to mitigate this rapid collapse.

There are two main suspects which have been considered for this task, one being magnetic fields, and the other turbulence. Historically, the first to be considered were magnetic fields (c.f. Shu et al., 1987). If magnetic pressures are sufficiently large to halt collapse in a star-forming core, making the core 'subcritical', the structure can then exist in a quasi-equilibrium state where collapse occurs on the timescale for the neutral gas to slowly slip through the field lines relative to the ionized gas (a process called ambipolar diffusion). However, both observational (Crutcher, 1999), and theoretical (Nakano, 1998) arguments have suggested that most cores in molecular clouds are instead supercritical, that is, their mass and therefore gravitational energy is large enough to overcome that of their magnetic field. Yet, although they may not have a dominant role in the collapse of a star-forming core, magnetic fields may provide important mechanisms for governing momentum transport in disks, and to launch the jets observed towards young stars (see Section 1.1.3). In addition, results from recent dynamical simulations (Vázquez-Semadeni et al., 2005; Price & Bate, 2009) suggest that, in conjunction with turbulence, magnetic pressures mitigate but do not halt collapse; making them an important factor in recovering the observed low star

formation efficiencies.

The internal random motions observed in molecular clouds, known as turbulence, provide another means to support them against collapse. These both sub- and supersonic motions are observed down to the scales of the smallest cloud cores, with power-law correlations between the velocity dispersion and the size, mass and density of the observed regions (e.g. Larson, 1981). For instance, the velocity dispersion in a cloud σ is related to the size of the cloud L by the relationship $\sigma(\mathrm{kms}^{-1}) = 1.10\ L(\mathrm{pc})^{0.38}$. Such results suggest molecular clouds may actually be structured by turbulence, as supersonic motions can create large density fluctuations via shocks. Therefore turbulence can globally support giant molecular clouds, while locally shock-created density fluctuations become unstable to collapse. However, it is not yet clear what the dominant method of generation of turbulence in molecular clouds is (possibilities include injection of momentum from jets and outflows, Nakamura & Li, 2007, or driving via galactic tidal forces, Ballesteros-Paredes et al., 2009) nor whether the motions are decaying from an initial injection of turbulence or if they are continually driven (Offner et al., 2008).

Whether the collapse of a core occurs dynamically over short timescales (estimated by the free fall timescale, which depends on the initial density: $t_{\mathrm{ff}} = (3\pi/32G\rho)^{1/2} \sim 10^4 - 10^6$ yr), or is slow and mediated by processes such as magnetic fields, occurring on timescales several to a hundred times larger than that of the dynamical timescale ($\sim 10^6 - 10^8$ yr), the result is a centrally condensed envelope with a density profile, in the case of an isothermal core, falling off as $\rho \propto r^{-2}$ (see Larson, 2003, and references therein). Simulations of the spherical collapse of a non-magnetized core (Larson, 1969; Penston, 1969; Hunter, 1977) show that the core becomes opaque to thermal radiation, and the temperature in the central region rises to support it against gravity, creating a hydrostatic core of approximately $0.01\,\mathrm{M}_\odot$ and a radius of several AU. This hydrostatic core then continues to accrete from its surrounding envelope until it reaches temperatures of $\sim 2000\,\mathrm{K}$, above which the molecular hydrogen dissociates and a second central collapse occurs to form the protostellar core (c.f. Masunaga et al., 1998). This protostar, composed of ionized hydrogen, has an initial mass of $< 0.001\,\mathrm{M}_\odot$ and a radius of $\sim 1\,R_\odot$. After quickly accreting the first central core, the protostar finally settles into radiative equilibrium, subsequently accreting the majority of its mass from the surrounding envelope. In the case of a core which has slowly condensed via ambipolar diffusion (referred to as a single isothermal sphere or SIS, Shu, 1977), the

collapse is assumed to begin from rest at the point of formation of the central protostar, and undergo collapse 'inside-out', giving a constant infall rate of $\dot{M} \sim c_s^3/G$. In this case, a constant temperature of 10 K gives an infall rate of 10^{-6} $M_\odot yr^{-1}$. The remaining spherical collapse of a non-magnetized core predicts a higher initial accretion rate onto the protostar due to the higher density of the infalling envelope, and also due to the fact that the core is not initially at rest, but infalling, at the point of formation of the central object. Subsequently, the infall into the dynamically evolving core decreases rapidly as the material in the surrounding envelope is depleted. This decrease in accretion with time is supported by observations; for example, André et al. (2000) found decreasing accretion rates in protostellar cores by comparing their outflow momenta as a function of envelope mass.

1.1.2 The Formation of a Disk

If the collapsing core described in Section 1.1.1 has any rotation, then the conservation of angular momentum dictates a disk will form with radius $R_d = \Omega_0^2 \varpi_0^4 / G M_{\rm sys}$, where Ω_0, ϖ_0, and $M_{\rm sys}$ are the initial angular velocity, cylindrical radius and mass of the system respectively. For an isothermal, slowly rotating core of initially constant density, collapse occurs to form an infinitely thin disk with a surface density profile of $\Sigma \propto \varpi^{-1}$ (e.g. Saigo & Hanawa, 1998). The material accretes through the disk more slowly than in the non-rotating case of dynamical collapse given by Larson, Penston and Hunter (1969, 1969 and 1977 respectively), with an infall rate of $\dot{M} \sim c_s^3/G$, and a constant rotation speed throughout.

However, if the core is already centrally condensed before collapse, and contains a central accreting object, the collapse occurs slowly from inside-out. With the assumptions that the density is distributed uniformly at large radii and the central source dominates the dynamics, both Ulrich (1976) and Cassen & Moosman (1981) found the density and velocity structure of such a rotating core. In their models, the infalling matter spirals in towards the star on parabolic trajectories until it accretes onto the disk, which is formed at the centrifugal radius R_d given above. The material arrives at the disk with sub-Keplerian velocities, and therefore in the absence of any other forces the material slowly spirals inward. This solution for the disk density and dynamics has also been joined at larger radii to the solution expected for the collapse of a SIS by Terebey et al. (1984).

Another way in which the disk itself can be modelled is to assume that the rotation of the disk is Keplerian, and that self-gravity is unimportant. As the rotation is centrifugally

balanced, some form of energy loss causing the matter to accrete is required. This has been commonly added to disks via an 'alpha prescription', where the angular momentum loss between two adjoining annuli is assumed to be caused by viscous dissipation from rotational shear (Shakura & Sunyaev, 1973; Pringle, 1981). If the viscosity is caused by turbulence in the disk, the effective kinematic viscosity can be given as $\nu \sim \upsilon \times l$, where l and υ are the size and velocity of the largest eddies. For a disk with a finite height, the maximum eddy size must be smaller than the disk height H, which also dictates that the velocity of the eddies should be smaller than the sound speed c_s, as the sound speed sets the height of the disk in hydrostatic equilibrium. These requirements can be written as $\nu = \alpha c_s H$, where $\alpha \leq 1$. To reproduce T Tauri star accretion rates of $\sim 10^{-8}\,\mathrm{M}_\odot\ \mathrm{yr}^{-1}$, Hartmann et al. (1998) found $\alpha \sim 0.01$.

Assuming hydrostatic equilibrium, the vertical structure of a disk is given by:

$$\rho = \rho_0(\varpi) \exp\left[-\frac{1}{2}(z/H)^2\right], \tag{1.2}$$

where z is the distance from the disk midplane, $\rho_0(\varpi)$ is the radial density structure of the disk in the midplane along the cylindrical radius ϖ, H is the disk scale height ($H = c_s\varpi/\upsilon_K$), and υ_K is the Keplerian velocity. As the gravitational force towards the disk compared to the force due to thermal pressure diminishes with increasing radius ϖ, H is an increasing function of radius, and the disk is flared. Hence the vertical structure of the disk generally depends on the disk temperature profile. When the alpha prescription outlined above is assumed, the density along the midplane can also be derived, giving $\rho_0(\varpi) \propto (1/\varpi)^{3+3q/2}\left(1-\sqrt{R_0/\varpi}\right)$ where q is the radial dependence on temperature ($T \propto \varpi^q$).

For a 'passive' thin disk solely receiving and re-radiating energy from the central protostar as a blackbody, the disk temperature has a power law decreasing as $T \propto \varpi^{-3/4}$ (Adams & Shu, 1986). However, taking into account the flared nature of the disk produces a different temperature structure. This has been derived self-consistently with the vertical structure of the disk by D'Alessio et al. (1998), who find a shallower temperature dependence of $T \propto \varpi^{-1/2}$, which can be explained by the fact that a flared disk intercepts more of the stellar radiation at larger radii than a flat disk.

There are physical mechanisms of angular momentum transport which may be able to take the place of the parameterized viscosity above, such as more rigorous hydrodynamics,

magnetic rotational instability (MRI, Balbus & Hawley, 1991) or self-gravitation. In the case of self-gravitation, the disk becomes unstable to fragmentation, developing large density perturbations. These density fluctuations create gravitational stresses that aid the transport of angular momentum. A measure of a disk's susceptibility to fragmentation is the Toomre Q parameter, which balances the effects of thermal and rotational support against self-gravity:

$$Q = \frac{c_s \Omega}{\pi G \Sigma}, \tag{1.3}$$

where c_s is the speed of sound in the gas, Ω is the angular velocity of the disk, and Σ is the surface density. Sufficiently small values of Q ($\lesssim 1$), lead to disk instability. For a given rotation rate, the interplay between these factors may cause more massive disks around high-mass stars to fragment (e.g. Kratter & Matzner, 2006). This will be revisited in Chapter 3 where the stability of the disk around the accreting high-mass star IRAS 20126+4104 will be investigated.

1.1.3 Observational Signatures of Low-Mass Star Formation

1.1.3.a Spectral Energy Distributions

The continuum flux from a protostar and its surrounding accreting envelope and disk as a function of wavelength, or its spectral energy distribution (SED), can be a powerful tool in determining its evolutionary status. When the protostar first begins accretion, the inner parts of the envelope are opaque at shorter wavelengths, so that only the outer layers emit in the far-IR and sub-mm. As the envelope disperses due to accretion, the central regions become less and less obscured, so that the emission from the central object is slowly revealed, and the peak of the SED shifts to shorter wavelengths. At early times, the majority of this continuum emission is produced by either scattering, or absorption and thermal emission from dust grains contained within the surrounding circumstellar material. These grains are composed mostly of silicate and carbon, with sizes in the range $\sim$0.01-1μm (e.g. Mathis et al., 1977). Compared to the mass in gas, this dust constitutes only about 1% of the total mass within molecular clouds.

As mentioned above, the shape of protostellar SEDs can be used to determine where young stellar objects (YSOs) are in their evolution. The general shapes of SEDs have been divided into four categories, which are thought to represent an evolutionary progression:

Class 0, I, II and III. Classes I-III were originally defined by the spectral slopes of the SEDs between near- and mid-IR wavelengths (Lada, 1987), which decrease with age due to the dispersion of circumstellar material. Class 0 was added later by André et al. (1993), when a new class of object, undetectable at $<10\,\mu m$ at the time, was discovered at sub-mm wavelengths. Correspondingly, Class 0 sources are highly embedded and emit a significant portion of their flux at these wavelengths. In addition, although they are the most short-lived objects of the four classes, with ages on the order of 10^4 yr (André et al., 2000), the majority of the surrounding circumstellar material is accreted by the protostar during this stage. In comparison, Class I objects have ages of $\sim 10^5$ yr, and Class II and III sources have ages >1 M yr.

In agreement with theory, observations in the 1980s began to show that the circumstellar material surrounding young stars that have dispersed the majority of their envelope was not spherically distributed, but concentrated into a disk (e.g. Cohen & Schwartz, 1983; Appenzeller et al., 1984). This led Shu & Adams (1987) to propose a four-stage evolutionary sequence which consisted of: i) the slow formation of a core via ambipolar diffusion ii) the collapse of the core to form a central protostar with a nebular disk and accreting envelope, iii) the formation of bipolar cavities which are cut out of the envelope by a stellar wind allowing the formation of a jet or outflow, and iv) the dissipation of the envelope to reveal a remnant nebular disk. The final three stages of this process correspond conceptually to Classes 0-II.

Due to the presence of a non-spherical circumstellar geometry, the simplified observational classification scheme described above can sometimes be incorrect due to inclination effects (e.g. Whitney et al., 2003). For example, if a Class II source with a disk is seen edge-on, the optical depth towards the star is increased and can therefore lead to an incorrect classification as a younger object. Conversely, Class I objects may be misclassified as Class II if they are observed pole-on, and bipolar cavities in the envelope have been carved out by a jet or outflow (see Section 1.1.3.d).

When modelling the radiative processes which govern the emission from an embedded protostar, the emergent SED may be used to infer the temperature and density structure of the circumstellar material. With several assumptions about the dust and geometry, it is possible to obtain spatial information solely from the SED. These assumptions include that the gas and dust are coupled and therefore share the same temperature, a prescription for

the dust properties, and that a specific type of geometry describes the source, such as a power-law envelope, a disk, or both. Such modelling has been carried out for low-mass pre-main sequence stars by many authors; famous examples include Adams et al. (1987), Kenyon & Hartmann (1987) and Chiang & Goldreich (1997). More recent examples also include Robitaille et al. (2007) and Alcalá et al. (2008), who modelled the SEDs of the YSOs in Taurus and Chamaeleon respectively. In addition to modelling SEDs, images of YSOs have also been used to further constrain the geometry. For example, Cotera et al. (2001) and Pinte et al. (2008) modelled both the SED and images of the T Tauri stars HH30 and IM Lupi respectively. Chapters 3 and 4 will present similar in-detail modelling of two more luminous YSOs, IRAS 20126+4104 and AFGL 2591.

1.1.3.b The luminosity problem

The expected luminosity of an accreting source can be expressed as the potential energy lost by matter falling from infinity on to the stellar radius:

$$L_{\rm acc} = f_{\rm acc}\frac{GM_\star\dot{M}_\star}{R_\star}, \tag{1.4}$$

where $M_\star$ and $R_\star$ are the stellar mass and radius, $f_{\rm acc}$ is the fraction of this energy actually dissipated in accretion, and $\dot{M}_\star$ is the accretion rate. If the majority of accretion has occurred after $\sim 10^5$ yr, at the end of the Class I phase, this requires an accretion rate of $5\times10^{-6}\,{\rm M}_\odot\,{\rm yr}^{-1}$ over this period to build a 0.5 solar mass star. From these values, and assuming $f_{\rm acc}\sim 1$ and an upper limit to the stellar radius of $R_\star \sim 4R_\odot$ (Masunaga & Inutsuka, 2000), equation 1.4 gives $L_{\rm acc}\sim 20\,{\rm L}_\odot$, much higher than the observed luminosities of Class I objects in Taurus, which are found to be $\sim 0.5\,{\rm L}_\odot$ (White & Hillenbrand, 2004). This is the basis of what has been called 'the luminosity problem' (Kenyon et al., 1990). However, there are several ways in which this discrepancy may be addressed. For instance it is unlikely that $f_{\rm acc}=1$, and mechanisms such as absorption of energy by the star or removal of momentum by outflows may be able to reduce this fraction. In addition, Kenyon et al. (1990) suggested two further solutions - that the accretion could continue significantly to later stages, or that accretion occurs episodically during the main accretion stage, so that accreting stars intermittently become highly luminous FU Orionis objects. Accretion decreases sharply towards the T Tauri stage, with typical accretion rates of $10^{-7}-10^{-9}$ ${\rm M}_\odot\,{\rm yr}^{-1}$ (Gullbring et al., 1998), so extended accretion can be ruled out. However, recent results from evolutionary

models including episodic accretion (Dunham et al., 2010) suggest that currently this is the best explanation for the discrepancy. Thus it may be that the material is accreted at a much higher rate through the surrounding envelope, and is then 'stored' in the disk until the next burst of accretion.

1.1.3.c Disks around Low-Mass Stars

In this section concerning disks around low-mass stars, a summary of the properties of revealed disks around T Tauri stars, which correspond to the later stages of pre-stellar evolution, will be presented, followed by a description of more recent studies of disks around low-mass protostars still embedded in their infalling gas envelopes.

In the case of disks around T Tauri stars, a wealth of information concerning their properties has been gleaned from using submillimetre and millimetre interferometric imaging. Observations of dust continuum emission have provided measurements of disk radii, which have a distribution peaking at ∼200 AU, and disk masses, which are on order of $10^{-3} - 10^{-1}\,M_{\odot}$ (e.g. Kitamura et al., 2002; Andrews & Williams, 2007). In addition, they also show that the radial surface density distributions of these disks vary as $\Sigma \propto r^{-p}$ with $p = 0 - 1$.

A further finding is that the observed slopes of the SEDs of revealed disks at sub-mm/mm wavelengths are shallower than for the emission from dust in the interstellar medium (ISM). For optically thin dust emission, $F_\nu = \kappa_\nu B_\nu(T)$, where F_ν is the observed flux, κ_ν is the dust opacity, and $B_\nu(T)$ is the blackbody emission from a source at a given temperature T. Therefore the SEDs can be explained by a shallower opacity dependance compared to that for dust in the ISM, which is $\kappa \propto \nu^2$ (Kim et al., 1994), suggesting that grain growth has occurred in these disks, possibly up to millimetre and centimetre sizes. This process is thought to occur via collisions, where the grains coagulate, then decouple from the gas and settle to the disk midplane. This material is then thought to take part in the building of planets. Both optical and near-IR images have also shown that these disks are not flat, but have flared geometries as expected if they are in hydrostatic equilibrium (e.g. Burrows et al., 1996, see also Section 1.1.2).

Observations of T Tauri disks in molecular line emission such as CO(J=2-1) show that they are in Keplerian rotation (e.g. Simon et al., 2000). The inner most radii of disks can also be observed using transitions of CO, water and H_2 at UV and near-IR wavelengths (Na-

jita et al., 2007). Such observations show that the gas in disks is truncated at $\sim$0.04$-$0.1 AU, whereas the dust is sublimated further out at temperatures of $\sim$1600 K, at typically 0.1$-$0.3 AU (Eisner et al., 2005b).

Measurements of the fraction of sources with disks in clusters of different ages show that most disks have been dissipated by 6 Myr (e.g. Haisch et al., 2001). Furthermore, for solar mass stars and higher, the disk lifetime is inversely correlated with the mass of the star (Hillenbrand & Hartmann, 1998; Hernández et al., 2007). This has important implications for the lifetimes of disks around massive stars, for which revealed disks are very rare, suggesting they are dispersed very soon after the envelope is dissipated. A process which aids the dissipation of disks and therefore reduces their lifetimes is photoevaporation. In low-mass stars, the surface layers of the disk are ionized by EUV, FUV and X-ray photons from accretion and excess chromospheric activity from the central star, and also from other massive stars in their vicinity. The increased thermal energy of the ionized gas allows it to escape the gravitational potential of the star, and flow off the disk (see e.g. Dullemond et al., 2007).

Revealed disks around low-mass stars are often observed to be accreting; this is inferred from disk infrared excesses which are higher than expected from disks solely irradiated by their central stars (e.g. Hillenbrand & Hartmann, 1998), and in the continuum veiling of photospheric absorption and emission lines in the UV by shocked gas accreting onto the stellar surface. As mentioned in Section 1.1.3.b, these accretion rates are found to range between 10^{-7} and 10^{-9} $M_\odot\,yr^{-1}$ (Gullbring et al., 1998), and also decrease over time (e.g. Hartmann et al., 1998), which is a natural consequence of disk dissipation.

More recently, studies of disks still embedded within their accreting envelopes have also been carried out. These studies commonly employ radiation transfer modelling of mm images, and in some cases the source SED and infrared images, to disentangle the signatures of the disk and envelope (e.g. Looney et al., 2003; Eisner et al., 2005a; Jørgensen et al., 2009). The results of these studies disagree on whether the disk masses for Class 0 and I sources are similar to those for more evolved Class II or T Tauri disks. With disk masses ranging from 0.0 to 0.12 $M_\odot$, Looney et al. (2003) found no significant difference in the disk masses of Class 0 stars to that of Class I/II objects. Similarly, Jørgensen et al. (2009) found that there appeared to be no correlation of the disk mass with evolutionary stage in their results, with disk masses of $\sim 0.05\,M_\odot$ for their embedded sources. If these findings are confirmed,

they suggest that the disk mass is set early-on in the evolution of the protostar, and that the processing of matter through the disk is relatively stable over the duration of its formation. In contrast, Eisner et al. (2005a) found that the disks of their observed Class I objects have masses ranging up to $1\,M_{\odot}$, suggesting that they are close to or larger than the limit for gravitationally stable disks, which may lead to episodes of enhanced accretion caused by gravitational instabilities. A similar result was found by Enoch et al. (2009) who uncovered a massive ($\sim$$1\,M_{\odot}$) disk around the source Serpens FIRS1.

When determined, the sizes of embedded disks are several hundreds of AU, similar to their more evolved counterparts (e.g. Pudritz et al., 1996; Jørgensen et al., 2005; Enoch et al., 2009). For Class I sources, the dynamics in their disks have also been found to be Keplerian (Jørgensen et al., 2009), but for the younger objects in this study, outflows or envelope emission hampered the measurement of their disk dynamics.

As the timescale for the formation of massive stars, which will be discussed in Section 1.2, is far shorter than in the case of their low-mass counterparts, the disks around these objects spend the majority of their existence embedded in a surrounding envelope. Therefore it is the properties of disks around low-mass Class 0 and I objects which are likely to correspond to those around massive stars. This also explains the difficulty of observing disks around massive stars, as their emission is often confused with optically thick envelope or outflow emission, so that specific disk-tracing molecular transitions are required, to unambiguously trace the dense gas within the disk.

1.1.3.d Jets and Outflows

The jets and outflows observed towards low-mass young stars are thought to be symptoms of the same process. Rows of bright, optically visible knots which extend out to distances of several pc from the powering source, known as Herbig-Haro objects, were the first evidence that matter was being ejected from young stars. These were later realized to be sections of jets, with aspect ratios of 10-100:1 that reach velocities in excess of $100\,\mathrm{kms}^{-1}$, creating both internal and terminal bow shocks as they interact with the surrounding core and ambient cloud. Outflows, on the other hand, are large amounts of ambient molecular material (up to $10^{-6}\,\mathrm{M}_{\odot}\,\mathrm{yr}^{-1}$, Bontemps et al., 1996), observed in molecular lines at (sub-)millimetre wavelengths, which have been carried along by the original wind or jet. These outflows, which are in general less collimated than their associated jets, usually extend between 0.1

to 1 pc from the central object at velocities typically between $10-100\,\mathrm{kms}^{-1}$ (Arce et al., 2007).

Jets can be observed via several tracers, including optical Hα and forbidden lines (e.g. Bacciotti et al., 2000), near-IR and near-UV (Coffey et al., 2007, 2010), X-rays (Güdel et al., 2008), and continuum emission at radio wavelengths (Rodríguez et al., 1995; Anglada, 1996). As the post-shock gas in a jet is heated to $\sim 10^4$ K, the material is partially ionized. The electron density, ionization fraction and temperatures in the jets can be determined from line ratios, and are found to be $n_e = 50 - 3 \times 10^3$ cm^{-3}, $x_e = 0.03 - 0.6$ and $T_e = 1.3 - 1.8 \times 10^4$ K (Podio et al., 2006). Mass loss rates can therefore be calculated by combining these results with the observed velocities of the jet, giving values of $\sim 5 \times 10^{-8}\,\mathrm{M}_\odot\mathrm{yr}^{-1}$, which are 5−10% of the accretion rates determined via continuum veiling (Ray et al., 2007). This result suggests that the jet launching mechanism is linked directly to accretion.

Evidence for a link between small-scale jets and large-scale outflows can be seen from the centimetre emission observed towards the majority of the youngest objects (Anglada, 1996). For resolved sources, this emission is usually elongated and aligned with the large-scale molecular outflow (e.g. Rodríguez et al., 1995), with an extent for low-mass sources of ∼100 AU; therefore it is likely this emission traces a jet at the base of the flow. These jets have velocities measured from proper motion studies of several hundreds of $\mathrm{km\,s}^{-1}$, and are sometimes one-sided, which cannot be due to extinction effects at radio wavelengths. Instead, this may be due to inhomogeneities in the surrounding material which the jet ploughs into. A good example of such an asymmetric jet is seen towards the embedded B-type star AFGL 2591, presented in Figure 4.4 of this thesis. The spectral index of these compact jets, α, where $S_\nu \propto \nu^\alpha$, is consistent with thermal free-free emission, with values intermediate between -0.1 expected for optically thin emission, and 2 for optically thick. While it may be possible to explain the observed centimetre fluxes of high luminosity sources by photoionization by the central star, as their FUV fluxes are, in principle, large enough to ionize their surroundings and reproduce the observed fluxes, the cm emission from young low-mass sources is many orders of magnitude too high to be explained by this mechanism. Instead, this emission can be modelled successfully by shock-ionized gas in a collimated stellar wind (Curiel et al., 1989; this 'stellar' wind may be instead a disk or X-wind, see below). Correlations between the observed centimetre flux and the source bolometric luminosity, or alternatively

the centimetre flux with the momentum outflow rate of the large-scale associated CO outflow (e.g. Cabrit & Bertout, 1992; Anglada, 1996; Shirley et al., 2007), are further evidence towards the idea that small-scale jets and larger-scale outflows are related, and are different manifestations of the same process.

Further power-law correlations can be derived between the bolometric luminosities of YSOs and their large-scale outflow energetics, such as momentum outflow rate and outflow mass (e.g. Wu et al., 2004). These correlations exist over five decades of luminosity, ranging from $\sim 1 - 10^5\,L_\odot$, therefore encompassing both low and high-mass stars. This provides strong evidence for a similar outflow mechanism for all stellar masses, which will be revisited in Section 1.2.

For well collimated sources, there is also a relation between the flow velocity and the distance from the powering source, commonly referred to as the Hubble law for outflows, in which the maximum velocity of the outflowing gas increases approximately linearly with distance from the source (as the entrained material is slowly accelerated by the jet). Jets and outflows sometimes have multiple bow-shock or expanding shell morphologies, supporting the idea that they are episodically accreting. In addition, the collimation of outflows is seen to decrease with time (Arce & Sargent, 2006), and with the luminosity of the central object (Wu et al., 2004).

The two main models put forward as the driving mechanisms of outflows have been jets and winds. For a jet-driven outflow, the ambient material is collected behind the jet bow-shocks, therefore creating a high density shell of material around the jet which flows away transversely from the shock. However, the jet-only driven model cannot explain the wide-angle outflows observed towards some sources. Wind-driven models instead model outflows as a wide-angle wind which ploughs the ambient material producing a “wind-swept shell" (Shu et al., 1991). In many cases, the observations suggest a combination of these, with a central high-velocity jet surrounded by a slower wide-angle wind (Arce et al., 2007).

As to the cause of these jet/wind mechanisms, magneto-hydrodynamical (MHD) winds driven from the disk are able to provide an explanation. If a rotating disk is threaded by magnetic field lines, these can centrifugally launch the material in the upper layers of the disk which are ionized and heated by stellar irradiation (see Section 1.1.3.c). Collimation of the launched material then occurs via the “hoop stresses" of the magnetic field lines that

are coiled around the axis of the disk by its rotation. The two main theoretical mechanisms put forward to produce both a dense jet surrounded by a wide-angle wind, differ principally in the locus of launching. "X-winds" (Shu et al., 1994) are launched from radii just outside the co-rotation radius, at the point where the stellar rotational velocity equals that of the disk, whereas "disk-winds" (Pudritz et al., 2007) are launched from a larger range of disk radii. Due to the close proximity of the magnetic launch points in the disk to the star, X-wind models produce jets with terminal speeds of $\sim 100\,\mathrm{kms}^{-1}$. Alternatively, disk-wind models have a larger range of magnetic foot points in the disk, and therefore initial rotational speeds, leading to a range of terminal outflow velocities. Several studies find that the observed jets have such a range in velocities, consisting of a lower velocity component surrounding a central high velocity component, suggesting that the disk-wind hypothesis is most likely (e.g. Hirth et al., 1997; Pyo et al., 2005).

Finally, outflows have important implications when it comes to the star-forming efficiency of the core, clump and entire cloud they form within, lowering the mass available for accretion, and injecting energy into the parent cloud.

1.2 The Formation of Massive Stars

A brief overview of the current paradigm of low-mass star formation was given in Section 1.1. The following question arises: can this theory be directly applied to massive stars, specifically those with masses greater than $8\,M_\odot$ (B3 spectral types and earlier)? One problem with this proposal can be seen by comparing the Kelvin-Helmholtz contraction timescale of a massive protostar, given by $t_{KH} = GM_\star^2/RL$, where $M_\star$ is the mass of the protostar, and R and L its radius and luminosity, to its accretion timescale $t_{\rm acc} \sim M_\star/\dot{M}_\star$, where the accretion rate is given by $\dot{M}_\star$. For massive stars, $t_{KH} < 10^5\,$yr (see Figure 4 of Zinnecker & Yorke, 2007), on order of $t_{\rm acc}$ ($\lesssim 10^5\,$yr, Osorio et al., 1999). Consequently, massive stars can reach the main-sequence and begin to produce significant amounts of radiation and strong stellar winds before they have finished accreting. This is in direct contrast to low-mass stars, which disperse almost all of their natal material before they reach the main sequence. The potential effects of this difference will be discussed in Section 1.2.1 below.

In addition, in Section 1.1.1 it was mentioned that the Jeans mass in the densest parts of cold, hierarchically structured, molecular clouds was $\sim 1\,{\rm M}_\odot$. Therefore, without any further forces or heating processes acting upon the gas, high-mass cores, which form only one massive star, cannot exist, as they will fragment down to the Jeans mass of the highest density fluctuations within them. This issue has motivated several theories of massive star formation that work to reconcile the problem in different ways. These will be discussed in Section 1.2.2.

Finally, observations of massive stars will be reviewed in Sections 1.2.3 to 1.2.5, including the observed evolutionary stages of massive star formation, disks and outflows observed towards forming massive stars, and SED modelling of these objects.

1.2.1 Radiation Pressure and Ionization Feedback

Larson & Starrfield (1971) first explored the idea that the pressure and ionization caused by radiation could inhibit accretion onto a forming massive star, finding an upper mass limit of $50-60\,M_\odot$. This pioneering work was soon followed by simulations of the effect of radiation pressure on dust grains in accreting matter (Kahn, 1974; Yorke, 1977; Wolfire & Cassinelli, 1987). These studies gave upper limits to the mass which could be accreted, or suggested that the dust around the stars must be altered, or that the accretion must be variable, to

allow sufficient accretion to make a massive star. However, these early simulations assumed that the accretion was spherically symmetric. Instead, it is likely that accretion proceeds through a disk (see Section 1.2.4 concerning observations of disks around massive stars). In this case, radiation pressure can then be funneled out perpendicular to the disk plane, creating a 'flashlight' effect (e.g. Yorke & Sonnhalter, 2002).

Another way to overcome radiation pressure is to simply increase the accretion rate above the values assumed for low-mass stars ($> 10^{-5}\,M_{\odot}$ yr^{-1}). This would push material inside the dust destruction radius, so that then, having its main source of opacity removed, it could accrete unimpeded onto the protostar. The expected rise in temperature of the circumstellar material around a massive star would also increase the sublimation radius, aiding this effect. This is supported by modelling of several massive "Hot Cores" (see Section 1.2.3.b) by Osorio et al. (1999), who found higher accretion rates for these objects ($\gtrsim 6 \times 10^{-4}\,M_{\odot}$ yr^{-1}).

In addition, varying the dust grain properties, such as increasing the average dust grain size, or lowering the effective opacity of the surrounding material, can allow material to continue accreting. One way the effective opacity can be reduced is to accrete material in 'blobs' rather than continuously, the extreme form of this being the coalescence of two protostars to produce one higher mass object (e.g. Bonnell et al., 1998), which will be discussed further in Section 1.2.2.

Recent 3D simulations of the accretion onto forming massive stars have also suggested that outflow cavities and Rayleigh-Taylor instabilities in the interface between the radiation bubble and the accreting material (or accretion 'fingers') can also allow matter to be more efficiently accreted, and therefore overcome radiation pressure (e.g. Krumholz et al., 2005b).

The interaction between an accretion flow and ionizing radiation was first discussed by Walmsley (1995), who found an expression for the mass accretion rate required to 'choke off' the formation of an HII region[1]:

$$\dot{M}_{\rm crit} = \left(8\pi N_{\rm phot} G M_{\star} m_H^2/\alpha\right)^{1/2}, \tag{1.5}$$

where $N_{\rm phot}$ is the ionizing photon flux from the star, m_H is the mass of a hydrogen atom, and α is the recombination coefficient to excited states of hydrogen. This work was extended

[1]The factor of two difference to his equation accounts for the assumption that the accreting material is in free-fall from infinity to the stellar surface, rather than having a Keplerian velocity.

by Keto (2002) and Omukai & Inutsuka (2002), who found that, for a given accretion rate $\dot{M}_\star$, the radius of equilibrium can be expressed as:

$$R_{\rm HII} = R_\star \exp\left[\left(\dot{M}_{\rm crit}/\dot{M}_\star\right)^2\right]. \tag{1.6}$$

Accretion can therefore occur through an HII region, so that there is an ionized gas accretion flow onto the star. Hence the development of an HII region may not immediately halt the accretion process. If accretion can occur through an HII region, this infers that as the star accretes mass and therefore increases in luminosity, the HII region must accordingly evolve.

Taking $R_{\rm HII}$ from equation 1.6 above as the radius of ionization equilibrium, and $R_G = GM_*/2c_s^2$ to be the gravitational radius of the accretion flow, which is the radius at which gravity balances the outward pressure of the ionized gas, the evolution of a spherically symmetric HII region can be followed (c.f. Keto, 2002). At early times, when $R_{\rm HII} < R_G$, the HII region is "trapped" within the accretion flow, and the HII region is a stationary R-type ionization front. For a $10\,{\rm M}_\odot$ B star, and a sound speed c_s of $\sim 10\,{\rm kms}^{-1}$ in ionized gas, $R_G \sim$40 AU; therefore an HII region would be confined by accretion into a very small region surrounding the star. As material is further accreted onto the star, $R_{\rm HII}$ can increase until it is greater than R_G, which itself increases more slowly as mass is added to the star. At the point where $R_{\rm HII} > R_G$ the HII region halts further accretion and begins hydrodynamical expansion.

However, it is again possible to relax the assumption of spherical symmetry for the accreting gas. Recently, Keto (2007) introduced an ionized accretion flow through a disk. To conserve angular momentum, the disk forms at R_D, where the infall velocity equals the rotational velocity and the centrifugal and gravitational forces balance: $R_D = GM_\star/\upsilon_{\rm rot}^2$, where $\upsilon_{\rm rot}$ is the rotational velocity of the disk at R_D. The stages of the evolution of the HII region are then very similar to the spherical case described above, except that due to higher densities in the disk, $R_{\rm HII}$ is now a function of the angle from the disk axis. At first the protostar has not reached the main sequence, so $R_{\rm HII} = 0$ and accretion proceeds through a massive molecular disk. When the star reaches the main sequence and its UV radiation 'turns on', the HII region can expand more rapidly in the direction of the poles while the HII region is trapped along the midplane. As the protostar accretes more material, the HII region will expand to completely engulf the disk, and to ionize more of the actual disk itself. Finally

the HII region will start expanding along the disk via thermal pressures, and halt accretion through the disk; this will occur when $R_{\rm HII}$ along the disk equals R_G. If $\upsilon_{\rm rot} > \sqrt{2}c_s$, so that the radius of disk formation is within the gravitational radius, all of the accreting material within the disk will have been ionized before accretion is halted.

The picture above can also apply to models of photoevaporating disks (Hollenbach et al., 1994). In a similar way to the photoevaporation of low-mass disks (see Section 1.1.3.c), and the ionized accretion scenario described above, the ionized gas is bound to the star within the gravitational radius R_G. Outside this radius, the sound speed in the ionized upper layers of the disk ($\sim 10\,{\rm kms}^{-1}$) exceeds the escape velocity, and the ionized gas expands away from the disk as a wind with a velocity of $\sim 10 - 50\,{\rm kms}^{-1}$.

If the ram pressure of the stellar wind from the central source exceeds the thermal pressure of the photoevaporative 'disk wind' then the upper layers of the disk are also removed within R_G so that the ionizing radiation can travel further into the disk. In addition, the disk wind is pushed out and concentrated by the ram pressure of the stellar wind to radii larger than R_G. From this model, Hollenbach et al. (1994) calculated that disks with masses $2 - 10\,{\rm M}_\odot$ would have lifetimes of $\gtrsim 10^5\,{\rm yr}$.

These calculations were also supported by simulations by Yorke & Welz (1996) and Richling & Yorke (1997), who also found that the combination of the ionized stellar and disk wind were hydrodynamically focused perpendicular to the disk, suggesting that this could be an outflow collimating mechanism which may act instead or in conjunction with the effect of magnetic fields.

1.2.2 Competing Theories in Massive Star Formation

One of the first theories concerning the formation of massive stars was put forward by Shu et al. (1987), who suggested that massive supercritical cores, whose gravity was sufficient to overcome their magnetic pressures, would collapse quickly to form massive stars.

However, in a picture which has evolved to favour the importance of the role of turbulence over magnetic fields in the star formation process, a model which utilizes turbulence as a means of supporting a massive protostellar core against fragmentation has been suggested (McKee & Tan, 2003). In this model, the material which accretes onto the star is sourced almost exclusively from a single massive core that collapses to form the (proto)star.

The core itself is approximated as a polytrope (described by a centrally condensed density power-law) and is stabilized by turbulence, which is assumed to act as a confining pressure. This assumption holds if the core is a quasi-stable entity which exists for several free fall times.

Evidence for an alternative picture of massive star formation is that most, if not all, stars form in clusters (Lada & Lada, 2003), and therefore the formation of stars is intrinsically linked to the formation of clusters. In this picture, the initial fragments which become bound in a turbulent molecular cloud are determined by the approximately solar Jeans mass. The amount of subsequent Bondi accretion of the remaining inter-core gas will then be determined by the core's position in the potential well of the proto-cluster, so that the cores at the centre of the cluster will accrete the largest fraction of the material, and become massive stars. Therefore, in this picture (referred to as 'competitive accretion'), the most massive stars should be found at the centre of clusters, which is in agreement with observations (e.g. Hillenbrand & Hartmann, 1998). The result of these fragmentation and accretion processes also reproduces the stellar initial mass function (Bonnell et al., 2001).

Whenever there are two theories, one is likely to find exception with the other. Dobbs et al. (2005) used simulations to model a massive 'turbulent core', and found that by using either an isothermal or baryotropic equation of state, the massive core fragmented into smaller objects. To address this, Krumholz (2006) and Krumholz et al. (2007) included radiative heating from accretion in simulations of a massive collapsing core, and found that the heating was sufficient to keep the local Jeans mass high enough to inhibit further fragmentation of a massive core, allowing it to collapse to form a massive star.

Conversely, 'competitive accretion' simulations were criticized on the basis that the kinetic energy in their simulations compared to the gravitational energy of the gas (the virial parameter) was lower than observed (McKee & Tan, 2003), and that competitive accretion would not be efficient if the gas was less bound. However, Clark et al. (2008) carried out simulations with a range of virial parameters, which although changed the efficiency with which stars formed from the gas, did not change the physics. In addition, the criticism that Bondi-Hoyle accretion would not be significant in a turbulent medium where the stars have high velocities with respect to the gas (Krumholz et al., 2005a) was countered by the fact that at early times, when the stars are not virialised, the gas and cores do not have high

relative motions, which therefore allows accretion.

Another more extreme mechanism of forming massive stars which has been put forward is stellar mergers. If the (proto-)stellar density in a cluster is high enough to allow significant numbers of mergers to occur ($> 10^8$ (proto-)stars pc^{-3}), this may be an alternative method of forming massive stars (e.g. Bonnell & Davies, 1998; Bonnell & Bate, 2002). However, stellar densities as large as this are not commonly observed, although it has also been suggested that the coalescence of binary systems in accreting clusters could form massive stars, with a more realistic required stellar density of $> 10^6$ pc^{-3} (Bonnell, 2005). Therefore this may be a method to produce massive stars in the most dense OB superclusters.

1.2.3 The Observed Stages of Massive Star Formation

There appears to be four main observational stages of massive star formation suggested by observations. In order of their proposed evolution, they are: High-Mass Starless Cores (HMSCs), High-Mass Protostellar Objects (HMPOs), Hyper Compact HII (HC HII) regions, and Ultra Compact HII (UC HII) regions.

1.2.3.a High Mass Starless Cores (HMSCs)

HMSCs represent the earliest stage of massive star formation known to-date. However, they were not known of until the ISO and MSX missions, with the discovery of Infrared Dark Clouds (IRDCs, e.g. Egan et al., 1998), which were subsequently found to have corresponding millimetre dust continuum or molecular line emission tracing high-mass cores. These cores did not show any infrared emission, suggesting that they did not yet have protostars in their centres, and represented the first stages of massive star formation.

Several surveys have found examples of HMSCs. Garay et al. (2004) was one of the first to present a small number of examples of these cores. Subsequently, Sridharan et al. (2005) provided a list of candidate HMSCs by comparing 1.2 mm emission from Beuther et al. (2002b) with 8.3 μm MSX images. Another survey, carried out using the SEST millimetre telescope by Hill et al. (2005), searched for 1.2 mm emission towards known sites of maser emission or UC HII regions. They also found that a subset of the cores discovered in their fields, which had neither associated maser emission nor UC HII regions, also did not have corresponding MSX emission. Nine IRDCs were surveyed by Pillai et al. (2006) in the first two inversion transitions of ammonia, who found their cores to be cold ($T < 10$ K) and

turbulent ($\Delta v \sim 1-3\,\mathrm{kms}^{-1}$). These dense ($10^5\,\mathrm{cm}^{-3}$, Sridharan et al., 2005) cores are also found to be undergoing global infall (e.g. Peretto et al., 2006), with sizes of approximately $0.25-0.5\,\mathrm{pc}$ and masses between 100 and $1000\,\mathrm{M}_\odot$. Therefore, it is likely that some of these objects are actually cluster forming clumps as opposed to objects which will form one massive star. HMSCs also appear to be very rare, as many of the IRDCs which have been followed up have been shown to have star formation activity (e.g Rathborne et al., 2005). However, recent surveys, such as the Bolocam galactic plane survey (BGPS, Rosolowsky et al., 2010), the APEX telescope large area survey of the galaxy (ATLASGAL, Schuller et al., 2009), and the Hi-GAL survey (the Herschel Space Observatory galactic plane survey at infrared wavelengths, Molinari et al., 2010) should reveal significant numbers of HMSCs across the galactic plane.

1.2.3.b High Mass Protostellar Objects (HMPOs)

When a protostar forms at the centre of a massive core, several observables accompany it. Along with the previously observable core tracers at millimetre and submillimetre wavelengths, infrared emission from the protostellar radiation reprocessed by the heated circumstellar material appears, and often outflows can be observed towards the source. However, no centimetre continuum emission is observed. This may be because the protostar has not yet reached the main sequence, or that the HII region has been 'quenched' by a high accretion rate (see Section 1.2.1 and Walmsley, 1995). Consequently, the bolometric luminosity of the protostar may actually be dominated by its accretion luminosity.

HMPOs are a subset of Hot Cores (the term Hot Core expands to include cores which also have associated HII regions: Garay & Lizano, 1999, Kurtz et al., 2000, Churchwell, 2002). Observationally, Hot Cores are found to be compact (diameters < 0.1 pc), dense ($\geq 10^5$ cm^{-3}) and hot (T > 50 K), with masses ranging between 100 to $300\,\mathrm{M}_\odot$ (Garay & Lizano, 1999).

Maser emission is commonly observed towards HMPOs (Walsh et al., 1998; Beuther et al., 2002c; Codella et al., 2004). This includes methanol, OH and water masers, the first two of which are strongly associated with sites of massive star formation. However it is not yet clear what the dense gas which is masing in these instances is tracing. Usually an outflow or disk origin for the emission is argued. For example, a disk is argued to be the source of OH maser emission towards AFGL 2591 (Hutawarakorn & Cohen, 2005), a forming (proto)star

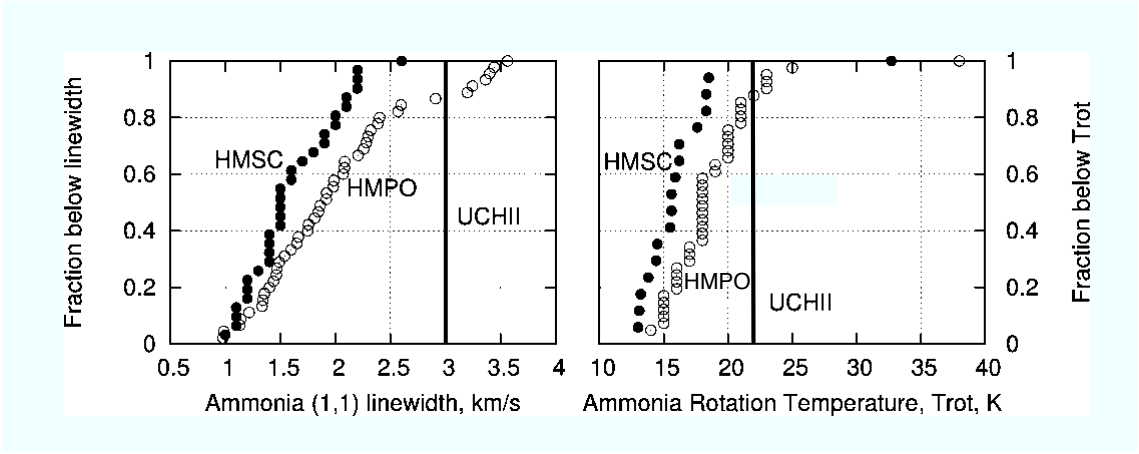

Figure 1.1: The cumulative distributions of line widths and rotation temperatures of the High-Mass Starless Cores and High-Mass Protostellar Objects from Sridharan et al. (2002) and Sridharan et al. (2005), compared with the mean values (3 $\mathrm{km\,s^{-1}}$and 22K) found by Churchwell et al. (1990) for high mass cores associated with UC HII regions.

that will be studied in detail in Chapter 4.

Several authors have studied the dust emission towards HMPOs (e.g. Beuther et al., 2002b; Molinari et al., 2002; Mueller et al., 2002a). The density distributions of these cores are often modelled by radially decreasing power laws with $\rho \sim r^{-1.5}$ (e.g. Beuther et al., 2002b; Williams et al., 2005).

There also appears to be a progression in the measured line widths and temperatures from HMSCs to cores associated with UC HII regions. For example, Sridharan et al. (2002) finds that the $NH_3(1,1)$ line widths measured for HMPOs are less than those towards UC HII regions (a mean of 2.1 $\mathrm{km\,s^{-1}}$ compared to 3 $\mathrm{km\,s^{-1}}$ found by Churchwell et al., 1990). This progression is continued down to HMSCs, where an average linewidth of 1.6 $\mathrm{km\,s^{-1}}$ was measured (Sridharan et al., 2005). Figure 1.1, which is adapted from Sridharan et al. (2005), compares the ammonia line widths and rotation temperatures of the HMSCs, HMPOs, and UCHII regions from the above papers. The decrease in line widths and rotation temperatures towards HMSCs supports the view that these objects do represent the youngest, quiescent stages of massive star formation, and that massive stars evolve from HMSCs to HMPOs to UC HII regions.

1.2.3.c HC HII and UC HII regions

HC HII and UC HII regions are the result of the protostar reaching the main sequence, and hence producing large amounts of UV radiation which photoionizes the surrounding gas. The smallest HII regions that have been found, HC HII regions ($\leq$ 0.05pc), are dense ($\geq 10^6\,\mathrm{cm}^{-3}$) and have large emission measures ($\geq 10^{10}$ pc cm^{-6}). Their radio recombination lines also show broad line profiles ($\Delta v \sim$ 40-50 km s^{-1} e.g. Sewilo et al., 2004). These large line widths are of a non-thermal origin (see Garay & Lizano, 1999), and are most likely due to bulk gas motions such as accretion, outflow or rotation (Keto et al., 2008).

The radio spectral index of HC HII regions α, where $S_\nu \propto \nu^\alpha$, is usually found to be ~ 1 at centimeter wavelengths. This is intermediate between values expected for an optically thin HII region ($\alpha = -0.1$) and optically thick emission ($\alpha = +2$). Such objects have been modelled by HII regions with density gradients (e.g. Avalos et al., 2006), which may be due to the ionized gas being created by an ionized stellar wind - the spectral index expected for a spherically symmetric wind being 0.6 (Panagia & Felli, 1975). However, the fluxes and derived electron densities are too high to fit this explanation. As described in Section 1.2.1, the HII region may instead be 'trapped' by a dense accretion flow, or is the photoevaporative flow from the surface of a disk. In addition, Ignace & Churchwell (2004) modelled the spectra of several UC and HC HII regions as groups of clumps with a power-law distribution of optical depths, and were able to reproduce the intermediate spectral indices observed. Finally, Tan & McKee (2003) have also determined the expected density and shape of cavities created by both disk and X-winds, and ionized this density distribution numerically. From this they were able to successfully reproduce the radio spectrum of the source I in the Orion Hot Core.

UC HII regions are the more evolved counterparts of HC HII regions and were defined observationally by Wood & Churchwell (1989) to be HII regions with sizes < 0.1 pc, densities $\geq 10^4$ cm^{-3} and emission measures (EM) $\geq 10^7$ pc cm^{-6}. While HC HII regions have only been observed fairly recently, the first in-depth study of UC HII regions was performed by Wood & Churchwell (1989). Later corroborated by subsequent surveys (Walsh et al., 1998, Kurtz et al., 1999, and more recently De Pree et al., 2005), they found that the observed UC HII regions fell into several different morphologies, including cometary, spherical, shell-like, irregular and core-halo. Figure 1.2, adapted from Hoare et al. (2007), provides some

examples of these. Any discrepancy between the results of these surveys may be due to the fact that, as mentioned by Wood & Churchwell (1989), spherical UC HII regions usually have a more ordered morphology when observed at higher spatial resolutions. Therefore it is important to be aware that the morphology given to a UC HII region is reasonably dependent on the sensitivity and resolution of the observations.

There are many theories which have been put forward to explain the range of morphologies observed. Some which are commonly invoked include champagne flows, infall models, photo-evaporating disks, or stellar wind supported bow shocks. These and several others are discussed in Churchwell (1999). However none of them can explain both the observed morphology and lifetimes of UC HII regions, as well as their derived properties, such as densities and emission measures. Churchwell (2002) suggested that all of these explanations may be valid at different times throughout the evolution of an UC HII region.

Bipolar UC HII regions (see Figure 1.2, Top left) are a further morphological type which has been observed, which was not mentioned in Wood and Churchwell's survey. Examples of this type are NGC 7538 IRS 1 (Campbell, 1984b; Franco-Hernández & Rodríguez, 2004), G45.48 +0.13 (Garay et al., 1993), and K3-50A (de Pree et al., 1994). Properties of these sources are their broad radio recombination lines ($\sim$ 30-40 $\mathrm{km\,s^{-1}}$ e.g. Afflerbach et al., 1996), and strong velocity gradients along their bipolar axes. These steep gradients (for instance, the source K3-50A has a velocity gradient of $\sim$ 150 $\mathrm{km\,s^{-1}pc^{-1}}$ along its major axis) suggest a wind or jet origin for the ionized gas towards these sources. However, the morphology may also be due in part to the ionized gas being confined by dense circumstellar molecular gas in a flattened envelope or disk.

The number of observed HII regions is actually so large that it presents a problem with the expected lifetimes of UC HII regions. This number suggests a lifetime of $\sim 10^5$ yr, while dynamical arguments give a lifetime of 10^4 yr. Different mechanisms to confine the expansion of the HII region have been suggested, including thermal, turbulent and magnetic pressures, as well as accretion (see section 1.2.1). Another way to prolong the lifetimes of UC HII regions would be to continually introduce neutral material into the ionized region.

There are also relations between the properties of HC and UC HII regions and their physical size L, namely that their electron densities, n_e, and emission measures, EM, both increase with decreasing size. These relationships are given by $n_e = 7.8 \times 10^2\ L^{-1.19\pm0.05}$ and

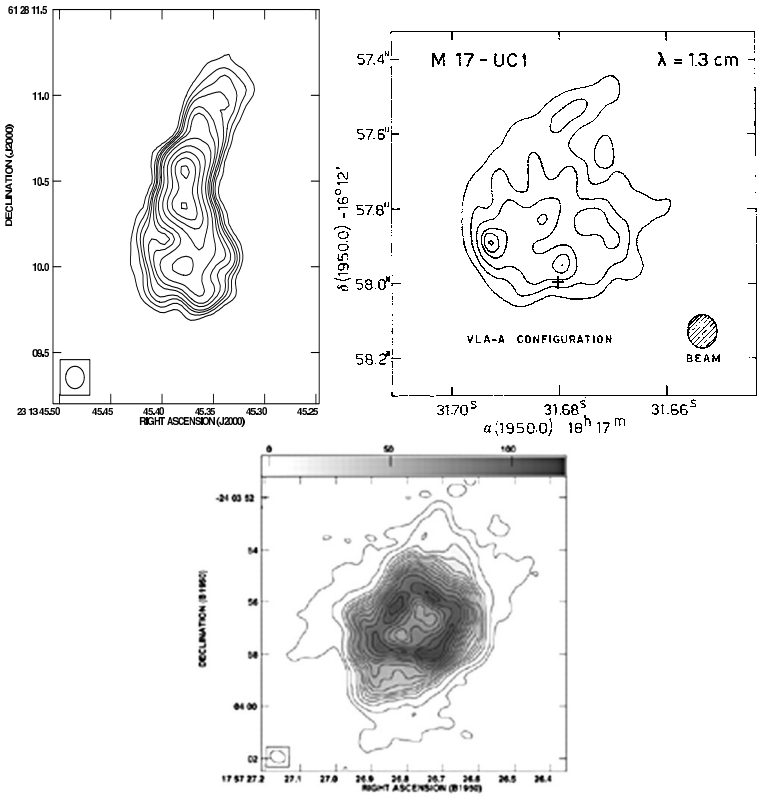

Figure 1.2: Some examples of the observed morphologies of UC HII regions. Top left: the bipolar source NGC 7538 IRS 1 (Franco-Hernández & Rodríguez, 2004), Top right: the cometary source M17 UC1 (Felli et al., 1984), Bottom: the shell-like source G5.89 -0.39 (Wood & Churchwell, 1989)

EM$= 6.3 \times 10^5\ L^{-1.53\pm0.09}$, where L is in pc, n_e is in cm^{-3}, and EM is in pc cm^{-6} (Garay & Lizano, 1999).

In addition to observing their free-free emission in the centimetre regime, HC and UC HII regions can also be observed in the sub-millimetre and infrared, down to around 2μm, where the surrounding dust becomes optically thick. The emission at these wavelengths is instead dominated by dust which has been heated mainly by a combination of direct stellar radiation and Lyman continuum photons scattered in the surrounding ionized gas (Natta & Panagia, 1976; Hoare et al., 1991). Due to this, the dust grains reach temperatures of several hundred Kelvin, causing their infrared emission to peak shortward of 100 μm. Both IRAS and the MSX survey have been used to study UC HII regions (e.g. Hoare et al., 2004), and far-IR colours from IRAS are commonly used to select sources that are UC HII regions for follow-up at longer wavelengths.

1.2.4 Disks and Outflows of Massive Stars

Massive (proto)stars with spectral types up to B0 have been observed to have disks (Cesaroni et al., 2007, and references therein). From the compilation of massive stars with disks given in Cesaroni et al. (2007), it can be seen that they generally have radii $\gtrsim$ 500 AU and masses of several times that of the Sun, making them larger and more massive than their low-mass counterparts (see Section 1.1.3.c). While these structures appear to be in centrifugal equilibrium, there also exists a class of large non-equilibrium flattened rotating objects observed around more massive protostars, whose accretion timescales are commonly smaller than their rotation timescales, and are therefore considered transient objects, not disks (e.g. Reid & Matthews, 2008). These objects have been coined 'toroids' (Cesaroni, 2005). Whether the non-detection of actual disks around O-protostars is merely due to instrumental or distance biases, or due to the altered physics of massive star formation is still not clear. It may be that most toroids, having masses which are a large fraction of the central (proto)star, are self-gravitating objects which therefore will not exhibit Keplerian rotation curves. In addition, they may not be tracing a disk, but instead the inner parts of flattened accretion flow around the star, which therefore would not require to be stable objects existing longer than several rotations.

From the HMPO stage onward, molecular outflows are observed towards massive stars (e.g. Shepherd & Churchwell, 1996b). There are several trends in the properties of outflows towards massive stars which are shared with outflows from low-mass objects (see Section 1.1.3.d). These include the correlation of outflow energetics, such as outflow mass, mass outflow rate, momentum or mechanical luminosity, with the bolometric luminosity of the protostar. These relations are seen over several orders of magnitude in luminosity (e.g. Bally & Lada, 1983; Cabrit & Bertout, 1992; Wu et al., 2004), and contain no 'kinks' or 'knees' that would point to a change in mechanism at higher masses, suggesting that there is a similar outflow driving process for stars of all luminosities. Also, the position-velocity diagrams of outflows towards high-mass (proto)stars often exhibit many similar features to those from low-mass stars (Beuther et al., 2004).

In addition, the collimation of massive outflows appears to decrease with increasing mass: there are examples of protostars with highly collimated jets up to early B spectral types (e.g. HH80-81: Heathcote et al., 1998). However, there are no convincing examples

of highly collimated outflows towards O stars (Beuther & Shepherd, 2005). Therefore, other mechanisms than magnetically driven disk or X-winds may be the cause of the wide-angle or 'explosive' outflows observed towards O stars, such as protostellar interactions (Bally & Zinnecker, 2005), or a stellar wind interacting with non-uniform surrounding material. Further, the absence of collimated outflows towards forming O stars could suggest a different formation mechanism. For instance, if the most massive stars formed via mergers, we would expect the outflows of these protostars to be completely disrupted by such events. However, it may be that their environments and fast formation timescales make it hard to observe them in their earliest stages, when their outflows would be collimated. Also, when an O star reaches the main sequence, the evolution of the HII region around the O star may be so rapid it would be unlikely to observe a stage where the outflow is not disrupted by its expansion.

In addition to collimated jets observed in molecular lines and the near-IR, small-scale ionized jets have been observed towards high-mass (proto)stars up to early B-types (e.g. Martí et al., 1993; Hofner et al., 1999; Shepherd & Kurtz, 1999), some of which agree with shock-ionized wind models (see Anglada, 1996). However, if the central stars have reached the main sequence, it is likely that their ionizing UV radiation would start to contribute significantly to the emission from the source.

Almost all sources which have examples of well collimated jets (collimation factors > 5), have ages less than 10^4yr, and have therefore not yet reached the main sequence (e.g. IRAS 05358+3543 Beuther et al., 2002c). Sources with poorly collimated flows (e.g. W75N VLA 2 Torrelles et al., 2003), usually have ages of several 10^5 yr and have a HC or UC HII region. Therefore, it seems that the evolution of these protostars or the appearance of an associated UC HII region changes their outflow properties. It could be plausible that the accretion onto the protostar, or the physics of outflow production, changes in some way to cause this. If the outflow is being created by a disk wind (see Pudritz et al., 2007), properties such as the amount of mass loading of the magnetic field, or the ionization fraction of the disk could change the outflow collimation. This led Beuther & Shepherd (2005) to propose an evolutionary sequence to explain these observations, which is shown schematically in Figure 1.3. This picture suggests that outflows become wider with time as the protostar evolves, which may be due to one of two scenarios. In the first, a B-type star evolves to form an HC HII region, and subsequently an UC HII, which disrupt and widen the outflow. In the second, O stars begin their accretion as intermediate mass or B-type stars and develop wider HII regions

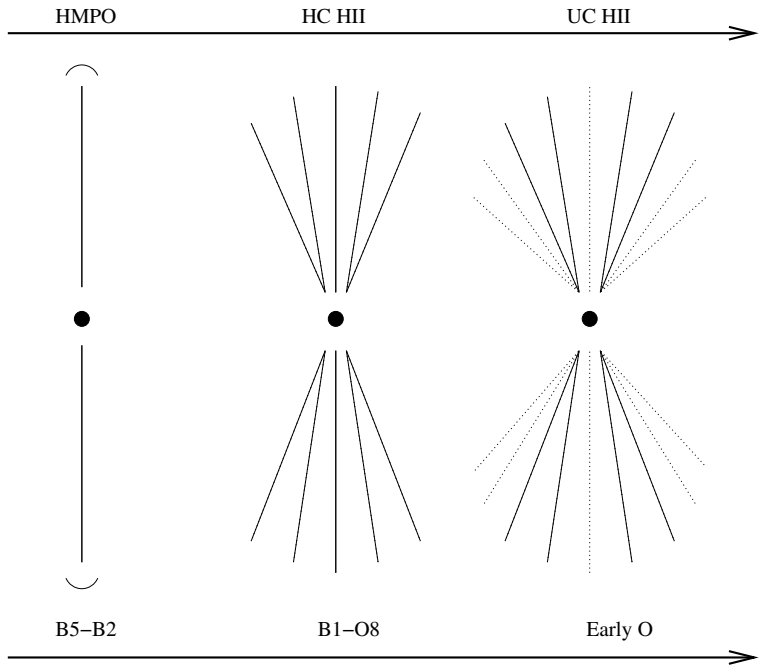

Figure 1.3: The evolutionary sequence for outflows from massive stars proposed by Beuther & Shepherd (2005), in which they proposed two scenarios. The first scenario explains the observed widening of outflows by the development of an HII region around a B-type star, and the second by the accretion and evolution of a B-type star to become an O star.

as they accrete. If this hypothesis is the case, then it would provide an explanation as to why no collimated flows are observed towards O-type stars.

1.2.5 Modelling of the SEDs and Images of Massive Stars

Although in its infancy, the number of studies modelling SEDs and images of massive stars is steadily increasing. Simplistic models, which involve fitting SEDs with two greybody components (i.e. opacity-modified blackbodies), have been used to obtain an initial understanding of the massive star formation process (e.g. Sridharan et al., 2002; Hill et al., 2009). In addition, the SEDs of a large number of massive sources have been fitted either with 1D models (e.g. de Wit et al., 2009) or 2D axis-symmetric models (e.g. Molinari et al., 2008). In particular, Molinari et al. (2008) found that the objects they modelled fit into a three-stage classification system mirroring the Class 0-I-II system defined for low-mass stars, and related this to their positions in a bolometric luminosity versus envelope mass diagram. This diagram, they suggest, which is used to discriminate between evolutionary schemes in low-mass star formation studies, can also be used to rule out different formation theories. They tentatively suggested that their results indicated formation via the 'turbulent core' scenario

or equivalently a scaled-up version of low-mass star formation, but more objects are needed to confirm this. Their modelling also determined the accretion rates and therefore formation timescales for massive stars, giving a formation time of 10^5 yr for a $40\,M_\odot$ star, and 4×10^5 yr for a star which finally attains $6\,M_\odot$. These values are in agreement with earlier values found by Osorio et al. (1999). In addition, as many of their observed sources are coincident with clusters which contain lower mass stars with formation timescales of 10^6 yr, they point out that it appears that the observed forming massive stars must have formed later on (or 'last') in the cluster evolution.

Many SEDs and images of single massive sources have also been modelled. A few examples include the luminous (proto)star AFGL 2591 (van der Tak et al., 1999, Preibisch et al., 2003 and Chapter 4), an edge-on disk observed in silhouette in the M17 star-forming region (Steinacker et al., 2006), and a similar edge-on source seen at near-IR wavelengths, CAHA J23056+6016 (Quanz et al., 2010). The latter two studies have concentrated on modelling of the near-IR emission from these sources using 2-D radial power-law flared disk geometries, and in the case of CAHA J23056+6016 an additional density to describe the outflow cavity. The modelling by Steinacker et al. (2006) determined that the observed dark-lane in M17 could be modelled by a 3000 AU disk of up to $5\,M_\odot$. They also found a large ratio of H/R (where H is the scale height and R is the disk radius) of ~ 0.5, much larger than commonly found for low-mass objects, and determined that although massive, the disk should nonetheless be influenced by self-gravity only at the outermost radii.

Simultaneous modelling of the long-wavelength SED and ammonia lines of the hot core G31.41+0.31 has been carried out by Osorio et al. (2009), using a simple accreting 'singular logotropic sphere' model, determining properties of the envelope and source, such as temperature, density, velocity and ammonia abundance. They also include deviations from spherical symmetry in their model, allowing them to fit the rotation, elongation of the core and the inclination of the system. In contrast, Indebetouw et al. (2006) presented 3D clumpy models of circumstellar material around massive stars, showing that the geometry and inclination can have large effects on the observed spectrum at near-IR wavelengths. They applied this to the infrared SEDs of several UC HII regions, and found that they could all be described simply by varying the viewing angle in a single model. Hence the assumed geometry has a strong effect on the emergent SED at shorter wavelengths.

Finally, the recent increase in high resolution far-IR data provided by the Herschel infrared galactic plane survey (Hi-GAL) has allowed SED fitting of a large number of massive sources to be carried out. Elia et al. (2010) fitted the Hi-GAL data, combined with ancillary mid-IR and mm fluxes, with both greybodies (if this approximated the SED acceptably) and a grid of axis-symmetric 2D models comprising of envelope plus disk geometries around a central (proto)star (Robitaille et al., 2006). Their modelling, in combination with placing these objects on a $L_{\rm bol}$ vs. $M_{\rm env}$ plot, suggested that of their two example fields, the sources at a galactic longitude of $l = 59°$ were at an earlier evolutionary stage than those at $l = 30°$.

1.3 Summary and Thesis Outline

Massive stars suffer from several biases which have made them difficult to study. They exist in regions of high extinction, associated and therefore confused with many low-mass objects forming in their vicinities. Also, due to their rarity, they are found at much farther distances than examples of low-mass star formation, and hence the resolution with which we can study them is restricted. They also form very quickly, in approximately $\sim 10^5$ yr, making them hard to catch before their natal material is dispersed. However, as the last section demonstrates, these barriers are slowly being overcome to produce a consistent picture of how massive stars form.

This thesis contains studies of both the large-scale regions in which massive stars form, and of their individual environments. In Chapter 2, I present a study of several massive star-forming regions, comparing both their molecular and ionized gas content. In Chapters 3 and 4, I will provide studies of two luminous embedded forming stars, IRAS 20126+4104 and AFGL 2591, including in-depth multi-wavelength modelling of their SEDs and, in the case of AFGL 2591, a study of the associated ionized and molecular gas at high angular resolution. Most importantly, these two forming stars were studied to determine the applicability of the low-mass star formation scenario. Finally, I summarise my conclusions in Chapter 5.

2

Ionized Gas Towards Molecular Clumps

Adapted from *Johnston et al., 2009, ApJ,* ***707****, 283*

One of the key differences of forming massive stars to their low-mass counterparts is that they produce significantly larger amounts of ionizing Far-UV radiation. The work laid out in this Chapter aims to provide preliminary studies of a selection of sites containing intermediate- and high-mass star formation, specifically to uncover the presence of ionized gas towards them. In addition, it aims to study the relationship in these regions between the star-forming gas, traced by millimetre continuum emission from dust, and the ionized gas created by massive stars, traced by radio continuum emission. These regions have also been chosen so that the most promising objects with associated ionized gas can be followed up with higher resolution observations in future, to study how the formation of an HII region affects the material within several hundreds of AU of their embedded accreting stars. Conversely, in the cases where no centimetre emission is detected, these regions allow the earliest stages of massive star formation to be studied, where no HII region has yet formed.

To fulfil these aims, radio continuum observations at 3.6 cm of 31 clumps detected in previous millimetre continuum observations were conducted, using the Very Large Array

(VLA) of the National Radio Astronomy Observatory [1]. Ten sources were selected from preliminary images from the Bolocam Galactic Plane Survey (BGPS, Aguirre et al. 2010, submitted), and 5 were selected from Beltrán et al. (2006, hereafter B06). The remaining 16 sources were observed serendipitously, as their positions lay within the observed VLA 3.6 cm fields. These sources were also selected to be within a declination range suitable for future study with both the Atacama Large Millimeter Array (ALMA) and the Expanded Very Large Array (EVLA). Note that, in this work, the terminology that a molecular core produces a single star (or close binary system), while molecular clumps form clusters of stars, is adopted. In this study of massive star-forming regions, the selected sources are several kiloparsecs away and, thus, are likely to be clumps forming one or more massive stars along with many lower mass stars.

Section 2.1 presents the selection criteria for the observed millimetre sources. Section 2.2 provides details of the observations and data reduction. Section 2.3 presents the observed 3.6 cm continuum images of each field; lists the measured positions, fluxes, and angular sizes of each detected VLA source; compares these results to existing millimetre and mid-IR observations; and presents derived properties for each source. The discussion is presented in Section 2.4. Finally, the Chapter summary is given in Section 2.5.

2.1 Source Selection

Clumps of molecular gas which are in the process of collapsing to form stars contain dust at temperatures of several tens of Kelvin. This dust is assumed to radiate as a grey body - a black body modified by a frequency dependent opacity, producing emission peaking at far-IR and sub-millimetre wavelengths. Thus observations in the millimetre regime are able to detect possible sites of star formation. The selected molecular clumps have masses large enough to harbour a forming intermediate or high-mass star, ranging from approximately 50 to 2500 $M_{\odot}$. Sources were chosen from BGPS preliminary images and the source list of B06. The BGPS (Aguirre et al. 2010, submitted) is a 1.1 mm continuum survey of 170 square degrees of the Galactic Plane visible from the northern hemisphere, including a contiguous strip from l = -10.5 to 90.5, $b = \pm 0.5$, as well as selected regions beyond the solar circle. The survey has a limiting non-uniform 1-σ noise level in the range 11 to 53 mJy beam^{-1} rms at

[1]The National Radio Astronomy Observatory is a facility of the National Science Foundation operated under cooperative agreement by Associated Universities, Inc.

an effective resolution of 33". The observations of B06 were taken with the 37-channel SEST Imaging Bolometer Array (SIMBA) on the Swedish-ESO Submillimetre Telescope (SEST) to identify 1.2 mm continuum emission within a 15' by 6.6' region centred on selected IRAS sources. These observations have a resolution of 24". Sources for the survey presented here were chosen to have:

1. A near distance of $\sim$1 kpc, for clumps selected from the BGPS. A description of how the BGPS clump distances were calculated is given in Section 2.1.1. However, HI observations subsequently showed many of the selected BGPS clumps to be at the far distance (see Section 2.1.1). Clumps from B06 were selected to have distances given in their Table 1 of less than 4 kpc. Two of these sources however were also subsequently found to be at the far distance.

2. A clump mass greater than 1 $M_{\odot}$ at the near distance, with a preference for more massive clumps. A description of how the BGPS source masses were calculated is given in Section 2.1.1. Masses of B06-selected sources are taken from their Table 2.

3. Little or no associated emission in the NRAO VLA Sky Survey (NVSS, Condon et al., 1993) 1.4 GHz continuum images and MSX E band (21.34 μm) images (Price et al., 2001), suggesting that any massive protostellar objects are young, and/or deeply embedded. The rms noise in the NVSS and MSX E band images is 0.45 mJy beam^{-1} (in a synthesised beam size of 45"), and $\geq$13.3 MJy sr^{-1} respectively.

4. A declination between -20 and +40° (J2000). The lower declination limit of the VLA is -48°, however, to ensure the observations had a reasonable beam shape, a lower declination limit of -20° was chosen. To avoid excessive shadowing in ALMA's compact configurations in follow up studies, an upper declination limit of +40° was also taken.

Preference was given to sources with no previous VLA observations at 3.6 cm that have sensitivities $\lesssim$30 μJy beam^{-1}. Fifteen sources were selected based on the above criteria while another sixteen were serendipitously present within the observed fields. Table 2.1 presents these sources, giving their positions; the velocity of associated ^{13}CO Galactic Ring Survey (Jackson et al., 2006, GRS) emission, if available; their near and far distances; the assumed distance (near or far); the luminosity of associated IRAS sources; the millimetre flux (at 1.1 or 1.2 mm); and the estimated mass of the millimetre clumps. Millimetre clumps

that were observed serendipitously are identified by "Serend." in column 14 while clumps initially selected are identified by "Select." The determination of the BGPS-selected source properties given in Table 2.1 is described in Section 2.1.1. B06-selected source properties in Table 2.1 are taken from their Tables 1 and 2, apart from the exceptions described below.

It was possible to determine the velocities and distances of the clumps towards IRAS 18424-0329 and IRAS 18571+0349, using the same methods as for the BGPS-selected sources (outlined in Section 2.1.1). Clumps associated with IRAS 18424-0329 were found to be at the far distance (see Section 2.1.1), and IRAS 18571+0349 was assumed to be at the far distance following the results of Kuchar & Bania (1994). Therefore the values of B06 are appropriately scaled to the far distance for these sources, and the velocity and distances found by the methods in Section 2.1.1 are quoted in columns 6-8 of Table 2.1.

2.1.1 Properties of the BGPS Millimetre Sources

The BGPS sources were identified by eye in preliminary BGPS images, prior to the final data release (Aguirre et al. 2010, submitted). Several of the sources have a low-signal-to-noise and are therefore not included in the final BGPS catalog (Rosolowsky et al., 2010), which is designed to minimise false detections, however sources were confirmed by detection of morphologically similar emission in the ^{13}CO(J=1-0) channel maps of the Boston University-Five College Radio Astronomy Observatory Galactic Ring Survey (Jackson et al., 2006, GRS). In order to extract flux densities for the selected objects, the images were reprocessed using the BGPS catalog pipeline, seeding the source identification portion of the catalog with the by-eye positions. This enabled the catalog routine to extract source properties that directly correspond to the fields observed. Source properties are determined as for the BGPS catalog; the integrated flux densities listed in Table 2.1 are determined using the same method as the flux density S in Rosolowsky et al. (2010), whereby the flux is integrated across regions determined using a seeded watershed algorithm which assigns progressively fainter pixels to a region of emission or source. These regions are originally seeded by peaks in the image. The quoted uncertainties for the integrated flux densities shown in Table 2.1 are due to the photometry only; an additional 11% error should be added to account for the uncertainty in the absolute flux calibration (10% random and 5% systematic, Aguirre et al. 2010, submitted).

Table 2.1. Observed Millimetre Clumps

(1) Source Name	(2) R.A. (2000) (h m s)	(3) Dec. (2000) (° ' ")	(4) Gal. ℓ (deg.)	(5) Gal. b (deg.)	(6) $\upsilon_{^{13}CO}$ (kms^{-1})	(7) d_{near} (kpc)	(8) d_{far} (kpc)	(9) Assumed Distance	(10) L_{IRAS} (10^3 $L_\odot$)	(11) $S_{1.1/1.2mm}$ (Jy)	(12) M ($M_\odot$)	(13) Ref.	(14) Source Type
G044.521+00.387	19 11 24.7	+10 28 43	44.5211	0.3871	51.3 ± 0.7	$3.8 \pm^{0.8}_{0.6}$	8.3 ±1.2	Near, HISA	0.932 - 2.13	0.49 ± 0.11	56	BGPS	Serend.
G044.587+00.371	19 11 35.6	+10 31 47	44.5871	0.3711	16.3 ± 1.5	$1.2 \pm^{0.3}_{0.2}$	10.9 ±1.4	Far, HISA	···	0.56 ± 0.14	528	BGPS	Select.
G044.617+00.365	19 11 40.3	+10 33 13	44.6171	0.3652	17.7 ± 1.4	$1.3 \pm^{0.3}_{0.2}$	10.8 ±1.4	Far, HISA	···	0.16 ± 0.08	148	BGPS	Serend.
G044.661+00.351	19 11 48.3	+10 35 10	44.6611	0.3512	17.6 ± 1.8	$1.3 \pm^{0.3}_{0.2}$	10.8 ±1.4	Far, HISA	24.3 - 24.6	0.62 ± 0.12	574	BGPS	Select.
G048.540+00.040	19 20 19.9	+13 52 25	48.5405	0.0398	15.6 ± 1.5	$1.2 \pm^{0.3}_{0.2}$	10.0 ±1.3	Far, HISA	···	0.42 ± 0.12	333	BGPS	Serend.
G048.580+00.056	19 20 21.0	+13 54 59	48.5805	0.0558	16.2 ± 1.8	$1.2 \pm^{0.3}_{0.2}$	10.0 ±1.3	Far, CA	···	3.16 ± 0.29	2508	BGPS	Select.
G048.598+00.252	19 19 40.3	+14 01 27	48.5984	0.2518	8.4 ± 2.4	0.6 ±0.2	10.6 ±1.4	Far, CA	···	1.32 ± 0.23	1177	BGPS	Select.
G048.605+00.024	19 20 30.8	+13 55 21	48.6045	0.0238	18.0 ± 1.8	$1.4 \pm^{0.3}_{0.2}$	9.9 ±1.3	Far, CA	927 - 932	7.36 ± 0.55	5725	BGPS	Serend.
G048.610+00.220	19 19 48.7	+14 01 11	48.6104	0.2198	9.2 ± 2.8	$0.7 \pm^{0.3}_{0.2}$	10.5 ±1.4	Far, CA	···	0.24 ± 0.10	210	BGPS	Serend.
G048.616+00.088	19 20 18.2	+13 57 48	48.6165	0.0878	16.9 ± 1.3	$1.3 \pm^{0.3}_{0.2}$	10.0 ±1.3	Far, CA	···	0.61 ± 0.13	484	BGPS	Select.
G048.634+00.230	19 19 49.3	+14 02 44	48.6344	0.2298	9.4 ± 3.6	0.7 ±0.3	10.5 ±1.4	Far, CA	60.5 - 168	0.62 ± 0.14	543	BGPS	Serend.
G048.656+00.228	19 19 52.3	+14 03 51	48.6564	0.2278	12.7 ± 2.5	$1.0 \pm^{0.3}_{0.2}$	$10.3 \pm^{1.4}_{1.3}$	Far, CA	···	0.67 ± 0.16	564	BGPS	Select.
G048.751-00.142	19 21 24.0	+13 58 25	48.7506	-0.1421	66.3 ± 1.0	5.3 ±0.7 $^\diamond$	5.3 ±0.7 $^\diamond$	Far, HISA	···	0.39 ± 0.12	87	BGPS	Select.
G048.771-00.148	19 21 27.6	+13 59 18	48.7706	-0.1481	66.9 ± 1.2	5.3 ±0.7 $^\diamond$	5.3 ±0.7 $^\diamond$	Far, HISA	···	0.14 ± 0.08	31	BGPS	Serend.
G049.830+00.370	19 21 37.9	+15 10 03	49.8303	0.3703	5.2 ± 1.8	$0.4 \pm^{0.2}_{0.1}$	10.6 ±1.4	Far, CA	127	1.09 ± 0.18	972	BGPS	Serend.
G049.912+00.370	19 21 47.5	+15 14 23	49.9123	0.3704	8.1 ± 1.4	$0.6 \pm^{0.2}_{0.1}$	$10.3 \pm^{1.4}_{1.3}$	Far, HISA	7.61 - 21.2	0.50 ± 0.13	421	BGPS	Select.
G050.271-00.442	19 25 27.5	+15 10 18	50.2706	-0.4415	14.8 ± 1.3	1.2 ±0.2	9.7 ±1.3	Far, HISA	0.960 - 254	0.21 ± 0.10	157	BGPS	Select.
G050.283-00.390	19 25 17.6	+15 12 25	50.2826	-0.3895	16.1 ± 1.5	$1.2 \pm^{0.3}_{0.2}$	9.6 ±1.3	Far, CA	281 - 286	1.40 ± 0.21	1024	BGPS	Select.
IRAS 18256-0742 Clump 1	18 28 18.9	-07 40 06	23.4730	1.6041	···	3.0	···	Near, B06	10.5	0.59 ± 0.09	52	B06	Select.
IRAS 18424-0329 Clump 2	18 45 00.5	-03 27 04	29.1280	-0.1449	47.4 ± 1.5	3.2 ± 0.5	11.6 ± 1.5	Far, HISA	55 †	0.53 ± 0.08	710	B06	Select.

By comparing the flux densities quoted in the final BGPS v1.0 catalog to those given in Motte et al. (2007) and Matthews et al. (2009), it has been found that in order to match these values, the BGPS fluxes were required to be multiplied by a factor of approximately 1.5±0.15 (Aguirre et al. 2010, submitted). However, it is not currently clear what is the root of this discrepancy. In addition, the BGPS fluxes used in this Chapter were determined using an earlier version of the BGPS pipeline, and hence this correction factor may not apply. However, it should be noted that this may systematically change the fluxes by +50%. As is discussed below, the error in the calculated dust masses is approximately a factor of 2, which is dominated by the uncertainty in the opacity. Therefore a further uncertainty of 50%, if applicable, will not significantly change the results of this Chapter.

Distances to BGPS-selected molecular clumps were determined using velocities of the corresponding ^{13}CO emission. The velocity v_R of each source was measured from the GRS ^{13}CO channel maps, taking the mean velocity of the associated ^{13}CO cloud at the source position. The distances of the clumps were calculated assuming a flat Galactic rotation curve, and circular orbits around the centre of the Galaxy. IAU values were assumed for the radius of the Sun's orbit around the galaxy $R_\odot$, and the velocity of the Sun around the Galaxy $v_\odot$ ($R_\odot = 8.5 \pm 1.1$ kpc, $v_\odot = 222 \pm 20$ kms^{-1}, Kerr & Lynden-Bell, 1986). Uncertainties of the calculated distances were estimated using a Monte Carlo simulation, assuming Gaussian errors for $R_\odot$, $v_\odot$ and the measured velocity v_R.

Following a similar method to that outlined in Roman-Duval et al. (2009), distance ambiguities were resolved by examining HI channel maps from the VLA Galactic Plane Survey (VGPS, Stil et al., 2006) towards each source. Two methods of distance determination were used. Firstly, the HI channel maps were inspected for HI self-absorption (HISA) at the velocity assigned to each millimetre clump. Cool HI in the outer layers of clouds can absorb emission from the warm diffuse galactic HI background; clouds at the near distance should show HISA of diffuse HI emission at the far distance, whereas clouds at the far distance will not since there is no background to absorb. It should be noted, however, that the presence of 21 cm continuum emission from HII regions in the cloud in question can provide a background to absorb even at the far distance. Therefore, a second method of distance determination was employed for sources that displayed HI absorption at the same velocity as the cloud, but also significant 21 cm emission with the same morphology. This continuum emission can also be absorbed by clouds in the line of sight. If the cloud is at the near

Table 2.1 (continued)

(1) Source Name	(2) R.A. (2000) (h m s)	(3) Dec. (2000) (° ' ")	(4) Gal. ℓ (deg.)	(5) Gal. b (deg.)	(6) $v_{^{13}CO}$ (kms^{-1})	(7) d_{near} (kpc)	(8) d_{far} (kpc)	(9) Assumed Distance	(10) L_{IRAS} (10^3 $L_\odot$)	(11) $S_{1.1/1.2mm}$ (Jy)	(12) M ($M_\odot$)	(13) Ref.	(14) Source Type
IRAS 18424-0329 Clump 4	18 45 01.6	-03 27 20	29.1261	-0.1510	47.6 ± 1.4	3.2 ± 0.5	11.6 ± 1.5	Far, HISA	55 †	0.28 ± 0.04	372	B06	Serend.
IRAS 18424-0329 Clump 6	18 45 00.5	-03 27 36	29.1201	-0.1490	47.6 ± 1.7	3.2 ± 0.5	11.6 ± 1.5	Far, HISA	55 †	0.24 ± 0.04	326	B06	Serend.
IRAS 18571+0349 Clump 1	18 59 42.7	+03 53 42	37.3409	-0.0615	55.5 ± 1.0	$3.7 \pm^{0.6}_{0.5}$	9.8 ± 1.3	Far, KB94	106	1.55 ± 0.23	1509	B06	Select.
IRAS 18571+0349 Clump 3	18 59 49.0	+03 56 30	37.3944	-0.0635	56.7 ± 2.6	$3.8 \pm^{0.7}_{0.6}$	9.7 ± 1.3	Far, KB94	···	0.31 ± 0.05	291	B06	Select.
IRAS 18571+0349 Clump 4	18 59 51.2	+03 55 18	37.3808	-0.0808	57.1 ± 1.1	$3.8 \pm^{0.7}_{0.6}$	9.7 ± 1.3	Far, KB94	···	0.23 ± 0.03	217	B06	Serend.
IRAS 18586+0106 Clump 1	19 01 15.8	+01 12 28	35.1276	-1.6345	···	2.7	···	Near, B06	···	1.47 ± 0.22	110	B06	Select.
IRAS 18586+0106 Clump 3	19 00 59.8	+01 13 40	35.1150	-1.5661	···	2.7	···	Near, B06	···	0.43 ± 0.06	32	B06	Serend.
IRAS 18586+0106 Clump 4	19 01 01.4	+01 13 16	35.1121	-1.5751	···	2.7	···	Near, B06	···	0.52 ± 0.08	39	B06	Serend.
IRAS 18586+0106 Clump 5	19 01 12.1	+01 10 44	35.0949	-1.6340	···	2.7	···	Near, B06	4.4	0.49 ± 0.07	36	B06	Serend.
IRAS 18586+0106 Clump 6	19 01 27.0	+01 10 28	35.1193	-1.6912	···	2.7	···	Near, B06	···	0.30 ± 0.04	22	B06	Serend.
IRAS 18586+0106 Clump 7	19 00 59.3	+01 11 08	35.0765	-1.5835	···	2.7	···	Near, B06	···	0.21 ± 0.03	16	B06	Serend.

Note. — Columns: 1. Millimetre clump name. 2. & 3. Equatorial J2000 coordinates of millimetre clump. 4. & 5. Galactic coordinates of millimetre clump. 6. Mean velocity of associated GRS ^{13}CO emission at position of mm source. 7. & 8. Near and far distance to millimetre clump in kpc. 9. Assumed distance used to calculate the IRAS luminosity and clump mass. The method used to determine whether the source is at the near or far distance is also given: HISA: HI self-absorption, CA: 21 cm continuum absorption, B06: taken from B06. KB94: Kuchar & Bania (1994). 10. Luminosity derived from associated IRAS source fluxes. 11. Millimetre flux measured at a wavelength of 1.1 mm for the sources taken from the BGPS, and 1.2 mm for those taken from B06. The errors in the fluxes taken from B06 were taken to be 15% as quoted in their Section 3. 12. The calculated dust mass of the millimetre clump. 13. References – BGPS: Bolocam Galactic Plane Survey preliminary images, Aguirre et al. (2010, submitted). B06: Beltrán et al. (2006) 14. Denotes whether source was selected (Select.) or serendipitously fell within the VLA field (Serend.).

† It is not certain which of the clumps listed by B06 is associated with IRAS 18424-0329, however the general 1.2 mm emission in this field is coincident with the IRAS source.

◇ The velocity of this source is too high to be explained by the galactic rotation curve at this galactic longitude, therefore the highest possible velocity at this longitude was instead assumed. These sources were originally thought to be at a different velocity, placing them at $d_{near} \sim 1$ kpc.

distance, the HI channel maps and profile will exhibit absorption features at velocities only less than that of the cloud, and if the cloud is at the far distance, there will be absorption features present up to the tangent point velocity (see Figure 2 of Roman-Duval et al., 2009). Table 2.1, column 9, indicates whether the near or far distance has been chosen based on the above methods, indicating whether presence or lack of HISA or 21 cm continuum absorption (CA) was the deciding factor.

It was possible to determine the velocities and distances to the clumps associated with IRAS 18424-0329 and IRAS 18571+0349 using the above methods, as they have corresponding GRS and VGPS data. The clumps towards IRAS 18424-0329 were found to be at the far distance. The distances for the clumps towards IRAS 18571+0349 could not unambiguously be determined using the above methods, however HI observations by Kuchar & Bania (1994) found the molecular cloud towards these sources to be at the far distance. Therefore the luminosities and masses quoted in B06 for these sources are accordingly scaled to the far distance.

Several of the selected clumps lie within the GRS clouds with distance determinations listed in Roman-Duval et al. (2009). These clouds are: GRSMC G029.14-00.16, GRSMC-G048.59+00.04, GRSMCG048.84+00.24, and GRSMC G050.29-00.46, which were all determined to be at the far distance, in agreement with the findings of this work.

The luminosities of IRAS sources associated with BGPS-selected millimetre clumps (at the distances given in Table 2.1) were calculated by first integrating the flux under the four 12 to 100 μm IRAS fluxes, and then adding the integrated flux of a blackbody peaking at 100 μm for wavelengths longer than 100 μm. When an upper limit was given for any of the four IRAS fluxes, the upper limit to the integrated flux was found by integrating under these values, and the corresponding lower limit was then found by setting the fluxes in question to zero before integration. When two values for the IRAS luminosity are given in Table 2.1, separated by a dash, they denote the lower and upper limits to the luminosity respectively. Uncertainties in the IRAS luminosity due to the distance uncertainty are not given in Table 2.1, however these can be found by scaling the given luminosities to the upper and lower distance limits.

The masses of the observed BGPS clumps were found using the equation

$$M_{gas} = \frac{g S_\nu d^2}{B(\nu, T)\kappa_\nu} \tag{2.1}$$

where g is the gas-to-dust ratio, taken to be 100, S_ν is the integrated flux density, d is the clump distance, $B(\nu, T)$ is the black body function, which is a function of frequency ν and temperature T, and κ_ν is the frequency-dependent opacity. A temperature of 30 K was assumed for all sources, as a compromise between the dust and NH_3 temperature results of Sridharan et al. (2002), who found an average dust temperature from IRAS emission towards their selection of high-mass stellar objects of 40 K, and an average rotation temperature from (1, 1) and (2, 2) lines of NH_3 of 20 K. Following Enoch et al. (2006), an opacity of 1.14 $cm^2 g^{-1}$ at 1.1 mm was assumed, derived from the results of Ossenkopf & Henning (1994).

The uncertainty in the 1.1 mm flux densities varies from $\sim$ 10-60%. The temperatures of the observed clumps also may lie between 15 and 60 K (from both NH_3 and dust temperature measurements from Sridharan et al., 2002). Assuming the Rayleigh-Jeans approximation holds, mass is approximately inversely proportional to temperature. Therefore as the temperature is assumed to be 30 K, the maximum error in the temperature is 100%, and will give rise to the same error in the mass. Table 2.1 shows that the uncertainty in the clump distances lies in the range 10-20%, and therefore contributes an error to the mass of 40%. The opacity is uncertain by a factor of two or less (Ossenkopf & Henning, 1994), and the gas-to-dust ratio has been derived, using extinction and gas-phase abundance measurements respectively, to be approximately 100 and 140 (Draine et al., 2007), giving an error of at least 40%. Therefore the calculated masses are accurate to within a factor of approximately 2, as the uncertainty is dominated by the uncertainty in the opacity.

2.2 Observations

The selected millimetre sources were observed on two occasions with the D configuration of the National Radio Astronomy Observatory VLA, in 3.6 cm (8.4 GHz) continuum mode on 2007 April 6 and on 2007 May 1, under the program AS895. VLA continuum mode consists of four bands, each having 50 MHz bandwidth; two of these bands are centred on a frequency of 8.435 GHz, and the remaining two are centered on 8.485 GHz. The baseline lengths in D array range from 35 m to 1.03 km, resulting in the largest angular

scale of observable structure being approximately 3' at 3.6 cm. However, note this value was lower in some instances due to flagging of the shortest baselines during data reduction. The average angular resolution of the final images is 8.35".

The on-source integration time for each observation was approximately 30 minutes, which corresponds to a theoretical rms noise of $\sim$ 30 μJy beam^{-1}, and $\sim$ 20 μJy beam^{-1} in overlap regions of mosaicked fields. Twenty-six antennas were available for the first set of observations, and twenty-five were available during the second. The data were taken during the transition to the new VLA correlator controller, which resulted in there being a larger fraction of data than expected with poor phases or amplitudes that had to be flagged, decreasing the final sensitivity in the images. As well as flagging to remove erroneous data, some of the shorter baselines (in the u-v plane) were flagged to improve the final images, when bright, large-scale structure could not be adequately imaged. The percentage of data flagged for each field ranged from 33 to 47%. These values include $\sim$10% of the data that was previously flagged by the on-line system.

The pointing centres for most target fields were shifted between the April 6 and May 1 observations (presented in Table 2.2). This was done primarily to move several bright sources on the edge of the VLA fields closer to the phase center of the map, to improve image deconvolution. For most of the observations, 1922+155 was used as a phase calibrator, with the exception of the source IRAS 18256-0742, which used 1822-096, and IRAS 18424-0329 and IRAS 18586+0106 which used 1832-105. The fluxes found during calibration for 1822-096, 1832-105 and 1922+155 were 1.34, 1.43 and 0.68 Jy, respectively.

Data reduction was carried out using the Common Astronomy Software Applications (CASA)[2] package. The phase calibrator 1922+155 was extended, and therefore self-calibration was performed on 1922+155 before deriving and applying phase calibration to the target source data. The primary flux calibrator was 1331+305 (3C286), which has a flux of 5.23 Jy at a wavelength of 3.6 cm. A model of 1331+305 was used for flux calibration, as this source was slightly resolved, allowing data at all UV distances to be used for flux calibration. The error in absolute flux calibration is approximately 2%. All of the data, with the exception of IRAS 18256-0742 and IRAS 18586+0106, were imaged with CASA's multi-scale mosaic deconvolution routine, which is based on the CLEAN algorithm, using either three or four

[2]http://casa.nrao.edu

Table 2.2. Summary of VLA Pointing Centres

Source Name	Observation Date	Pointing Centre	
		R.A. (2000)	Decl. (2000)
G044.587+00.371	2007 Apr 6	19 11 36.2	+10 31 47.0
···	2007 May 1	19 11 33.9	+10 31 13.0
G044.661+00.35	2007 Apr 6	19 11 48.5	+10 35 10.0
···	2007 May 1	19 11 46.2	+10 34 48.0
G044.580+00.056	2007 Apr 6	19 20 22.0	+13 54 52.0
···	2007 May 1	19 20 25.4	+13 52 22.3
G048.598+00.252	2007 Apr 6	19 19 40.4	+14 01 22.0
···	2007 May 1	19 19 43.9	+14 01 48.2
G048.616+00.088	2007 Apr 6	19 20 18.8	+13 57 44.0
···	2007 May 1	19 20 22.8	+13 56 18.6
G048.656+00.228	2007 Apr 6	19 19 53.3	+14 03 53.0
···	2007 May 1	19 19 53.9	+14 03 53.2
G048.751-00.142	2007 Apr 6	19 21 23.4	+13 58 27.0
···	2007 May 1	19 21 23.4	+13 58 27.4
G049.912+00.370	2007 Apr 6	19 21 48.3	+15 14 32.0
···	2007 May 1	19 21 47.7	+15 14 09.0
G050.271-00.442	2007 Apr 6	19 25 28.3	+15 10 22.0
···	2007 May 1	19 25 27.7	+15 10 22.0
G050.283-00.390	2007 Apr 6	19 25 19.3	+15 12 23.0
···	2007 May 1	19 25 22.6	+15 13 03.1
IRAS 18256-0742	2007 Apr 6	18 28 20.5	-07 40 22.0
IRAS 18424-0329	2007 Apr 6	18 45 03.2	-03 26 48.0
···	2007 May 1	18 45 01.2	-03 26 58.0
IRAS 18571+0349	2007 Apr 6	18 59 40.0	+03 53 34.0
···	2007 May 1	18 59 42.9	+03 54 20.0
IRAS 18586+0106	2007 Apr 6	19 01 10.5	+01 11 16.0
···	2007 May 1	19 01 10.5	+01 11 16.0

scales. Imaging of the remaining two sources was performed using multi-scale CLEAN, as they share the same pointing center in both observations.

2.3 Results

Panels a) and b) of Figures 2.1 to 2.10 present images of the VLA 3.6 cm continuum emission tracing ionized gas, and the millimetre continuum emission from the BGPS and B06 tracing warm dust, in the 10 observed fields. Panel a) of Figures 2.1 to 2.10 presents the observed VLA 3.6 cm fields in greyscale and contours. Panel b) of Figures 2.1 to 2.10 compares the 3.6 cm images, in contours, to the corresponding BGPS 1.1 mm or SEST SIMBA 1.2 mm images (from B06), shown in greyscale. The BGPS 1.1 mm images have been Gaussian smoothed using σ =1.5 pixels.

Hereafter, sources selected from the BGPS will be quoted in the format G44.587, as this is sufficient to discriminate between them. Several of the observed BGPS sources are close enough to one another to be shown in the same figure; these are G44.587 & G44.661, G48.580 & G48.616, G48.598 & G48.656, and G50.271 & G50.283.

The noise in the 3.6 cm images was found not to be Gaussian, due to poor UV coverage of extended and very bright emission in the observed fields (causing stripes in the deconvolved images). Therefore an estimate of the noise in the image ΔS was taken to be above any residual artefacts. The 3.6 cm contour levels presented in Figures 2.1 to 2.10 are given in multiples of ΔS.

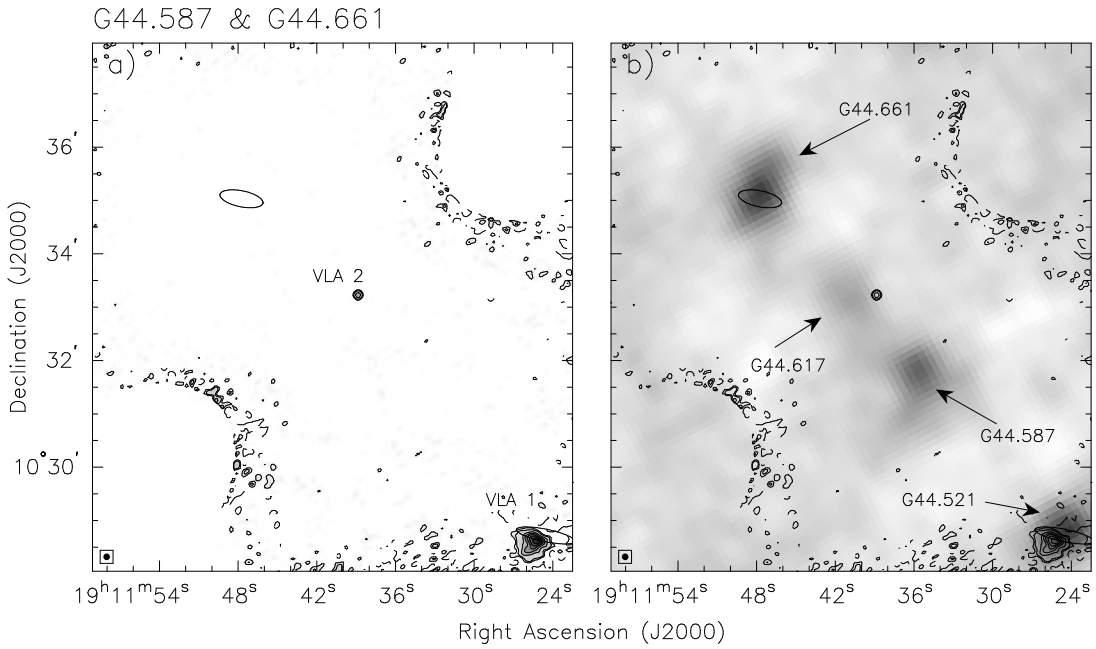

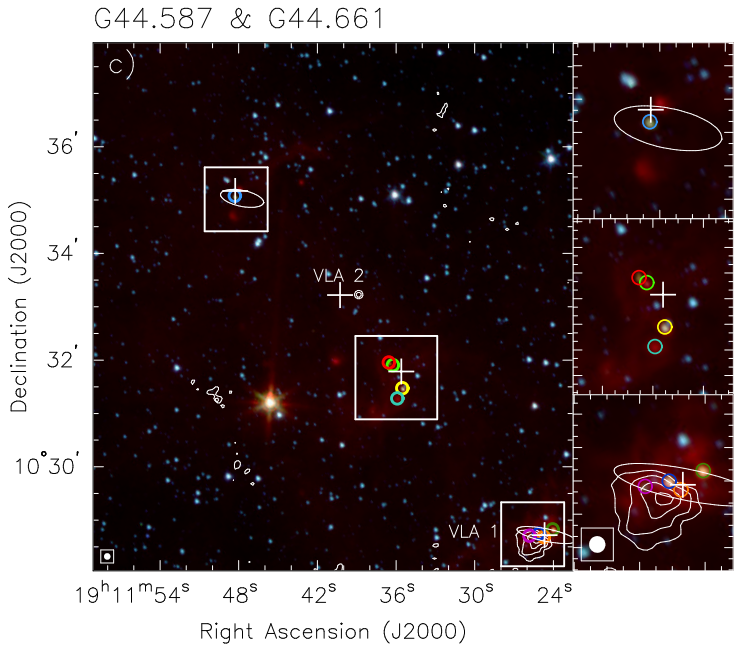

Figure 2.1: a) VLA 3.6 cm D-array continuum, b) Bolocam Galactic Plane Survey 1.1 mm, and c) three-colour mid-IR (Red: 8μm, Green: 4.5μm, Blue: 3.6μm) GLIMPSE images of the G44.587 & G44.661 field. Each image is overlaid with contours of 3.6 cm continuum emission. The detected 3.6 cm and 1.1 mm sources are labeled in panels a) and b) respectively. In all three panels, ellipses mark the positions of any associated IRAS sources. Panel a) Contour levels: -3, 3, 5, 10, 15, 20, 25, 30 $\times \Delta S = 0.07$ mJy beam^{-1}. Synthesised beam: 7.5 × 7.5" P.A.=38 degrees. Range of greyscale: 0.07 - 2.7 mJy beam^{-1}. Panel b) Contour levels and beam as in a). Range of greyscale: -0.03 - 0.3 Jy beam^{-1}. Panel c) Contour levels: 5, 10, 20, 30 $\times \Delta S = 0.07$ mJy beam^{-1}. Synthesised beam: 7.5 × 7.5" P.A.=38 degrees. GLIMPSE image stretch: logarithmic, R: 20-500, G: 5-500, B: 5-500 MJy Sr^{-1}. Inset or smaller panels cover the area shown by the boxes displayed in the main panel. Crosses show the peak positions of detected millimetre sources in the field, and coloured circles show the positions of GLIMPSE sources mentioned in Section 2.3.2.

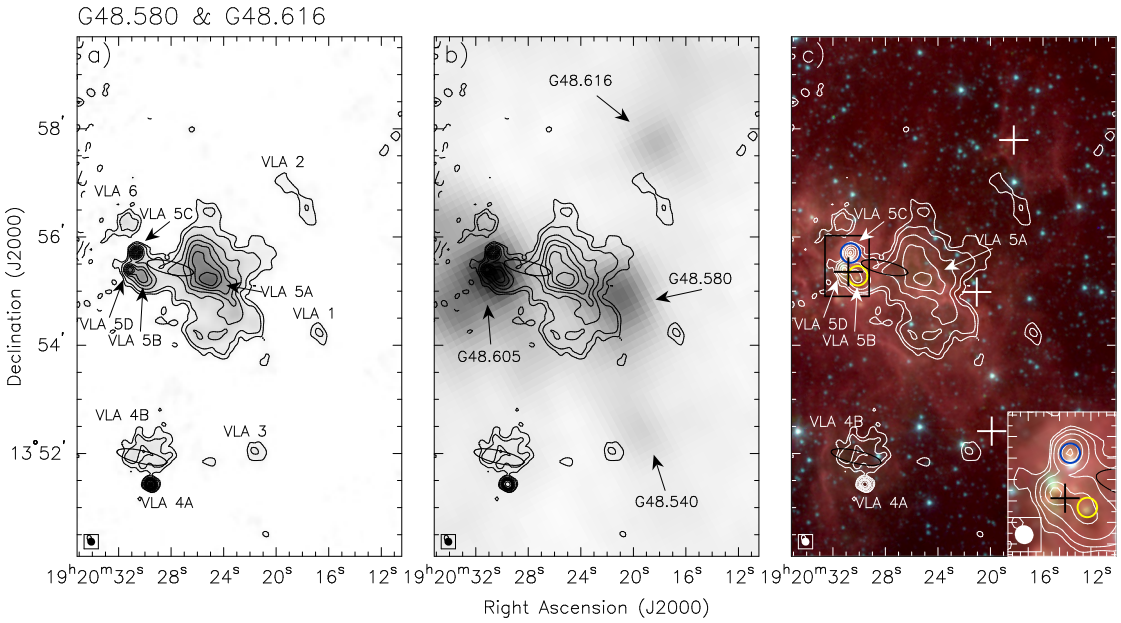

Figure 2.2: a) 3.6 cm continuum, b) 1.1 mm, and c) GLIMPSE images of the G48.580 & G48.616 field. Each image is overlaid with contours of 3.6 cm continuum emission. The detected 3.6 cm and 1.1 mm sources are labeled in panels a) and b) respectively. Panel a) Contour levels: -3, 3, 5, 10, 15, 20, 25, 30, 35, 40, 60 $\times \Delta S = 1.2$ mJy beam^{-1}. Synthesised beam: 9.1 × 8.7" P.A.=56 degrees. Range of greyscale: 1.2 - 68 mJy beam^{-1}. Panel b) Contour levels and beam as in a). Range of greyscale: -0.06 - 1.3 Jy beam^{-1}. Panel c) Contour levels: 3, 5, 10, 20, 30, 40, 60 $\times \Delta S = 1.2$ mJy beam^{-1}. Synthesised beam: 9.1 × 8.7" P.A.=56 degrees. GLIMPSE image stretch: logarithmic, R: 20-1300, G: 2-600, B: 2-1000 MJy Sr^{-1}.

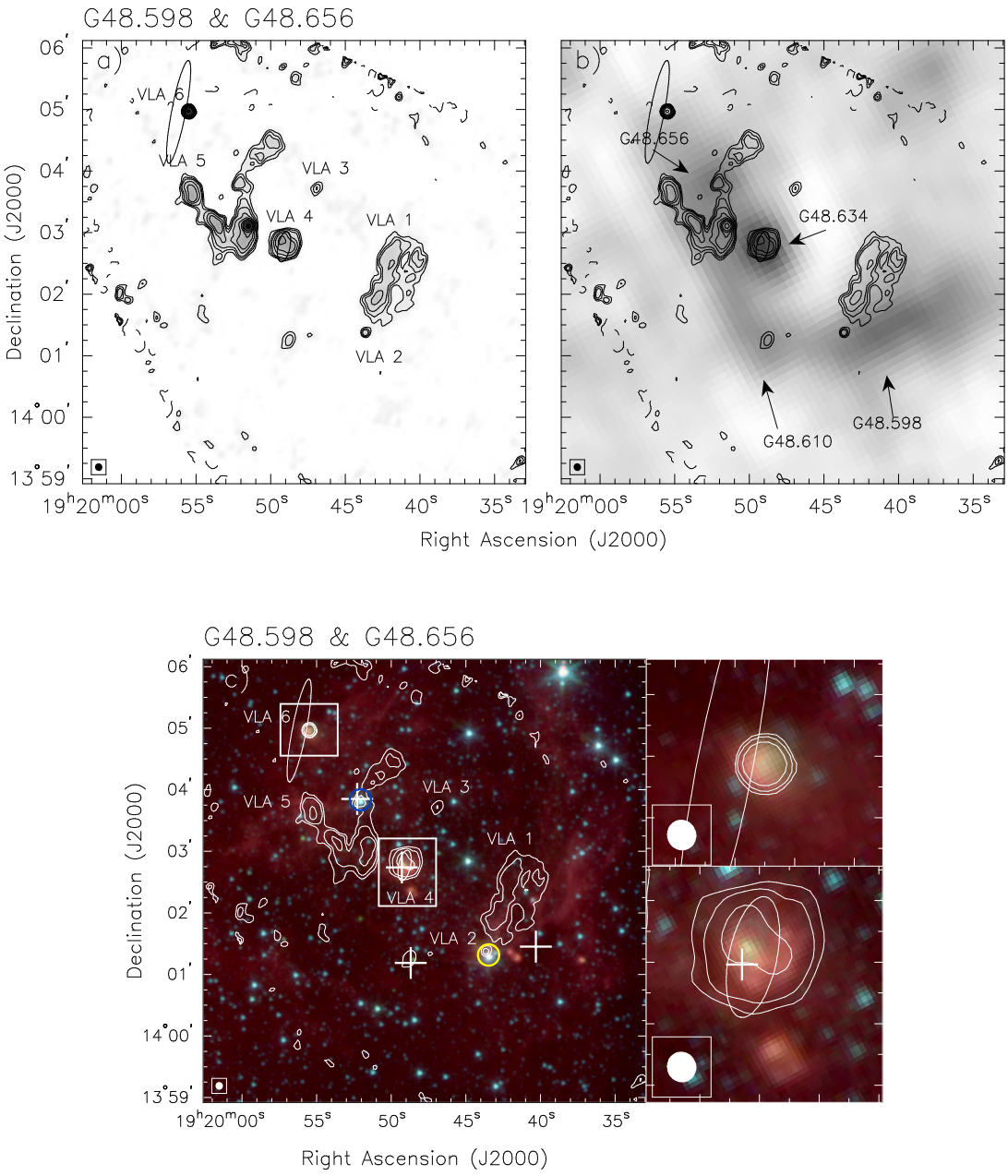

Figure 2.3: a) 3.6 cm continuum, b) 1.1 mm, and c) GLIMPSE images of the G48.598 & G48.656 field. Each image is overlaid with contours of 3.6 cm continuum emission. The detected 3.6 cm and 1.1 mm sources are labeled in panels a) and b) respectively. Panel a) Contour levels: -3, 3, 4, 5, 7, 9, 12, 15, 20, 30 $\times \Delta S = 0.21$ mJy beam^{-1}. Synthesised beam: 7.5 × 7.3" P.A.=36 degrees. Range of greyscale: 0.21 - 6.8 mJy beam^{-1}. The subcomponents of VLA 5 in the G48.598 & G48.656 field are not labeled, but are shown instead in Figure 2.11. Panel b) Contour levels and beam as in a). Range of greyscale: -0.04 - 0.4 Jy beam^{-1}. Panel c) Contour levels: 3, 5, 10 $\times \Delta S = 0.21$ mJy beam^{-1}. Synthesised beam: 7.5 × 7.3" P.A.=36 degrees. GLIMPSE image stretch: logarithmic, R: 20-1300, G: 2-600, B: 2-1000 MJy Sr^{-1}.

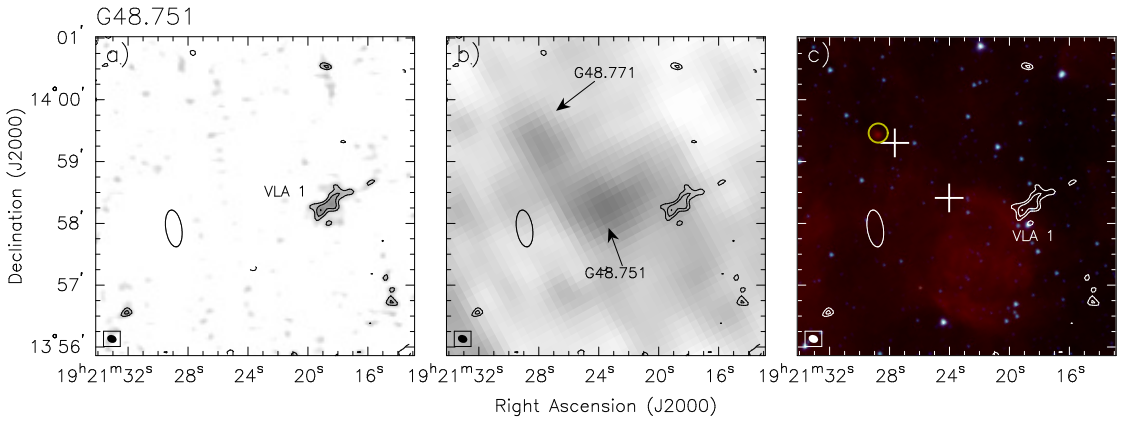

Figure 2.4: a) 3.6 cm continuum, b) 1.1 mm, and c) GLIMPSE images of the G48.751 field. Each image is overlaid with contours of 3.6 cm continuum emission. The detected 3.6 cm and 1.1 mm sources are labeled in panels a) and b) respectively. Panel a) Contour levels: -3, 3, 4, 5 $\times\Delta S$ = 0.07 mJy beam^{-1}. Synthesised beam: 9.6 × 7.5" P.A.=71 degrees. Range of greyscale: 0.07 - 0.43 mJy beam^{-1}. Panel b) Contour levels and beam as in a). Range of greyscale: -0.03 - 0.3 Jy beam^{-1}. Panel c) Contour levels: 3, 4, 5 $\times\Delta S$ = 0.07 mJy beam^{-1}. Synthesised beam: 9.6 × 7.5" P.A.=71 degrees. GLIMPSE image stretch: logarithmic, R: 30-500, G: 10-700, B: 5-1000 MJy Sr^{-1}.

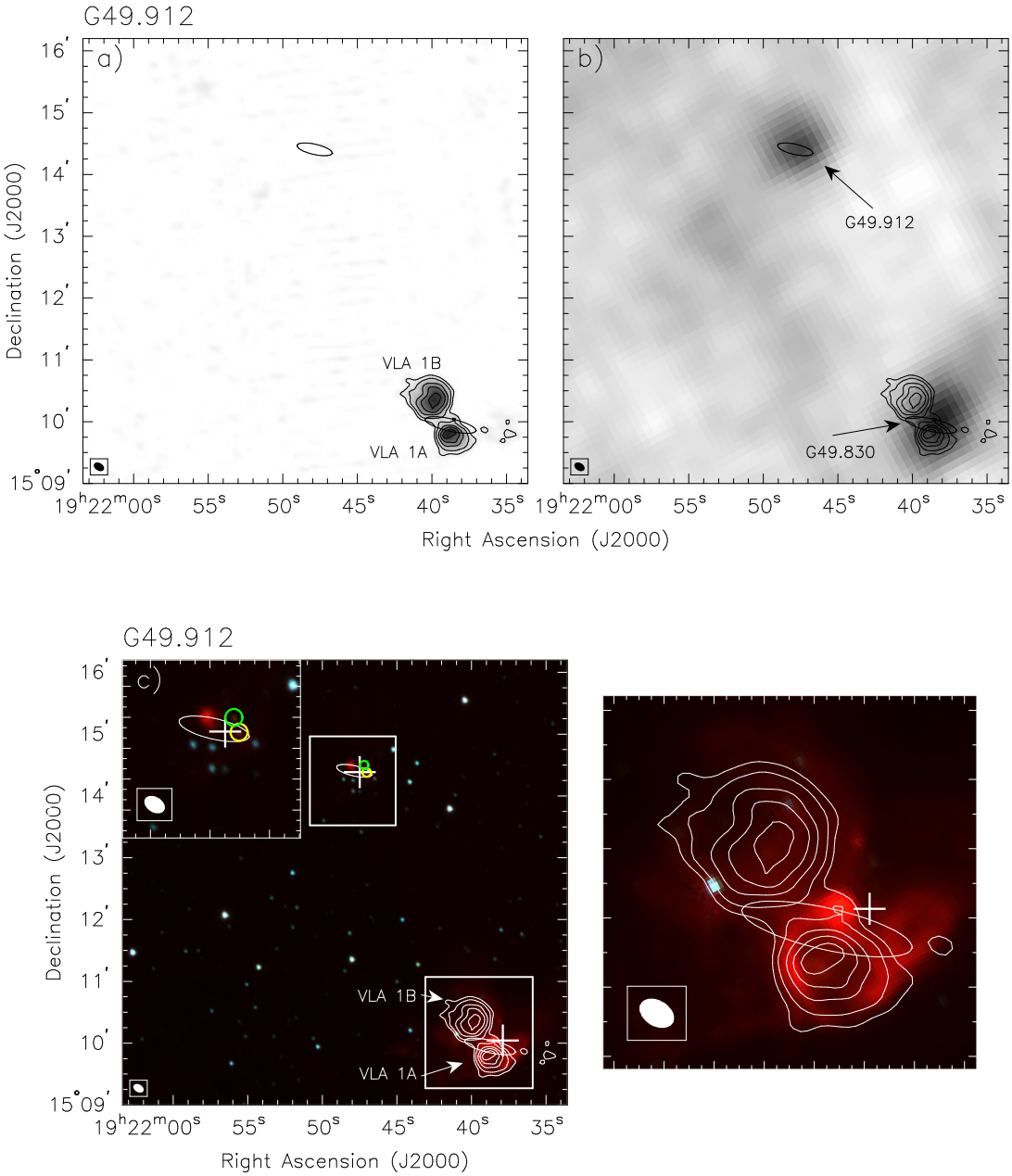

Figure 2.5: a) 3.6 cm continuum, b) 1.1 mm, and c) GLIMPSE images of the G49.912 field. Each image is overlaid with contours of 3.6 cm continuum emission. The detected 3.6 cm and 1.1 mm sources are labeled in panels a) and b) respectively. Panel a) Contour levels: -5, 5, 10, 20, 30, 40 $\times\Delta S$ = 0.04 mJy beam^{-1}. Synthesised beam: 11.1 × 7.5" P.A.=61 degrees. Range of greyscale: 0.04 - 2.1 mJy beam^{-1}. Panel b) Contour levels and beam as in a). Range of greyscale: -0.04 - 0.4 Jy beam^{-1}. Panel c) Contour levels: 5, 10, 20, 30, 40 $\times\Delta S$ = 0.04 mJy beam^{-1}. Synthesised beam: 11.1 × 7.5" P.A.=61 degrees. GLIMPSE image stretch: linear, R: 0-500, G: 0-400, B: 10-600 MJy Sr^{-1}.

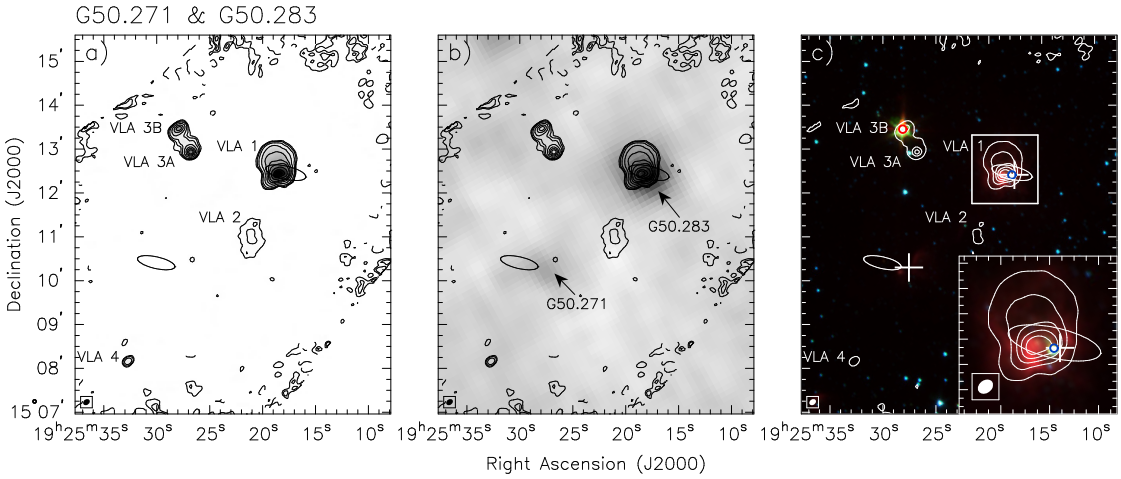

Figure 2.6: a) 3.6 cm continuum, b) 1.1 mm, and c) GLIMPSE images of the G50.271 & G50.283 field. Each image is overlaid with contours of 3.6 cm continuum emission. The detected 3.6 cm and 1.1 mm sources are labeled in panels a) and b) respectively. Panel a) Contour levels: -3, 3, 5, 10, 25, 50, 75, 100, 150, 200, 225 $\times\Delta S = 0.15$ mJy beam^{-1}. Synthesised beam: 10.0 × 7.6" P.A.=-57 degrees. Range of greyscale: 0.15 - 34 mJy beam^{-1}. Panel b) Contour levels and beam as in a). Range of greyscale: -0.07 - 0.7 Jy beam^{-1}. Panel c) Contour levels: 5, 50, 100, 150, 200 $\times\Delta S = 0.15$ mJy beam^{-1}. Synthesised beam: 10.0 × 7.6" P.A.=-57 degrees. GLIMPSE image stretch: linear, R: 0-800, G: 0-150, B: 0-150 MJy Sr^{-1}.

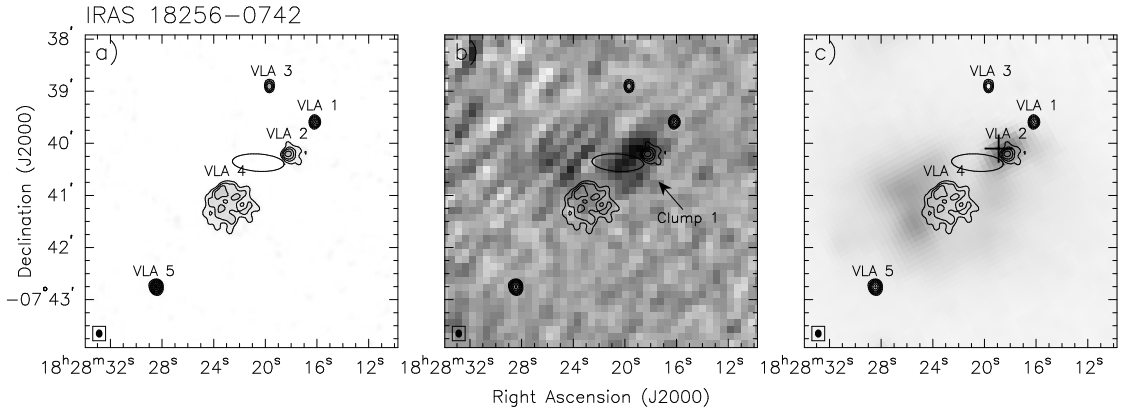

Figure 2.7: a) 3.6 cm continuum, b) SEST 1.2 mm, and c) MSX A Band (8.28μm) images of the IRAS 18256-0742 field. Each image is overlaid with contours of 3.6 cm continuum emission. The detected 3.6 cm and 1.2 mm sources are labeled in panels a) and b) respectively. Panel a) Contour levels: -3, 3, 5, 7, 10, 15, 20, 30, 40 $\times\Delta S = 0.05$ mJy beam^{-1}. Synthesised beam: 9.5 × 7.8" P.A.=-179 degrees. Range of greyscale: 0.05 - 2.0 mJy beam^{-1}. Panel b) Contour levels and beam as in a). Range of greyscale: -0.15 - 0.25 Jy beam^{-1}. Panel c) Contour levels and beam as in a). MSX 8.28μm image stretch: linear, Range: 0.0-5.0 × 10^{-5} Wm^{-2}sr^{-1}.

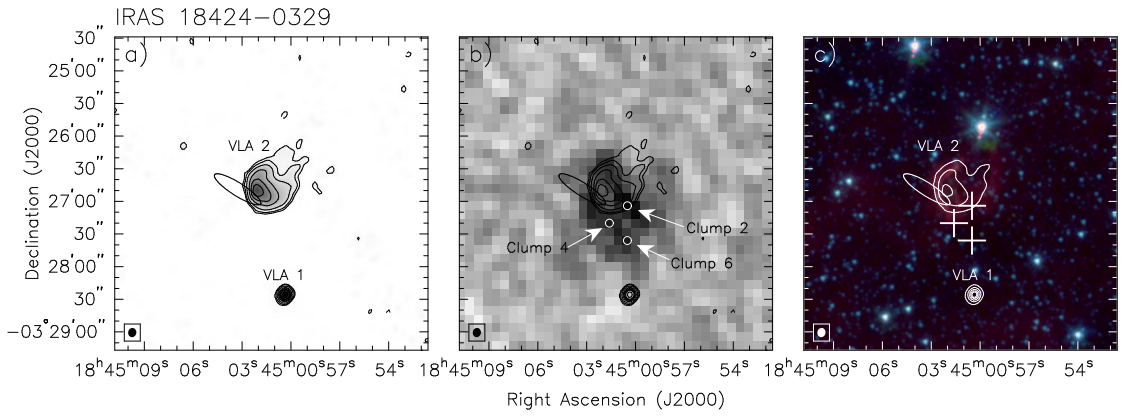

Figure 2.8: a) 3.6 cm continuum, b) SEST 1.2 mm, and c) GLIMPSE images of the IRAS 18424-0329 field. Each image is overlaid with contours of 3.6 cm continuum emission. The detected 3.6 cm and 1.2 mm sources are labeled in panels a) and b) respectively. Panel a) Contour levels: -3, 3, 5, 10, 20, 30, 40, 50, 75, 100 $\times \Delta S = 0.09$ mJy beam^{-1}. Synthesised beam: 8.5 × 7.5" P.A.=-10 degrees. Range of greyscale: 0.09 - 6.0 mJy beam^{-1}. Panel b) Contour levels and beam as in a). Range of greyscale: -0.1 - 0.2 Jy beam^{-1}. The white circles mark the positions of Clumps 2, 4 and 6 listed in B06. Panel c) Contour levels: 5, 20, 40, 60, 75, 100 $\times \Delta S = 0.09$ mJy beam^{-1}. Synthesised beam: 8.5 × 7.5" P.A.=-10 degrees. GLIMPSE image stretch: logarithmic, R: 60-2000, G: 5-2000, B: 3-2000 MJy Sr^{-1}.

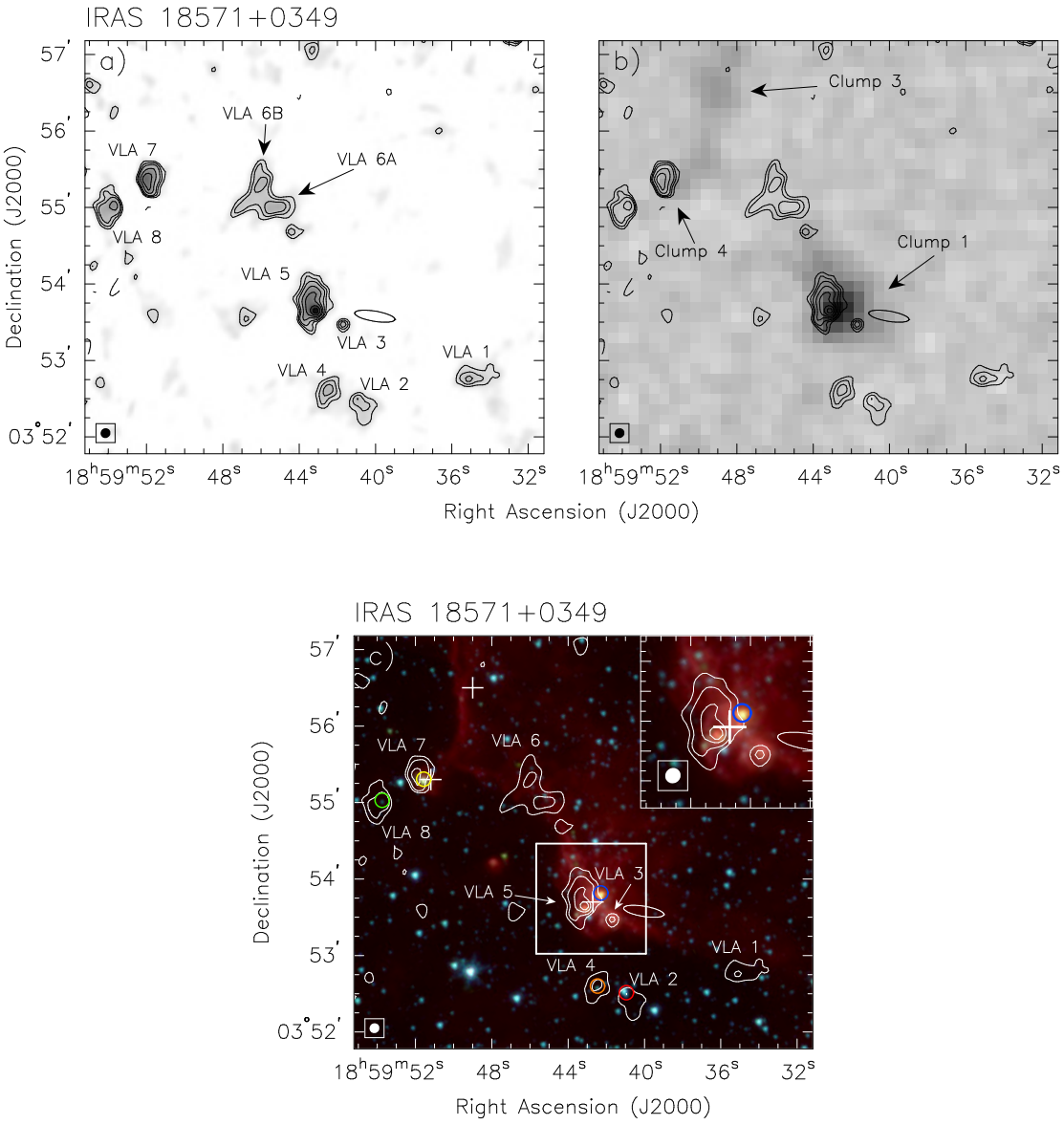

Figure 2.9: a) 3.6 cm continuum, b) SEST 1.2 mm, and c) GLIMPSE images of the IRAS 18571+0349 field. Each image is overlaid with contours of 3.6 cm continuum emission. The detected 3.6 cm and 1.2 mm sources are labeled in panels a) and b) respectively. Panel a) Contour levels: -3, 3, 4, 5, 7, 9, 12, 15 $\times \Delta S = 0.24$ mJy beam^{-1}. Synthesised beam: 7.9 × 7.5" P.A.=-48 degrees. Range of greyscale: 0.24 - 4.1 mJy beam^{-1}. Panel b) Contour levels and beam as in a). Range of greyscale: -0.2 - 0.68 Jy beam^{-1}. Panel c) Contour levels: 3, 5, 9, 13, 17 $\times \Delta S = 0.24$ mJy beam^{-1}. Synthesised beam: 7.9 × 7.5" P.A.=-48 degrees. GLIMPSE image stretch: logarithmic, R: 50-1000, G: 5-500, B: 5-700 MJy Sr^{-1}.

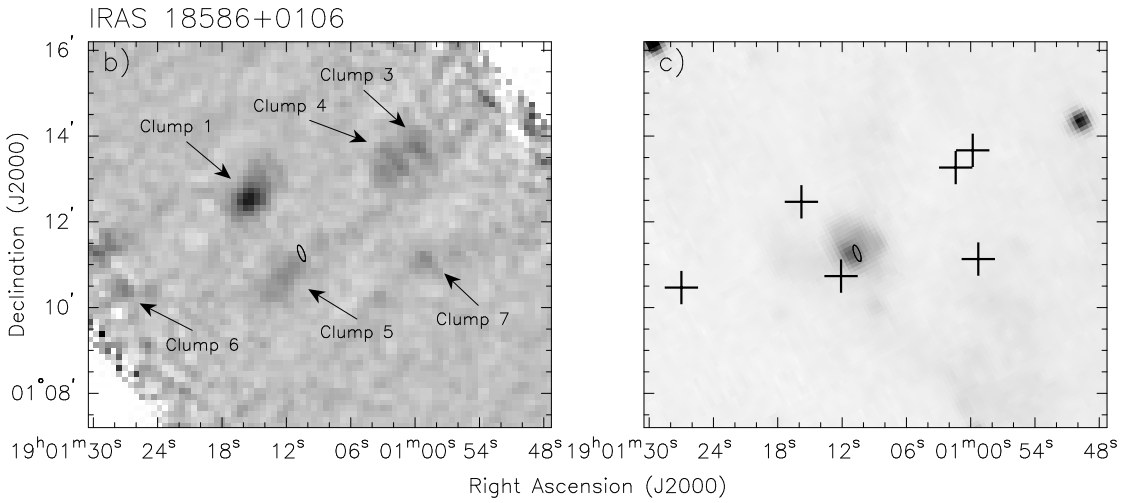

Figure 2.10: b) SEST 1.2 mm, and c) MSX A Band (8.28μm) images of the IRAS 18586+0106 field. No significant 3.6 cm emission above 3 $\times\Delta S$ was detected in this field, ΔS = 0.16 mJy beam^{-1}, therefore the 3.6 cm image is not shown. Synthesised beam: 9.6 × 8.0" P.A.=-39 degrees. Panel b) Range of greyscale: -0.2 - 0.6 Jy beam^{-1}. The detected 1.2 mm sources are labeled. Panel c) MSX 8.28μm image stretch: linear, Range: 0.0-3.0 × 10^{-5} Wm^{-2}sr^{-1}.

2.3.1 Positions, Fluxes and Angular Sizes of Detected 3.6 cm Sources

In the 10 observed fields, 35 HII regions are identified, of which 20 are newly discovered. Table 2.3 lists the integrated flux density, peak position, peak flux density, angular size, position angle, and solid angle for each VLA source detected above 5×ΔS in the observed fields. Also listed in the final column of Table 2.3 are any pre-existing identifiers for each VLA source. For newly discovered radio continuum sources, this column contains the flag "New". Sub-sources are denoted by "A,B,C...", and sources or components of sources which are fully or nearly unresolved (e.g., point-like), are denoted by "-P."

With the exception of point-like sources (-P), measurements of the integrated and peak flux density were carried out using a custom-made irregular aperture photometry program. The integrated flux density was measured using a 1×ΔS cut-off, within apertures placed so that they included all of the 1×ΔS contour for each source. Errors in the aperture fluxes were calculated to be a combination of the error due to the image noise over the aperture, and the VLA absolute flux error, which is 2% for 3.6 cm VLA calibration. Similarly, the peak flux error was found by combining the 1×ΔS flux density with the VLA absolute flux error.

Table 2.3. Observed Parameters of VLA 3.6 cm Sources

Observed Field	VLA Source Name	Flux Density (mJy)	Peak Position R.A. (J2000)	Peak Position Dec. (J2000)	Peak Flux (mJy beam^{-1})	Angular Size (arcsec) °	Position Angle (deg.) □	Solid Angle (steradians $\times 10^{-8}$)†	Alternative Identifiers for VLA Source
G44.587 & G44.661	VLA 1	231 ± 5	19 11 25.1	+10 28 37	31.6 ± 0.6	52 × 40	110	4.08	IRAS 19090+1023, G44.521+0.388 (Bronfman et al., 1996)
···	VLA 2	1.34 ± 0.04	19 11 38.8	+10 33 13	1.40 ± 0.08	···	···	···	New
···	VLA 2-P	1.43 ± 0.04	19 11 38.8	+10 33 14	1.52 ± 0.03	< 1.1	unres.	···	New
G48.580 & G48.616	VLA 1	51.8 ± 1.5	19 20 16.6	+13 54 14	10.6 ± 1.2	27 × 18	20	2.57	New
···	VLA 2	168 ± 4	19 20 17.6	+13 56 32	10.8 ± 1.2	68 × 23	40	7.62	···
···	VLA 3	42.0 ± 1.2	19 20 21.7	+13 52 04	7.28 ± 1.21	24 × 23	50	2.73	New
···	VLA 4	434 ± 9	19 20 29.6	+13 51 26	140 ± 3	79 × 62	0	11.0	G48.54-0.00 (Matthews et al., 1978), IRAS 19181+1346
···	VLA 4A	140 ± 3 ◇	19 20 29.6	+13 51 26	140 ± 3	···	···	···	···
···	VLA 4A-P	140 ± 3	19 20 29.6	+13 51 26	141 ± 3	1.8 × <1.3	59	···	···
···	VLA 4B	294 ± 6 ◇	19 20 31.2	+13 51 56	15.4 ± 1.2	64 × 55	90	9.91	···
···	VLA 5	3230 ± 65	19 20 30.7	+13 55 42	127 ± 3	187 × 144	50	51.6	NRAO 608, W51D, RRF 376, IRAS 19181+1349, G48.61+0.02
···	VLA 5A	2370 ± 48 ◇	19 20 25.4	+13 55 14	49.8 ± 1.6	180 × 130	10	43.4	G48.59+0.04 (Matthews et al., 1978)
···	VLA 5B	360 ± 7 ◇	19 20 30.2	+13 55 16	63.0 ± 1.7	44 × 43	0	3.20	48.603+0.026 (Zoonematkermani et al., 1990), G48.60+0.03
···	VLA 5C	254 ± 5 ◇	19 20 30.7	+13 55 42	127 ± 3	50 × 24	70	2.25	IRAS 19181+1349, G48.61+0.02
···	VLA 5C-P	231 ± 5	19 20 30.7	+13 55 42	120 ± 2	9.8 × 7.2	160	···	IRAS 19181+1349, G48.61+0.02
···	VLA 5D	252 ± 5 ◇	19 20 31.2	+13 55 24	109 ± 2	34 × 28	0	2.70	IRAS 19181+1349, G48.61+0.02
···	VLA 5D-P	284 ± 6	19 20 31.0	+13 55 23	94.3 ± 1.9	14.2 × 11.0	48	···	IRAS 19181+1349, G48.61+0.02
···	VLA 6	293 ± 6	19 20 31.5	+13 56 18	34.2 ± 1.4	51 × 30	140	5.03	···
G48.598 & G48.656	VLA 1	72.8 ± 1.6	19 19 42.9	+14 01 56	1.85 ± 0.21	94 × 59	170	12.3	1917+1356 (Taylor et al., 1996)
···	VLA 2	3.21 ± 0.14	19 19 43.6	+14 01 22	1.52 ± 0.21	···	···	···	1917+1356 (Taylor et al., 1996)
···	VLA 2-P	2.83 ± 0.07	19 19 43.6	+14 01 23	1.38 ± 0.03	8.7 × 6.5	134	···	1917+1356 (Taylor et al., 1996)
···	VLA 3	7.69 ± 0.27	19 19 46.9	+14 03 44	1.60 ± 0.21	···	···	···	New
···	VLA 3-P	6.65 ± 0.15	19 19 46.9	+14 03 43	1.44 ± 0.03	17.2 × 11.3	135	···	New
···	VLA 4	28.0 ± 0.6	19 19 49.3	+14 02 52	3.38 ± 0.22	36 × 35	140	3.04	WFS70, WFS71, IRAS 19175+1357
···	VLA 5	189 ± 4	19 19 51.5	+14 03 06	11.0 ± 0.3	143 × 98	150	15.5	New
···	VLA 5A	19.1 ± 0.5 ◇	19 19 49.9	+14 04 28	2.97 ± 0.22	25 × 24	50	1.73	New
···	VLA 5B	16.5 ± 0.4 ◇	19 19 50.6	+14 04 14	2.41 ± 0.22	31 × 26	140	1.79	New
···	VLA 5C	58.1 ± 1.2 ◇	19 19 51.5	+14 03 06	11.0 ± 0.3	65 × 29	0	4.23	New
···	VLA 5C-P	25.5 ± 0.5	19 19 51.6	+14 03 06	9.43 ± 0.19	10.4 × 9.0	0	···	New

Table 2.3 (continued)

Observed Field	VLA Source Name	Flux Density (mJy)	Peak Position R.A. (J2000)	Peak Position Dec. (J2000)	Peak Flux (mJy beam^{-1})	Angular Size (arcsec) °	Position Angle (deg.) □	Solid Angle (steradians $\times 10^{-8}$)†	Alternative Identifiers for VLA Source
···	VLA 5D	11.7 ± 0.3 ◇	19 19 52.1	+14 03 48	2.49 ± 0.22	22 × 22	60	1.38	New
···	VLA 5E	42.9 ± 0.9 ◇	19 19 53.5	+14 03 06	4.48 ± 0.23	54 × 40	40	3.73	New
···	VLA 5F	40.3 ± 0.9 ◇	19 19 55.3	+14 03 34	5.75 ± 0.24	38 × 32	30	2.60	New
···	VLA 6	28.7 ± 0.6	19 19 55.4	+14 04 58	25.5 ± 0.6	···	···	···	IRAS 19176+1359, New
···	VLA 6-P	29.8 ± 0.6	19 19 55.5	+14 04 58	27.0 ± 0.5	2.4 × 2.3	129	···	IRAS 19176+1359, New
G48.751	VLA 1	5.74 ± 0.14	19 21 18.5	+13 58 19	0.431 ± 0.071	47 × 21	130	5.25	New
G49.912	VLA 1	459 ± 9	19 21 39.0	+15 09 45	52.0 ± 1.0	98 × 55	40	9.47	G49.8+0.4 (?), IRAS 19193+1504, RFS 849
···	VLA 1A	313 ± 6 ◇	19 21 39.0	+15 09 45	52.0 ± 1.0	44 × 43	120	3.90	···
···	VLA 1B	145 ± 3 ◇	19 21 40.0	+15 10 13	18.7 ± 0.4	57 × 47	40	5.57	···
G50.271 & G50.283	VLA 1	463 ± 9	19 25 18.5	+15 12 27	55.9 ± 1.1	71 × 59	160	7.90	IRAS 19230+1506, G50.28-0.39 (Watson et al., 2003)
···	VLA 2	17.8 ± 4.1	19 25 21.1	+15 11 05	1.16 ± 0.15	55 × 38	170	7.31	New
···	VLA 3	163 ± 3	19 25 27.9	+15 13 29	45.4 ± 0.9	57 × 36	30	4.61	050.318-0.418, 050.308-0.418 (Zoonematkermani et al., 1990)
···	VLA 3A	69.1 ± 1.4 ◇	19 25 26.8	+15 12 57	35.6 ± 0.7	···	···	···	050.308-0.418 (Zoonematkermani et al., 1990)
···	VLA 3A-P	61.4 ± 1.2	19 25 26.8	+15 12 57	34.2 ± 0.7	8.9 × 6.0	35	···	050.308-0.418 (Zoonematkermani et al., 1990)
···	VLA 3B	93.5 ± 1.9 ◇	19 25 27.9	+15 13 29	45.4 ± 0.9	···	···	···	050.318-0.418 (Zoonematkermani et al., 1990)
···	VLA 3B-P	84.4 ± 1.7	19 25 28.0	+15 13 28	44.2 ± 0.9	10.7 × 6.3	127	···	050.318-0.418 (Zoonematkermani et al., 1990)
···	VLA 4	12.2 ± 0.3	19 25 32.7	+15 08 09	11.2 ± 0.3	···	···	···	New
···	VLA 4-P	12.2 ± 0.3	19 25 32.7	+15 08 09	11.2 ± 0.2	3.7 × 1.1	150	···	New
IRAS 18256-0742	VLA 1	1.29 ± 0.03	18 28 16.2	-07 39 36	1.32 ± 0.06	···	···	···	New
···	VLA 1-P	1.35 ± 0.11	18 28 16.2	-07 39 36	1.35 ± 0.07	1.5 × < 1.8	153	···	New
···	VLA 2	2.15 ± 0.06	18 28 18.2	-07 40 12	0.630 ± 0.052	30 × 24	40	2.24	Mol 57, New
···	VLA 3	0.912 ± 0.028	18 28 19.7	-07 38 54	0.890 ± 0.053	···	···	···	New
···	VLA 3-P	0.958 ± 0.116	18 28 19.7	-07 38 54	0.895 ± 0.066	4.3 × < 2.2	178	···	New
···	VLA 4	9.96 ± 0.21	18 28 23.7	-07 41 00	0.460 ± 0.051	66 × 61	100	8.88	New
···	VLA 5	6.83 ± 0.14	18 28 28.4	-07 42 46	6.27 ± 0.14	···	···	···	Mol 57
···	VLA 5-P	6.74 ± 0.18	18 28 28.4	-07 42 46	6.28 ± 0.14	2.5 × 2.0	59	···	Mol 57

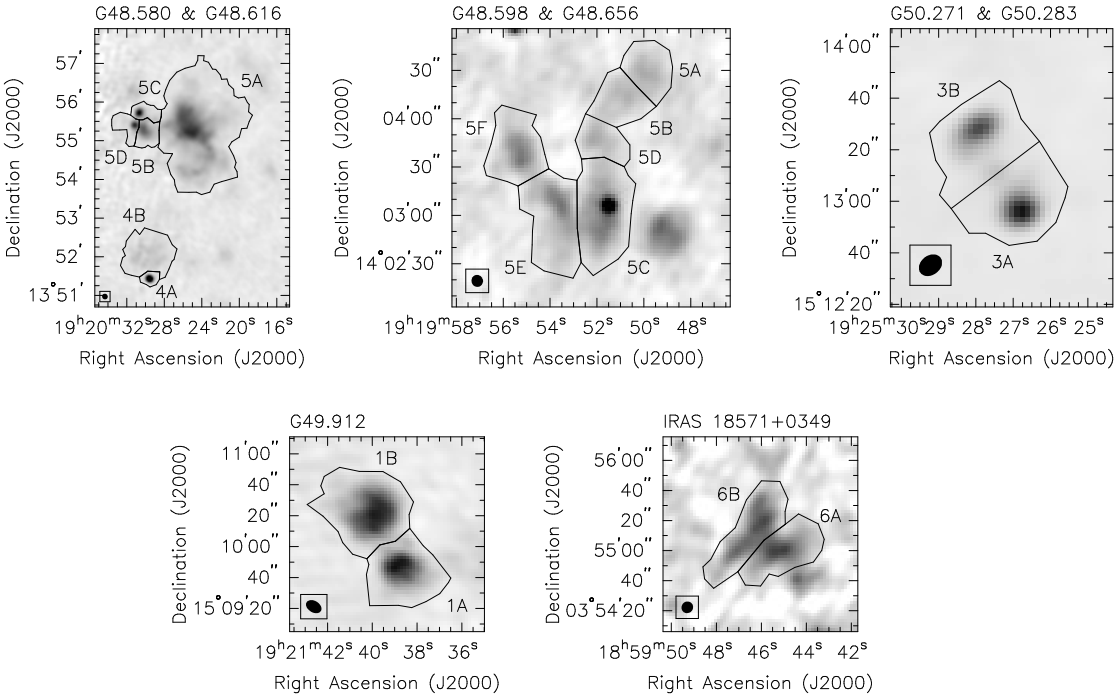

Figure 2.11: Photometry apertures used for the six multiply peaked sources detected in the 3.6 cm VLA observations. VLA sub-sources are labeled in each panel. Greyscale in each panel: VLA 3.6 cm emission. Greyscale ranges: G48.580 & G48.616 field: -5 − 50 mJy beam^{-1}, G48.598 & G48.656 field: -0.5 − 5 mJy beam^{-1}, G50.271 & G50.283 field: -2 − 20 mJy beam^{-1}, G49.912 field: -0.2 − 2 mJy beam^{-1}, and IRAS 18571+0349 field: -0.2 − 2 mJy beam^{-1}. When calculating the integrated fluxes, a cut-off above the $1\times\Delta S$ level was applied within the aperture. An additional 10-20% error should be added to the measured integrated fluxes for these sub-sources, due to the arbitrary nature of the positions of the aperture boundaries which have been chosen to separate the source components.

The apertures for source sub-components were unavoidably arbitrary, as they cut across $1\times\Delta S$ contours or higher. Figure 2.11 shows the chosen apertures for sub-sources, denoted by "A,B,C..." in Table 2.3. In addition to the noise and absolute flux errors mentioned above, which are accounted for and quoted for each sub-component in Table 2.3, an additional 10-20% uncertainty in the integrated flux density should also be included for sub-sources, to account for the arbitrary placing of apertures.

Values for the solid angle quoted in Table 2.3 are given for irregular or extended sources only, and are derived from the number of pixels above the $1\times\Delta S$ contour within each photometry aperture.

For all extended sources, the angular size of the source at the $3\times\Delta S$ level was measured by taking the major axis of the source to be along the direction which it is most extended, to within a position angle of 10 degrees.

Table 2.3 (continued)

Observed Field	VLA Source Name	Flux Density (mJy)	Peak Position R.A. (J2000)	Peak Position Dec. (J2000)	Peak Flux (mJy beam^{-1})	Angular Size (arcsec) °	Position Angle (deg.) □	Solid Angle (steradians $\times 10^{-8}$)†	Alternative Identifiers for VLA Source
IRAS 18424-0329	VLA 1	14.7 ± 0.3	18 45 00.4	-03 28 26	13.1 ± 0.3	···	···	···	Mol 70, 029.107-0.155 (Becker et al., 1994)
···	VLA 1-P	14.0 ± 0.3	18 45 00.3	-03 28 26	13.5 ± 0.3	2.0 × 0.7	114	···	Mol 70, 029.107-0.155 (Becker et al., 1994)
···	VLA 2	44.9 ± 0.9	18 45 02.1	-03 26 50	4.35 ± 0.13	70 × 50	140	7.78	029.134-0.148 (Becker et al., 1994)
IRAS 18571+0349	VLA 1	22.9 ± 0.6	18 59 35.1	+03 52 46	2.58 ± 0.25	35 × 18	100	2.82	New
···	VLA 2	15.9 ± 0.4	18 59 40.9	+03 52 28	1.79 ± 0.24	27 × 22	10	2.65	New
···	VLA 3	3.07 ± 0.15	18 59 41.7	+03 53 28	1.47 ± 0.24	···	···	···	New
···	VLA 3-P	3.37 ± 0.16	18 59 41.7	+03 53 27	1.31 ± 0.05	10.3 × 9.1	6	···	New
···	VLA 4	13.9 ± 0.4	18 59 42.5	+03 52 36	1.90 ± 0.24	28 × 20	150	2.39	New
···	VLA 5	27.8 ± 0.6	18 59 43.1	+03 53 38	4.11 ± 0.25	49 × 31	10	4.32	Mol 86
···	VLA 5-P	13.1 ± 0.3	18 59 43.2	+03 53 40	3.78 ± 0.09	12.5 × 11.8	35	···	Mol 86
···	VLA 6	36.1 ± 0.8	18 59 45.9	+03 55 20	2.04 ± 0.24	51 × 48	140	5.81	New
···	VLA 6A	15.0 ± 0.4 ◇	18 59 45.5	+03 55 00	1.84 ± 0.24	30 × 26	100	2.74	New
···	VLA 6B	21.1 ± 0.5 ◇	18 59 45.9	+03 55 20	2.04 ± 0.24	54 × 22	150	3.08	New
···	VLA 7	48.0 ± 1.0	18 59 52.0	+03 55 22	9.85 ± 0.31	30 × 24	10	1.98	New
···	VLA 8	83.3 ± 1.8	18 59 53.8	+03 55 02	11.6 ± 0.3	35 × 24	170	2.29	New
IRAS 18586+0106	···	···	···	···	···	···	···	···	···

°For regular sources, the angular size is that directly measured. For -P sources, the angular size is the deconvolved angular size.

□The position angle is measured to be positive east of north.

†The solid angle is given for irregular/extended sources only, found from the number of pixels above $1\times\Delta S$ within the photometry aperture.

◇An additional error of ∼10-20% of the measured flux should be added to the flux errors of the components of multiply peaked sources. This is to account for the uncertainty in where the aperture is placed to divide the components of the source.

The peak and integrated flux densities, the angular size, and the position angle of fully or nearly unresolved sources (-P) were determined using the AIPS task IMFIT.

The reported peak positions are measured from the peak pixel of the source, except for fully or nearly unresolved sources, whose peak positions are determined from the peak in the fitted Gaussian.

It is important to note that, due to the removal of some of the shortest baselines (c.f. Section 2.2), and the fact that VLA D array observations are only sensitive to size scales less than 3', some of the measured 3.6 cm source flux densities may suffer from missing extended flux. This would have an impact on the derived properties of these sources by, for example, underestimating the luminosities and masses of their exciting stars (see Sections 2.3.3 and 2.4.4).

2.3.2 Analysis of Individual Fields

Panel c) of Figures 2.1 to 2.10 presents a three-colour (Red: 8μm, Green: 4.5μm, Blue: 3.6μm) *Spitzer* IRAC (Fazio et al., 2004) GLIMPSE (Benjamin et al., 2003) image of the observed fields, or an MSX (Price et al., 2001) A Band (8.28μm) image for the two observed VLA fields not covered by the GLIMPSE survey, overlaid with contours of VLA 3.6 cm emission.

Table 2.4 provides a summary of the evolutionary indicators associated with each millimetre clump. Column 2 of Table 2.4 lists whether there is 3.6 cm emission detected within 60" of each clump peak position, and columns 3 to 7 list whether maser emission, dense gas tracers, GLIMPSE or MSX mid-IR emission, outflows, or IRAS sources have been detected towards each clump. The final column of Table 2.4 provides the IRAS luminosities of the associated IRAS sources, calculated using the method outlined in Section 2.1.1.

In the following subsections, Spitzer GLIMPSE point-source catalog names have been shortened to start with "GL" (e.g., SSTGLMC G044.6598+00.3503 is shortened to be GL044.6598 +00.3503). A single source from the GLIMPSE Archive (indicating the photometry is less reliable) is indicated with the full name SSTGLMA G050.3179-00.4186.

Table 2.4. Evolutionary Indicators Associated with the Observed Millimetre Clumps

Millimetre Clump Name	3.6 cm Emission Within 60"?	Maser Emission	Dense Gas	Mid-IR Emission?	Outflow?	IRAS Source	L_{IRAS} (10^3 $L_\odot$)
G044.521+00.387	Y	···	CS [1]	Y	···	IRAS 19090+1023	0.932 - 2.13
G044.587+00.371	N	···	···	Y	···	···	···
G044.617+00.365	Y	···	···	N	···	···	···
G044.661+00.351	N	···	···	Y	···	IRAS 19094+1029	24.3 - 24.6
G048.540+00.040	Y	···	···	N	···	···	···
G048.580+00.056	N	···	···	N	···	···	···
G048.598+00.252	Y	···	···	Y	···	···	···
G048.605+00.024	Y	H_2O [2,3], OH [3]	CO [4,5,6] CS [1,6,7,8] HCN [8]	Y	Y*	IRAS 19181+1349	927 - 932
G048.610+00.220	N	···	···	N	···	···	···
G048.616+00.088	N	···	···	Y	···	···	···
G048.634+00.230	Y	···	CO[9,10] CS [11] 1.2 mm [11], Others [12]	Y	···	IRAS 19175+1357	60.5 - 168
G048.656+00.228	Y	···	···	Y	···	···	···
G048.751-00.142	N	···	···	N	···	···	···
G048.771-00.148	N	···	···	Y	···	···	···
G049.830+00.370	Y	···	···	Y	···	IRAS 19193+1504	127
G049.912+00.370	N	···	···	Y	···	IRAS 19195+1508	7.61 - 21.2
G050.271-00.442	N	···	···	Y	···	IRAS 19232+1504	0.960 - 254
G050.283-00.390	Y	OH? [13,14]	CS [1]	Y	Y*	IRAS 19230+1506	281 - 286
IRAS 18256-0742 Clump 1	Y	···	CO [15] NH_3 [16]	Y	N	IRAS 18256-0742	10.5
IRAS 18424-0329 Clump 2	Y	OH? [17]	CO [15] NH_3 [16]	Y	N	IRAS 18424-0329	55 †

2.3.2.a G44.587 & G44.661

The G44.587 & G44.661 field (Figure 2.1) contains two 3.6 cm sources. VLA 1 is in the far S-W of the image, and is associated with the millimetre source G44.521. VLA 2 is found near the centre of the field, close to the millimetre source G44.617. There is no significant ionized emission found towards either G44.587 or G44.661.

The GLIMPSE image of the G44.587 & G44.661 field, presented in Figure 2.1c), shows that there are clusters of mid-IR sources and diffuse 8.0 μm emission associated with each of the three millimetre clumps. The inset panels show the areas marked by white boxes in the main panel, which surround the millimetre sources (corresponding from top to bottom) G44.661, G44.587, and G44.521.

The GLIMPSE source GL044.6598+00.3503, associated with the millimetre clump G44.661, and marked by a light blue circle in Figure 2.1c), has both IRAC colors [3.6] - [4.5] and [5.8] - [8.0] greater than 0.6 suggesting that the source is deeply embedded (Allen et al., 2004). There are also two extended mid-IR sources to the northwest and south of GL044.6598 +00.3503.

The millimetre clump G44.587 is associated with a cluster of GLIMPSE sources which have positive IRAC colors or rising mid-IR SEDs: GL044.5823+00.3689, GL044.5901+00.3697, GL044.5914+00.3689, and GL044.5802+00.3660 (marked by a yellow, light green, red, and turquoise circle respectively). This is also the case for G44.521, which is associated with GL044.5215+00.3902, GL044.5223+00.3858, GL044.5206+0.3866, and GL044.5231 +00.3828 (marked by dark green, orange, dark blue, and magenta circles respectively). Both the reddened and clustered nature of these sources suggest that the millimetre clumps G44.521, G44.587, and G44.661 are associated with star-forming clusters. However, the lack of ionized emission towards these clusters suggests that their members are either low-mass or very young.

2.3.2.b G48.580 & G48.616

Figure 2.2 shows that there are six sources detected in the G48.580 & G48.616 field with 3.6 cm emission greater than $5\times\Delta S$. The emission is dominated by the HII region VLA 5, the most extended source in the field; the integrated flux of VLA 5 is 3.23 Jy, constituting $\sim 3/4$ of the total emission from sources in the field brighter than $5\times\Delta S$. Both VLA 4 and VLA 5

Table 2.4 (continued)

Millimetre Clump Name	3.6 cm Emission Within 60"?	Maser Emission	Dense Gas	Mid-IR Emission?	Outflow?	IRAS Source	L_{IRAS} (10^3 $L_\odot$)
IRAS 18424-0329 Clump 4	Y	OH? [17]	CO [15] NH_3 [16]	N	N	IRAS 18424-0329	55 †
IRAS 18424-0329 Clump 6	Y	OH? [17]	CO [15] NH_3 [16]	N	N	IRAS 18424-0329	55 †
IRAS 18571+0349 Clump 1	Y	···	CO [15]	Y	N	IRAS 18571+0349	106
IRAS 18571+0349 Clump 3	N	···	CO [15]	N	N	···	···
IRAS 18571+0349 Clump 4	Y	CH_3OH [18]	CO [15]	Y	N	···	···
IRAS 18586+0106 Clump 1	N	···	CO [15]	N	N	···	···
IRAS 18586+0106 Clump 3	N	···	CO [15]	N	N	···	···
IRAS 18586+0106 Clump 4	N	···	CO [15]	N	N	···	···
IRAS 18586+0106 Clump 5	N	OH [17]	CO [15] NH_3 [16]	Y	N	IRAS 18586+0106	44
IRAS 18586+0106 Clump 6	N	···	CO [15]	N	N	···	···
IRAS 18586+0106 Clump 7	N	···	CO [15]	N	N	···	···

Note. — References: [1] Bronfman et al. (1996) [2] Kurtz & Hofner (2005) [3] Forster & Caswell (1989) [4] Shepherd & Churchwell (1996a) [5] Solomon et al. (1987) [6] Plume et al. (1992) [7] Shirley et al. (2003) [8] Wu & Evans (2003) [9] Sridharan et al. (2002) [10] Thomas & Fuller (2008) [11] Beuther et al. (2002b) [12] Fuller et al. (2005) [13] Te Lintel Hekkert & Chapman (1996) [14] Baudry et al. (1997) [15] Zhang et al. (2005) [16] Molinari et al. (1996) [17] Edris et al. (2007) [18] Pandian et al. (2007)

†It is not certain which of the clumps listed by B06 is associated with IRAS 18424-0329, however the general 1.2 mm emission in this field is coincident with the IRAS source.

*Diffuse 4.5μm emission towards the source suggests the presence of an outflow.

consist of several components. VLA 4 has a compact component to the south, (VLA 4A) and an extended component to the north (VLA 4B). VLA 5 consists of an extended western component, approximately extended along the NE-SW direction (VLA 5A), two compact components which also include some fainter diffuse emission (VLA 5C and VLA 5D being the NE and SE components respectively), and a component which extends from VLA 5D to the southeast: VLA 5B. The edge of VLA 5A is associated with the millimetre source G48.580. The sources VLA 5B, VLA 5C, and VLA 5D are associated with the millimetre clump G48.605.

VLA 5 has been observed previously by many authors; it is known most commonly as G48.6+0.0 or IRAS 19181+1349. HI, OH and H_2CO absorption have been detected towards VLA 5 (Caswell et al., 1975; Wilson et al., 1978; Silverglate & Terzian, 1978; Downes et al., 1980; Kuchar & Bania, 1994), placing this source at the far kinematic distance, between 10.3 and 12.0 kpc. This is consistent with the finding in this work that the millimetre sources G48.580 and G48.605, are at the far distance ($d \sim 10$ kpc, see Section 2.1.1).

VLA 5A, 5B, 5C, and 5D have been observed in radio continuum observations by Matthews et al. (1978), Zoonematkermani et al. (1990), and Kurtz et al. (1999, using the VLA D array at 3.6 cm, see their Figure 7). Although the integration time of the original D array observations of this field was four times longer than those of Kurtz et al. (1999), the same sensitivity was obtained in the final image (1.2 mJy beam^{-1}). Nevertheless, the image of the observations taken in this work is shown as it presents a larger field of view which covers both millimetre sources G48.580 and G48.616.

In addition, 5C and 5D were observed at higher resolution by Kurtz et al. (1994), at 2 and 3.6 cm with the VLA in B array. The spectral index of VLA 5C and VLA 5D between 2 and 3.6 cm was calculated using only the B array flux densities given in Kurtz et al. (1994), as they result from the most similar UV coverages. The spectral index S_ν is defined as $S_\nu \propto \nu^\alpha$, where α is the spectral index. The spectral index of VLA 5C, named G48.609+0.027 by Kurtz et al. (1994), was found to be -0.4±0.2, which is consistent with mixed thermal and non-thermal (synchrotron) emission from ionized gas. The spectral indices of the two components of VLA 5D resolved by the VLA B array observations, G48.606+0.023 and G48.606+0.024, were found to be 0.2±0.1 and 0.3±0.5 respectively, which are consistent with an ionized wind. However, in the case of G48.606+0.024, the larger error also allows the spectral index to be explained by optically thin free-free emission.

De Buizer et al. (2005) have performed a high resolution (∼1-2") mid-infrared survey towards sites of water maser emission, in which mid-IR emission was detected towards VLA 5C and VLA 5D. Both water and hydroxyl masers have been detected towards VLA 5D (e.g., Forster & Caswell, 1989), and a wealth of molecular tracers have also been observed (e.g. CS(J=7-6) and CO(J=3-2) Plume et al., 1992). Mueller et al. (2002a) have also detected the source in the far-IR, at 350μm. These detections, in combination with the coincidence of VLA 5D with the millimetre source G48.605, suggest this source is at a very early stage of evolution.

Figure 2.2c) presents a GLIMPSE image of the G48.580 & G48.616 field. The crosses mark the positions of the millimetre clumps (in increasing R.A.: G48.616, G48.540, G48.580, and G48.605). The inner panel shows the sources VLA 5B, 5C and 5D, and covers the area shown by the black box in the main panel. Comparison between the GLIMPSE and VLA 3.6 cm images reveals that VLA 5B is associated with the GLIMPSE source GL048.6021+00.0257, and VLA 5C is associated with the GLIMPSE source GL048.6093+00.0270 (whose positions are shown by yellow and blue circles respectively in Figure 2.2c). There are no mid-IR IRAC sources directly associated with the peak of the compact HII region VLA 5D, in fact the source appears to lie within a dark filament. However, VLA 5D appears to have associated 4.5 μm emission (green) extending in the N-S direction. Emission in the 4.5 μm band is thought to be produced by shocked H_2 or CO gas in outflows (see Cyganowski et al., 2008, and references within). If this emission is tracing shocked gas from the outflow of this source, it provides further evidence towards its youth, and suggests it may still be in the process of outflow and accretion.

In summary, there are several newly discovered HII regions in the field, for example VLA 1 and VLA 3. However these HII regions are not coincident with any BGPS clumps. In contrast, the extended bright HII region VLA 5 contains several compact components: VLA 5B, C and D, of which VLA 5C and a sub-component of VLA 5D have spectral indices that cannot be explained by optically thin free-free emission expected from classical HII regions. There are also many indicators of (massive) star formation towards these components, in particular VLA 5D, including mid-IR, maser, and 350μm emission. Therefore VLA 5 is determined to be a current site of massive star formation.

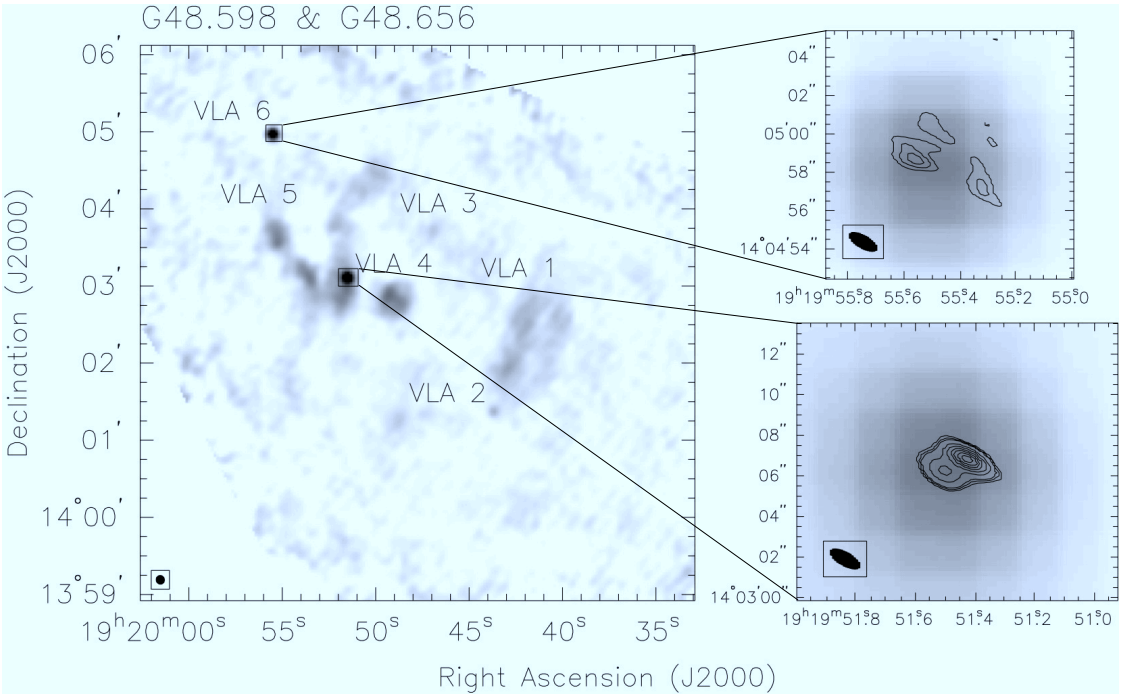

Figure 2.12: VLA 3.6 cm B and D array continuum images of the G48.598 & G48.656 field. *Left panel:* VLA 3.6 cm D array greyscale image of the entire region. Greyscale range: 0.0 - 5.0 mJy beam^{-1}. *Top right panel:* VLA 6. Contours: VLA 3.6 cm B array image, levels: -3, 3, 4, 5 $\times\sigma$ = 0.1 mJy beam^{-1}. Synthesised beam: 1.7 × 0.7", P.A.=61°. Greyscale: VLA 3.6 cm D array image, range: 0.2 - 14 mJy beam^{-1}. *Bottom right panel:* VLA 5C. Contours: VLA 3.6 cm B array image, levels: -3, 3, 4, 5, 10, 15, 20, 25, 30, 35 $\times\sigma$ =0.1 mJy beam^{-1}. Synthesised beam: 1.7 × 0.7", P.A.=61°. Greyscale: VLA 3.6 cm D array image, range: 0.2 - 14 mJy beam^{-1}.

2.3.2.c G48.598 & G48.656

Figure 2.3 shows there are six 3.6 cm sources in the G48.598 & G48.656 field. VLA 1 is a diffuse extended source, lying along the NW-SE direction. VLA 2 is an unresolved source, found to the south of VLA 1. VLA 3 is again an unresolved source, and VLA 4 is a roughly circular source to the west of VLA 5. VLA 5 is a complex extended source, with 6 components (A to F in increasing R.A., which are labeled in Figure 2.11). Component VLA 5C is composed of a brighter unresolved source surrounded by fainter extended emission. VLA 6 is also unresolved, with the brightest peak flux in the field (25.5 mJy beam^{-1}).

VLA 4 is coincident with the millimetre source G48.634, and VLA 5D is coincident with G48.656. The millimetre source G48.610 is also associated with slightly resolved 3.6 cm emission at the $4\times\Delta S$ level.

Sridharan et al. (2002) have carried out VLA B array observations of this field at 3.6 cm, with a sensitivity of 0.1 mJy beam^{-1}. As the 3.6 cm images were not presented in Sridharan et al. (2002), the data was obtained from the NRAO archive[3] (observation date: 1998 July 2, project code: AS643) and the field around the observed source 19175+1357, which is coincident with G48.634, was imaged. Sources VLA 5C and VLA 6 were detected in their B array observations; Figure 2.12 presents both B and D array observations of these sources in its right hand panels, with the B array image shown in contours, and the D array image in greyscale. The subcomponent VLA 5C, which is observed as an unresolved source in the D array observations at 3.6 cm, is resolved into a double-peaked source in the B array observations, the northwest lobe being its brightest component. VLA 6 is also detected as faint ($\sim$5-σ) emission in the B array observations, which contains two 5-σ peaks.

The distance towards G48.598 and G48.656 has been determined, using observations of radio recombination lines (H110α and H138β), and H_2CO and HI absorption, to be between 10.5 and 12.5 kpc (Planesas et al., 1991; Kuchar & Bania, 1994; Watson et al., 2003). This is consistent with the finding of this work that these sources are at the far distance, with distances of 10.6 and 10.3 kpc respectively (see Section 2.1.1).

Beuther et al. (2002b) has observed the field at 1.2 mm using the MAMBO bolometer array at the IRAM 30 m telescope. Comparing their Figure 1, panel 19175+1357, to the

[3] http://archive.cv.nrao.edu/

Bolocam observations of the field shown in Figure 2.3 of this work, one can see that very similar dust structures are traced by the two sets of observations. The MAMBO resolution of 11" at 1.2 mm resolves both millimetre sources G48.634 and G48.610 into two components; these are identified by Beuther et al. as sources 1 and 2, and 4 and 5 respectively. Source 1 is coincident with the HII region VLA 4, and G48.598 and G48.656 correspond respectively to sources 6 and 7. Williams et al. (2004) have observed G48.634 at 450 and 850 μm, detecting two sources: WFS70 and WFS71, whose positions are proximate to the Beuther et al. sources 19175+1357:2 and 1 respectively (with offsets of 2.9" and 6.2").

Figure 2.3c) shows a three-colour *Spitzer* IRAC GLIMPSE image of the G48.598 & G48.656 field, overlaid with contours of the VLA 3.6 cm emission. The white crosses mark the positions of the millimetre clumps (in increasing R.A.: G48.598, G48.610, G48.634, and G48.656). The two right panels show the areas of the *Spitzer* IRAC image marked by white boxes in the left panel, and are also overlaid with contours of 3.6 cm emission. The bottom right panel shows the IRAC emission towards G48.634. There are two extended sources shown in this panel, one to the north which is associated with VLA 4, and a smaller extended source to the south, which is coincident with 19175+1357:2, and WFS70. By studying the separate IRAC band images, the northern source was found to contain three point sources superimposed upon the extended emission, at approximately $19^h19^m49^s.2$ +14°02'49", $19^h19^m49^s.0$ +14°02'46" and $19^h19^m48^s.6$ +14°02'52" (J2000). The top right panel shows a close up of the IRAC emission towards VLA 6. The mid-IR emission associated with this source is mostly extended, and is therefore not in the GLIMPSE catalog. However there is a central point source seen in IRAC band 1, at $19^h19^m55^s.5$ +14°04'58" (J2000).

The GLIMPSE source GL048.6557+00.2285 appears to be associated with VLA 5D, and the source GL048.6024+00.2394 is close to VLA 2. The positions of these two GLIMPSE sources are shown in Figure 2.3c) by blue and yellow circles respectively. In addition, two extended GLIMPSE sources are associated with the millimetre source G48.598, near VLA 2, with positions $19^h19^m41^s.6$ +14°01'19" and $19^h19^m42^s.1$ +14°01'24".

Therefore, by comparing the 3.6 cm, 1.1 mm and GLIMPSE images, several sites of massive star formation in the G48.598 & G48.656 field have been found. Two examples are VLA 4 and VLA 5D, which are coincident with several signposts of massive star formation (e.g. dust continuum, mid-IR and ionized gas emission).

2.3.2.d G48.751

There is one faint (F_{peak}=0.431 mJy beam^{-1}) VLA 3.6 cm source detected above 5×ΔS in the G48.751 field shown in Figure 2.4. This source is not associated with any of the detected Bolocam millimetre sources in the field. There is a nearby IRAS source, IRAS 19191+1352, however it is not related to any millimetre or 3.6 cm continuum emission. The extended GLIMPSE source GL048.7750-00.1507 (whose position is shown by a yellow circle in Figure 2.4c) is $\sim$ 20" from the peak of G48.771, but still appears to be associated with the extended millimetre dust emission towards this source. There is also extended 8μm emission covering a large proportion of the bottom half of Figure 2.4c), which extends to the south of G48.751 and VLA 1. Therefore it appears that the G48.751 field contains two mostly quiescent clumps, one of which may now contain a protostar shown in the mid-IR by GL048.7750-00.1507.

2.3.2.e G49.912

The 3.6 cm image of the G49.912 field shown in Figure 2.5 uncovers no significant emission from ionized gas towards G49.912. However there is a double-lobed 3.6 cm source, VLA 1, in the S-W of the field, which is associated with the millimetre source G49.830.

Figure 2.5c) shows a three-colour GLIMPSE image of the region. The white crosses mark the positions of the millimetre clumps (in increasing R.A.: G49.830 and G49.912). Figure 2.5c) shows that there is a cluster of mid-IR sources associated with G49.912 (see the inset panel, which covers the area marked by the top white box in the main panel). The most conspicuous source in the cluster at these wavelengths is an extended mid-IR source at $19^h21^m48^s.1$ +15°14'32" (J2000). There are several other mid-IR sources in the cluster having IRAC colours which suggest they are young objects. The sources GL049.9113+00.3719 and GL049.9134+00.3723 (indicated by yellow and green circles respectively in Figure 2.5c) both have IRAC [3.6] - [4.5] and [5.8] - [8.0] colours greater than 0.6 showing that they are deeply embedded. This, in combination with the clustering of these sources and the presence of an associated millimetre clump, provides evidence that these stars constitute a young star-forming cluster. However, as no significant ionized gas emission is observed towards G49.912, it appears that there are either no stars in the cluster massive enough to produce significant free-free emission, or that any forming massive stars have not yet reached the main sequence.

Emission at 8 μm can originate from polycyclic aromatic hydrocarbons (PAHs) which are thought to fluoresce at the boundaries of HII regions (Churchwell et al., 2004), and, indeed, the 8 μm emission associated with the HII region VLA 1A & 1B traces the edges of the two observed lobes of ionized gas (Figure 2.5c, right panel). The presence of PAH emission near the boundaries of this bipolar, ionized gas structure suggests that VLA 1A & 1B represent the bipolar, ionized outflow lobes from a massive star or star cluster rather than an extragalactic radio galaxy. The morphology of IRAC emission is also similar to the bipolar bubble (S97 and S98) observed by Churchwell et al. (2006, see their Figure 2f).

There is an extended mid-IR source lying between the two lobes of the VLA 1, slightly offset to the west of the axis of this bipolar source, which the shape of the 3.6 cm emission can be seen to follow. It may be that this extended mid-IR source marks the current site of star formation towards VLA 1.

Therefore, the presented observations reveal that there is a star-forming cluster embedded in the clump G49.912 which may only be forming low-mass stars, or has not yet formed a massive star detectable in the 3.6 cm observations. In contrast, the clump G49.830 is coincident with an evolved bipolar HII region, however there is a mid-IR source which may be the site of current star formation in this clump.

2.3.2.f G50.271 & G50.283

There are four 3.6 cm continuum sources detected above $5\times\Delta S$ in the G50.271 & G50.283 field (Figure 2.6). VLA 1 dominates the integrated flux in the region; the source has an extended peak which is elongated in roughly the E-W direction, and two fainter lobes. The main lobe extends to the north, and the second to the S-E. The source VLA 2 is to the S-E of VLA 1, detected at the $5\times\Delta S$ level. VLA 3 is a double-lobed source, and VLA 4 is an unresolved source in the far S-E of the field.

VLA 1 is coincident with the millimetre source G50.283, however the peak of the ionized gas emission is slightly offset (14") from the millimetre peak. There is no significant 3.6 cm emission associated with the other millimetre source in the field, G50.271.

Using H110α recombination line and H_2CO absorption observations, Watson et al. (2003) found the distance to VLA 1 to be 10.0 kpc. This is consistent with the determination of this work that the source is at a far distance of $\sim$ 9.6 kpc (see Section 2.1.1).

Figure 2.6c) shows a three-colour GLIMPSE image of the G50.271 & G50.283 field, overlaid with contours of the VLA 3.6 cm emission. The white crosses mark the positions of the millimetre clumps (in increasing R.A.: G50.283, and G50.271). The inset panel shows a close up of the IRAC emission associated with G50.283 (also VLA 1), the area of which is marked by the white box in the main panel. From Figure 2.6c) it can be seen that the 8 μm PAH emission associated with VLA 1 traces out the edges of the northern lobe of ionized gas, which is similar to the IRAC emission associated with VLA 1 in Figure 2.5c).

The GLIMPSE source GL050.2830-00.3904 (indicated by a blue circle in Figure 2.6c), which is located within the HII region VLA 1, is coincident with the peak of G50.283. There is also a diffuse 4.5 μm extension of GL050.2830-00.3904 that points into the main northern lobe, which may be either tracing a less luminous source, or instead is shocked emission from an outflow associated with GL050.2830-00.3904. Thus, the mid-IR emission from G50.283, in conjunction with the existence of warm dust and ionized gas shown by the 1.1 mm and 3.6 cm images, points to this being a site of current massive star formation. There is a fainter point source, not listed in the GLIMPSE catalogs, at $19^h25^m18^s.49$ +15°12'28.5" (J2000), which is closer to the peak position of VLA 1 than GL050.2830-00.3904. It is possible that this point source is instead creating the HII region VLA 1. A saturated GLIMPSE source, SSTGLMA G050.3179-00.4186 (indicated by a red circle in Figure 2.6c), is associated with VLA 3B. There is also diffuse IRAC emission near the millimetre source G50.271; however, as there are no associated IRAC point sources and no coincident ionized gas emission, this clump appears to be quiescent, or at an early stage of star formation.

Therefore it can be concluded that VLA 1, which is coincident with the millimetre clump G50.283, is a site of current massive star formation, and that the clump G50.271 is quiescent or in a very early stage of star formation.

2.3.2.g IRAS 18256-0742

The VLA 3.6 cm image of the IRAS 18256-0742 region, shown in Figure 2.7, contains five sources. VLA 1, 3 and 5 are compact sources, whilst VLA 2 and 4 are extended. VLA 2 is associated with the millimetre Clump 1 in the IRAS 18256-0742 field observed by B06. Molinari et al. (1998) have previously detected the source VLA 5 at 6 cm using B configuration VLA observations.

As there is no GLIMPSE coverage of this field, an MSX A band image of the field at 8.28μm is shown in Figure 2.7c). There is 8μm emission associated with VLA 2 and millimetre Clump 1. Therefore this clump is likely to be a current site of massive star formation. There is also a "shell" of 8μm emission surrounding VLA 4, tracing PAH emission at the boundary of the HII region. As the HII region VLA 4 is approximately circular, has a diameter of almost a parsec, and is not associated with any dense gas traced by millimetre emission, it is consistent with being more evolved than VLA 2.

2.3.2.h IRAS 18424-0329

Figure 2.8 shows that there are two 3.6 cm continuum sources detected in the IRAS 18424-0329 field. VLA 1 is a compact unresolved source in the south of the field, and VLA 2 is cometary in shape and lies close to the field centre. VLA 2 is also associated with millimetre emission (shown in Figure 2.8b). B06 find three millimetre clumps listed to be within $\sim$ 1' of VLA 2: Clumps 2, 4, and 6. The given positions of these three clumps are shown by small circles in Figure 2.8b). The peak of VLA 2 lies closest to Clump 2. Becker et al. (1994) have previously observed both VLA 1 and 2 at 1.4 and 5 GHz, and Molinari et al. (1998) have also detected VLA 1 at 6 cm.

As can be seen from the GLIMPSE image of the region (Figure 2.8c) there is diffuse 8.0μm PAH emission which follows the edges of VLA 2. VLA 2 has a calculated physical size, Δs, of 3.33 pc and is therefore a highly evolved HII region. It may be that the massive star which created VLA 2 formed from part of the same cloud of molecular gas as the three existing clumps, which do not yet appear to have formed stars. It is also possible that VLA 2 is not physically associated with Clumps 2, 4, and 6 from B06, and that these clumps constitute a quiescent complex of molecular gas. There is no IRAC emission associated with the HII region VLA 1.

2.3.2.i IRAS 18571+0349

The 3.6 cm image of the field surrounding IRAS 18571+0349 (Figure 2.9) shows that there are eight sources in the field detected at greater than $5\times\Delta S$. All of the sources bar one, VLA 3, are extended. VLA 3 and VLA 5 are associated with the most massive millimetre clump in this field, Clump 1. In addition, VLA 7 is associated with the millimetre Clump 4.

Molinari et al. (1998) have previously detected VLA 5 at 6 cm using the VLA in B array. HI absorption observations taken by Kuchar & Bania (1994) indicate that the sources in this field are at the far distance (d=10.4 kpc). Therefore, the far distances calculated from the measured GRS ^{13}CO velocities in Section 2.1 were assumed for all clumps in the field, and the clump properties given by B06 have been scaled accordingly.

The IRAC *Spitzer* image of the region (Figure 2.9c) shows a ridge of diffuse mid-IR emission, with condensations containing bright objects or clusters situated along it. The VLA 3.6 cm sources VLA 3, 5 and 7 are associated with GLIMPSE sources in this ridge. The compact source VLA 3 is associated with extended mid-IR emission at approximately $18^h59^m41^s.6$ +3°53'30" (J2000), and the peak of VLA 5 is associated with another mid-IR source with the position $18^h59^m43^s.0$ +3°53'37" (J2000). There is also a bright GLIMPSE source associated with VLA 5, GL037.3418-00.0591 (identified by a blue circle in Figure 2.9c), which has IRAC colours [3.6] - [4.5]=2.31 and [5.8] - [8.0]=1.07, showing that this is a highly embedded object. The clustering of these sources, along with the associated ionized and molecular gas, suggest that this is a current site of clustered massive star formation.

Further to the north, there is also a dust condensation (Clump 4 in B06, associated with VLA 7) in a "pillar" which extends from the ridge to the S-E. The ridge contains a GLIMPSE source (GL037.3815-00.0820, indicated by a yellow circle in Figure 2.9c) that has a rising SED between 2.17μm (2MASS K band) and 8.0μm. Methanol masers have also been detected towards Clump 4 (VLA 7) by Pandian et al. (2007) within a 40" beam, suggesting star formation is currently occurring within it. It is interesting to note however that the peak of VLA 7 is not coincident with the GLIMPSE source, but instead is displaced to the east by 7.5". It may be that the object associated with GL037.3815-00.0820 is not creating an HII region, but instead a nearby star, such as the one directly west of the tip of the pillar, is ionizing molecular material in its proximity. The peak of the source VLA 8 is coincident with the GLIMPSE source GL037.3816-00.0922 (shown by a green circle in Figure 2.9c).

Although unrelated to any diffuse mid-IR emission, VLA 2 and 4 appear to be related to the GLIMPSE sources GL037.3199-00.0641 and GL037.3241-00.0690 respectively (indicated by a red and orange circle in Figure 2.9c).

In summary, the field surrounding IRAS 18571+0349 contains several sites of massive star formation; in particular, those surrounding Clumps 1 and 4 observed by B06.

2.3.2.j IRAS 18586+0106

There were no detections above $3\times\Delta S$ (=0.48 mJy beam^{-1}) in the IRAS 18586+0106 field (Figure 2.10). Deconvolution of the image was hampered, and therefore the rms noise in the final image was increased, by a bright source (G35.20-1.74) on the edge of the field, which caused significant stripes through the image. Molinari et al. (1998) detected a faint source in this field at 6 cm, denoted Mol 87, lying between Clumps 1 and 5 ($19^h01^m15^s.271$ +01°11'00.04", J2000) with a peak flux density of 6.89 mJy beam^{-1}.

As there are no *Spitzer* IRAC images which cover this field, instead an MSX A band image of the field is shown in Figure 2.10b). The 8μm emission is coincident with the IRAS source, however these are both displaced from the peak of the nearest millimetre clump, Clump 5.

2.3.3 Derived Properties of HII Regions

Table 2.5 lists the derived physical properties of the detected VLA 3.6 cm sources given in Table 2.3. Properties of unresolved and partially resolved sources were derived assuming they are spherically symmetric, optically thin, homogeneous, and ionization-bounded HII regions. In the case of irregularly shaped sources, it is assumed that they are optically thin, homogeneous, and ionization-bounded HII regions, and that the observed area in the plane of the sky is projected along a depth Δs, estimated from the geometrical mean of the size of the source on the sky. The effect of dust was not taken into account in the calculations below, and therefore the calculated spectral types and luminosities are in fact lower limits. It is also assumed that shocks in outflows do not contribute a significant amount to the ionized gas emission.

In Table 2.5, the assumed distance d in kpc for each 3.6 cm source was taken to be the distance of the millimetre source closest in projection on the sky within the observed fields. The effective angular diameter of the source $\Delta\theta$, given in degrees, was found by calculating the geometrical mean of the angular sizes given in Table 2.3. For unresolved and partially unresolved sources, it was necessary to correct the Gaussian angular diameter $\Delta\theta$ to the angular size of a sphere, using the multiplicative correction factors given in Panagia & Walmsley (1978).

Table 2.5. Derived Physical Properties for VLA 3.6 cm Sources

Observed Field	VLA Source Name	Irr./ Unres.	d (kpc)	$\Delta\theta$ (")	Δs (pc)	T_b (K)	$\tau_\nu \times 10^3$	$EM/10^6$ (pc cm^{-6})	$n_e/10^3$ (cm^{-3})	U (pc cm^{-2})	$\log N_{Ly}$ (s^{-1})	Spectral Type	$L_{cm}/10^3$ ($L_\odot$)
G44.587 & G44.661	VLA 1	I	3.8	46	0.84	2.57	0.314	0.066	0.28	17.99	47.47	B0	25.12
···	VLA 2	U	10.8	···	···	···	···	···	···	···	46.14	B0.5	10.96
···	VLA 2-P	U	10.8	<2.1	<0.11	>7.78	>0.949	>0.200	1.64	7.74	46.17	B0.5	10.96
G48.580 & G48.616	VLA 1	I	10.0	22	1.07	0.92	0.112	0.024	0.15	14.98	47.66	O9.5	38.02
···	VLA 2	I	10.0	40	1.92	1.00	0.122	0.026	0.12	22.77	48.17	O8.5	53.70
···	VLA 3	I	10.0	23	1.14	0.70	0.085	0.018	0.13	14.28	47.57	B0	25.12
···	VLA 4	I	10.0	70	3.39	1.79	0.219	0.046	0.12	40.46	48.59	O7	100.00
···	VLA 4A	U	10.0	···	···	···	···	···	···	···	48.10	O9	45.71
···	VLA 4A-P	U	10.0	<2.9	<0.14	>414.62	>51.886	>10.916	10.83	33.88	48.09	O9	45.71
···	VLA 4B	I	10.0	59	2.88	1.35	0.165	0.035	0.11	32.95	48.42	O8	64.57
···	VLA 5	I	9.9	164	7.88	2.86	0.349	0.073	0.10	82.84	49.45	O5.5	398.11
···	VLA 5A	I	10.0	153	7.42	2.48	0.302	0.064	0.09	75.87	49.32	O5.5	398.11
···	VLA 5B	I	9.9	43	2.09	5.13	0.626	0.132	0.25	41.54	48.50	O7.5	83.18
···	VLA 5C	I	9.9	35	1.66	5.15	0.628	0.132	0.28	35.73	48.35	O8	64.57
···	VLA 5C-P	U	9.9	15.1	0.72	24.98	3.051	0.642	1.15	39.80	48.30	O8	64.57
···	VLA 5D	I	9.9	31	1.48	4.25	0.518	0.109	0.27	31.02	48.34	O8	64.57
···	VLA 5D-P	U	9.9	21.9	1.05	14.62	1.784	0.375	0.73	42.65	48.39	O8	64.57
···	VLA 6	I	9.9	39	1.88	2.65	0.324	0.068	0.19	31.06	48.41	O8	64.57
G48.598 & G48.656	VLA 1	I	10.6	74	3.83	0.27	0.033	0.007	0.04	23.28	47.86	O9.5	38.02
···	VLA 2	U	10.6	···	···	···	···	···	···	···	46.51	B0.5	10.96
···	VLA 2-P	U	10.6	13.4	0.69	0.39	0.047	0.010	0.15	9.60	46.45	B0.5	10.96
···	VLA 3	U	10.5	···	···	···	···	···	···	···	46.88	B0	25.12
···	VLA 3-P	U	10.5	23.9	1.22	0.29	0.035	0.007	0.10	12.69	46.82	B0	25.12
···	VLA 4	I	10.5	35	1.81	0.42	0.051	0.011	0.08	16.37	47.44	B0	25.12
···	VLA 5	I	10.5	118	6.03	0.55	0.068	0.014	0.05	40.11	48.27	O8.5	53.70
···	VLA 5A	I	10.3	24	1.22	0.50	0.061	0.013	0.10	13.41	47.26	B0	25.12
···	VLA 5B	I	10.3	28	1.42	0.42	0.051	0.011	0.09	13.93	47.19	B0	25.12
···	VLA 5C	I	10.5	43	2.21	0.62	0.076	0.016	0.09	21.39	47.76	O9.5	38.02
···	VLA 5C-P	U	10.5	17.0	0.86	2.18	0.266	0.056	0.31	19.87	47.40	B0	25.12
···	VLA 5D	I	10.3	22	1.10	0.38	0.047	0.010	0.09	11.41	47.04	B0	25.12
···	VLA 5E	I	10.3	46	2.32	0.52	0.064	0.013	0.08	20.81	47.61	O9.5	38.02
···	VLA 5F	I	10.3	35	1.74	0.70	0.086	0.018	0.10	18.98	47.58	B0	25.12

Table 2.5 (continued)

Observed Field	VLA Source Name	Irr./ Unres.	d (kpc)	$\Delta\theta$ (")	Δs (pc)	T_b (K)	$\tau_\nu \times 10^3$	$EM/10^6$ (pc cm^{-6})	$n_e/10^3$ (cm^{-3})	U (pc cm^{-2})	$\log N_{Ly}$ (s^{-1})	Spectral Type	$L_{cm}/10^3$ ($L_\odot$)
···	VLA 6	U	10.3	···	···	···	···	···	···	···	47.43	B0	25.12
···	VLA 6-P	U	10.3	4.5	0.22	37.02	4.525	0.952	2.54	20.64	47.45	B0	25.12
G48.751	VLA 1	I	5.3	31	0.81	0.05	0.006	0.001	0.04	4.70	46.16	B0.5	10.96
G49.912	VLA 1	I	10.6	73	3.77	2.20	0.269	0.057	0.12	46.51	48.66	O7	100.00
···	VLA 1A	I	10.6	43	2.24	3.65	0.446	0.094	0.20	38.82	48.50	O7.5	83.18
···	VLA 1B	I	10.6	52	2.66	1.19	0.145	0.030	0.11	29.98	48.16	O8.5	53.70
G50.271 & G50.283	VLA 1	I	9.6	65	3.01	2.66	0.325	0.068	0.15	42.63	48.58	O7	100.00
···	VLA 2	I	9.6	46	2.13	0.11	0.014	0.003	0.04	11.73	47.17	B0	25.12
···	VLA 3	I	9.6	45	2.11	1.60	0.196	0.041	0.14	28.38	48.13	O9	45.71
···	VLA 3A	U	9.6	···	···	···	···	···	···	···	47.75	O9.5	38.02
···	VLA 3A-P	U	9.6	13.2	0.62	8.66	1.056	0.222	0.74	25.07	47.70	O9.5	38.02
···	VLA 3B	U	9.6	···	···	···	···	···	···	···	47.89	O9.5	38.02
···	VLA 3B-P	U	9.6	14.8	0.69	9.47	1.156	0.243	0.73	27.88	47.84	O9.5	38.02
···	VLA 4	U	9.7	···	···	···	···	···	···	···	47.01	B0	25.12
···	VLA 4-P	U	9.7	3.9	0.18	20.03	2.446	0.515	2.06	14.74	47.01	B0	25.12
IRAS 18256-0742	VLA 1	U	3.0	···	···	···	···	···	···	···	45.01	B1	5.25
···	VLA 1-P	U	3.0	<3.1	<0.05	>3.39	>0.413	>0.087	1.69	3.23	45.03	B1	5.25
···	VLA 2	I	3.0	27	0.39	0.04	0.005	0.001	0.05	2.77	45.24	B1	5.25
···	VLA 3	U	3.0	···	···	···	···	···	···	···	44.86	B2	2.88
···	VLA 3-P	U	3.0	<5.8	<0.08	>0.70	>0.085	>0.018	0.56	2.89	44.89	B2	2.88
···	VLA 4	I	3.0	63	0.92	0.05	0.006	0.001	0.04	5.18	45.90	B0.5	10.96
···	VLA 5	U	3.0	···	···	···	···	···	···	···	45.74	B1	5.25
···	VLA 5-P	U	3.0	4.3	0.06	9.02	1.101	0.232	2.36	5.53	45.73	B1	5.25
IRAS 18424-0329	VLA 1	U	11.6	···	···	···	···	···	···	···	47.25	B0	25.12
···	VLA 1-P	U	11.6	2.2	0.13	69.05	8.457	1.779	4.61	17.38	47.23	B0	25.12
···	VLA 2	I	11.6	59	3.33	0.26	0.032	0.007	0.04	21.04	47.73	O9.5	38.02
IRAS 18571+0349	VLA 1	I	9.8	25	1.19	0.37	0.045	0.009	0.09	11.90	47.29	B0	25.12
···	VLA 2	I	9.8	24	1.16	0.27	0.033	0.007	0.08	10.54	47.13	B0	25.12
···	VLA 3	U	9.8	···	···	···	···	···	···	···	46.42	B0.5	10.96
···	VLA 3-P	U	9.8	17.0	0.81	0.29	0.035	0.007	0.12	9.66	46.46	B0.5	10.96
···	VLA 4	I	9.8	24	1.12	0.26	0.032	0.007	0.08	10.24	47.08	B0	25.12
···	VLA 5	I	9.8	39	1.85	0.29	0.036	0.007	0.06	14.75	47.38	B0	25.12

The physical size Δs in pc was calculated from $\Delta\theta$ and d. In the case of unresolved and partially unresolved sources, Δs was taken to be the physical diameter of the spherical HII region. For irregular sources, by assuming that the size of the sources in the plane of the sky is similar to that along the line of sight, Δs was taken to be the depth of the emitting region.

The brightness temperature T_b was found using the Rayleigh-Jeans approximation:

$$T_b = \frac{S_\nu 10^{-29} c^2}{2\nu^2 k \Omega_s} \text{ (K)}, \tag{2.2}$$

where S_ν is the integrated flux density of the source in mJy, c is the speed of light in ms^{-1}, ν is the frequency of the radiation in Hz, k is the Boltzmann constant, and Ω_s is the solid angle covered by the source. For unresolved and partially unresolved sources, $\Omega_s = \pi\Delta\theta^2/4$. For irregular sources, Ω_s was found by summing the area of all pixels associated with the sources with a flux density per beam above ΔS, the significance level in the image.

The optical depth, τ, was then calculated by rearranging the solution of the equation of radiation transfer $T_b = T_e(1 - e^{-\tau})$ for τ, assuming the emitting region is uniformly filled with $T_e = 8200\,\text{K}$ ionized gas. The assumed value for the electron temperature was calculated from the results of Quireza et al. (2006); the mean electron temperature of their observed sources was $T_e = 8200 \pm 2330$ K. The calculated values for the optical depth given in Table 2.5 are all less than 0.1. Therefore, with the exception of the sources G48.587 & G48.661 VLA 2-P, G48.580 & G48.616 VLA 4A-P, IRAS 18256-0742 VLA 1-P, and IRAS 18256-0742 VLA 3-P, for which the angular size is an upper limit, and hence their properties should be viewed with caution, the assumption holds that the observed sources are optically thin.

The emission measure, EM, is given by:

$$\text{EM} = \frac{\tau}{8.235 \times 10^{-2}\ \alpha(\nu, \text{T}_\text{e})\ \text{T}_\text{e}^{-1.35}\ \nu^{-2.1}} \text{ (cm}^{-6}\text{ pc)}, \tag{2.3}$$

where $T_e = 8200$ K and ν is in GHz. The correction factor $\alpha(\nu, T_e)$, which is of order unity, rectifies the small discrepancy between the approximation shown in equation 2.3, given by Altenhoff et al. (1960), and the original derivation by Oster (1961). The value of $\alpha(\nu, T_e)$, 0.9828, was taken from Table 6 in Mezger & Henderson (1967), for $T_e = 8000$ K and $\nu = 8\,\text{GHz}$.

Table 2.5 (continued)

Observed Field	VLA Source Name	Irr./ Unres.	d (kpc)	$\Delta\theta$ (")	Δs (pc)	T_b (K)	$\tau_\nu \times 10^3$	$EM/10^6$ (pc cm^{-6})	$n_e/10^3$ (cm^{-3})	U (pc cm^{-2})	$\log N_{Ly}$ (s^{-1})	Spectral Type	$L_{cm}/10^3$ ($L_\odot$)
···	VLA 5-P	U	9.8	21.1	1.00	0.73	0.089	0.019	0.17	15.21	47.05	B0	25.12
···	VLA 6	I	9.7	49	2.33	0.28	0.034	0.007	0.06	16.98	47.48	B0	25.12
···	VLA 6A	I	9.7	28	1.31	0.25	0.030	0.006	0.07	11.14	47.10	B0	25.12
···	VLA 6B	I	9.7	34	1.62	0.31	0.038	0.008	0.07	13.78	47.25	B0	25.12
···	VLA 7	I	9.7	27	1.26	1.10	0.134	0.028	0.15	17.78	47.61	O9.5	38.02
···	VLA 8	I	9.7	29	1.36	1.65	0.201	0.042	0.18	21.42	47.84	O9.5	38.02

For sources modelled as a spherical HII region, the number density of electrons, n_e, was estimated using

$$n_e = \sqrt{\frac{3\ \mathrm{EM}}{2\Delta s}}\ (\mathrm{cm}^{-3}) \tag{2.4}$$

where the factor of 2/3 is the ratio of the volume of a sphere to that of a cylinder. For irregular sources, the number density is given by:

$$n_e = \sqrt{\frac{EM}{\Delta s}}\ (\mathrm{cm}^{-3}). \tag{2.5}$$

For a spherical HII region, the excitation parameter U can be calculated using the equation

$$U = r n_e^{2/3} = 4.553 \left[\frac{\nu^{0.1} T_e^{0.35} S_\nu d^2}{\alpha(\nu, T_e)} \right]^{1/3}\ (\mathrm{pc\ cm}^{-2}), \tag{2.6}$$

which can be derived using equations 2.3 and 2.4, and by also assuming that the mean free path of photons within the HII region r is equal to $\Delta s/2$. The frequency ν is in GHz, T_e is in Kelvin, S_ν is in Jy, and d is in kpc. An equivalent expression can be derived for the excitation parameter U of irregular sources:

$$U = 3.669 \times 10^{-2} \left[\frac{\nu^{0.1} T_e^{0.35} S_\nu \Delta s^2}{\alpha(\nu, T_e)\Omega_s} \right]^{1/3}\ (\mathrm{pc\ cm}^{-2}). \tag{2.7}$$

The flux of >13.6 eV photons required to sustain the HII region, N_{phot}, can be estimated via the equation $N_{phot} = V n_e^2 \alpha_B$, where V is the volume of the nebula and α_B is the case B hydrogen recombination coefficient, which does not include recombinations to the ground level, as these are balanced by the diffuse radiation field due to recombinations of the ionized gas. The recombination coefficient α_B was taken to be $2.59\times10^{-13}\,\mathrm{s}^{-1}\mathrm{cm}^3$ (Table 2.1 of Osterbrock & Ferland, 2006, for $T = 10^4$ K).

Therefore, for both spherical and irregular cases, the ionization rate N_{phot} can be expressed as:

$$N_{phot} = 3.020 \times 10^{45} \frac{T_e^{0.35} \nu^{0.1} d^2 S_\nu}{\alpha(\nu, T_e)} \ (\mathrm{s}^{-1}). \quad (2.8)$$

Assuming the observed HII regions are created by single OB stars, the corresponding spectral type and luminosity, L_{cm}, of the exciting star required to sustain each observed HII region are listed in Table 2.5. These were found using the results of Panagia (1973).

Table 2.5 shows that there is a large range in the properties of the observed HII regions. For instance, their physical sizes extend from <0.05 pc to 7.88 pc, and their spectral types cover B2 to O5.

2.3.3.a Uncertainties on Derived HII Region Properties

Uncertainties on the properties quoted in Table 2.5 were calculated using a Monte Carlo error propagation code, assuming Gaussian errors for the 3.6 cm integrated flux density, the 3.6 cm source size, the assumed distance for each 3.6 cm source, and the electron temperature T_e. The error in the source size was estimated to be 5" in the case of extended sources, and in the case of unresolved sources the errors given by IMFIT were assumed, which was usually $\lesssim$ 5%. However the sources G50.271 & G50.283 VLA 4-P; IRAS 18256-0742 VLA 3-P; IRAS 18256-0742 VLA 5-P; and IRAS 18424-0329:VLA 1-P have uncertainties in their sizes ranging from 10 to 40%, and the size of IRAS 18256-0742: VLA 1-P has a 110% uncertainty. The additional uncertainty on the integrated fluxes due to aperture placement (see Section 2.3.1) was not included in the error analysis.

The approximate uncertainties in the calculated HII region properties are as follows: uncertainty in $\Delta\theta \sim 9\%$, uncertainty in $\Delta s \sim 20\%$, uncertainty in $T_b \sim 15\%$, uncertainty in $\tau_\nu \sim 45\%$, uncertainty in EM $\sim 20\%$, uncertainty in n_e and $U \sim 15\%$, and uncertainty in $\log_{10} N_{Ly} \sim 15\%$. Therefore, the quoted spectral types are at least correct to within a sub-spectral type, which is also the case for the corresponding luminosities.

2.4 Discussion

2.4.1 Association of Molecular and Ionized Gas

Table 2.6 lists the nearest 3.6 cm source in projection to each millimetre clump, noting whether the peak of the associated ionized gas is observed within a radius of 60". Columns 4 and 5 of Table 2.6 list the projected distances, in arcseconds and parsecs respectively, to the peak of the nearest 3.6 cm emission, and the final column provides the stellar luminosity required to create the nearest HII region within 60", taken from the results in Table 2.5.

Figure 2.13 shows the distribution of millimetre clumps as a function of their projected distance from the nearest ionized gas in parsecs. Similarly, Figure 2.14 shows the relationship between the mass of the millimetre clumps and their projected distance in parsecs from the nearest ionized gas. It can be seen from Figure 2.13 that the observed millimetre clumps tend to be associated with the ionized gas. This is not an artefact of the selection criteria, which selected millimetre clumps with little or no 21 cm continuum emission towards them in the NVSS. In Figure 2.14, there appears to be no obvious correlation between the mass of a clump and the projected distance to the peak of the nearest ionized gas emission.

It can be seen from Figures 2.1 to 2.10 that although the ionized gas tends to be associated with the millimetre clumps, there exist examples of HII regions which, if at the same distance as the observed clumps, appear to have formed at the edges of the dense gas, but are not directly associated with it. For instance, in the field G48.580 & G48.616, the sources VLA 1, 2 and 3 do not appear to be associated with the millimetre emission in the field. This may be evidence that massive stars can also form at the edges of their parent molecular clouds. Therefore, it would be interesting to carry out follow up observations of these sources to determine whether they do lie at the same velocities as the millimetre clumps in each field. Alternatively, it may be that these sources are background objects such as Active Galactic Nuclei (AGN). Examples of sources that are either unresolved or double-lobed with no associated mm emission, and are therefore prospective AGN, include G48.580 & G48.616 VLA 2 and VLA 4A, G50.271 & G50.283 VLA 3A and VLA 3B, IRAS 18256-0742 VLA 5 and IRAS 18424-0329 VLA 1. Previous observations at cm wavelengths of several of these sources (see Table 2.3) allow their spectral indices to be calculated. For instance, using the integrated fluxes published in Zoonematkermani et al. (1990) the spectral indices

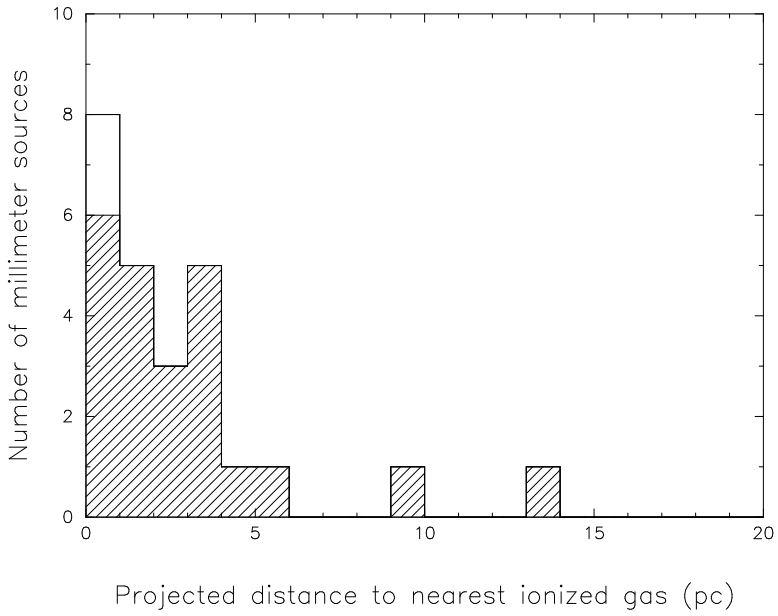

Figure 2.13: Distribution of projected distances (in parsecs) between the position of the millimetre clump peak and the peak of the nearest ionized gas. The hatched histogram shows the sources at the far distance, and the empty-outlined histogram shows all sources, including those at the near distance.

of G50.283 VLA 3A and VLA 3B between 3.6 and 20 cm were calculated to be roughly flat, with values of 0.0 and -0.1 respectively, which suggests they are produced by thermal free-free emission from ionized gas. In contrast, G48.580 & G48.616 VLA 4A, IRAS 18256-0742 VLA 5 and IRAS 18424-0329 VLA 1 were found to have spectral indices between 3.6 and 6 cm of -0.3, -1.0 and -1.0 respectively. Therefore the emission from these sources is likely to be at least partially caused by non-thermal synchrotron emission, which is uncommon in galactic sources but often seen in extra-galactic jets. Hence these sources may in fact be extra-galactic, but further follow-up observations are required to confirm this.

Table 2.6. Ionized Gas Associated with Observed Millimetre Clumps

Millimetre Clump Name	Nearest 3.6 cm Source	3.6 cm Emission Within 60"?	Distance to Nearest 3.6 cm Emission (arcsec)	(pc)	$L_{cm}/10^3$ $L_\odot$
G044.521+00.387	G44.587 & G44.661 VLA 1	Y	9	0.2	25.12
G044.587+00.371	G44.587 & G44.661 VLA 2	N	98	5.2	···
G044.617+00.365	G44.587 & G44.661 VLA 2	Y	22	1.2	10.96
G044.661+00.351	G44.587 & G44.661 VLA 2	N	183	9.6	···
G048.540+00.040	G48.580 & G48.616 VLA 3	Y	34	1.6	25.12
G048.580+00.056	G48.580 & G48.616 VLA 5A	N	66	3.2	···
G048.598+00.252	G48.598 & G48.656 VLA 1	Y	48	2.5	38.02
G048.605+00.024	G48.580 & G48.616 VLA 5D	Y	6	0.3	64.57
G048.610+00.220	G48.598 & G48.656 VLA 2	N	75	3.8	···
G048.616+00.088	G48.580 & G48.616 VLA 2	N	76	3.7	···
G048.634+00.230	G48.598 & G48.656 VLA 4	Y	8	0.4	25.12
G048.656+00.228	G48.598 & G48.656 VLA 5D	Y	3	0.2	25.12
G048.751-00.142	G48.751 VLA 1	N	81	2.1	···
G048.771-00.148	G48.751 VLA 1	N	146	3.8	···
G049.830+00.370	G49.912 VLA 1A	Y	24	1.2	83.18
G049.912+00.370	G49.912 VLA 1B	N	273	13.6	···
G050.271-00.442	G50.271 & G50.283 VLA 2	N	105	4.9	···
G050.283-00.390	G50.271 & G50.283 VLA 1	Y	13	0.6	100.00
IRAS 18256-0742 Clump 1	IRAS 18256-0742 VLA 2	Y	12	0.2	5.25
IRAS 18424-0329 Clump 2	IRAS 18424-0329 VLA 2	Y	28	1.6	38.02
IRAS 18424-0329 Clump 4	IRAS 18424-0329 VLA 2	Y	31	1.7	38.02
IRAS 18424-0329 Clump 6	IRAS 18424-0329 VLA 1	Y	50	2.8	25.12

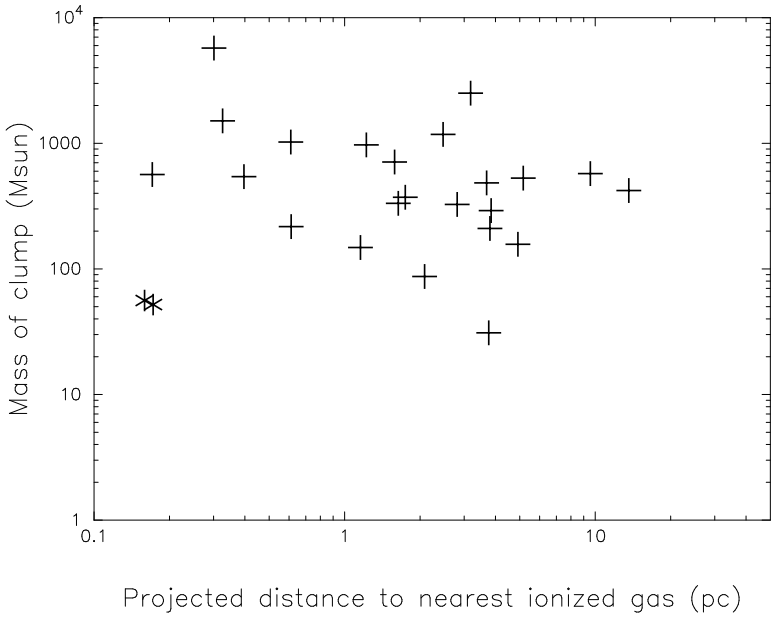

Figure 2.14: Mass of the molecular clump taken from Table 2.1 plotted against the projected distance, in parsecs, between the millimetre clump peak positions and the nearest ionized gas peak. Asterisks represent sources at the near distance, while crosses represent sources at the far distance.

2.4.2 Inferred Ages of the Observed Sites of Star Formation

Single early B stars ($M_\star \sim 10\ M_\odot$) reach the Zero-Age Main Sequence (ZAMS) in about 10^5 yr whereas mid-O stars with $M_\star \gtrsim 25 M_\odot$ reach the ZAMS in $\sim 5 \times 10^4$ yr (e.g., Yorke, 2004, and references therein). In comparison, the timescale for the formation of O star clusters for which the most massive star in the cluster has a mass $M_\star > 25 M_\odot$ (roughly a mid-O star) appears to be <3 Myr (Massey et al., 1995). Early B stars in these clusters continue to form at least 1 Myr after the formation of the O stars.

Several fields show examples in which HII regions are interspersed throughout the gas and dust traced by 1 mm emission: the HII region G48.598 & G48.656 VLA 5 (Figure 2.3) is produced by a cluster of early B to late O stars, and G48.580 & G48.616 VLA 5 (Figure 2.2) by a late O star cluster. The presence of such a well-defined cluster suggests that these regions are likely to be more evolved (since multiple ZAMS stars have formed already) and, indeed, the HII regions tend to be extended and/or complex. Yet there is the potential for significantly more star formation to occur, as there are still large amounts of gas (∼1000-5000 $M_\odot$) traced by warm dust emission that are able to continue to form massive stars in the cluster. Given the presence of ongoing massive star formation in these two clusters, their age is likely to be greater than 0.1 but less than 3 Myr.

Several regions also have massive millimetre clumps that show only a singly peaked HII region forming at or near the centre of a millimetre clump. Examples include G44.587 & G44.661 VLA1 (Figure 2.1), that has the required luminosity of an early B star, and G50.271 & G50.283 VLA1 (Figure 2.6) with the luminosity of a late O star. The presence of a single HII region suggests that these sites have just started the massive star formation process and only a single star or a compact star cluster producing the HII region has reached the ZAMS so far. These regions are likely to be roughly 5×10^4 to 10^5 years old.

A number of regions have millimetre clumps that show no ionized gas emission near the warm dust peak. Examples include the clump G48.616 with a mass of 484 $M_\odot$; G48.540 with a mass of 333 $M_\odot$ (both Figure 2.2), and G50.271 with a mass of 157 $M_\odot$ (Figure 2.6). Thus, these sources are candidate sites for the earliest stages of star formation in which any massive forming star has not yet reached the ZAMS. If this is the case, they are likely to be less than $\sim 5 \times 10^4$ years old. Alternatively, these millimetre sources could represent sites of more evolved low-mass star formation. The sources G44.587 and G44.661 are good

Table 2.6 (continued)

Millimetre Clump Name	Nearest 3.6 cm Source	3.6 cm Emission Within 60"?	Distance to Nearest 3.6 cm Emission (arcsec)	(pc)	$L_{cm}/10^3$ $L_\odot$
IRAS 18571+0349 Clump 1	IRAS 18571+0349 VLA 5	Y	7	0.3	25.12
IRAS 18571+0349 Clump 3	IRAS 18571+0349 VLA 7	N	82	3.8	···
IRAS 18571+0349 Clump 4	IRAS 18571+0349 VLA 7	Y	13	0.6	38.02
IRAS 18586+0106 Clump 1	···	N	···	···	···
IRAS 18586+0106 Clump 3	···	N	···	···	···
IRAS 18586+0106 Clump 4	···	N	···	···	···
IRAS 18586+0106 Clump 5	···	N	···	···	···
IRAS 18586+0106 Clump 6	···	N	···	···	···
IRAS 18586+0106 Clump 7	···	N	···	···	···

examples of this, where the GLIMPSE image of this field (Figure 2.1c) shows that there are clusters associated with these two millimetre clumps.

2.4.3 Comparison of 1 mm and ^{13}CO Images

Figure 2.15 presents a comparison of the millimetre continuum emission (from BGPS or B06) tracing warm dust, the ^{13}CO emission from the GRS survey (Jackson et al., 2006) tracing gas at comparatively lower densities and temperatures than the 1 mm images, and the locations of the detected ionized gas peaks, for several of the observed fields. Only those sources with GRS data (8 of the 10 observed fields) are presented. Integrated ^{13}CO emission is shown in greyscale, warm dust emission in contours, and cross symbols mark the peak positions of the HII regions listed in Table 2.3. The integrated ^{13}CO images were made by integrating the channels containing ^{13}CO emission from the clouds associated with each millimetre clump. In many cases, the same cloud contained several of the clumps in the field. From Figure 2.15, it can be seen that in all cases, the warm, 1 mm dust emission follows the morphology of the ^{13}CO gas emission. This demonstrates how it was possible to match the morphologies of the millimetre and ^{13}CO emission, and therefore assign velocities and distances to the millimetre sources with confidence.

Masses of the material associated with the observed millimetre clumps were also derived from the ^{13}CO and $\sim$1 mm emission over the area of sky covering the ^{13}CO cloud, using the same photometry aperture for both images. The ^{13}CO masses were derived using the equations of Scoville et al. (1986), assuming the emitting material is optically thin. A temperature of 10K was also assumed, in agreement with the results of Rathborne et al. (2009), and the required [^{12}CO/^{13}CO] abundance ratios were found from the results of Wilson & Rood (1994). The millimetre dust masses were calculated using the same method as outlined in Section 2.1.1. For dust masses calculated from the B06 1.2 mm images, the dust opacity was assumed to be 1 cm^2 g^{-1}, consistent with their assumed value.

Table 2.7 presents the calculated masses of the associated cloud material in ^{13}CO and 1 mm dust emission, $M_{cloud}(^{13}CO)$ and $M_{cloud}(1\,mm)$ respectively, along with the ratios $M_{cloud}(1\,mm)/M_{cloud}(^{13}CO)$ and $\Sigma M_{clump}(1\,mm)/M_{cloud}(^{13}CO)$.

The value $\Sigma M_{clump}(1\,mm)/M_{cloud}(^{13}CO)$ is the sum of the masses of the associated millimetre clumps selected from BGPS or B06 over the total cloud mass traced by ^{13}CO. The

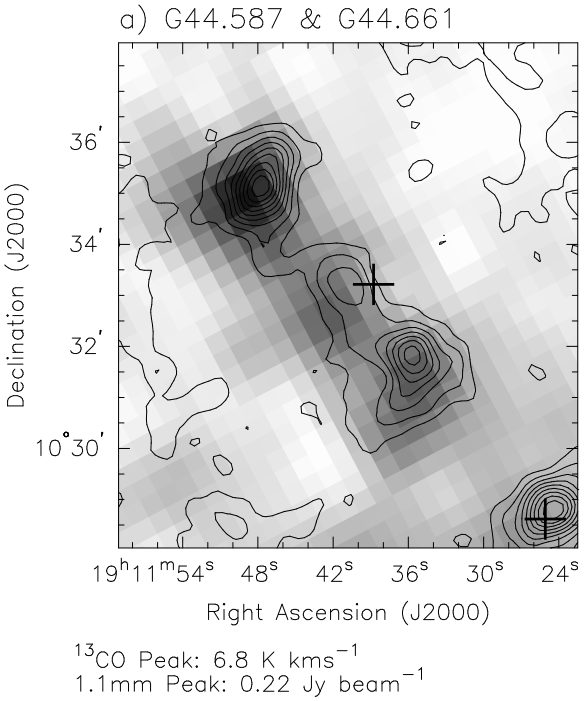

Figure 2.15: Comparison of the dense gas traced by ^{13}CO(J=1-0), molecular clumps traced by millimetre continuum, and ionized gas peaks for each field. ^{13}CO(J=1-0) is shown in greyscale ranging from 0 to 1.1 times the peak flux density. Contours trace the millimetre continuum emission with contour levels plotted from 10 to 90% of the peak emission, in steps of 10%. The peak ^{13}CO(J=1-0) temperature and 1.1 or 1.2 mm flux density are given below each sub-figure. The locations of the ionized gas peaks from HII regions shown in Figure 1 are shown by crosses.

Table 2.7. Comparison of Cloud and Clump Masses Derived from ^{13}CO and 1 mm

Observed Field	Associated Millimetre Clumps	$M_{cloud}(^{13}CO)$ ($M_\odot$)	M_{cloud}(1 mm) ($M_\odot$)	$\frac{M_{cloud}(1\,mm)}{M_{cloud}(^{13}CO)}$	$\frac{\Sigma M_{clump}}{M_{cloud}(^{13}CO)}$
G44.587 & G44.661	G44.521	1200	310 †	0.26	0.05
G44.587 & G44.661	G44.587, G44.617, G44.661	9200	2600	0.28	0.14
G48.580 & G48.616	G48.580, G48.616, G48.540, G48.605	42000	15000	0.36	0.22
G48.598 & G48.656	G48.598, G48.656, G48.634, G48.610	53000	5700	0.11	0.05
G48.751	G48.751, G48.771	2700	650	0.24	0.04
G49.912	G49.830	13000	2500	0.19	0.07
G49.912	G49.912	3200	1400	0.44	0.13
G50.271 & G50.283	G50.271	2100	940	0.45	0.07
G50.271 & G50.283	G50.283	2400	2400	1.00	0.43
IRAS 18424-0329	Clumps 2, 4 and 6	29000	2200	0.08	0.05
IRAS 18571+0349	Clumps 1, 3 and 4	12000	2500	0.21	0.17

†The photometry apertures were different for this source to avoid unrelated emission in the 1 mm image.

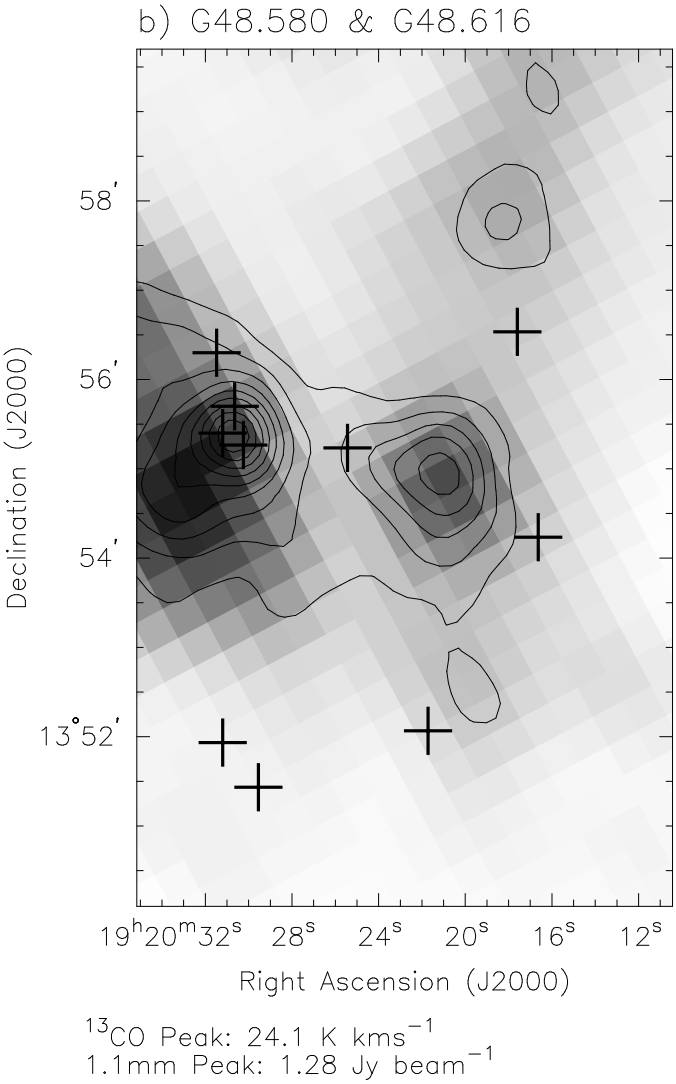

Figure 2.15: continued

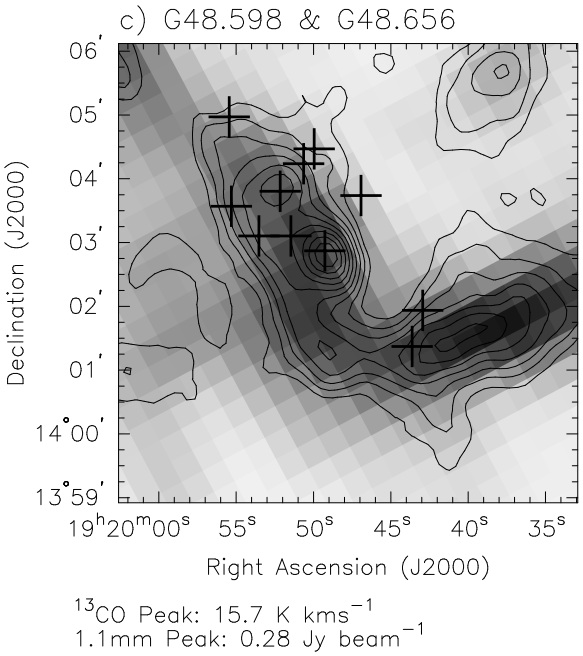

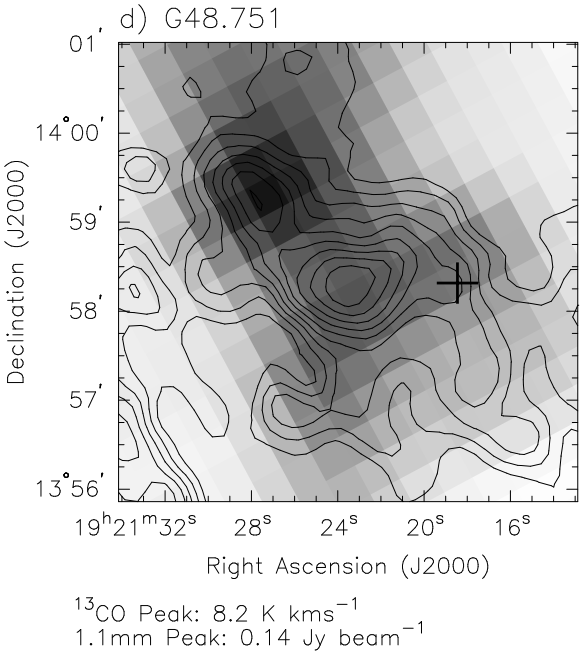

Figure 2.15: continued

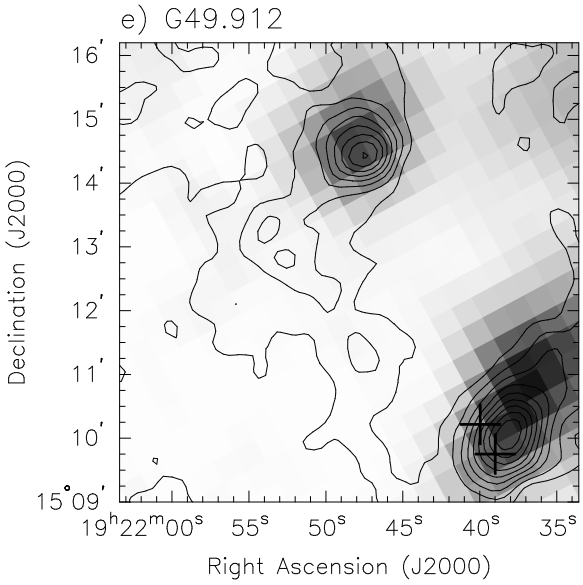

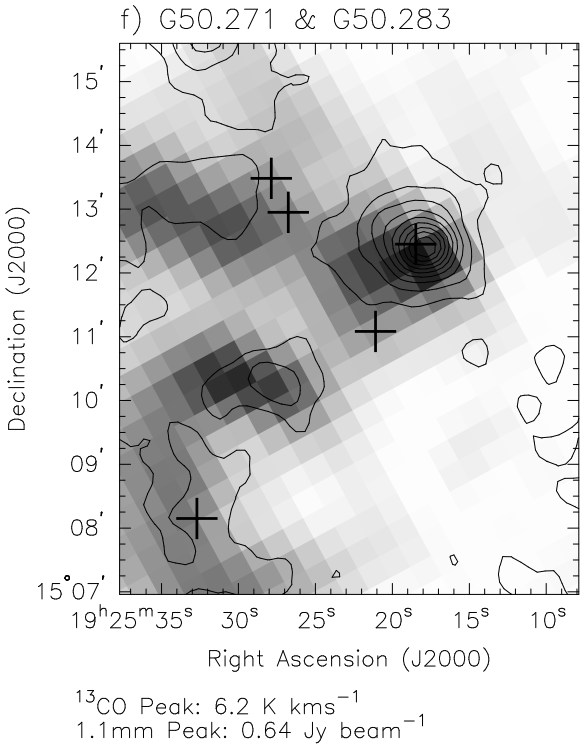

Figure 2.15: continued

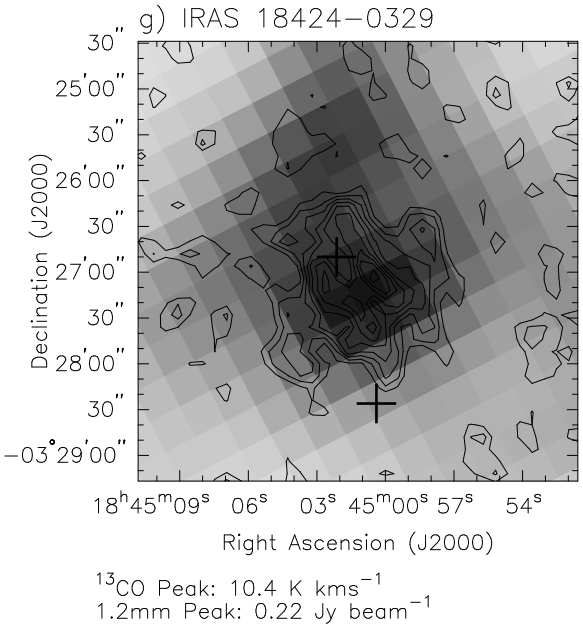

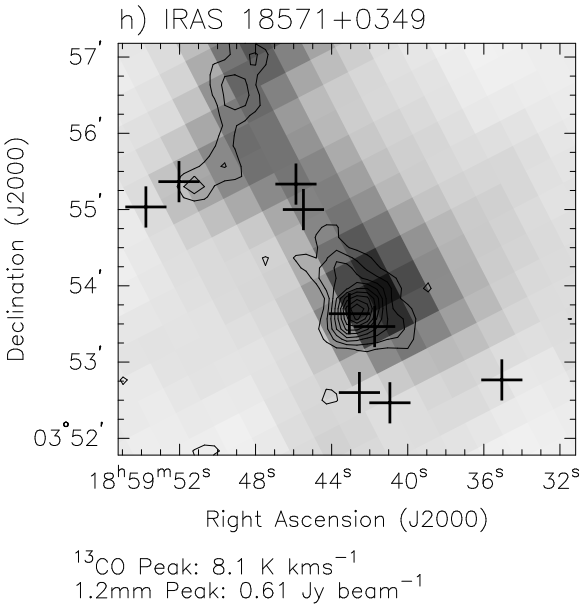

Figure 2.15: continued

cloud masses given are highly uncertain, due to the arbitrary apertures used, and therefore the ratio $\Sigma M_{clump}(1\,mm)/M_{cloud}(^{13}CO)$ is correspondingly uncertain. However, as the cloud masses have been calculated from the fluxes measured in the same photometry apertures, their ratio, $M_{cloud}(1\,mm)/M_{cloud}(^{13}CO)$, does not suffer from this uncertainty.

The ratio $M_{cloud}(1\,mm)/M_{cloud}(^{13}CO)$ ranges from 0.08 to 1.0 with a mean and median value of 0.33±0.25 and 0.26, respectively. This ratio gives an estimate of the fraction of the cloud mass taken up by warm, more compact, dust structures traced by 1 mm emission, compared to the cooler, lower density material traced by ^{13}CO.

The ratio $\Sigma M_{clump}(1\,mm)/M_{cloud}(^{13}CO)$ gives an estimate of the amount of mass the most compact structures, traced by the detected clumps in the 1 mm images, contribute to the mass of the cloud. The values for this ratio range from 0.04 to 0.43 with a mean and median of value 0.13±0.12 and 0.07, respectively.

2.4.4 Comparison of the Mass of Embedded Stars to Clump Masses

Table 2.8 compares the mass of each millimetre clump, M_{clump}, with the combined mass of its embedded ionizing stars, $M_\star$, derived from the luminosities given in Table 2.5. Only sources where the millimetre and centimetre emission are directly coincident (i.e. overlapping), suggesting that the massive star producing the ionized gas is associated with the millimetre clump, are included in Table 2.8. These sources are therefore a subset of those shown in Table 2.6, which provides the projected distance to the nearest cm emission for all of the observed mm sources. The stellar masses were calculated using the relation $L_{cm} \propto M_\star^{3.6}$. The final column of Table 2.8 gives the ratio $M_\star/(M_{clump}+M_\star)$. This quantity represents the instantaneous massive star formation efficiency (MSFE) in the dense gas traced by warm dust emission. The MSFEs in these millimetre clumps range from a few percent to 25%, while the mean MSFE is 7 ± 8%.

Figure 2.16 shows the relationship between M_{clump} and $M_\star$. A polynomial function was fit to the results of Panagia (1973), to find a function describing the relationship between $\log_{10} N_{Ly}$ and $\log_{10} L_{cm}$. Assuming $L_{cm} \propto M_\star^{3.6}$, the relationship between $\log_{10} N_{Ly}$ and $\log_{10} M_\star$ was derived, from which values and the uncertainties of $\log_{10} M_\star$ could be calculated. Due to the different calculation method, the values of $M_\star$ plotted in Figure 2.16 differ slightly from those given in Table 2.8.

Table 2.8. Comparison of Clump and Stellar Masses

Millimetre Clump Name	Associated 3.6 cm Source	M_{clump} $M_\odot$	$M_\star$ $M_\odot$	$M_\star/(M_{clump}+M_\star)$
G044.521+00.387	G44.587 & G44.661 VLA 1	56	17	0.23
G048.605+00.024	G48.580 & G48.616 VLA 5B, C, D †	5725	67	0.01
G048.634+00.230	G48.598 & G48.656 VLA 4	543	17	0.03
G048.656+00.228	G48.598 & G48.656 VLA 5D	564	17	0.03
G049.830+00.370	G49.912 VLA 1A and B †	972	44	0.04
G050.283-00.390	G50.271 & G50.283 VLA 1	1024	24	0.02
IRAS 18256-0742 Clump 1	IRAS 18256-0742 VLA 2	52	11	0.17
IRAS 18571+0349 Clump 1	IRAS 18571+0349 VLA 5	1509	17	0.01
IRAS 18571+0349 Clump 4	IRAS 18571+0349 VLA 7	217	19	0.08

†The stellar masses derived for VLA 5B, C, and D were summed to find the stellar mass associated with G48.605. Similarly, the stellar masses derived for VLA 1A and VLA 1B were also combined for the millimetre source G48.830.

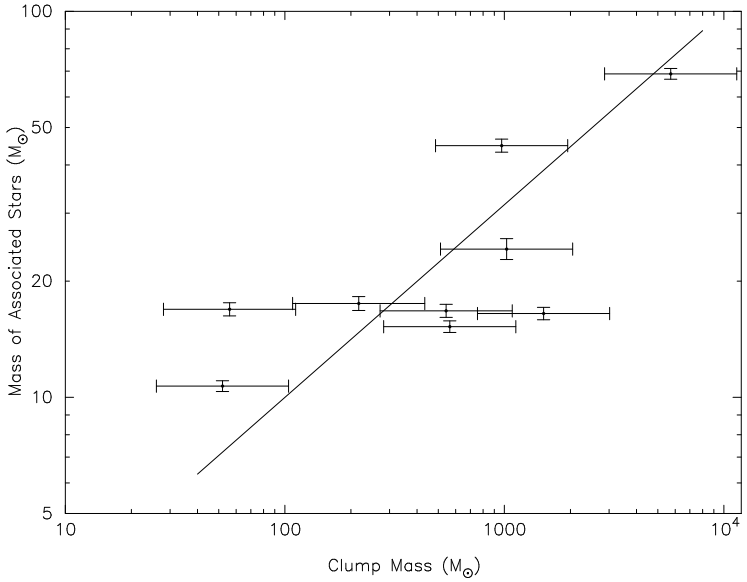

Figure 2.16: Mass of the associated ionizing stars, derived from the HII region properties given in Table 2.5, plotted against the clump mass. A line of best fit is plotted upon the data.

Error bars are shown in Figure 2.16. The error in the clump mass M_{clump} is approximately a factor of two (see Section 2.1.1). The main source of error in the combined stellar mass $M_\star$ originates from the uncertainties in the distance to the HII region and the electron temperature T_e, which are the largest errors involved in the calculation of N_{phot}. However, it is possible that the assumptions, such as that each HII region is powered by a single star, are incorrect, which may explain the large scatter in the data around the trend line.

Figure 2.16 shows a possible power-law relationship between M_{clump} and $M_\star$. These data can be fitted by the following power law: $M_\star = 1.0 \pm 0.9 \times M_{clump}{}^{0.5\pm0.1}$, which is drawn upon the data in Figure 2.16. The correlation coefficient between $\log_{10} M_{clump}$ and $\log_{10} M_\star$ was found to be 0.74, with a corresponding significance p=0.02, which gives the probability that there is in fact no underlying correlation. This relationship is consistent with the idea that the mass of the clump determines the mass of the massive stars forming within it. A similar relationship was found by Ho et al. (1981), using a comparable number of observed HII regions. Larson (1982) also discovered a similar result when comparing the mass of the most massive star in nearby young clusters to their associated cloud masses, finding $M_\star(\max) \propto 0.33\, M_{cloud}{}^{0.43}$. In addition, Larson (2003) found a relationship between the most massive star and the total stellar mass of these clusters, given by $M_\star(\max) \propto 1.2\, M_{cluster}{}^{0.45}$, which has also been studied more recently by Weidner et al. (2010).

These two relationships of the most massive star with cluster or clump mass would be expected to have the same slope if the mass of a clump is directly related to the total mass of stars that form from it by an efficiency which is constant with clump mass. In addition, it is interesting to note that this relationship also relates to the slope of the stellar initial mass function (IMF):

$$dN = N_0 m^{-x} d\log m \qquad \text{OR} \qquad dN = N_0 m^{-(x+1)} dm, \tag{2.9}$$

where N_0 is a normalisation factor containing information about how many stars are in the cluster, or equivalently, the cluster mass. To find a relationship between N_0 and $M_{\max}$, the mass function is integrated between $M_{\max}$ and infinity, and N is set to 1, producing

$$M_{\max} \propto N_0^{1/x}. \tag{2.10}$$

Hence the relationship between $M_\star(\max)$ versus M_{clump} determined from centimetre and

millimetre continuum observations is a powerful tool to constrain the upper mass function of a forming cluster, that does not require resolution of individual stars or depend on the poor counting statistics at the upper end of the IMF. In addition, the low extinctions at radio wavelengths allow for observations of forming clusters across the galaxy.

For a Salpeter slope, it has been pointed out by Larson (2003) that the expected relationship between $M_{\rm max}$ and N_0 should be a power-law with slope 1/1.35=0.74. However, the findings above suggest a steeper mass function slope of ∼1/0.45=2.2. Recent analysis of star formation in turbulent molecular clouds that form via competitive accretion find that the mass function of the forming objects should have a steeper slope at the high-mass end at earlier times in the simulations (Maschberger et al., 2010). This is expected, as the mass of the cores which initially fragment are of order of the Jeans mass, so therefore require time to accrete up to their final masses. Hence an observable of competitive accretion is that the upper *protostellar* mass function should be initially steeper than a Salpeter slope, tending towards a slope of $x = 1.35$ with time, or equivalently, that the upper mass limit of the cluster increases with time. The fact that massive stars are still accreting after they reach the main sequence, means that embedded massive stars will not have reached their final mass while their HII regions are observable, and hence they provide a way of measuring the upper end of the 'proto'-IMF.

It is also important to explore the predictions of other star formation theories on the protostellar mass function (e.g. McKee & Offner, 2010), so that these can also be compared to observations, however this is beyond the scope of this work. It would also be useful for future studies to confirm whether the same result is found for a larger number of clumps with embedded massive stars traced by ionized gas emission. Recent large (sub)millimetre datasets such as the BGPS and ATLASGAL, as well as centimetre continuum surveys such as the 6 cm follow up of the Red MSX Source (RMS) Catalog (Urquhart et al., 2009) may fulfil these requirements.

2.4.5 Follow-up of the Observed Fields with the EVLA and ALMA

By comparing 3.6 cm, ∼1 mm, ^{13}CO, and mid-IR observations, insight into several regions of massive star formation has been obtained. However future studies with the EVLA and ALMA will be able to further enhance our understanding of these regions. The EVLA will have 5-20 times the continuum sensitivity of the current VLA, allowing the detection of

fainter centimetre continuum emission from ionized gas. In addition, just over a third of the detected 3.6 cm sources are unresolved: 17 of the 47 detected sources (including subcomponents). Therefore follow-up EVLA continuum observations in A, B, and C array of these fields will allow us to further resolve the ionized gas towards these star formation regions.

ALMA is set to revolutionise our understanding of star formation. This is primarily because it will provide spatial resolutions on the order of 0.01" at 1 mm, which is a vast improvement in resolution over the ∼1 mm observations presented here (33" and 24"). Even at distances of 10 kpc this will still provide a physical resolution of 100 AU, which will be sufficient to map any outflows and disks around the youngest massive stars. Examples of some of the transitions which will be observable at these wavelengths are ^{13}CO(J=2-1), ^{13}CO(J=3-2), HCN(J=3-2), CS(J=7-6), and CH_3CN(J=12-11), all suitable for tracing outflows or disks around forming stars.

One example of where EVLA and ALMA observations would improve our understanding of the observed 3.6 cm and 1.1 mm sources is the millimetre clump G48.605, which is coincident with the 3.6 cm HII region VLA 5D. High sensitivity A array 3.6 cm observations of this region may further resolve the two centimetre continuum sources G48.606+0.023 and G48.606+0.024 towards VLA 5D detected by Kurtz et al. (1994), and also be able to pick up fainter compact emission towards them. In addition, ALMA observations would be able to determine whether there is an outflow towards VLA 5D which could produce shocked H_2 emission at 4.5μm, and also be able to study the molecular lines in this region to detect any disk or torus-like structures.

2.5 Chapter Summary

Using 3.6 cm continuum observations with the VLA, the ionized gas towards 31 intermediate and massive molecular clumps previously observed at millimetre wavelengths has been surveyed. These millimetre clumps were selected from preliminary 1.1 mm Bolocam Galactic Plane Survey images, and the 1.2 mm observations of Beltrán et al. (2006).

In the 10 observed fields, 35 HII regions were identified, 20 of them being newly discovered. The observed HII regions display a wide range of morphologies, and many are multiply peaked, indicating the presence of a cluster of massive stars.

Images comparing the warm dust and ionized gas emission in the 10 observed fields are presented, as well as GLIMPSE survey images of *Spitzer* IRAC emission in these fields. The properties of the millimetre continuum clumps and the HII regions were calculated, and are listed in Tables 2.1 and 2.5. There is a large range in the properties of the observed HII regions; their physical sizes extend from <0.05 pc to 7.88 pc, and their spectral types cover B2 to O5. The wealth of information which has been provided for the observed millimetre clumps allows them to be followed up in future with more powerful instruments such as the EVLA and ALMA.

By comparing the positions of the millimetre clumps and ionized gas, it has been shown that the ionized gas tends to be associated with the millimetre clumps, however this association does not depend on the mass of the clump. Of the 31 millimetre clumps observed, 9 appear to be physically related to ionized gas, and a further 6 have ionized gas emission within 1'.

Several "types" of millimetre clump have been inferred from the observations: those with multiply peaked 3.6 cm continuum emission, indicating they are clusters, are most likely to pinpoint the most evolved sites of star formation. These are followed by millimetre clumps associated with singly peaked HII regions, which are likely to be a single star or compact cluster, and finally millimetre clumps with no associated ionized gas emission may provide examples of the youngest sources.

By comparing the 1 mm Bolocam or SEST images with ^{13}CO images from the Galactic Ring Survey (GRS), it has been shown that the emission from these two tracers is correlated, confirming that distance determinations using ^{13}CO data can be made for the observed 1 mm clumps.

The masses of massive stars or star clusters have been compared to the actual amount of gas available traced by millimetre emission to provide an estimate of the instantaneous massive star formation efficiency for a clump, giving values ranging from a few percent to 25%, with an average of 7 ± 8%.

The mass of a clump was found to be correlated with the mass of the massive stars which form within it, and this relationship is consistent with a power law, suggesting that the final mass of a massive star is determined by the mass of the clump in which it forms. The link between this relationship and the IMF may in future be used to determine the slope

of the upper protostellar mass function, and may be able to provide a diagnostic for different theories of massive star formation.

Chapter Acknowledgements: I would like to thank M. T. Beltrán for providing digital versions of four maps from B06; T. Robitaille for providing the background matched *Spitzer* GLIMPSE images used in panel c) of Figures 2.1 to 2.10, and for many helpful discussions; J. Roman-Duval for providing results from Roman-Duval et al. (2009) before publication and giving invaluable advice concerning distance determinations; S. Kurtz for advice on the calculation of HII region properties; and D. Johnstone for helpful comments. I am also very grateful for the help and support provided by the Bolocam Galactic Plane Survey Team.

This work makes use of molecular line data from the Boston University-FCRAO Galactic Ring Survey (GRS). The GRS is a joint project of the Boston University and the Five College Radio Astronomy Observatory, funded by the National Science Foundation under grants AST-9800334, AST-0098562, AST-0100793, AST-0228993, and AST-0507657. This research has made use of data products from the Midcourse Space Experiment. Processing of the MSX data was funded by the Ballistic Missile Defense Organization with additional support from NASA Office of Space Science. This work relies on observations made using the Spitzer Space Telescope, and uses the NASA/ IPAC Infrared Science Archive, which are operated by the Jet Propulsion Laboratory, California Institute of Technology, under contract with the National Aeronautics and Space Administration. The VGPS is supported by a grant from the Natural Sciences and Engineering Research Council of Canada and from the U.S. National Science Foundation.

3

Multi-Wavelength Modelling of IRAS 20126+4104

Adapted from *Johnston et al., submitted to MNRAS*

As mentioned in Chapter 1, the fact that massive stars have Kelvin-Helmholtz timescales which can be shorter than their accretion timescales (e.g. Kahn, 1974), leads to the consequence that their main-sequence radiation can affect their own formation. For instance, several processes such as radiation pressure and ionization (see Section 1.2.1) may halt, decrease or alter accretion on to the star.

With the hypothesis that these differences do not radically change the formation of massive stars, the main aim of this Chapter is to find observational evidence to suggest the contrary. The goal of the work laid out in this Chapter is to determine whether the standard envelope plus disk model used to reproduce the SEDs of low-mass stars (e.g. Adams et al., 1987; Kenyon et al., 1993; Wood et al., 2002b; Whitney et al., 2003) is able to reproduce the SED and observed infrared images of the nearby forming early B-type star IRAS 20126+4104.

Keto & Zhang (2010, henceforth KZ10) have recently modelled the line profiles of several millimetre-wavelength transitions of NH_3, $C^{34}S$ and CH_3CN towards IRAS 20126+4104, fitting these data with two models, the first consisting of an azimuthally symmetric rotationally

flattened envelope, and the second also including a flared Keplerian disk. They found that the addition of a disk was required to reproduce the velocity structure of the accreting gas within 0.128 pc of the star, providing a better fit than the without-disk model. Additionally, as the model with a disk was able to adequately reproduce the data, their results showed no evidence that ionization or radiation pressure are profoundly altering the dynamics of the surrounding accretion flow. In this Chapter, the same experiment is carried out by instead modelling the SED and observed infrared images of IRAS 20126+4104.

In comparison to the molecular line data, the SED and infrared images of IRAS 20126+4104 probe different aspects of the circumstellar material. The molecular line observations are able to measure the velocity of the gas at different temperatures, however their density determinations depend on abundances that are highly uncertain. In contrast, the SED and infrared images probe the dust out to the edge of the envelope, which can be used to infer the structure of the gas. Hence, comparing the results from both these datasets will allow a more complete picture of the star formation processes occurring in IRAS 20126+4104 to be obtained.

IRAS 20126+4104 is a well studied example of a nearby forming massive star ($L_{\rm bol} = 1.3\times10^4\,{\rm L}_\odot$, B0.5, Cesaroni et al., 1999b). Found within the Cygnus-X star-forming region, it is assumed to be at the same distance as the Cygnus OB associations (1.7 kpc, Wilking et al., 1990; Massey & Thompson, 1991). Several observations of molecular tracers at millimetre wavelengths have uncovered a $\sim$0.25 pc NW-SE inner jet feeding a large-scale North-South bipolar outflow (Cesaroni et al., 1997, 1999b; Shepherd et al., 2000; Lebrón et al., 2006; Su et al., 2007). In addition, high resolution centimetre continuum images of the ionized gas towards IRAS 20126+4104 have been presented by Hofner et al. (2007).

Observations of transitions of $C^{34}S$, CH_3CN, CH_3OH and HCO^+ (Cesaroni et al., 1997, 1999b, 2005), and NH_3 (Zhang et al., 1998, KZ10) have uncovered a rotating flattened disk-like structure, perpendicular to the inner flow, with a radius between 800 and 12,000 AU, and a gas mass estimated from both dust continuum and molecular line observations of 0.65-10 $M_\odot$. Further evidence for a disk is also provided by near and mid-infrared images of IRAS 20126+4104 (Sridharan et al., 2005; De Buizer, 2007), which show a dark lane with a similar size and orientation to the disk seen in radio observations. A large (radius$\sim$1000 AU) rotating structure traced by OH masers was also found by Edris et al. (2005), which is

coincident with the dark lane observed in the infrared. Recently however, de Wit et al. (2009) have presented a high-resolution (0.6") 24.5μm image of IRAS 20126+4104, at a slightly longer wavelength than those presented in De Buizer (2007, 12.5 and 18.3μm), which does not contain a dark lane.

The infrared to sub-millimetre SED of IRAS 20126+4104 has been previously modelled on several occasions. Both Cesaroni et al. (1999b) and Shepherd et al. (2000) modelled the far-IR to millimetre SED using a simple greybody to determine the dust temperature and the dust emissivity index. van der Tak et al. (2000), Williams et al. (2005) and de Wit et al. (2009) also modelled the SED of IRAS 20126+4104 using spherically symmetric models, to determine the properties of the envelope. More recently, Hofner et al. (2007) modelled IRAS 20126+4104 using the radiation transfer code previously employed in Olmi et al. (2003). Their model consisted of a spherical halo with a power-law density between radii of 850 AU and 0.54 pc, plus a constant density cylindrical edge-on disk with radii between 34-850 AU and a height of 640 AU. The model provided a good fit to the data down to $\sim$8μm, however they suggested that adding further components to the model, such as bipolar cavities and a more complex disk geometry, would improve the fit, especially in the near- to mid-IR section of the SED. The work in this Chapter improves significantly upon previous infrared modelling, and derives complementary information about the properties of IRAS 20126+4104 not previously obtainable from molecular line observations.

The observed SED, infrared images and measured brightness profiles of IRAS 20126+4104 are presented in Section 3.1; Section 3.2 describes the radiation transfer dust code used to model them; Section 3.3 details the modelling, including model input assumptions and the genetic search algorithm used to search for the best-fitting set of model parameters; and Section 3.4 presents the results, including a comparison to the results of KZ10. The Chapter conclusions are given in Section 3.5.

3.1 The Data

3.1.1 Near-IR to Sub-millimetre SED

The observed near-IR to sub-millimetre SED of IRAS 20126+4104 is shown in Figure 3.1. The overplotted solid and dashed lines (respectively the best-fitting models for an envelope plus disk and without a disk) are discussed further in Section 3.4. The SED data points were

Table 3.1: Observed near-IR to sub-millimetre fluxes for IRAS 20126+4104, collected from the literature. Apparent magnitudes are given where the flux was derived from these magnitudes. References are given in parentheses: (1) Jarrett et al. (2000), (2) this work, (3) Qiu et al. (2008), (4) Price et al. (2001) , (5) Cesaroni et al. (1999b), (6) De Buizer (2007), (7) de Wit et al. (2009), (8) Joint Iras Science (1994)

Wavelength (μm)	Flux (mJy)	Apparent magnitude	Description / Origin
1.235	4.7 ± 49%	13.939 ± 0.527	2MASS Extended Source Catalog, J band (1)
1.662	30.1 ± 8.8%	11.333 ± 0.095	2MASS Extended Source Catalog, H band (1)
2.159	134 ± 2.3%	9.242 ± 0.025	2MASS Extended Source Catalog, K band (1)
3.6	790		IRAC band 1, photometry: (2), image: (3)
4.5	2.1×10^3		IRAC band 2, photometry: (2), image: (3)
5.8	1.9×10^3		IRAC band 3, photometry: (2), image: (3)
8.0	1.4×10^3		IRAC band 4, photometry: (2), image: (3)
8.28	965 ± 4.2%		MSX band A (4)
10.2	320		UKIRT, MAX (5)
12.13	1.10×10^3 ± 8.2%		MSX band C (4)
12.5	1.89×10^3 ± 10%		Gemini North, Michelle (6)
14.65	3.98×10^3 ± 6.2%		MSX band D (4)
18.3	2.35×10^4 ± 15%		Gemini North, Michelle (6)
19.9	3.0×10^4		UKIRT, MAX (5)
21.3	4.43×10^4 ± 6.0%		MSX band E (4)
24.5	6.0×10^4		Subaru telescope, COMICS (7)
25	1.09×10^5 ± 5%		IRAS 25μm (8)
60	1.38×10^6 ± 12%		IRAS 60μm (8)
100	1.95×10^6 ± 13%		IRAS 100μm (8)
350	$2.92\times10^5\pm 9.0\times10^4$		JCMT, SCUBA (5)
443	$1.62\times10^5\pm 2.4\times10^4$		JCMT, SCUBA (5)
750	$2.5\times10^4\pm 5\times10^3$		JCMT, SCUBA (5)
863	$1.9\times10^4\pm 3\times10^3$		JCMT, SCUBA (5)

collected from the literature; Table 3.1 lists the wavelength, flux and reference for the data displayed in Figure 3.1. If the fluxes were derived from apparent magnitudes, these are also given in Table 3.1. In all cases, an effort was made to check the fluxes used contained all of the flux from the source. For instance, the 2 Micron All Sky Survey (2MASS) extended source catalog fluxes were used for the near-IR points.

3.1.2 Infrared Images

A three-colour Infrared Array Camera (IRAC) image of the mid-IR emission observed towards IRAS 20126+4104, previously published by Qiu et al. (2008), is shown in the middle panel of Figure 3.2, where red: 8.0μm, green: 4.5μm and blue: 3.6μm. In this figure, two lobes of emission oriented similarly to the NW-SE jet observed by Su et al. (2007) can be seen, which are most obvious at 3.6 and 4.5μm, while the 8.0μm IRAC emission mostly traces the central source.

To obtain IRAC fluxes for IRAS 20126+4104, irregular aperture photometry was carried out on the images previously published in Qiu et al. (2008), using the post-Basic Calibrated Data (post-BCD) mosaics produced by the *Spitzer* Science Center (SSC) pipeline version S18.7. The photometry was carried out on the short exposure (0.4 s) images, as there were

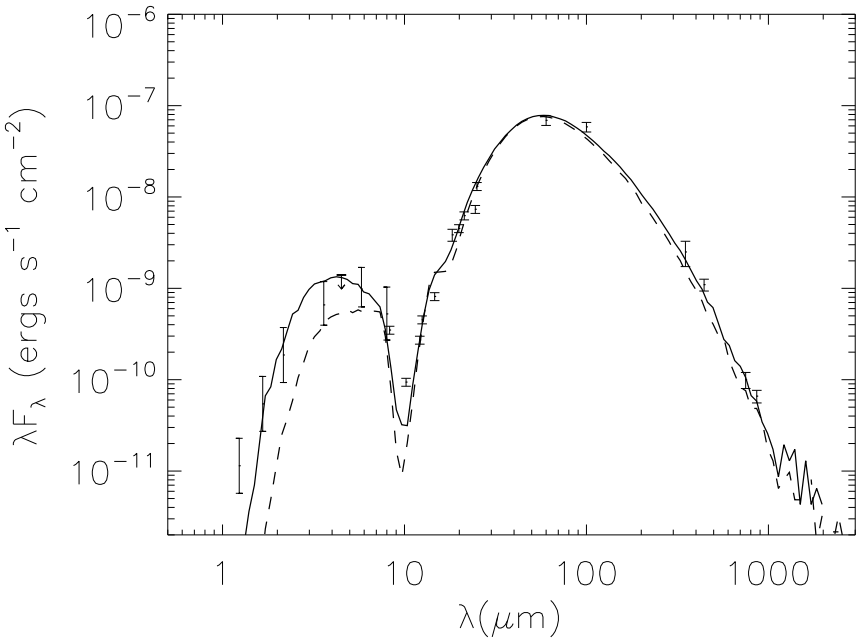

Figure 3.1: The Spectral energy distribution (SED) of IRAS 20126+4104. The best-fitting models for an envelope plus disk and without disk (overplotted solid and dashed lines respectively) are discussed in Section 3.4. The errors shown are those reset to 10% if the error in the measured flux was <10%, and the errors in the 2MASS JHK fluxes to a factor of two. The IRAC 4.5μm flux was assumed to be an upper limit due to possible contamination by H_2 line emission.

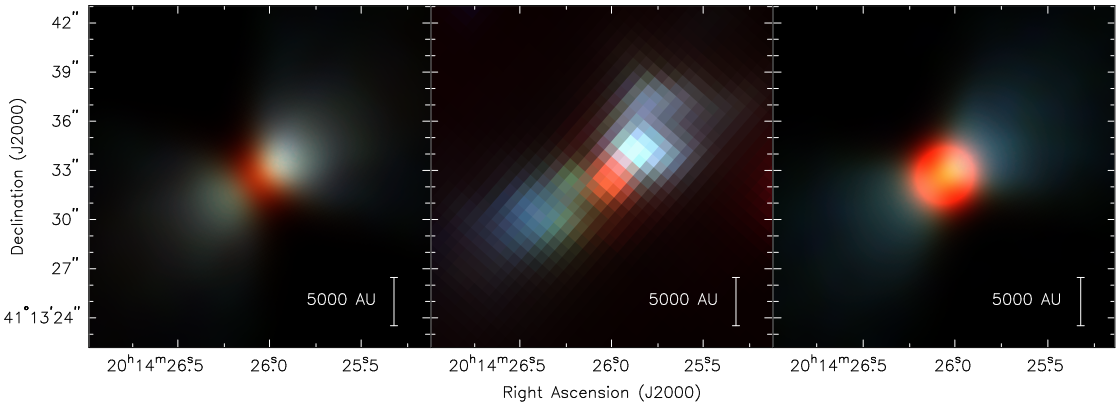

Figure 3.2: *Left panel:* Model IRAC image for envelope plus disk model. *Middle panel:* Observed IRAC three-colour RGB image of IRAS 20126+4104, previously presented by Qiu et al. (2008). *Right panel:* Model IRAC image for envelope without disk model. The model images have been normalised to the total integrated fluxes given in Table 3.1, in order that the morphology of the emission can be easily compared. Stretch: red: 8 μm, 0-1200 MJy sr^{-1}; green: 4.5 μm, 0-1800 MJy sr^{-1}, blue: 3.6 μm, 0-670 MJy sr^{-1}

several artifacts in the longer exposure (10.4 s) mosaics. The apertures were drawn to best avoid any foreground stars in the images.

Measurement uncertainties were <5% at 3.6 and 4.5 μm, ∼10% at 5.8 μm, and ∼30% at 8 μm, due to the increasing variance of the background in the longer wavelength bands. In addition, this should be combined with a calibration uncertainty of 10% for pipeline post-BCD mosaics[1]. Furthermore, due to scattering of flux throughout the image by the IRAC optics, fluxes of extended sources are highly uncertain. Therefore, at a conservative estimate, these fluxes were taken to be accurate to within a factor of two. However, this is adequate for the purpose of fitting a model to the observed SED.

The middle panels of Figure 3.3 also show the observed K-band, 12.5, 18.3, and 24.5 μm images presented in Sridharan et al. (2005), De Buizer (2007) and de Wit et al. (2009), along with corresponding model images (left and right panels) which will be discussed in Section 3.4.

3.1.3 Brightness Profiles

Flux profiles of IRAS 20126+4104, summed across a 15.1" thick strip aligned with the source outflow axis (P.A.=303.5 degrees), were measured for the four IRAC bands and at the two wavelengths observed by De Buizer (2007): 12.5 and 18.3 μm. The normalised profiles are shown in Figure 3.4 along with the best-fitting models to both the SED and profiles, for envelope plus disk and without disk models (blue and red solid lines respectively), which will be discussed further in Section 3.4. The errors in the profiles shown in each panel of Figure 3.4 reflect the uncertainty in the background underlying the source emission due to background fluctuations, and are calculated as the standard deviation of the profiles measured in two strips either side of the main profile, which were assumed to contain minimal source flux.

3.2 The Radiation Transfer Dust Code

The SED of IRAS 20126+4104 was modelled between near-IR and sub-mm wavelengths using the 2D Monte Carlo dust radiation transfer code previously employed in Wood et al. (2002a) and modified in Akeson et al. (2005). For a given source and surrounding dust geometry sampled in a spherical-polar grid, the code models the anisotropic scattering and

[1]Section 4.3 of the IRAC Instrument Handbook, version 1.0

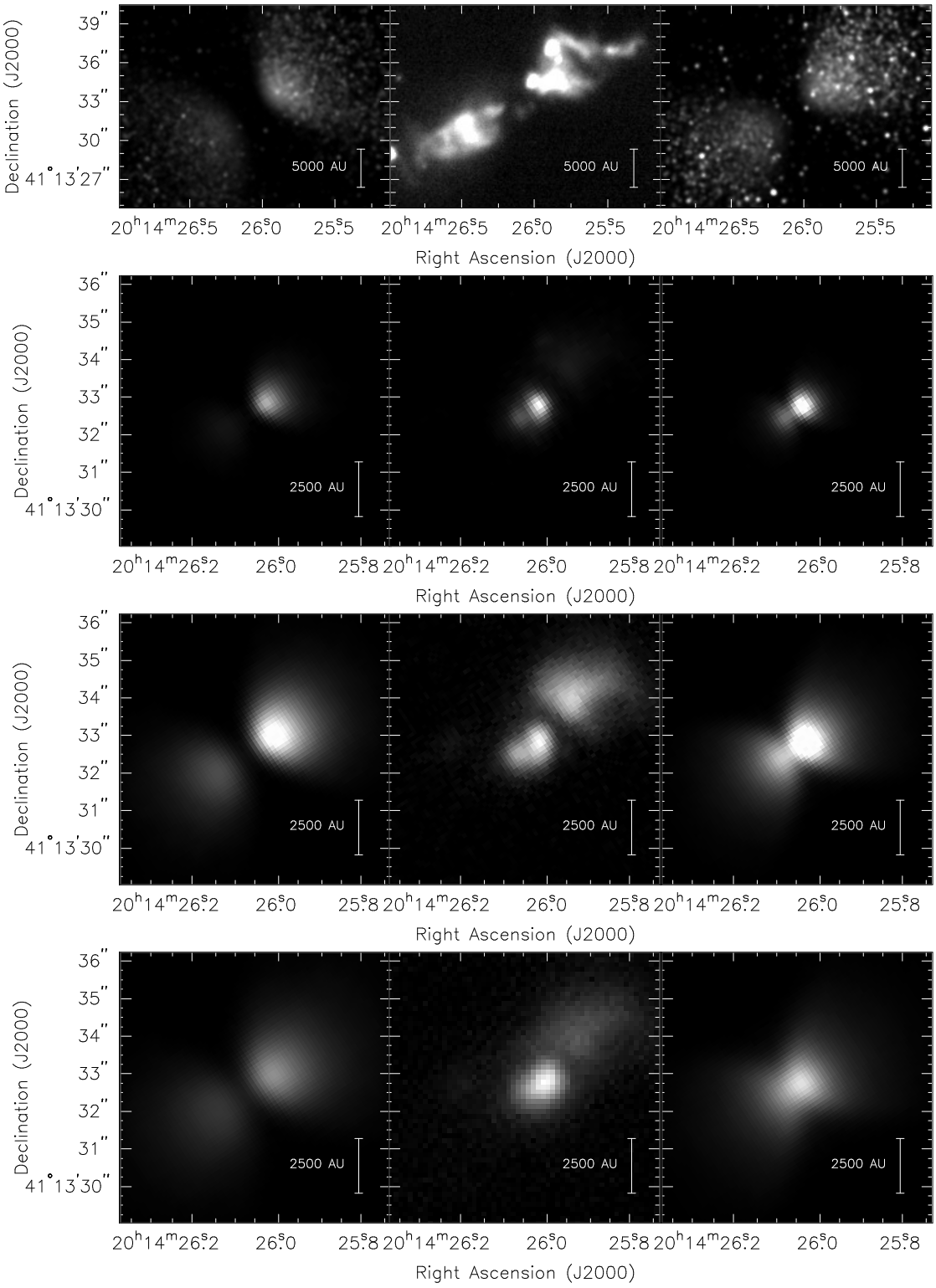

Figure 3.3: Observed (middle panels) and corresponding envelope plus disk and without disk model images (left and right panels respectively) for several near- and mid-IR observations of IRAS 20126+4104. From top to bottom: K band (Sridharan et al., 2005), 12.5 and 18.3μm (De Buizer, 2007), and 24.5μm (de Wit et al., 2009). The model images have been normalised to the total integrated fluxes given in Table 3.1, so that the morphology of the emission can be easily compared. Image stretches (top to bottom): 0-80.7 MJy sr^{-1}, 0-8.98 $\times 10^4$ MJy sr^{-1}, 0-2.67$\times 10^5$ MJy sr^{-1}, 0-2.03$\times 10^6$ M Jy sr^{-1}

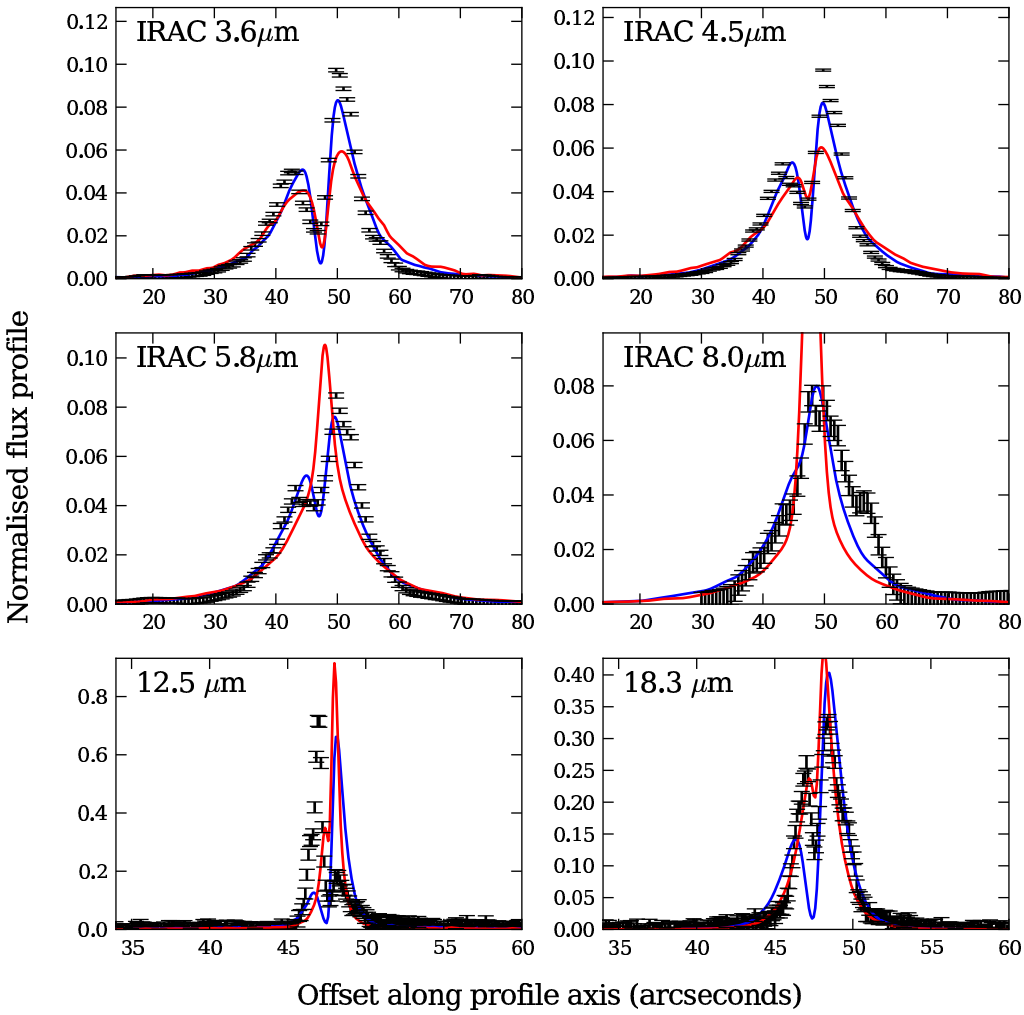

Figure 3.4: Black error bars: normalised flux profiles for the four IRAC bands and the two wavelengths observed by De Buizer (2007): 12.5 and 18.3 μm. Blue and red lines: the profiles of the best-fitting models to both the observed SED and profiles, for envelope plus disk and without disk models respectively.

thermal emission by/from dust, calculating radiative equilibrium dust temperatures (using the technique of Bjorkman & Wood, 2001), and producing SEDs and multi-wavelength images. Dust and gas are assumed to be coupled in the code, so that the bulk of the material which surrounds IRAS 20126+4104 is assumed to be probed. In this section, the density structure of the disk, envelope and outflow cavity in the model is described, followed by a description of the heating of the star via accretion on to its surface, and the dissipation of energy via disk accretion.

The circumstellar geometry of IRAS 20126+4104 was modelled with the same envelope plus disk geometry successfully employed to model the SEDs and scattered light images of low-mass protostars (e.g. Wood et al., 2002b; Whitney et al., 2003; Robitaille et al., 2007), as well as the molecular line emission from IRAS 20126+4104 (KZ10). The two dimensional flared disk density is described between inner and outer radii $R_{\rm min}$ and $R_{\rm disk}$ by

$$\rho_{\rm disk}(\varpi,z) = \rho_0 \left[1-\sqrt{\frac{R_\star}{\varpi}}\right] \left(\frac{R_\star}{\varpi}\right)^{\alpha} \exp\left(-\frac{1}{2}\left[\frac{z}{h(\varpi)}\right]^2\right), \tag{3.1}$$

where $R_\star$ is the stellar radius, ϖ is the cylindrical radius, z is the height above the disk midplane and ρ_0 is set by the total disk mass $M_{\rm disk}$, by integrating the disk density over both z, ϖ and ϕ, the azimuthal angle. The scaleheight $h(\varpi)$ increases with radius: $h(\varpi) = h_0\left(\varpi/R_\star\right)^{\beta}$ where h_0 is the scaleheight at $R_\star$, and the disk is assumed to be in hydrostatic equilibrium at the dust sublimation radius. A value of $\beta = 1.25$ was assumed, derived for irradiated disks around low-mass stars (D'Alessio et al., 1998), and α was taken to be 2.25 to provide a surface density of $\Sigma \sim \varpi^{-1}$.

The density of the circumstellar envelope was taken to be that of a rotationally flattened collapsing spherical cloud (Ulrich, 1976; Terebey et al., 1984) with radius $R_{\rm env}^{\rm max}$,

$$\rho_{\rm env}(r,\mu) = \frac{\dot{M}_{\rm env}}{4\pi\left(GM_\star R_c^3\right)^{1/2}} \left(\frac{r}{R_c}\right)^{-3/2} \left(1+\frac{\mu}{\mu_0}\right)^{-1/2} \left(\frac{\mu}{\mu_0}+\frac{2\mu_0^2 R_c}{r}\right)^{-1} \tag{3.2}$$

where $\dot{M}_{\rm env}$ is the accretion rate through the envelope, $M_\star$ is the stellar mass, r is the spherical radius, R_c is the centrifugal radius, μ is the cosine of the polar angle ($\mu = \cos\theta$), and μ_0 is the cosine of the polar angle of a streamline of infalling particles in the envelope as

$r \rightarrow \infty$. The equation for the streamline is given by

$$\mu_0^3 + \mu_0(r/R_c - 1) - \mu(r/R_c) = 0 \tag{3.3}$$

which can be solved for μ_0. In the model, the centrifugal radius is assumed to also be the radius at which the disk forms, so that $R_c = R_{\rm disk}$.

To reproduce the near-IR (Sridharan et al., 2005) and IRAC (Qiu et al., 2008) images of IRAS 20126+4104, bipolar cavities are also included in the model geometry with density $\rho_{\rm cav}$, and a shape described by

$$z(\varpi) = \pm z_0 \varpi^{b_{\rm cav}} \tag{3.4}$$

where the shape of the cavity is determined by the parameter $b_{\rm cav}$ which is set to be $b_{\rm cav} = 1.5$, and z_0 is chosen so that the cavity half-opening angle at $z = 10,000$ AU is $\theta_{\rm cav}$.

The inner radius of the dust disk and envelope $R_{\rm min}$ was set to the dust destruction radius $R_{\rm sub}$, found empirically by Whitney et al. (2004) to be

$$R_{\rm sub} = R_\star (T_{\rm sub}/T_{\star,\rm acc})^{-2.1} \tag{3.5}$$

where the temperature at which dust sublimates is assumed to be $T_{\rm sub} = 1600$K, and $T_{\star,\rm acc}$ is the temperature of the star, including heating by accretion shocks on to the stellar surface. $T_{\star,\rm acc}$ is calculated by assuming that the material accreting through the disk is in free-fall from the inner radius of the gas disk $R_{\rm gas}$ to $R_\star$ and that half of the energy lost by free-fall goes into heating the stellar surface (Calvet & Gullbring, 1998). The other half of this energy is assumed to go into X-ray emission, which was ignored in this Chapter. As virtually all of the X-rays are reprocessed for embedded sources like IRAS 20126+4104, the determined disk accretion rates may be a factor of two too high, as without X-ray emission the disk accretion rate has to be a factor of two higher to reproduce the same accretion luminosity. In keeping with findings for disks around low-mass stars (e.g. Shu et al., 1994), $R_{\rm gas}$ was set to $5R_\star$, however it should be noted that magnetic disk truncation may not occur for massive stars.

Therefore, the accretion luminosity which goes into heating the stellar surface is

$$L_{\rm heat} = \frac{GM_\star \dot{M}_{\rm disk}}{2}\left(\frac{1}{R_\star} - \frac{1}{R_{\rm gas}}\right), \tag{3.6}$$

and the effective temperature of the star is then

$$T_{\star,\mathrm{acc}} = T_\star \left(\frac{L_\star + L_{\mathrm{heat}}}{L_\star} \right)^{1/4}, \tag{3.7}$$

where $L_\star$ is the luminosity of the star, and $T_\star$ is the temperature of the stellar surface before taking into account accretion.

In addition to luminosity from the star, the dust disk emits due to accretion. The energy dissipated through dust radiation in a volume element between R_{min} and R_{disk} is given by the α-disk prescription (e.g. Shakura & Sunyaev, 1973; Kenyon & Hartmann, 1987; Whitney et al., 2003, and Chapter 1) ,

$$\frac{dL_{\mathrm{acc}}}{dV} = \frac{3GM_\star \dot{M}_{\mathrm{disk}}}{\sqrt{32\pi^3}\varpi^3 h(\varpi)} \left(1 - \sqrt{\frac{R_\star}{\varpi}} \right) \exp\left\{ -\frac{1}{2} \left[\frac{z}{h(\varpi)} \right]^2 \right\}, \tag{3.8}$$

with the wavelength of this emission determined by the local dust temperature and opacity.

The dust opacity and scattering properties determined by Kim et al. (1994) were adopted for the circumstellar dust properties, which were found empirically from observations of ISM dust, and are produced by grain sizes between 0.002 and 1 μm.

In order to compare the model to existing observations, synthetic model images were produced by the dust code using the *peel-off* approach (originally described in Yusef-Zadeh et al., 1984), whereby each time a photon interacts, the probability that the photon reaches the observer, and therefore the emergent intensity from that point, is found.

To produce the model IRAC images, IRAC filter spectral response curves were used, obtained from the SSC website[2]. The model images were also convolved with the FWHM of the IRAC point-spread function (PSF) for each band.

To produce the images at the four wavelengths shown in Figure 3.3 (K band, 12.5, 18.3 and 24.5μm), the correct band pass filters were applied, obtained from the United Kingdom infrared telescope (UKIRT)[3], the Gemini telescope web pages[4], and de Wit (private communication), and the images were convolved to the observed resolutions (K band: 0.3", 12.5μm: 0.33", 18.3μm: 0.48" and 24.5μm: 0.6").

[2]http://ssc.spitzer.caltech.edu/irac/calibrationfiles/spectralresponse
[3]http://irtfweb.ifa.hawaii.edu/~nsfcam2/Filter%20Profiles.html
[4]http://www.gemini.edu/sciops/instruments/michelle/imaging/filters

3.3 Modelling

In this section, the model input assumptions are firstly described, including the selection of sensible physical parameter ranges for IRAS 20126+4104. Secondly, the χ^2 fitting procedure carried out to compare the models to the data is detailed, and finally an outline of the genetic search algorithm which was used to search parameter space for the most suitable model is provided.

3.3.1 Input Assumptions: Model Parameters

A set of plausible ranges for parameters describing the model, in which the genetic algorithm (described in Section 3.3.3) searched for the best fit, is given in Table 3.2. Ranges for the first six parameters - stellar mass, envelope outer radius, cavity half-opening angle, inclination, disk mass and disk radius - were chosen using results from the literature, specifically Cesaroni et al. (1997, 1999a, 2005), Zhang et al. (1998), Edris et al. (2005), De Buizer (2007) and Qiu et al. (2008). Large ranges were assumed for the disk mass and radius, as although a disk-like rotating structure has been detected at the centre of IRAS 20126+4104 (e.g. Cesaroni et al., 2005), it is possible that these observations are also tracing part of the envelope.

The following three parameters in Table 3.2 - the envelope and disk accretion rates and cavity ambient density - were also given large but physically plausible ranges.

The final two parameters, the stellar radius and temperature, were determined from the sampled stellar mass for that model. To do this, the $\dot{M} \propto M^2$ evolutionary track presented in Figure 1 of Keto & Wood (2006) was used, which results from the stellar evolution models of Chieffi & Straniero (1989). These calculations show that, before taking into account heating from accretion shocks, the protostellar temperature and luminosity for stars which reach masses greater than $4M_\odot$ are equivalent to a zero-age main sequence (ZAMS) star. This can be seen in Figure 1 of Keto & Wood (2006), where for all the evolutionary tracks (or accretion rates), stars which reach masses greater than $4M_\odot$ follow the main-sequence line until their accretion is unable to counteract the production of helium in their cores, and they begin their post-main-sequence evolution.

Once the stellar mass, radius and temperature were determined, the stellar temperature including heating from shocks $T_{\star,\mathrm{acc}}$ and the surface gravity of the star were calculated. The

nearest solar metallicity ($Z = 0.02$) stellar model atmosphere from the grid of Castelli & Kurucz (2004), or a blackbody spectrum if the temperature was larger than 50,000 K, was then used to provide the spectrum of the central source.

3.3.2 Model Fitting

As part of the genetic algorithm described in Section 3.3.3, the models were fit to the data using the fitting algorithm described in Robitaille et al. (2007), where A_v, the interstellar visual extinction, was a free parameter in the fit. The distance was set to be 1.7 kpc, in keeping with the adopted distance to IRAS 20126+4104 (Wilking et al., 1990), and the extinction A_v was allowed to vary between 0 and 40 magnitudes.

Before fitting these models to the data, the observed flux errors were reset to 10% if they were below this value, and the 2MASS flux errors to a factor of two, so that these data points could not over-dominate the fit. In addition, as shocked H_2 emission may be contributing to the measured flux in the 4.5 μm IRAC band, this flux was set to be an upper limit. Each data point was also weighted by the distance in wavelength between its two adjacent data points. This was done to allow the algorithm to search for a model which reproduced the shape of the entire SED, not only the sections with a high density of data.

The models were also simultaneously fit to the six flux profiles shown in Figure 3.4, measured from the four IRAC images and the 12.5 and 18.3 μm images in De Buizer et al. (2005). The model flux profiles were found in the same way as the observed profiles, by summing the flux in the model images within a 15.1" wide strip aligned with and centred on the outflow axis, and normalising them to the total flux. When fit, the model profiles were allowed to be shifted by ±2" (with the same shift for all profiles) around the centre of the observed profile to produce the best fit. This was necessary since the position of the central source could not be accurately determined from the images.

The combined χ^2 for each model given as input to the genetic algorithm was calculated as

$$\chi^2_{\text{combined}} = \chi^2_{\text{SED}} + \chi^2_{\text{profiles}} \tag{3.9}$$

where χ^2_{SED} is the best-fitting reduced χ^2 value for the SED alone, and χ^2_{profiles} is the overall reduced χ^2 for the profile fits.

3.3.3 The Genetic Algorithm

In the context of SED modelling, genetic search algorithms (Holland, 1975; Goldberg, 1989) have previously been used by Hetem & Gregorio-Hetem (2007) to model the protoplanetary disks of T Tauri and Herbig Ae/Be stars. The algorithm used in this work (developed by T. Robitaille) is described below, which was used in conjunction with the radiation transfer dust code described in Section 3.2 to search for the best fitting model for IRAS 20126+4104.

Genetic algorithms are an alternative to traditional optimisation methods, such as Markov chain Monte Carlo or simulated annealing. They move towards the optimum solution in an evolutionary manner, by randomly generating generations of solutions or models, based on a given fitness statistic such as a χ^2 value. Along with simulated annealing, they have the advantage that they do not become stuck in local minima, as their solution probabilistically tends towards the global optimum. In addition, genetic algorithms suit this specific problem because they involve producing or running several models at the same time. As each of the models was run with one million Monte Carlo photons (actually energy packets, Bjorkman & Wood, 2001), taking approximately 30 minutes and 9 minutes per model to complete for the models with and without a disk respectively, this meant that parameter space could be explored much more efficiently than optimisation codes which run one model at a time.

To create the first generation of models, N models were generated by randomly sampling the parameters linearly or logarithmically within the ranges given in Table 3.2. The type of sampling (linear or log.) is also noted in the table. Here N was taken to be 100.

The second generation consisted of M models, where M was some fraction of N. Here M was chosen to be 20. Models in this and subsequent generations were computed by either the *mutation* of one existing model, or the *crossover* of two. *Tournament selection* was used to select which models were mutated or crossed. To create a tournament, a fraction of the models, k ($k = 10\%$ was chosen), were selected at random from the *gene pool* of N models. The winner of each tournament was determined by first sampling a random number q between 0 and 1. The probability p, between 0.5 and 1, which was chosen to be $p = 0.9$, was used to determine how likely a model is to win the tournament: if $q < p$, the model with the lowest χ^2 value was selected. If not, and $q < p(p-1)$, then the second best model was selected, and so on such that if $q < p(p-1)^{n-1}$, where n is the nth model in the list ordered by χ^2, the nth model wins the tournament. With this probabilistic selection,

Table 3.2: Assumed ranges for model parameters as input to genetic search algorithm.

Parameter	Description	Value/Range	Sampling
$M_\star$	Stellar mass ($M_\odot$)	5 – 25	logarithmic
$R_{\rm env}^{\rm max}$	Envelope outer radius (AU)	15,000 – 120,000	logarithmic
$\theta_{\rm cav}$	Cavity half-opening angle at 10^4 AU (degrees)	5 – 40	linear
i	Inclination w. r. t. the line of sight (degrees)	75 – 90	linear
$M_{\rm disk}$	Disk mass ($M_\odot$)	0.1 – 15	logarithmic
$R_{\rm disk}$	Disk or centrifugal radius (AU)	100 – 10,000	logarithmic
$\dot{M}_{\rm disk}$	Disk accretion rate ($M_\odot$ yr^{-1})	10^{-7} – 10^{-2}	logarithmic
$\dot{M}_{\rm env}$	Envelope accretion rate ($M_\odot$ yr^{-1})	10^{-7} – 10^{-2}	logarithmic
$\rho_{\rm cav}$	Cavity ambient density (g cm^{-3})	10^{-21} – 10^{-16}	logarithmic
$R_\star$	Stellar radius	Determined from stellar mass	
$T_\star$	Stellar temperature	Determined from stellar mass	

models that increase χ^2 are occasionally promoted so that the evolution of the final model is not always towards a minimum. Therefore the algorithm allows escape from local minima. For mutations, one tournament was required; for crossovers, the pair selected for crossing resulted from two tournaments.

A mutation was carried out by selecting one of the varied parameters at random and resampling it from the original ranges given in Table 3.2. A crossover was carried out by 'crossing' the parameters of the two selected models, by randomly sampling (either linearly or logarithmically) a value between the original parameters of the two models. In all generations following the first, 75% of the models were the result of mutations, and 25% were the result of crossovers.

When the M models of the next generation were added to the gene pool, the M worst (highest χ^2) models were removed so that the gene pool always contained N models. All following generations were created using the same method as the second. The code was stopped when the best fitting model produced a less than 5% reduction in χ^2 over 20 generations.

3.4 Results

The genetic code was run twice - firstly with the model parameter ranges given in Table 3.2 as input for all parameters, which will be referred to as the 'envelope plus disk' model. Secondly, the code was run with the parameter ranges given in Table 3.2 for all parameters except the disk mass and disk accretion rate, $M_{\rm disk}$ and $\dot{M}_{\rm disk}$, which were set to zero and were therefore not treated as model parameters. This second run will be referred to as the 'envelope without disk' model. The envelope without disk model was run to ascertain

whether the SED and images could be adequately produced without a disk, i.e. a simpler model which had two fewer parameters. For the envelope without disk model, $R_{\rm disk}$ was instead referred to as the centrifugal radius of the envelope, $R_{\rm c}$, as these two parameters are interchangeable in the models.

The genetic search algorithm codes were stopped after 61 and 48 generations for the envelope plus disk and without disk models respectively, when the convergence criteria were reached. This corresponds to 1300 models or 631 CPU hours for the envelope plus disk model, and 1040 models or 152 CPU hours for the envelope without disk model. The resulting SEDs and profiles of these models are shown against the data in Figures 3.1 and 3.4, and the model images are compared to the observed images in Figures 3.2 and 3.3. The parameters of the best-fitting models are also given in Table 3.3.

3.4.1 High Signal-to-Noise Runs

The model SEDs shown in Figure 3.1 are the result of running one million photon models. To obtain higher signal-to-noise in the SED and images, the dust code was run with 10 million photons with the final set of parameters produced by the genetic code for both envelope plus disk and without disk models. The SEDs produced by the 10 million photon runs for both models are shown in the left and middle panels of Figure 3.5 as solid lines, compared to the SEDs from the genetic code one million photon runs, shown as dashed lines. The SEDs agree well below $\sim$100μm, but are slightly offset at far-IR wavelengths, due to the temperatures calculated by the dust code for the outer cells not being fully converged after one million photons, as few Monte Carlo photons have interacted in these cells.

A five million photon model, which provides a converged temperature and SED, takes up to several hours to run. As running the genetic code with five million photon models would therefore take several weeks, this effect of this difference is instead explored in Figure 3.5, from which it can be inferred that a small amount of cold material should be added to the outer layers of the envelope to fit the observed SED correctly. As an example, the right panel of Figure 3.5 shows the SEDs for the envelope plus and without disk models run with 10 million photons, with the same parameters as those produced by the genetic code but with $R_{\rm max}$=150,000 AU. Here it can be seen that the sub-mm fluxes are better reproduced. The profiles for the $R_{\rm env}^{\rm max}$=150,000 AU models also provide a similar fit to the observed profiles. Hence an outer envelope radius of approximately 150,000 AU probably is closer to the true

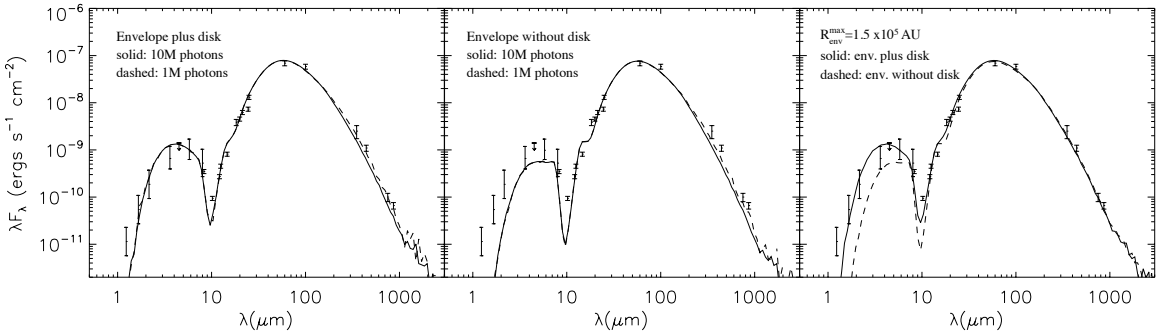

Figure 3.5: The left and middle plots show the small discrepancy between the SEDs produced by a 10 million photon run and a one million photon run for the envelope plus and without disk models respectively. This is due to the fact that after one million photons the temperature in the outer cells of the dust code is not fully converged, which occurs after approximately five million photons. To compensate for this, more cold dust needs to be added to the outer layers of the envelope of the model. Therefore, the right panel shows the SEDs for 10 million photon runs with the parameters set the same as those given in Table 3.3, but setting the envelope radius $R_{\rm env}^{\rm max} = 150,000$ AU. This appears to reproduce the far-IR fluxes well, with minimal change to the rest of the SED or images.

value for IRAS 20126+4104, which lies above the upper limit of the chosen ranges for $R_{\rm env}^{\rm max}$.

3.4.2 Parameter χ^2 Surfaces

To understand how well the parameters were determined, the reduced χ^2-values of all the models run were plotted against each parameter for $\chi^2 < 500$, shown in Figures 3.6 and 3.7. As the first generation of the genetic code was sampled uniformly within the chosen ranges, it was therefore possible to adequately sample parameter space to recover an approximation of the minimum χ^2 surface. Therefore, in addition, the solid lines in Figures 3.6 and 3.7 also show histograms of the minimum χ^2 model in each bin. From these Figures, it can be seen to what extent the observed SED and profiles of IRAS 20126+4104 constrain the properties of the source.

For the envelope plus disk model, Figure 3.6 shows that the stellar mass $M_\star$ and the envelope accretion rate $\dot{M}_{\rm env}$ are well-determined within the chosen ranges, having sharp minimum χ^2 surfaces. The other parameters are not as tightly constrained, however the envelope radius $R_{\rm env}^{\rm max}$, the disk radius $R_{\rm disk}$ and the disk mass $M_{\rm disk}$ tend to have better fits at higher values, and the cavity ambient density $\rho_{\rm cav}$ has a well-defined minimum near 10^{-18}g cm^{-3}. Also, the disk accretion rate $\dot{M}_{\rm disk}$ is not well fit by models with values above $\sim 10^{-3}$ M$_\odot$yr^{-1}. The least well-determined parameter is the cavity half-opening angle $\theta_{\rm cav}$.

For the envelope without disk model, Figure 3.7 shows that the parameters are constrained similarly to those in the envelope plus disk model. However, differences include that envelope accretion rates below $\sim$10^{-4} M$_\odot$yr^{-1} are strongly ruled out, there is a deeper

Table 3.3: Parameters of the genetic algorithm best-fitting models

Parameter	Description	Value for envelope plus disk model	Value for envelope without disk model
$M_\star$	Stellar mass ($M_\odot$)	12.7	11.8
$R_{\rm env}^{\rm max}$	Envelope outer radius (AU)	113,000†	79,100†
$\theta_{\rm cav}$	Cavity half-opening angle at 10^4 AU (degrees)	29.3	34.2
i	Inclination w. r. t. the line of sight (degrees)	85.2	83.4
$M_{\rm disk}$	Disk mass ($M_\odot$)	5.90	...
$R_{\rm disk}$ or $R_{\rm c}$	Disk or centrifugal radius (AU)	9200	300
$\dot{M}_{\rm disk}$	Disk accretion rate ($M_\odot$ yr^{-1})	2.58×10^{-5} $\diamond$	...
$\dot{M}_{\rm env}$	Envelope accretion rate ($M_\odot$ yr^{-1})	3.86×10^{-4}	5.35×10^{-4}
$\rho_{\rm cav}$	Cavity ambient density (g cm^{-3})	9.55×10^{-19}	6.27×10^{-19}
$R_\star$	Stellar radius ($R_\odot$)	4.53	4.34
$T_\star$	Stellar temperature (K)	28,700	27,800

$\dagger$ $R_{\rm env}^{\rm max}$ is likely to be larger ($\sim 150,000$ AU, see Section 3.4 and Figure 3.5)
$\diamond$ The disk accretion rate may be a factor of 2 too large due to X-rays not being included in the code (see Section 3.2).

minimum towards higher values of the cavity half-opening angle, and no models exist with $\chi^2 < 500$ for values of the cavity ambient density greater than 5×10^{-18} g cm^{-3}. In addition, both the inclination and centrifugal radius of the envelope $R_{\rm c}$ are very poorly constrained for the envelope without disk model.

3.4.3 Comparison to the Observed SED

It was found that the minimum reduced χ^2 for the best-fitting envelope plus disk model was 31.9, and the reduced χ^2 for the best-fitting envelope without disk model was 78.4, from which it can be inferred that the model with a disk provides a better fit to the SED and profiles. For the SED, this can be seen in Figures 3.1 and 3.5, where the envelope without disk model does not reproduce the observed near- and mid-IR fluxes.

3.4.4 Comparison to the Observed Profiles and Images

This section compares the model profiles and images to those observed. Figure 3.4 presents the model profiles for the envelope plus disk and without disk models (blue and red solid lines respectively). The left and right panels of Figure 3.2 also present three-colour RGB model images of the IRAC emission towards IRAS 20126+4104: red: 8 μm, green: 5.8 μm, and blue: 3.6 μm, for both envelope plus disk and without disk models.

Both the IRAC images in Figure 3.2 and the profiles in Figure 3.4 show that while both models are able to reproduce the observed angular size of the mid-IR emission, the envelope without disk model is not able to fully reproduce the shape of the IRAC emission, as the 8 μm

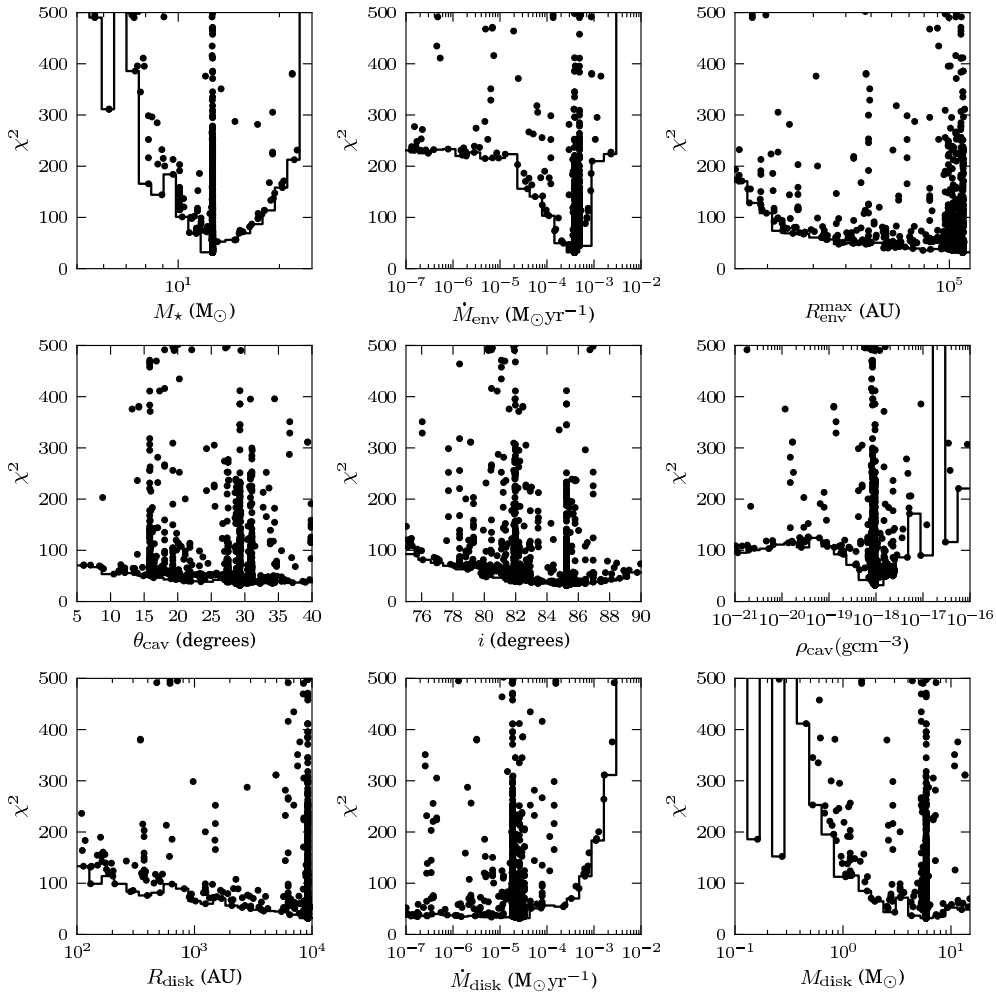

Figure 3.6: Plots of the χ^2-value for models with reduced $\chi^2 < 500$ against the nine varied model parameters for the envelope plus disk model. The solid line shows a histogram of the minimum χ^2-value in each bin, which provides a rough outline of the minimum χ^2 surface.

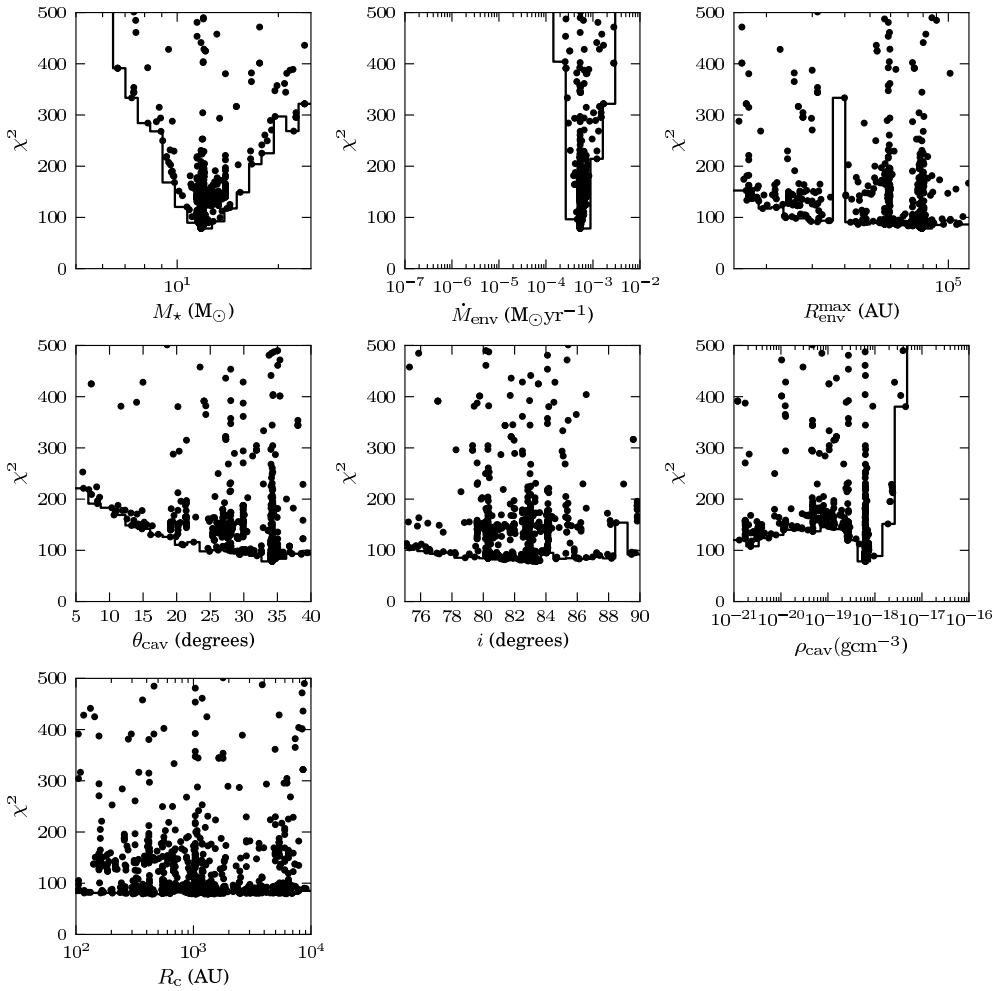

Figure 3.7: Plots of the χ^2-value for models with reduced $\chi^2 < 500$ against the seven varied model parameters for the envelope without disk model. The solid line shows a histogram of the minimum χ^2-value in each bin, which provides a rough outline of the minimum χ^2 surface.

model image is too centrally peaked.

Figure 3.3 also presents the observed and corresponding model images at the wavelengths and spatial resolutions observed in Sridharan et al. (2005), De Buizer (2007) and de Wit et al. (2009): K band, 12.5, 18.3 and 24.5μm. All model images in Figures 3.2 and 3.3 were roughly aligned to the observed images using the centre of the dark lane in the observed and envelope without disk model 12.5μm images, and were rotated clockwise by 56.5° to reproduce the observed position angle.

The morphology of the K band model images (top left and right panels of Figure 3.3) are able to roughly reproduce the two outflow cavities imaged by Sridharan et al. (2005), shown in the top middle panel of Figure 3.3. Comparing the mid-IR model images shown at the remaining three wavelengths, it can be seen that the mid-IR model images are strongly affected by the presence of a disk, specifically in the separation of the two outflow cavity emission lobes. In Figure 3.3, the mid-IR images produced by the envelope without disk model also reproduce the observed mid-IR images much better than those of the model with a disk. In addition, the lack of a dark lane in the observed 24.5μm image is also reproduced by the envelope without disk model, while a dark lane is still seen in the shorter wavelength images. Here the shadowing produced by a rotationally flattened envelope appears to be adequate to match the observed dark lane at 12.5 and 18.3μm.

However, there is further emission to the north west in the observed 12.5, 18.3 and 24.5 μm images, cut off by another 'dark lane', which cannot be reproduced by the models. Several possibilities which may explain this image morphology include:

1. There is a disk towards IRAS 20126+4104, in agreement with the observed SED and IRAC images. However, the disk is truncated or removed inside the radius delineated by the dark lane between the central emission and the northwest emission (at a radius of ∼1.1" or ∼1800 AU), so that the emission within this radius resembles the model without a disk. Mechanisms which would truncate the disk include stellar winds, ionization and heating, which would therefore imply a difference between IRAS 20126+4104 and its lower-mass counterparts.

2. Precession of the outflow axis with time, so that the outflow cavity at smaller radii is not aligned with the outflow cavity at larger radii, explaining the observed discontinuity in the images at a radius of ∼1800 AU. In fact, there is evidence that the outflow

IRAS 20126+4104 is precessing (Shepherd et al., 2000; Cesaroni et al., 2005).

3. The emission within ∼1800 AU is produced by a different young star to that producing the larger scale infrared emission. A companion is expected, as the binary fraction of massive stars is higher than their low-mass counterparts. In addition, a binary companion may explain the outflow precession.

3.4.5 Comparison with Molecular Line Modelling Results of KZ10

In this Section, the properties of IRAS 20126+4104 found using two different approaches are compared. The first has modelled the profiles of molecular lines observed towards IRAS 20126 +4104 in the millimetre (KZ10), and the second has modelled the near-IR to sub-millimetre continuum SED and images (this work). As both studies find models that require a disk to adequately fit the data, Table 3.4 compares the envelope plus disk model from this work and the parameters of the best-fitting disk model of KZ10.

In Table 3.4, it can be seen that both models find a similar stellar mass, disk mass and disk radius, as well as disk accretion rate, which was assumed in the KZ10 model to be equal to the envelope accretion rate.

The envelope outer radius was not fit in the KZ10 model, as their model only extended out to a radius of ∼26,400 AU or 0.128 pc. In addition, the inclination was assumed to be 90 degrees, similar to the fitted value of 85.2 degrees. As in the model presented here, the stellar radius and temperature in the KZ10 model were determined from the stellar mass.

The envelope accretion rate, $\dot{M}_{\rm env}$, the envelope density at the disk radius, ρ_0, and the total mass within a radius of 26,400 AU, $M_{\rm tot}$(0.128 pc), all have ∼3-5 times larger values for our envelope plus disk model than the KZ10 disk model. This discrepancy may be explained by the fact that our model probes the envelope out to larger radii, and therefore can more accurately determine the envelope density. Alternatively, since the mass density in KZ10 depends on an assumed NH_3 abundance, this discrepancy may also be resolved by increasing the assumed NH_3 abundance by a factor of ∼3-5.

The temperature in the midplane which was calculated by the dust code for the best-fitting envelope plus disk model was fitted with a power-law at radii greater than 10,000 AU, giving $T \propto R^{-0.34}$. In comparison, the temperature in the KZ10 disk model was found to decrease more steeply than $T \propto R^{-2/3}$, corresponding to $p < -1$, where p was used to define

Table 3.4: Comparison of parameters of genetic best-fitting envelope plus disk model with those from KZ10

Parameter	Description	Value for envelope plus disk model (this work)	Value for model with disk (KZ10)
$M_\star$	Stellar mass ($M_\odot$)	12.7	10.7
$R_{\rm env}^{\rm max}$	Envelope outer radius (AU)	113,000†	>26,400 (assumed)
$\theta_{\rm cav}$	Cavity half-opening angle at 10^4 AU (degrees)	29.3	...
i	Inclination w. r. t. the line of sight (degrees)	85.2	90 (assumed)
$M_{\rm disk}$	Disk mass ($M_\odot$)	5.90	2.5
$R_{\rm disk}$	Disk or centrifugal radius (AU)	9200	6900
$\dot{M}_{\rm disk}$	Disk accretion rate ($M_\odot$ yr^{-1})	2.58×10^{-5}	(7.6×10^{-5})
$\dot{M}_{\rm env}$	Envelope accretion rate ($M_\odot$ yr^{-1})	3.86×10^{-4}	7.6×10^{-5}
$\rho_{\rm cav}$	Cavity ambient density (g cm^{-3})	9.55×10^{-19}	...
$R_\star$	Stellar radius ($R_\odot$)	4.53	4.8
$T_\star$	Stellar temperature (K)	28,700	19,000
ρ_0	Env. density at R_d (cm^{-3})	2.39×10^5	7.9×10^4
p	Temperature power law exponent ($T \propto R^{-2/(4+p)}$)	1.8 (>10,000 AU, $T \propto R^{-0.34}$)	< -1 ($T \propto R^{-2/3}$)
Γ	Angular momentum (AU kms^{-1})	10,200	8100
A_ρ	Disk density ratio	0.792	5.1
B_T	Disk temperature factor	...	15.0
v_k	Velocity at R_d (kms^{-1})	1.11	1.2
$M_{\rm tot}$(0.128 pc)	Total mass within 0.128 pc ($M_\odot$)	49.7	12.6

$\dagger$ $R_{\rm env}^{\rm max}$ is likely to be larger ($\sim 150,000$ AU, see Section 3.4 and Figure 3.5)

the temperature power-law exponent in the envelope as $T \propto R^{-2/(4+p)}$.

The disk density ratio, A_ρ is the ratio of the disk density to the envelope density at the disk radius (equation 9 of KZ10). Although the two values of A_ρ given in Table 3.4 differ noticeably, this is due to different values of the envelope density ρ_0, while the disk densities at $R_{\rm disk}$ are similar. The disk temperature factor, B_T, is the coefficient in the expression describing the disk temperature given in equation 12 of KZ10. This parameter does not have an equivalent in the envelope plus disk model, as the temperatures for the models presented here were solved for by the radiation transfer dust code.

Finally, comparing the dynamics of the two models, it can be seen that the angular momentum and the velocity at the disk radius have similar values for both models.

3.4.6 Properties of the Disk

In addition to KZ10 and this work, Cesaroni et al. (2005) have also confirmed the existence of a disk around IRAS 20126+4104 via modelling of mm wavelength transitions of $C^{34}S$ and HCO^+. Their results gave a disk of radius 0.037 pc or $\sim$ 7600 AU rotating around a central protostar of 7$\pm$2 $M_\odot$. They also determined the temperature structure of the disk to vary as $R^{-0.57}$, and the density to range from $\sim 2.5 \times 10^5$ cm^{-3} at the outer radius of the disk to $\geq 2 \times 10^8$ cm^{-3} in its centre, with a power-law structure varying as R^p with p=-2.8 to -3.0. In addition, the total disk mass was determined via continuum observations to be between

1 and 4 $M_\odot$. They also estimated the accretion rate though the disk to be $2 \times 10^{-3}\,M_\odot yr^{-1}$, however this calculation assumed that the material in the disk could accrete in free-fall towards the star, without the need for removal of angular momentum via some mechanism such as disk viscosity.

In general the results from Cesaroni et al. (2005) compare well with those found in this Chapter. In comparison, the disk radius $R_{\rm disk}$ for the envelope plus disk model was found by the genetic code to be 9200 AU, and the central stellar mass was 12.7 $M_\odot$. As the central mass was determined by Cesaroni et al. (2005) via calculation of the central dynamical mass of a Keplerian disk seen exactly edge-on, but the disk may be actually slightly inclined, it is likely that 7 $M_\odot$ is an underestimate of the true protostellar mass. The temperature structure of the disk for the model assumed in this chapter ($R^{-1/2}$) is similar to their value of $R^{-0.57}$, and the density structure of the disk assumed here ($R^{-2.25}$), is also comparable to their result. Further, the disk masses found by the different methods are in reasonable agreement (1-4 $M_\odot$ compared to 5.9 $M_\odot$). Finally, the accretion rate found for the disk by Cesaroni et al. (2005) is much higher, however as mentioned above, this assumes the material in the disk is in free-fall towards the star, which is unlikely to be the case.

In the remainder of this Section, the properties of the disk around IRAS 20126+4104 which are suggested by the results of this work are discussed. For a Keplerian velocity of 1.11 kms^{-1} at $R_{\rm disk}$, the outer radius of the disk would therefore take $\sim 3 \times 10^5$ yr to complete one orbit. As this is on the order of the time massive stars spend in their accretion phase, it appears unlikely that the outer regions of the disk will have had the time to reach centrifugal or hydrostatic equilibrium, which would occur on approximately the same timescales. However, the results show that, in addition to the rotationally flattened envelope, extra mass arranged in some form of flattened structure is required, for radii up to 9200 AU, to reproduce the observed SED and profiles.

As the dust code calculates the temperature of the envelope and disk geometry, it was possible to calculate the Toomre Q parameter (Toomre, 1964, and Chapter 1) - a measure of stability to fragmentation - in the midplane of the disk as a function of radius,

$$Q = \frac{c_s \Omega}{\pi G \Sigma} \tag{3.10}$$

where c_s is the speed of sound in the gas, Ω is the angular velocity of the disk, G is the

gravitational constant and Σ is the surface density of the disk. The surface density as a function of radius was found by integrating equation 3.1 over the disk height z. To find the sound speed, an ideal molecular gas was assumed,

$$c_s = \sqrt{\frac{kT}{2.3m_H}} \tag{3.11}$$

where k is the Boltzmann constant, T is the temperature calculated by the dust code and $2.3m_H$ is the average molecular mass of the gas. The disk was found to be stable ($Q > 1$), with $Q > 10$ within 500 AU, and Q only reaching a value less than unity at radii greater than the disk radius. Thus the high temperatures within the disk stabilise it against local fragmentation.

3.5 Chapter Conclusions

In order to determine whether the standard model of low-mass star formation can also apply to massive stars, the near-IR to sub-millimetre SED and several mid-IR images of the accreting embedded massive star IRAS 20126+4104 were modelled, using model geometries which are commonly used to describe forming low-mass stars.

A Monte Carlo radiation transfer dust code was used to model the continuum absorption, emission and scattering through two scaled-up azimuthally symmetric dust geometries, the first consisting of a rotationally flattened envelope with outflow cavities, and the second which also includes a flared disk.

To find the best-fitting set of model parameters, a genetic algorithm was used to search parameter space, within parameter ranges which bracketed previous results or were physically plausible. This also allowed minimum χ^2 surfaces to be produced for each parameter, from which it could be inferred how well the SED and image profiles constrained them. The two parameters most constrained by the data were the stellar mass and envelope accretion rate, which were determined to be $\sim$13 $M_\odot$ and $\sim 4 \times 10^{-4}\,M_\odot yr^{-1}$ respectively for the envelope plus disk model, and $\sim$12 $M_\odot$ and $\sim 5 \times 10^{-4}\,M_\odot yr^{-1}$ for the envelope without disk model. These two parameters are actually proxies for other more directly determined properties of the source - the stellar mass in the models is a proxy for the stellar luminosity, and the envelope accretion rate is a proxy for the total mass in the envelope, which is constrained by the millimeter fluxes. The stellar luminosities for both the envelope plus and without disk

models respectively are 1.3×10^4 and $1.0 \times 10^4\,L_\odot$, and the total masses within a radius of 150,000 AU (or 0.73 pc) are 1.1×10^3 and $1.3 \times 10^3\,M_\odot$. The best-fitting values of the remaining parameters are given in Table 3.3.

These results show that the envelope plus disk model reproduces the observed SED and images better than the envelope without disk model, although the model without a disk appears to better-reproduce the morphology of the mid-IR emission within a radius of ∼1800 AU. Several possible causes of this discontinuity were outlined, such as inner disk truncation or outflow precession. It may be that the observed mid-IR images, which cannot be fully explained by the envelope plus disk model, are showing the effect of the radiation of a massive star on its accreting material. However, future observations and modelling are needed to determine whether precession and/or a young protostellar companion are more likely explanations.

Comparing these results to those of KZ10, it can be noted that both studies find that a model with a disk reproduces the observations more successfully than one without. Although both studies modelled completely different observations using different techniques, the best-fitting model parameters were found to be similar to those determined by KZ10. While a higher envelope accretion rate was found than KZ10, and therefore a slightly higher envelope density and total envelope mass, this difference may be due to the fact that the masses determined from the molecular line modelling depend on the assumed molecular abundances. For example, increasing the assumed molecular abundances by a factor of 3-5 would bring the values from both studies into agreement. In addition, as the observed SED is more sensitive to emission from the entire envelope, not only the material within a radius of 26,400 AU modelled by KZ10, it is possible to probe more of the mass in the envelope.

The best fitting envelope plus disk model has a disk radius of 9200 AU. As at this radius the disk requires $\sim 3 \times 10^5$ yr to complete one orbit, it is unlikely that the outer regions of the disk have had time to reach centrifugal or hydrostatic equilibrium. However, by using the temperature along the disk midplane found by the dust code, it was found that this disk would be stable to local fragmentation.

Chapter Acknowledgments

I would like to thank T.K. Sridharan, J. De Buizer, and W. de Wit for providing electronic versions of their infrared images to include in this work.

4

A Multi-Wavelength Study of AFGL 2591

Adapted from *Johnston et al., to be submitted to MNRAS*

In the previous Chapter, the SED and infrared images of the massive embedded star IRAS 20126+4104 were modelled to determine whether they could be reproduced by models commonly applied to low-mass protostars. This Chapter details a similar study of the forming (proto)star AFGL 2591, which in addition to modelling the SED and near-IR images of the source, also expands to include an analysis of the associated ionized and molecular gas emission.

AFGL 2591 is a well-studied example of a luminous ($2\times10^4\,L_\odot$ at 1 kpc) forming star. One of its most prominent features is a one sided conical reflection nebula observed in the near-IR (e.g Minchin et al., 1991; Tamura & Yamashita, 1992). Found within the Cygnus-X star-forming complex, the distance to the source is uncertain, and authors have assumed values between 1 and 2 kpc (e.g. Poetzel et al., 1992; Hasegawa & Mitchell, 1995); here a distance of 1 kpc is assumed, for ease of comparison with recent work (e.g. Trinidad et al., 2003; van der Tak & Menten, 2005). As will be described in this chapter, AFGL 2591 actually consists of several objects. However, as one source dominates the SED and infrared images, and hence

the luminosity, the name AFGL 2591 will be used henceforth to refer to this dominant source.

In part due to its proximity, many authors have studied and modelled AFGL 2591. One-dimensional modelling of the circumstellar geometry via the observed SED has been carried out by Guertler et al. (1991); van der Tak et al. (1999); Mueller et al. (2002b) and de Wit et al. (2009). Improving on these, Preibisch et al. (2003) used two models - one of a disk and the other of an envelope plus outflow cavities - to reproduce the 40 AU diameter bright disk of emission observed in their K-band image, and Trinidad et al. (2003) have modelled the millimetre emission from AFGL 2591 as an optically thick disk (without envelope). As part of their comprehensive study, van der Tak et al. (1999) also modelled their observed molecular lines (CS, HCN, HCO^+) including an outflow cavity in a power-law envelope, finding that an opening angle of 30° was able to better reproduce the line profiles. Building on previous work, the modelling presented in this Chapter includes the first simultaneous model of the near-IR through sub-mm SED, and near-IR images, of AFGL 2591 by radiation transfer through a two-dimensional axisymmetric geometry.

The ionized gas emission in the region surrounding AFGL 2591 has previously been observed by Campbell (1984b); Tofani et al. (1995); Trinidad et al. (2003) and van der Tak & Menten (2005) from 5 to 43 GHz. These observations showed that AFGL 2591 is in fact not an isolated forming star, uncovering four continuum sources in the region. The observed fluxes of two of these, VLA 1 and VLA 2, gave spectral indices consistent with optically thin free-free emission from HII regions, and a third source VLA 3, was measured to have a steeper spectral index, possibly indicating optically thick emission. VLA 3 is also coincident with the central illuminating source of AFGL 2591 observed at shorter wavelengths (Trinidad et al., 2003). A fourth radio continuum source has also been detected by Campbell (1984a) and Tofani et al. (1995) (their source 4 and n4 respectively), which shall be referred to as VLA 4 in the following sections. In addition, the 3.6 cm images presented in this chapter (Figure 4.4) uncover a fifth source, VLA 5, to the south west.

Knots of H_2 and [SII] Herbig Haro objects have been detected toward AFGL 2591 (Tamura & Yamashita, 1992; Poetzel et al., 1992), suggesting the presence of shocked gas. These are coincident with an east-west bipolar outflow (e.g. Lada et al., 1984; Hasegawa & Mitchell, 1995), which extends across 5' or 1.45 pc at 1 kpc, but also contains a more collimated central small-scale component with an extent of 90×20".

Evidence for the presence of a disk or rotationally flattened material around the central source of AFGL 2591 has been found by several authors. The near-IR imaging polarimetry observations of Minchin et al. (1991) showed that a disk or toroid of material was needed to appropriately scatter the emission. In addition, a large (50×80") flattened "disk" of material has been observed parallel to the outflow in observations of CS lines (Yamashita et al., 1987). At smaller scales, van der Tak et al. (2006) found evidence for a disk of diameter 800 AU in water molecular line observations, which exhibited a systematic velocity gradient perpendicular to the outflow. Finally, both OH and water masers have been observed towards VLA 3 (Trinidad et al., 2003; Hutawarakorn & Cohen, 2005), some of which trace rings with velocity gradients, near or coincident with the source. However, it is not clear exactly what these motions are tracing.

In this Chapter, a multi-wavelength approach has been used to further probe the circumstellar environment of AFGL 2591, and to address the question of whether it forms in a similar manner to its low-mass counterparts. Section 4.1 presents the near-IR to sub-mm SED, 2MASS photometry, measured brightness profiles, and Gemini North near-IR images of AFGL 2591. Section 4.2 then outlines the new observations carried out in this work, describing both the VLA 3.6 cm and 7 mm, as well as the CARMA[1] ^{13}CO, C^{18}O and 3 mm continuum observations. Section 4.3 presents the observational results for both the centimetre and millimetre wavelength datasets. Section 4.4 describes the modelling of the near-IR to sub-mm SED and near-IR images of AFGL 2591, and Section 4.5 models the ionized gas emission towards AFGL 2591-VLA 3 by ionizing the geometry determined in Section 4.4. Finally, the Chapter summary is given in Section 4.6.

4.1 SED and Near-IR Images

The observed near-IR to sub-millimetre SED of AFGL 2591 is shown in Figure 4.1. The overplotted solid and dashed lines (the best-fitting models for an envelope plus disk and without a disk respectively) are discussed further in Section 4.4. The SED data points were collected from the literature; Table 4.1 lists the wavelengths, flux densities and references for the data displayed in Figure 4.1. The 30 data points shown between 3.5 and 45 μm were sampled uniformly in log-space from the average of two highly processed ISO-SWS spectra of AFGL 2591 (Sloan et al., 2003) taken on different dates (1995 Dec 15 and 1996

[1]Combined Array for Research in Millimeter-wave Astronomy

Table 4.1: Observed near-IR to sub-millimetre fluxes for AFGL 2591, collected from the literature. References are given in parentheses: (1) Skrutskie et al. (2006), (2) Sloan et al. (2003), (3) Joint Iras Science (1994) (4) Lada et al. (1984) (5) Mueller et al. (2002a), (6) Jenness et al. (1995)

Wavelength (μm)	Flux Density (Jy)	Description / Origin
1.235	0.11 ± 10%	2MASS J band, photometry: this work; image, shown in Fig. 4.2: (1)
1.662	0.43 ± 10%	2MASS H band, photometry: this work; image, shown in Fig. 4.2: (1)
2.159	2.30 ± 10%	2MASS K band, photometry: this work; image, shown in Fig. 4.2: (1)
3.5 – 45	...	Sampled ISO-SWS spectrum (2)
60	5.31×10^3 ± 8%	IRAS 60μm (3)
95	5.8×10^3 ± 20%	KAO (4)
100	5.72×10^3 ± 16%	IRAS 100μm (3)
110	5.5×10^3 ± 20%	KAO (4)
160	3.4×10^3 ± 20%	KAO (4)
350	440 ± 20%	CSO (5)
450	170 ± 25%	JCMT (6)
850	19.0 ± 20%	JCMT (6)

Nov 7, observations IDs 02800433 and 35700734). The uncertainties for the averaged ISO-SWS spectrum were assumed to range from 4 to 22% as per the ISO handbook volume V[2]. As mentioned above, the SED and therefore flux densities of AFGL 2591 given in Table 4.1 were assumed to be dominated by one source. Evidence to support this assumption will be presented in Section 4.3, via a comparison of the SEDs of the resolved sources in the region.

4.1.1 Near-IR 2MASS Images

A three-colour 2MASS J, H, and K_s band image of the near-IR emission observed towards AFGL 2591 is shown in the middle panel of Figure 4.2, where red, green and blue are K_s, H and J bands respectively. This Figure shows the conical near-IR reflection nebula (previously observed by e.g. Kleinmann & Lebofsky, 1975; Minchin et al., 1991; Tamura & Yamashita, 1992), which is consistent with being a blue-shifted outflow lobe formed by the central source of AFGL 2591.

To obtain 2MASS fluxes for AFGL 2591, irregular aperture photometry was performed on 2MASS Atlas images. Photometric uncertainties on the fluxes are <1%, however it is likely the fluxes are more uncertain due to the choice of the irregular photometry apertures, and foreground or background stars being included within them. The uncertainty due to contaminating stars is likely dominated by the 2MASS source 20292393+4011105 at $20^h29^m23^s.93$ $+40°11'10".56$ (J2000; easily visible as a point source in the Gemini North near-IR images presented in Figure 4.6), as the apertures were placed to avoid all other point sources visible in the 2MASS images. The fluxes of this contaminating source are 0.011, 0.035 and 0.105 Jy at J, H and K_s bands respectively, with K_s band being an upper limit. Therefore, the uncer-

[2]http://iso.esac.esa.int/users/handbook/

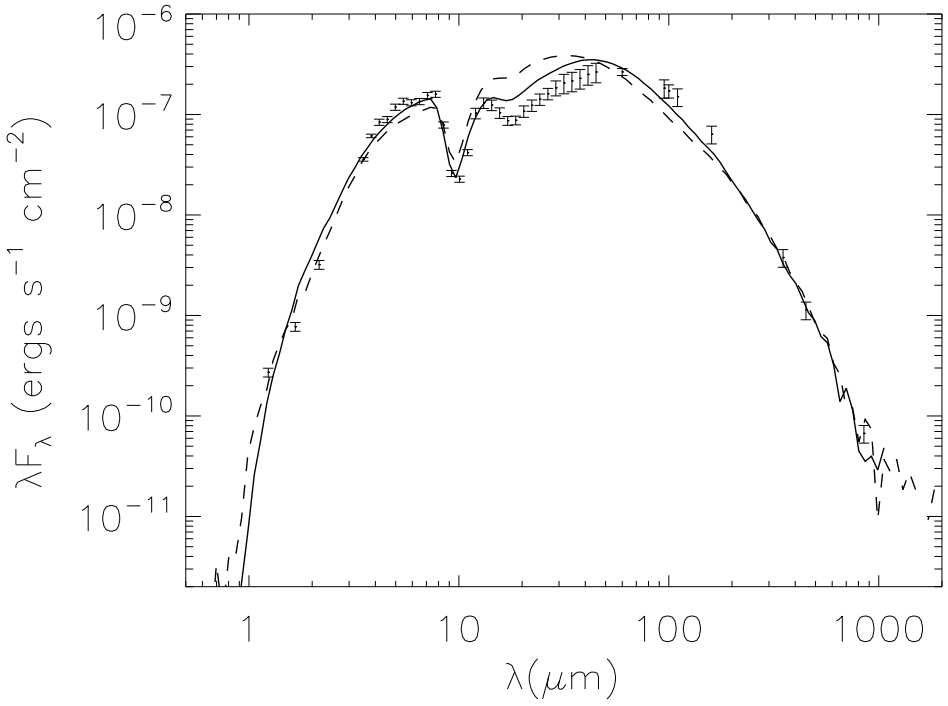

Figure 4.1: The SED of AFGL 2591, collated from the literature. The best-fitting models for an envelope plus disk and without disk (overplotted solid and dashed lines respectively) are discussed in Section 4.4.

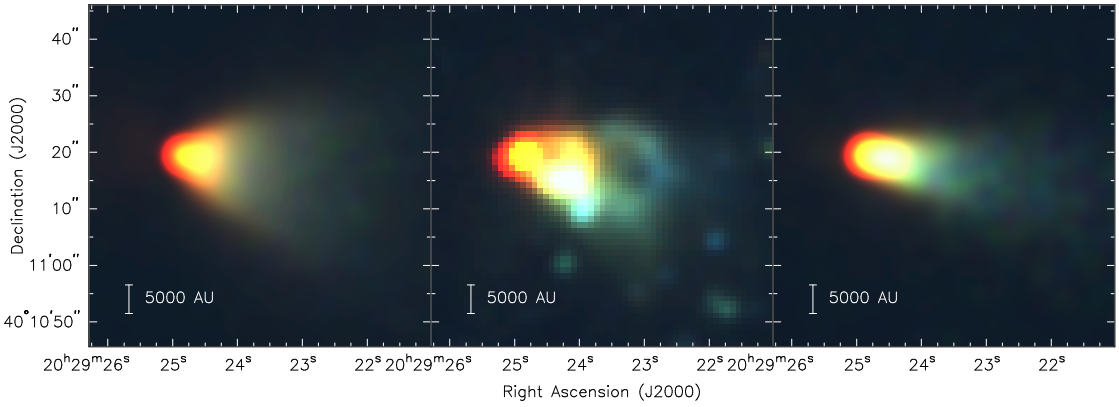

Figure 4.2: *Left panel:* Model three-colour J, H and K band image for the envelope plus disk model (RGB: K, H, and J bands respectively). *Middle panel:* Observed 2MASS three-colour image of AFGL 2591. *Right panel:* Model J, H, and K band image for the envelope without disk model. The model images have been normalised to the total integrated fluxes given in Table 4.1, in order that the morphology of the emission can be easily compared. Stretch: red: K band, 130-300 MJy sr^{-1}; green: H band, 95-150 MJy sr^{-1}, blue: J band, 30-60 MJy sr^{-1}.

tainty in the measured 2MASS fluxes of the AFGL 2591 outflow lobe was estimated to be ∼10%.

4.1.2 2MASS Brightness Profiles

Flux profiles of AFGL 2591, summed across strips aligned with and perpendicular to the source outflow axis (P.A.=256°, with thicknesses of 24.6" and 104" respectively), were measured for the three 2MASS bands. The background subtracted, normalised profiles are shown in Figure 4.3 along with the best-fitting models to both the SED and profiles, for envelope plus disk and without disk models (blue and red solid lines respectively), which will be discussed further in Section 4.4. The errors in the profiles shown in each panel of Figure 4.3 reflect the uncertainty due to background fluctuations, and are calculated as the standard deviation of the profiles measured in two strips either side of the main profile, which were assumed to contain minimal source flux. As the strips used to calculate the uncertainty in the perpendicular profiles contained several bright stars, iterative sigma clipping was performed, i.e. pixels lying more than 5 standard deviations away from the mean were then ignored and the mean and standard deviation were recalculated and the process was repeated until no pixels were rejected.

4.1.3 NIRI Gemini North Near-IR Images

High resolution Near-IR images of AFGL 2591 were obtained from the Gemini website, which were taken under program GN-2001A-SV-20 as part of the commissioning of Gemini North's NIRI instrument, and were available under public release. The total integration time was 2 min for J band and 1 min at H and K' bands. The images were aligned using Chandra X-ray sources in the field (Evans et al., 2010), giving a positional accuracy of 0.6". The FWHMs of the PSFs in the images range between 0.3-0.4". The peak position of the central source of AFGL 2591 in the J band image was found to be $20^{h}29^{m}24^{s}.86$ +40°11'19".5 (J2000), which was taken to be the position of the powering object. In Sections 4.3.1 and 4.3.2 these high-resolution images will be compared to the radio continuum and molecular line data observed for this work.

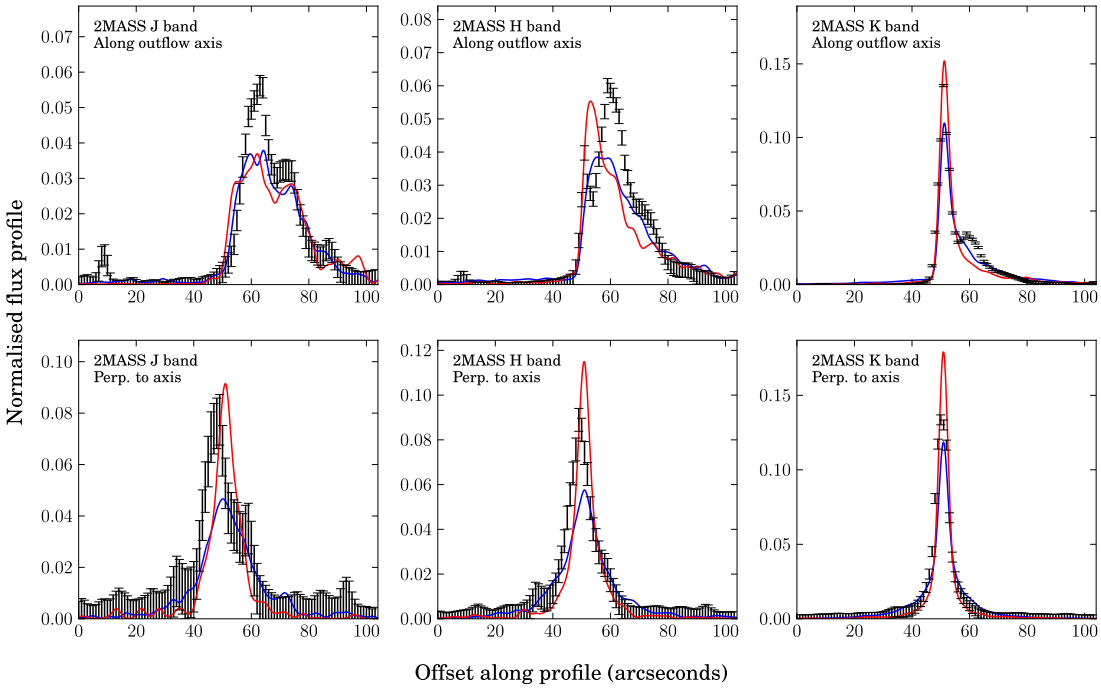

Figure 4.3: Black error bars: normalised flux profiles for the three 2MASS bands, aligned with (top) and perpendicular to (bottom) the outflow axis. Blue and red lines: the profiles of the best-fitting models to both the observed SED and profiles, for envelope plus disk and without disk models respectively.

4.2 Radio Interferometric Observations

4.2.1 VLA 3.6 cm and 7 mm Continuum

Multi-configuration radio continuum observations at 3.6 cm and 7 mm were conducted between April 2007 and March 2008 with the Very Large Array (VLA) of the National Radio Astronomy Observatory[3]. During this time frame, the VLA continuum mode consisted of four 50 MHz bands, two of which were placed at 8.435 GHz, and two at 8.485 GHz for 3.6 cm, and similarly two at 43.315 GHz and two at 43.365 GHz for 7 mm. At 3.6 cm, observations were taken in all four configurations of the VLA (A to D), and at 7 mm, observations were performed in B through D array and combined with A array archive data previously published in van der Tak & Menten (2005). When combined, these observations provided baseline lengths between 35 m and 36.4 km, giving information on angular scales from 0.24" to 3' for 3.6 cm, and 0.05 to 43" for 7 mm.

For each observation, Table 4.2 lists the observed wavelength, configuration, observation

[3]The National Radio Astronomy Observatory is a facility of the National Science Foundation operated under cooperative agreement by Associated Universities, Inc.

Table 4.2: Summary of VLA observations

Wavelength	Configuration	Date of observation	Program	No. of antennas	Time on-source (hr)	Pointing centre R.A.	Decl.	Phase calibrator flux density (Jy)
3.6 cm	A	2007 Jul 26	AJ337	26 (22)	1.75	20 29 24.90	+40 11 21.00 (J2000)	1.49
3.6 cm	B	2008 Jan 18	AJ337	26 (21)	1.96	20 29 24.90	+40 11 21.00 (J2000)	1.91
3.6 cm	C	2008 Mar 9	AJ337	27 (23)	1.97	20 29 24.90	+40 11 21.00 (J2000)	2.13
3.6 cm	D	2007 Apr 12	AJ332	26 (20)	0.37	20 29 24.90	+40 11 21.00 (J2000)	1.25
7 mm	A	2002 Mar 25	AT273	27 (23)	1.97	20 27 35.95	+40 01 14.90 (B1950)	3.44
7 mm	B	2008 Jan 18	AJ337	26 (24)	3.43	20 29 24.90	+40 11 21.00 (J2000)	3.15
7 mm	C	2008 Mar 9	AJ337	27 (25)	4.18	20 29 24.90	+40 11 21.00 (J2000)	4.46
7 mm	D	2007 Apr 28	AJ332	26 (17)	0.44	20 29 24.90	+40 11 21.00 (J2000)	1.64

date, program code, number of antennas in the array (with the number of antennas with useful data shown in brackets), time on-source, the pointing centre of the target, and the flux density of the gain calibrator determined from bootstrapping the flux from the primary flux calibrator. For all observations, the gain calibrator was 2015+371 and primary flux calibrator was 1331+305 (3C286).

Data reduction and imaging were carried out using the Common Astronomy Software Applications (CASA)[4] package. As 1331+305 was slightly resolved, a model was used for flux calibration, which has a flux of 5.23 Jy at 3.6 cm and 1.45 Jy at 7 mm, allowing data at all UV distances to be used. Antenna gain curves and an opacity correction (zenith opacity = 0.06) were applied for the 7 mm data. The error in absolute flux calibration is approximately 1-2% for the 3.6 cm band, and 3-5% for the 7 mm band, but may be larger at 7 mm due to incomplete correction for elevation-dependent atmospheric effects. The data were imaged using a CLEAN multi-scale deconvolution routine, using three scales, and Briggs weighting with a robust parameter of 0.5. The 7 mm data were mosaicked using standard gridding, as the offset between the pointing centres of the A array and remaining observations was small. The rms noise in the final combined images were 30 and 60 μJy beam^{-1} for the 3.6 cm and 7 mm images respectively, and the synthesised beams were 0.43 by 0.40", P.A.=43° and 0.11 by 0.11", P.A.=43°.

4.2.2 CARMA ^{13}CO, C^{18}O and 3mm Continuum

CARMA[5] observations at $\lambda \sim 3$ mm were taken on 10 July 2007 in D configuration (corresponding to baseline lengths between 11-150 m). A total of 14 antennas were used during the observations, five 10-m and nine 6-m in diameter.

[4] http://casa.nrao.edu

[5] Support for CARMA construction was derived from the states of California, Illinois, and Maryland, the James S. McDonnell Foundation, the Gordon and Betty Moore Foundation, the Kenneth T. and Eileen L. Norris Foundation, the University of Chicago, the Associates of the California Institute of Technology, and the National Science Foundation. Ongoing CARMA development and operations are supported by the National Science Foundation under a cooperative agreement, and by the CARMA partner universities.

The CARMA correlator is comprised of two side bands, placed either side of the chosen LO frequency, which for these observations was 108.607 GHz. Both the upper and lower side bands contained three spectral windows: one wide and two narrow, giving a total of six windows. The two wide spectral windows, centred on 106.7 and 110.5 GHz, had a bandwidth of 500 MHz and a total of 15 channels, and the four narrow spectral windows had a width of approximately 8 MHz and 63 channels, giving a spectral resolution of 122 kHz. The observed lines, ^{13}CO(J=1-0) and C^{18}O(J=1-0), lay in the two narrow spectral windows in the upper side band at 110.201355 and 109.782158 GHz, corrected for a cloud velocity of $v_{\rm LSR}$=-5.0 kms^{-1}. At these frequencies, the spectral resolution was $\sim$0.33 kms^{-1}.

The phase centre for AFGL 2591 was $20^{\rm h}29^{\rm m}24^{\rm s}.7$ $+40°11'18".9$ (J2000), and the total time on source was 2.5 hr. MWC349 was used as a gain and bandpass calibrator, and Neptune as a flux calibrator. Data calibration and imaging were carried out in CASA. To do this, the data was exported to CASA from its original MIRIAD format after applying line length corrections and Hanning smoothing. Using a flux for Neptune of $\sim$4.2 Jy at 108 GHz (W. Kwon, private communication), a flux of 1.2 and 1.3 Jy for MWC349 was derived for the upper and lower side bands respectively. As there was insufficient signal-to-noise on MWC349 in the narrow spectral windows, band pass calibration was only performed on the two wide spectral windows. To image the data, Briggs weighting and a robust parameter of 0.5 were used, giving a beam size and position angle of 4.4 $\times$ 3.7" and 96° in the ^{13}CO channel maps, and 4.5 $\times$ 3.6" and 93° in the C^{18}O channel maps.

4.3 Observational Results

4.3.1 3.6 cm and 7 mm Continuum

Figure 4.4 presents the observed multi-configuration 3.6 cm image of AFGL 2591. Panel a) shows the entire region surrounding the source, including the four sources first observed by Campbell (1984a) at 6 cm. In addition, a new, low surface brightness source was detected: VLA 5, which varies in peak flux from 3-5 σ. With the addition of shorter baselines, more extended emission is recovered compared to the 3.6 cm A array images of Tofani et al. (1995) and Trinidad et al. (2003). Most noticeably, the emission from source VLA 3, which is coincident with the position of the central source in the near-IR images, is better-determined; a close-up of the emission from this source is shown in panel b) of Figure 4.4. The 3.6 cm

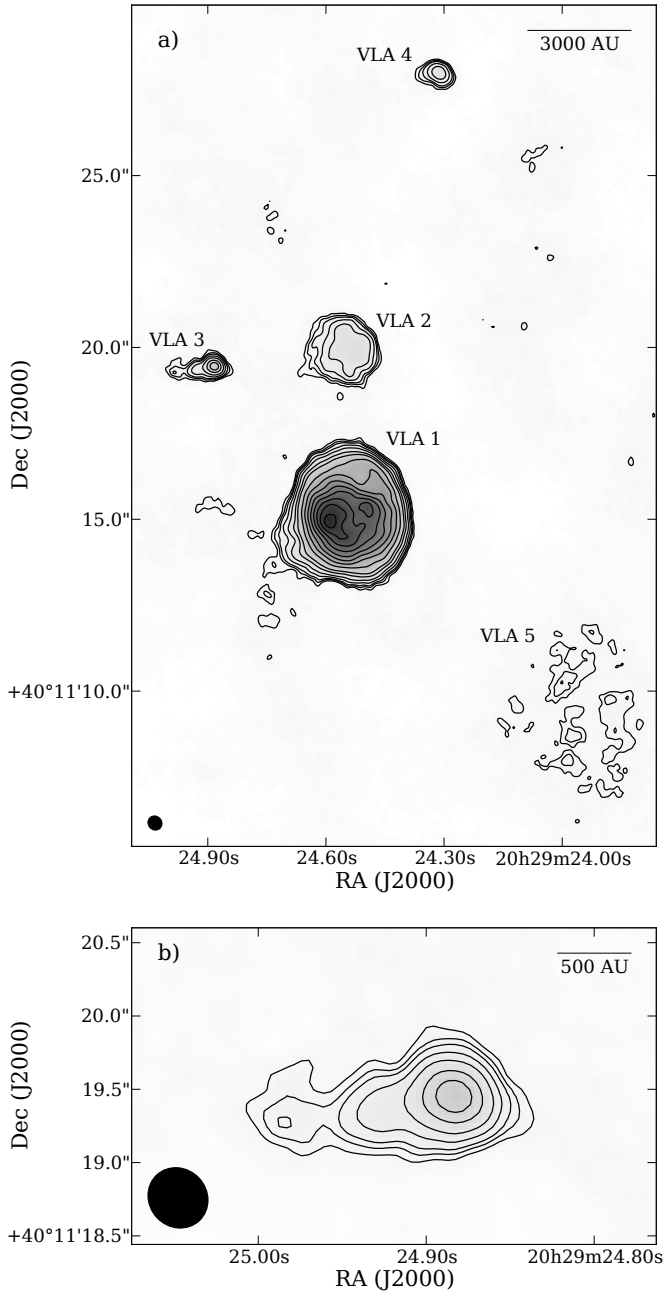

Figure 4.4: a) Map of the 3.6 cm continuum emission surrounding AFGL 2591. Contours are -3, 3, 4, 5, 7, 10, 15, 20, 30, 40, 50... 100 × rms noise = 30μJy beam^{-1}. Greyscale: -0.03 to 3.77 mJy beam^{-1} (1.2 × peak value). The synthesised beam is shown in the bottom left corner: 0.43 × 0.40", P.A. = 43°. b) Close-up of the 3.6 cm continuum emission towards VLA 3. Contours, greyscale and beam as in panel a).

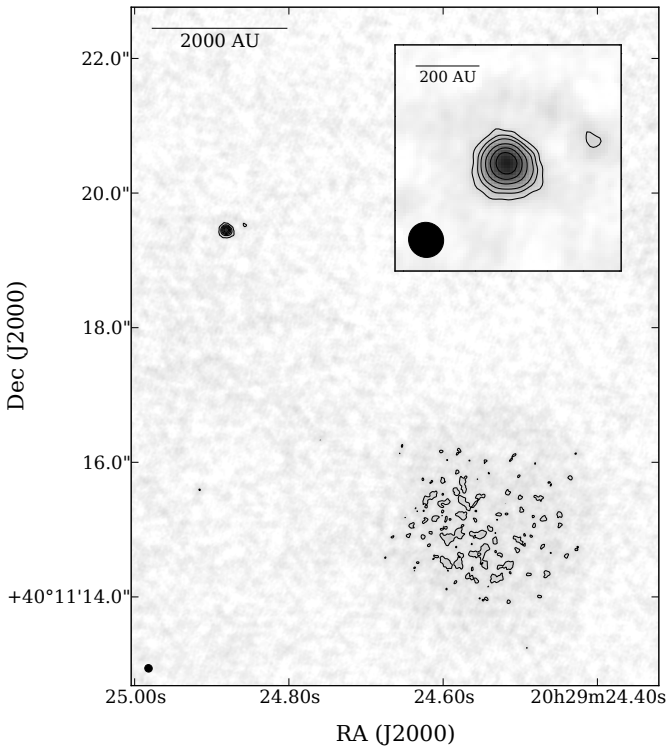

Figure 4.5: Map of the 7 mm continuum emission towards AFGL 2591. Contours are -4, 4, 7, 10, 15, 20, 25, 30 × rms noise = 60μJy beam^{-1}. Greyscale: -0.06 to 2.02 mJy beam^{-1} (1.2 × peak value). The inset panel shows a close-up of the 7 mm emission from VLA 3. The synthesised beam is shown in the bottom left corner of both images: 0.11 × 0.11", P.A. = 43°.

Table 4.3: Measured properties of the observed 3.6 cm (8.4 GHz) and 7 mm (43 GHz) continuum sources

Source name	ν (GHz)	Peak position (J2000)	Peak flux density (mJy beam^{-1})	Integrated flux density (mJy)
VLA 1	8.4	20 29 24.59 +40 11 15.0	3.14 ± 0.07	80 ± 1.6
	43.3	20 29 24.58 +40 11 14.5	0.43 ± 0.06	71 ± 3.5
VLA 2	8.4	20 29 24.52 +40 11 20.1	0.45 ± 0.03	5.2 ± 0.11
	43.3	...	...	...
VLA 3	8.4	20 29 24.88 +40 11 19.5	0.72 ± 0.03	1.52 ± 0.03
	43.3	20 29 24.88 +40 11 19.5	1.8 ± 0.11	2.5 ± 0.13
VLA 4	8.4	20 29 24.32 +40 11 28.0	0.39 ± 0.03	0.99 ± 0.02
	43.3	...	...	...
VLA 5	8.4	20 29 24.00 +40 11 10.3	0.15 ± 0.03	10.9 ± 0.22
	43.3	...	...	...

emission from VLA 3 is jet-like, extending to the east, with a deconvolved width and length of <0.2" and 1.2" (<200 AU and 1200 AU at 1 kpc), position angle of ∼100°, and an opening angle (at a radius of 1200 AU) of <10° derived from its deconvolved width and length. The east jet is resolved, ending in a 'knot' at $20^{h}29^{m}24^{s}.98$ +40°11'19".3 (J2000). There is also a smaller corresponding jet to the west, seen as a slight extension of the source in this direction. The morphology of VLA 3 is consistent with a jet-system which is approximately parallel to the larger-scale flow (observed by e.g. Hasegawa & Mitchell, 1995), and therefore these observations confirm the proposal of Trinidad et al. (2003) that VLA 3 is its powering source.

Figure 4.5 shows the 7 mm multi-configuration image of the region surrounding AFGL 2591, in which only VLA 1 and VLA 3 were detected. VLA 3 is compact, with a radius of < 150 AU, and is only slightly resolved in this image, showing no evidence of the jet seen in Figure 4.4 at 3.6 cm. However, the A array-only image of van der Tak & Menten (2005), which has a synthesised beam size of 43 by 37 mas, shows that the source is slightly extended to the south-west, on the opposite side of the flow to the dominant jet seen at 3.6 cm.

Table 4.3 provides the measured positions, as well as peak and integrated fluxes for the sources observed in the 3.6 cm (8.4 GHz) and 7 mm (43.3 GHz) images, which were measured in the same manner as the cm continuum flux densities presented in Chapter 2. As with any interferometric radio observation, it must be noted that these fluxes may only represent a fraction of the total flux at these wavelengths, due to the finite range in spatial scales which the observations probe, and are therefore lower limits. Keeping this in mind, the spectral types of the stars required to power each source were calculated, using the same method as outlined in Chapter 2, assuming they are HII regions with one powering star,

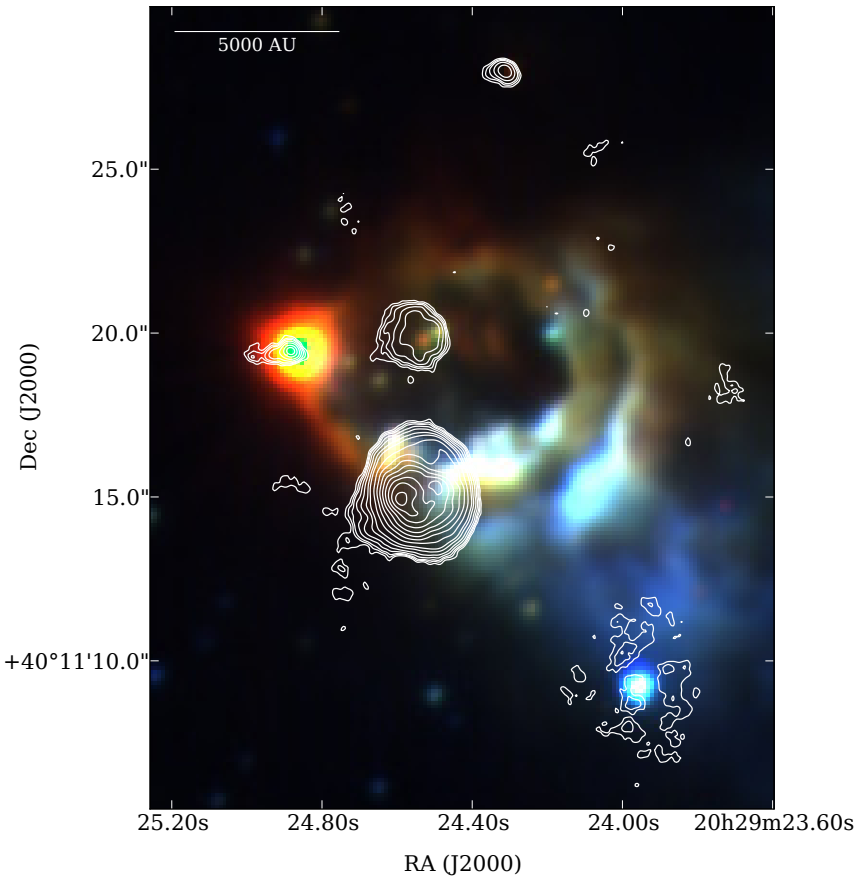

Figure 4.6: Three-colour JHK Germini-North image of AFGL 2591 overlaid with the 3.6 cm contours from Figure 4.4.

giving spectral types of B1, B2, B2, B3 and B2 at 1 kpc for VLA 1 to 5 respectively, which are similar to those found by Trinidad et al. (2003) to within a sub-spectral type. However, as VLA 3 has a jet morphology, it may be that its emission is not from an HC HII region, but is instead created by shock-ionized gas (see Sections 4.3.1.a and 4.5).

Figure 4.6 compares the 3.6 cm emission from the region to the near-IR emission recorded in the Gemini North images. The five detected HII regions line-up with several features in the near-IR image. Firstly, the peak of VLA 3 is coincident with that of the central source of AFGL 2591, at the apex of the one sided reflection nebula. VLA 1 is instead anti-correlated with the diffuse near-IR emission, which suggests that this UC HII region is at the same distance, and is expanding into the material illuminated by the central source of AFGL 2591. This dent or cavity in the cloud can be seen more clearly in the K band bispectrum speckle interferometry image of Preibisch et al. (2003). Therefore it seems likely that the object at approximately $20^{h}29^{m}24^{s}.6$ $+40°11'16".4$ (J2000) suggested to be an edge-on disk by

Table 4.4: Observed fluxes of VLA 1 and VLA 3. References are: (1) Campbell (1984a), (2) this work (3) van der Tak et al. (1999), (4) Marengo et al. (2000), (5) Trinidad et al. (2003)

Source name	ν or λ	Integrated flux density (mJy)	Ref.
VLA 1	5 GHz	79 ± 2.0	(1)
	8.4 GHz	80 ± 1.6	(2)
	43.3 GHz	71 ± 3.5	(2)
	87 GHz	87 ± 1.4	(3)
	106 GHz	71 ± 1.2	(3)
	106.7 GHz	$76 \pm 20\%$	(2)
	110.5 GHz	$72 \pm 20\%$	(2)
	115 GHz	93 ± 2.5	(3)
	18.0 μm	$7.96 \pm 0.8 \times 10^4$	(4)
	12.5 μm	$1.59 \pm 0.2 \times 10^4$	(4)
	11.7 μm	$1.84 \pm 0.2 \times 10^4$	(4)
VLA 3	5 GHz	0.4 ± 0.1	(1)
	8.4 GHz	1.52 ± 0.03	(2)
	22 GHz	1.57 ± 0.4	(5)
	43.3 GHz	2.5 ± 0.13	(2)
	87 GHz	29.5 ± 0.8	(3)
	106 GHz	38.7 ± 0.7	(3)
	106.7 GHz	$71 \pm 20\%$	(2)
	110.5 GHz	$79 \pm 20\%$	(2)
	115 GHz	52.9 ± 1.5	(3)
	226 GHz	$\sim 151 \pm 4.5$	(3)
	18.0 μm	$7.53 \pm 0.75 \times 10^5$	(4)
	12.5 μm	$7.45 \pm 0.75 \times 10^5$	(4)
	11.7 μm	$4.40 \pm 0.44 \times 10^5$	(4)

Preibisch et al. (2003) is instead the brightened rim of the expanding UC HII region, where it is interacting with the surrounding cloud. VLA 2 also appears to be coincident with the close binary discovered by Preibisch et al. (2003), and VLA 4 with a source in the Gemini North image at $20^h29^m24^s.3$ $+40°11'28"$ (J2000; however this source is too faint to be seen in Figure 4.6). In addition, VLA 5 may be powered by the bright source at $20^h29^m23^s.96$ $+40°11'09".25$ (J2000; which is the same source as 2MASS 20292393+4011105, previously mentioned in Section 4.1.1). The sources VLA 1 and VLA 3 are discussed in detail below.

4.3.1.a The Central Source of AFGL 2591, VLA 3

Figure 4.7 shows the SED in frequency space of the central source of AFGL 2591-VLA 3 in black error bars. The fluxes shown, which are taken from the literature and this work, are listed in Tables 4.1 (for λ <1 mm) and 4.4 (for λ >1 mm). At λ >1 mm, fluxes have been listed from the observations with the largest available uv-coverage.

A greybody was fitted to the fluxes between 95 and 850 μm, giving a temperature of 30 ± 1K and a dust emissivity exponent β of 2.0 ± 0.1. The fitted temperature is close to that found for the temperature at the outer radius of the envelope (28.7 K at a radius of

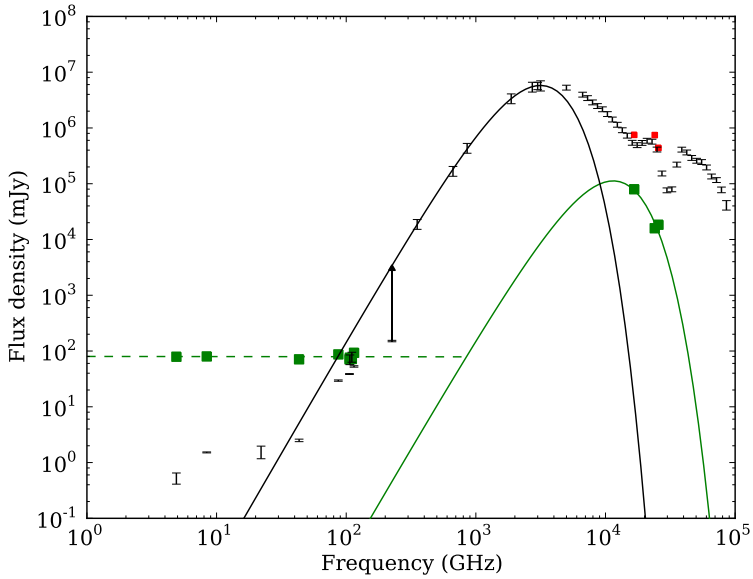

Figure 4.7: Radio-SEDs of AFGL 2591-VLA 3 and VLA 1. The SED of AFGL 2591-VLA 3 is show in black error bars, and the resolved fluxes of AFGL 2591-VLA 3 from Marengo et al. (2000) are shown as red squares, which confirm there is little difference in these resolved fluxes to those used for modelling the SED. Green squares show the fluxes of VLA 1 - errors are not shown as they are smaller than the markers. The black and green solid lines show greybody fits to the SEDs of AFGL 2591-VLA 3 between 95 and 850 μm, and VLA 1 at mid-IR fluxes, respectively (see Sections 4.3.1.a and 4.3.1.b). The green dashed line shows the fit to the long-wavelength fluxes for VLA 1.

30,000 AU) modelled by van der Tak et al. (1999).

It can be seen in Figure 4.7 that the fluxes at millimetre wavelengths (87-226 GHz) fall short of the flux expected from the fitted greybody. However, as these fluxes are taken from interferometric observations, it is likely that they only contribute a fraction of the actual flux. For instance, van der Tak & Menten (2005) note that their quoted 226 GHz continuum flux represents only 5% of the total flux, due to lack of shorter baselines. An arrow is shown on Figure 4.7 representing this correction, which agrees well with the flux expected at 226 GHz from the fitted greybody. Extrapolating this greybody to 7 mm, a flux of 5.1 mJy is expected. Hence, as the measured flux of VLA 3 at 7 mm is 2.5 mJy, it is likely that a portion of the 7 mm flux is due to dust emission, but a significant fraction is resolved out by the interferometer. To estimate this, an image was made at 850 μm of the best-fitting envelope with disk model found from the SED and image modelling presented in Section 4.4. At 850 μm, the signal-to-noise in the model image is higher than at 7 mm, although the morphology should be similar, as the emission should be optically thin at both wavelengths. The integrated flux of the dust emission in the model from the entire source, which included both the diffuse envelope and

the disk emission, was measured, as well as the flux found within a radius of 0.15" or 150 AU (which encompassed the size of the observed 7 mm emission). Comparing these, an upper limit of 10% for the 7 mm dust emission from the entire source actually detected by the interferometer was inferred. Therefore, of the estimated flux of 5.1 mJy at 7 mm from dust emission from the entire source, only < 10% of this, ∼0.5 mJy, would be observed. Hence, the remainder of the observed flux (> 2 mJy) should instead be due to ionized gas.

To measure the spectral index α (where $S_\nu \propto \nu^\alpha$) of VLA 3, which may give further insight into the nature of the emission, the 3.6 cm and 7 mm data were re-imaged using UV distances which were common to both datasets, from 4.5 to 1037 kλ, and the fluxes remeasured. The integrated fluxes were found to be 1.43±0.03 mJy for 3.6 cm and 3.6±0.18 mJy for 7 mm (which increased compared to the original 7 mm flux due to a reduction in resolution, so that fainter emission was brought above the noise level). Therefore the spectral index between 3.6 cm and 7 mm was found to be 0.56±0.02, where the quoted error in the spectral index is due solely to the photometric errors, similar to the spectral index expected for an ionized wind. However, as this value is measured from only two fluxes, it is likely to be more uncertain than the photometric errors given, and should also be taken as an upper limit, as some portion (< 20%) of the 7 mm flux is likely due to dust emission.

Several suggestions regarding the nature of the mm and cm continuum emission from VLA 3 have been made, including a core-halo HII region, an ionized wind plus dust disk (Trinidad et al., 2003), or emission from a spherical gravitationally confined HII region (van der Tak & Menten, 2005). As has been noted above, and can be seen in Figure 4.7, dust emission from the circumstellar environment such as an envelope or disk is likely to dominate the observed emission at wavelengths shorter than 7 mm, and to contribute a fraction (< 20%) of the flux at this wavelength. At 3.6 cm, the deeper observations presented here clearly show the emission to have a non-spherical jet-like morphology. Therefore, consistent physical scenarios to explain this emission include non-spherical gravitational confinement of an HII region by the centrally condensed density of a flattened accreting envelope and possibly disk (e.g. Keto & Wood, 2006; Keto, 2007), or ionizing shocks in an outflow. The first of these possibilities will be explored in Section 4.5 using a simple photoionization code to ionize the circumstellar geometry found from the SED and image modelling in Section 4.4. The implications of the second scenario, a shock ionized jet, are detailed below.

Firstly, without assuming a specific ionization mechanism, the mass loss rate of the jet can be estimated using the model of Reynolds (1986), which describes the emission from a partially optically thick ionized jet (their equation 19):

$$\frac{\dot{M}}{10^{-6}\,\mathrm{M_\odot yr^{-1}}} = 9.38\times10^{-2}\left(\frac{\upsilon}{100\,\mathrm{kms^{-1}}}\right)\left(\frac{1}{x_0}\right)\left(\frac{\mu}{m_p}\right)\left[\left(\frac{S_\nu}{\mathrm{mJy}}\right)\left(\frac{\nu}{10\,\mathrm{GHz}}\right)^{-\alpha}\right]^{0.75} \left(\frac{d}{kpc}\right)^{1.5}\left(\frac{\nu_m}{10\,\mathrm{GHz}}\right)^{-0.45+0.75\alpha}\theta^{0.75}\left(\frac{T}{10^4\,\mathrm{K}}\right)^{-0.075}(\sin i)^{-0.25}\,F^{-0.75} \tag{4.1}$$

where υ is the velocity of the jet, x_0 is the ionization fraction; μ/m_p is the mean particle mass per hydrogen atom of the ionized material, given by $1/(1+x_0)$; S_ν is the observed flux at the frequency ν; α is the spectral index; d is the distance to the source; ν_m is the turn-over frequency below which the emission becomes optically thick; θ is the opening angle of the flow, defined as the ratio of the projected width to the radius at the base of the jet; T is the temperature of the ionized gas; i is the inclination measured from the line-of-sight and F is a function of the spectral index and the dependance of optical depth on radius (see Reynolds, 1986, equation 17).

Assuming an isothermal, uniformly ionized jet with a density gradient of $\rho \sim r^{-2}$; $\upsilon = 500\,\mathrm{kms^{-1}}$ for the velocity of the jet, found for the blue-shifted HH objects towards AFGL 2591 (Poetzel et al., 1992); $x_0 = 0.1$ (commonly found for low-mass sources, e.g. Bacciotti & Eislöffel, 1999); $\nu_m = 50\,\mathrm{GHz}$; $\theta \sim 0.2$"/1.2", the ratio of the maximum deconvolved width to the maximum radius; $T = 10^4\,\mathrm{K}$, and $i = 45°$, taken from the results of the SED modelling presented in Section 4.4.4; F was found to be 1.6, and an upper limit for the mass loss rate of the jet observed at 3.6 cm was determined to be $2.0\times10^{-6}\,\mathrm{M_\odot yr^{-1}}$.

This value is approximately a hundred times larger than the jet mass loss rates seen for low-mass protostars, which are commonly found to be on the order of $10^{-8}\,\mathrm{M_\odot yr^{-1}}$ (see Section 1.1.3.d). However, it is only 0.5% of the best-fitting disk accretion rate found from the SED and image modelling in Section 4.4.4, which is an order of magnitude smaller than that found for low-mass protostars (5-10%, Section 1.1.3.d). The mass loss rate in this jet can also be compared to the mass loss rate of the small-scale red-shifted molecular flow observed by Hasegawa & Mitchell (1995) in ^{12}CO(J=3-2), which corresponds well to the position and direction of the outflow lobe suggested by the ionized jet, red-shifted C^{18}O

emission and bow shocks discussed in Section 4.3.2. For their optically thick case, Hasegawa & Mitchell find a mass loss rate of $6 \times 10^{-5}\,M_{\odot}yr^{-1}$. Since this value is 30 times larger than the jet mass loss rate found above for the ionized jet, this suggests that at least 96% of the gas in the ^{12}CO outflow is entrained. Multiplying the ionized jet mass loss rate by the velocity v, the momentum rate in the jet was determined to be $1.0 \times 10^{-3}\,M_{\odot}yr^{-1}kms^{-1}$, which is slightly larger than the momentum rates determined by Hasegawa & Mitchell (1995) for both the large and small scale red-shifted ^{12}CO outflows (7.5 and $7.2\times10^{-4}\,M_{\odot}yr^{-1}kms^{-1}$ respectively). Thus the jet itself may have enough momentum to drive the observed larger scale red-shifted outflow.

The ionization mechanism of the jet can be modelled as a plane-parallel shock in a homogeneous neutral 'stellar' wind (e.g. Curiel et al., 1989; Anglada, 1996). In this scenario, a large-scale outflow or wind undergoes a shock which produces the ionized gas. The momentum rate $\dot{P}$ in this large-scale outflow or wind can be expressed as:

$$\left(\frac{\dot{P}}{M_{\odot}\,yr^{-1}\,kms^{-1}}\right) = \frac{3.13\times10^{-4}}{\eta}\left(\frac{S_{\nu}d^2}{mJy\,kpc^2}\right)\left(\frac{v_{\star}}{200\,kms^{-1}}\right)^{0.32} \left(\frac{T}{10^4\,K}\right)^{-0.45}\left(\frac{\nu}{5\,GHz}\right)^{0.1}\left(\frac{\tau}{1-e^{-\tau}}\right) \tag{4.2}$$

where η is the shock efficiency, found to be $\sim$0.1 for low-mass sources, $v_{\star}$ is the initial velocity of the stellar wind or jet, taken to be $500\,kms^{-1}$, and τ is the optical depth of the emitting gas. Here, the flux S_{ν} is measured at 3.6 cm. The optical depth can be determined using equation 6 of Anglada et al. (1998):

$$\alpha = 2 + \frac{\ln\left[(1-e^{-\tau_1})/(1-e^{-\tau_1(\nu_1/\nu_2)^{2.1}})\right]}{\ln(\nu_1/\nu_2)} \tag{4.3}$$

Using the observed fluxes, the optical depth of the emission at 3.6 cm was estimated to be 2.9, giving a value for the required momentum rate in the large-scale outflow or wind of $3.3\times10^{-3}\,M_{\odot}yr^{-1}kms^{-1}$. This is larger than the momentum rates quoted above for the red-shifted outflow (Hasegawa & Mitchell, 1995) by a factor of $\sim 4-5$. If in fact the spectral index is -0.1 so that the emission is optically thin, and the initial velocity of the outflow is instead decreased to $10\,kms^{-1}$, the required momentum rate is $9.5\times10^{-4}\,M_{\odot}yr^{-1}kms^{-1}$, still slightly too large. If, in addition, the shock efficiency were closer to 1, the observed outflow momentum rate would then be sufficient. Therefore, although unlikely, it may be possible

for the 3.6 cm emission to be caused solely by shocks in the outflow.

4.3.1.b VLA 1

Figure 4.7 shows the SED of VLA 1 as green squares. This source was detected in the mid-IR by Marengo et al. (2000), as well as at several radio frequencies, for which the fluxes are listed in Table 4.4. The spectrum of VLA 1 appears to be flat at radio wavelengths, with a fitted spectral index α of 0.00 ± 0.04. The fitted power-law is shown as a dashed line. However, it must be investigated whether only a fraction of the flux of VLA 1 is being recovered at each wavelength. The flux of VLA 1 measured in our A-D array image is not larger than the fluxes measured in the A array only images in previous works (A-D array: 80 mJy, this work; A array only: 82 mJy, 94 mJy, Tofani et al. (1995) and Trinidad et al. (2003) respectively). In fact, there is a small decrease in the flux of VLA 1 for the larger uv-coverage data. Therefore it is likely that most of the flux from VLA 1 has been recovered by observations which are sensitive to scales up to 7", the largest observable angular scale of VLA A array observations at 3.6 cm. This is the case for all of the interferometric fluxes shown for VLA 1, hence the calculated flat spectral index of VLA 1 is not likely to be due to instrumental effects. The observed spectral index is close to that expected from optically thin free-free ionized gas emission ($\alpha = -0.1$). This, together with the roughly circular shape of VLA 1 (with a radius of $\sim$2" or $\sim$2000 AU at 1 kpc), supports the view that it is a UC HII region excited by one or more massive stars. The exciting star(s) of VLA 1 is not seen in either the 2MASS or Gemini North near-IR images. Assuming a single star, the zero-age main sequence (ZAMS) luminosities given in Panagia (1973) and a distance of 1 kpc, the spectral type of the calculated exciting star of VLA 1 (B1) corresponds to a 2MASS K_s band magnitude of 3.1. The detection limit of the 2MASS point source catalog in K_s band is 14.3 mag (Skrutskie et al., 2006), which indicates that there must be more than 11.2 mag of extinction at K_s band for this source to be obscured, corresponding to > 80 mag of extinction in the V band (Cardelli et al., 1989). These high extinctions, in addition to the indentation that VLA 1 has made in the ambient cloud traced by near-IR emission, suggest that VLA 1 lies within the same cloud core as AFGL 2591-VLA 3.

The mid-IR emission from VLA 1 is likely to arise from thermal emission from dust within the HII region. To estimate how much VLA 1 contributes to the total flux of the region, a greybody spectrum with a dust opacity index $\beta = 2$ was fit to the fluxes measured by

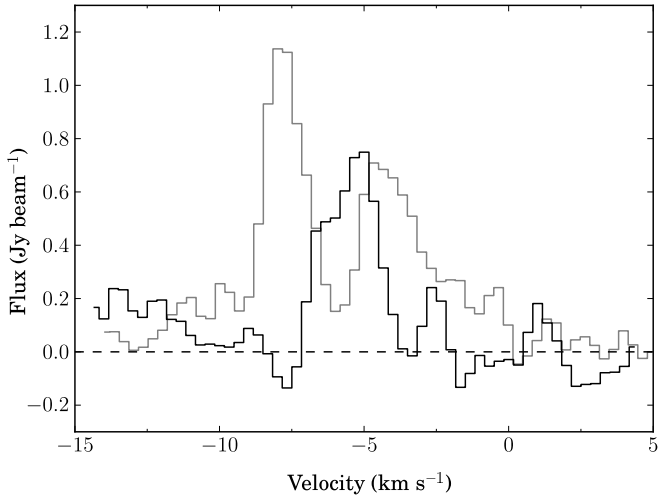

Figure 4.8: $C^{18}O$ (black line) and ^{13}CO (grey line) spectral profiles measured at the position of the central source of AFGL 2591: $20^h29^m24^s.86$ +40°11'19".5 (J2000).

Marengo et al. (2000). The best-fitting greybody has a temperature of 111±14 K and peaks at 26±3.3 μm with a flux of 112 Jy, which is uncertain by a factor of two. Therefore the thermal dust emission from VLA 1 never contributes more than ∼30% to the total flux from the region at wavelengths between 8 and 100 μm and a negligible fraction of the observed flux (< 0.5%) at other wavelengths, and therefore should not significantly affect the SED modelling results given in Section 4.4.4. The mid-IR fluxes for only the resolved central source of AFGL 2591 from Marengo et al. (2000) are plotted on Figure 4.7 (red squares) and agree well with the ISO-SWS data, which were used to cover the mid-IR to far-IR section of the SED.

4.3.2 $C^{18}O$ and 3 mm Continuum

This section details the properties of the dense molecular gas surrounding AFGL 2591 inferred from the $C^{18}O$ molecular line and millimetre continuum observations.

Figure 4.8 presents $C^{18}O$ and ^{13}CO line profiles at the position of the central source of AFGL 2591. The ^{13}CO observations were missing significant flux on extended scales which, in combination with self-absorption effects, is likely to be the cause of the dip in the ^{13}CO line profile seen in Figure 4.8. As there was a significant amount of missing flux in the ^{13}CO line, and the emission was distributed incoherently across the maps, it was not possible to interpret this emission. Therefore the ^{13}CO data will not be discussed further.

Figure 4.9 presents channel maps of the $C^{18}O$ emission towards AFGL 2591 between -9.3 and -3.0 kms^{-1} (where -5.0 kms^{-1} is the rest velocity of the cloud), and Figure 4.10 shows the $C^{18}O$ intensity-weighted first moment map. In both figures, the position of the central source of AFGL 2591 is marked by a cross. In Figure 4.10, the position and size of VLA 1 at 3.6 cm is also shown as a dashed circle. A blue-shifted velocity feature can be seen in Figure 4.10 to the west of the source, which decreases smoothly in velocity away from AFGL 2591-VLA 3, ranging from -5.3 to -8.0 kms^{-1}. This can be seen in the $C^{18}O$ channel maps (Figure 4.9), which also show that the shape of the emission becomes narrower away from the line centre and with distance from the source. This is most obvious in the -7.7 and -8.0 kms^{-1} channels. In addition, Figure 4.10 shows that there is a smaller intensity peak to the south of the central source. Here, the velocity instead decreases from northwest to southeast from approximately -5 to -6 kms^{-1}.

In Figure 4.11, integrated $C^{18}O$ emission in several velocity ranges is compared with the Near-IR Gemini image, and the positions of bow shocks detected in the K band Gemini North image (first noted by Preibisch et al., 2003). The bow shocks are shown approximately as white semi-ellipses, as they are too faint to be seen directly from Figure 4.11. The white dashed line also shows the direction of the ionized jet seen in the 3.6 cm images (Figure 4.4), with P.A. 100°. The contours show several emission features: the high-velocity red and blue-shifted gas (red and blue contours), and the emission in the central channel (white contours). Although the “high"-velocity channels referred to in this Chapter are high velocity relative to the observed line, it should be noted that more extended, higher velocity gas has been detected by Hasegawa & Mitchell (1995) using single dish ^{12}CO observations with 14.3" resolution, which extends in velocity from -45 to 35 kms^{-1}. Therefore, the observations presented here trace the higher density but comparatively lower-velocity gas, within a few kms^{-1} of the line centre.

To minimise confusion due to overlap in velocity of various components, the contours in Figure 4.11 only show integrated $C^{18}O$ emission from -4.0 to -3.3 kms^{-1} (red), -8.0 to -7.0 kms^{-1} (blue), and at -5.0 kms^{-1} (white). Firstly, it can been seen that the position of the blue contours in Figure 4.11 suggests that this emission is from the inner part of the blue-shifted outflow lobe of AFGL 2591. Further, both the red-shifted and blue-shifted contours are coincident with H_2 emission detected by Tamura & Yamashita (1992) (their peaks A and B respectively), suggesting that both the red and blue-shifted gas shown in Figure 4.11 are

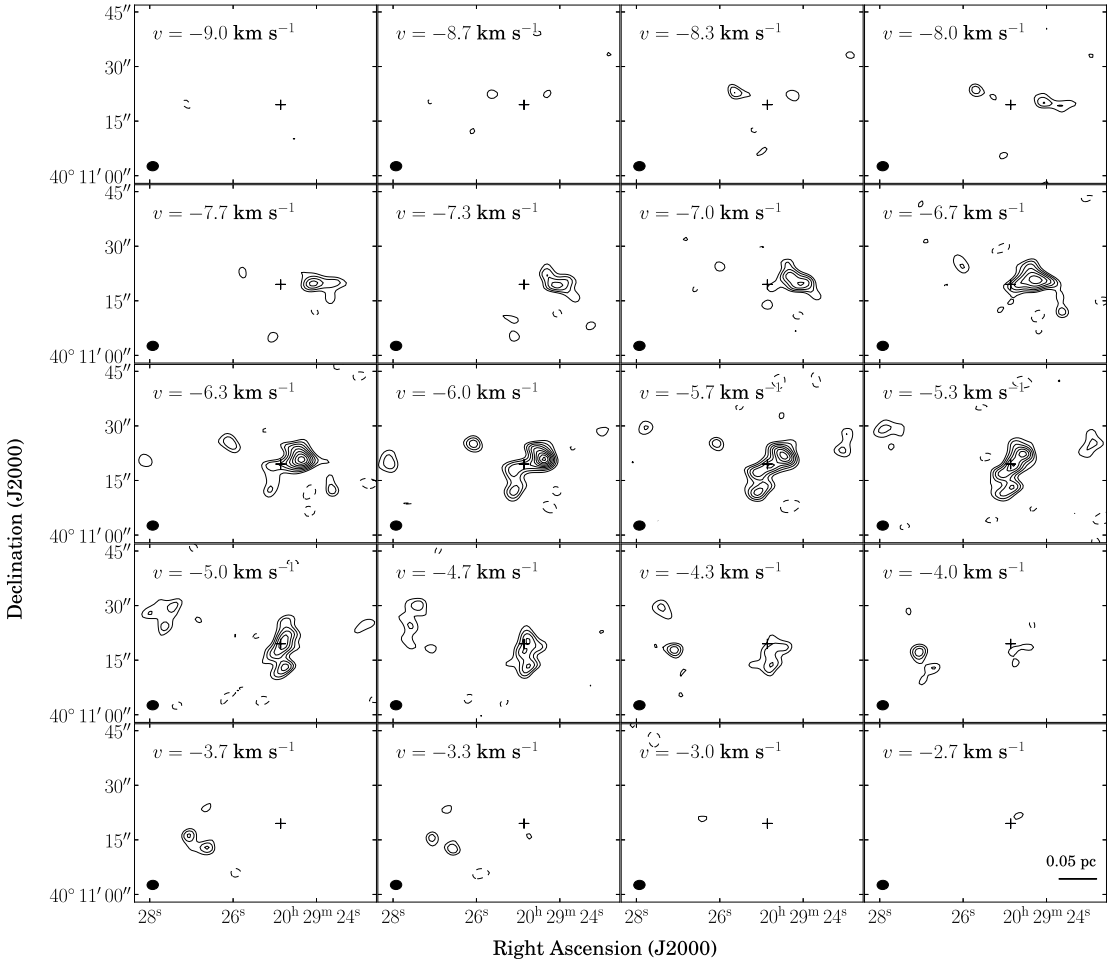

Figure 4.9: $C^{18}O$ channel map at 0.3 kms^{-1} resolution between -9.0 and -2.7 kms^{-1}. The rms in the map is σ=0.1 Jy $beam^{-1}$. The map peak flux is 1.1 Jy $beam^{-1}$. Contours are at -3, 3, 4, 5, 6, 7, 8, 9, 10, 11 $\times\sigma$. The synthesised beam is shown the bottom left-hand corner (4.5 × 3.6", P.A. 93°). A scale size of 0.05 pc is represented by a bar in the bottom right-hand panel. The cross shows the position of the central source of AFGL 2591 from the Gemini near-IR J band image. The rest velocity of the cloud is -5 kms^{-1}.

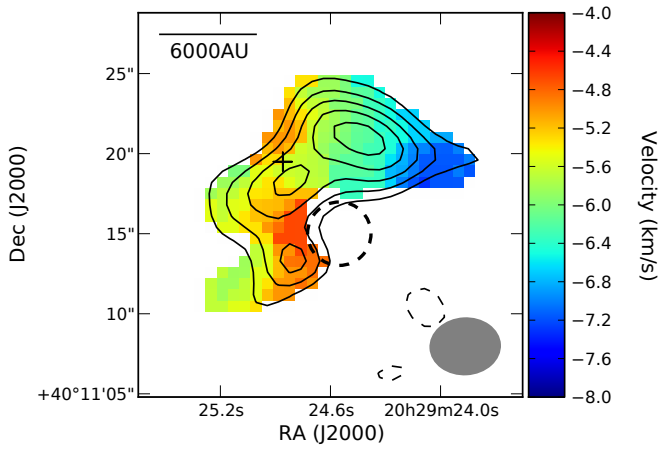

Figure 4.10: Shown in colour-scale: intensity-weighted first moment map of the $C^{18}O$ emission towards AFGL 2591. The corresponding velocities are shown on the colour-bar on the right. The cross indicates the position of the central source of AFGL 2591 from the Gemini near-IR J band image. A scale size of 6000 AU is represented by a bar in the upper left-hand corner. The dashed circle represents the position and size of VLA 1 at 3.6 cm. Shown in contours: the $C^{18}O$ integrated intensity map from -2.3 to -8.7 kms^{-1}. The peak flux of the integrated intensity map is 2.5 $Jy\,beam^{-1}\,kms^{-1}$. Contours are at -3, 3, 4, 5, 6, 7, 8 $\times\,\sigma$=0.33 $Jy\,beam^{-1}\,kms^{-1}$. The synthesised beam is shown in the lower right-hand corner (4.5 × 3.6", P.A. 93°). The rest velocity of the cloud is -5 kms^{-1}.

associated with shocked gas, likely due to a jet or wind interacting with the ambient cloud material. For the red-shifted emission, this is supported by the extrapolated direction of the ionized jet observed at 3.6 cm, which points directly through the red-shifted $C^{18}O$ contours to the bow-shocks. Hence this outlines a coherent picture in which the red-shifted outflow lobe of AFGL 2591 consists of a small-scale 1200 AU ionized jet that is part of a jet or wind extending out to ∼0.2 pc where the flow terminates against the surrounding cloud as bow-shocks. However it is interesting to note that the position angle of the jet and bow shocks do not exactly align with that of the blue-shifted reflection nebula or the elongation of the blue-shifted outflow observed by Hasegawa & Mitchell (1995). Therefore other stars in the vicinity, such as the powering star(s) of VLA 1, may be causing precession of the jet.

There is a clear Hubble law velocity trend that can be seen across the blue-shifted emission west of the central source in Figure 4.10. In addition, the emission is more collimated at more negative velocities, seen in Figure 4.9. If the blue-shifted $C^{18}O$ emission is also created by accelerated ambient cloud material, then this suggests that there is a high-velocity collimated component at the centre and front of this inner blue-shifted flow, which smoothly transitions into a surrounding lower-velocity wide-angle wind. Assuming that the observed blue-shifted $C^{18}O$ emission is the inner part of the entrained large-scale blue-shifted out-

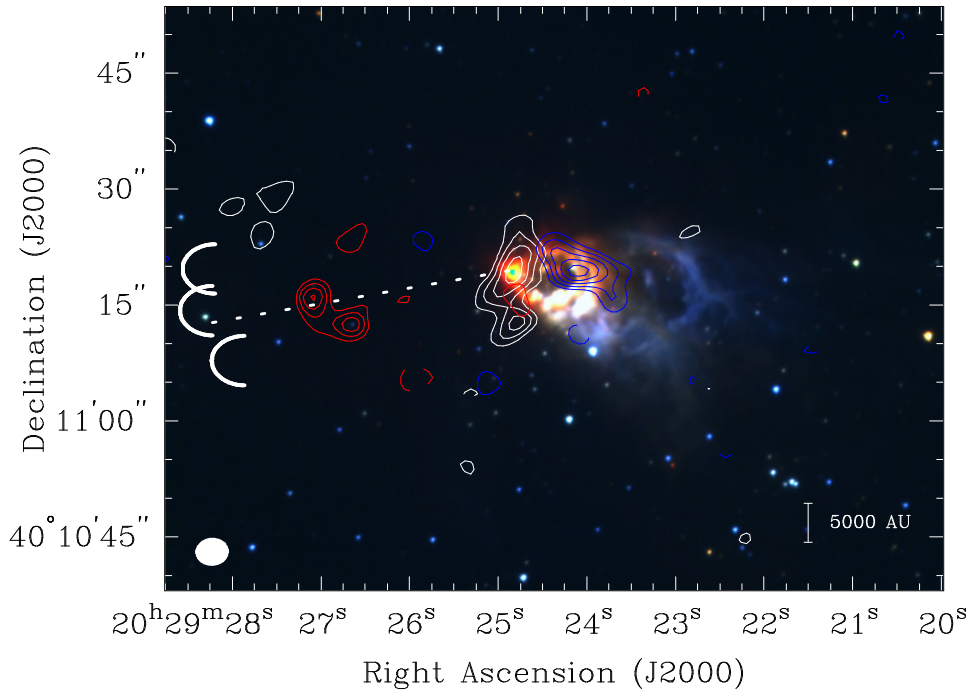

Figure 4.11: Gemini North three-colour JHK image of AFGL 2591 overlaid with contours of $C^{18}O$ emission integrated over -4.0 to -3.3 kms^{-1} (red), -8.0 to -7.0 kms^{-1} (blue), and at -5.0 kms^{-1} (white). The three arcs in the east of the image show the positions of bow shocks visible in the Gemini North image, but which are too faint to be seen directly in the Figure. The dashed line shows the direction of the ionized jet observed at 3.6 cm (P.A. 100°). Red-shifted contours are -3,3,4,5,6 × 0.08 Jy $beam^{-1}$ kms^{-1}, blue-shifted contours are -3,3,4,5,6,7 × 0.11 Jy $beam^{-1}$ kms^{-1}, and white contours are -3,3,4,5,6 × 0.04 Jy $beam^{-1}$ kms^{-1}. The synthesised beam is shown in the lower left-hand corner (4.5 × 3.6", P.A. 93°).

flow of AFGL 2591, the outflow properties were calculated, and are given in Table 4.5. The blue-shifted outflow mass was found assuming the gas was optically thin,

$$M_{\rm outflow} = 2.75 \times 10^{-5} \left[\frac{^{12}{\rm CO}}{{\rm C}^{18}{\rm O}}\right] \frac{(T + 0.882)}{e^{-5.27/T}}\, d^2 \int S_\nu \, d\nu \; ({\rm M}_\odot) \tag{4.4}$$

where $\left[\frac{^{12}{\rm CO}}{{\rm C}^{18}{\rm O}}\right]$ is the abundance ratio of ^{12}CO to C^{18}O, T is the temperature of the gas assuming local thermodynamic equilibrium, d is the distance to the source in kpc, and $\int S_\nu \, d\nu$ is the integral of the flux over the velocities of the blue-shifted emission. The flux in each channel was found by integrating the emission within an irregular aperture around only the blue-shifted outflow emission (i.e. not including emission from the resolved peak to the south of the central position of AFGL 2591). The abundance ratio $\left[^{12}{\rm CO}/{\rm C}^{18}{\rm O}\right]$ was calculated using the results given in Wilson & Rood (1994), where $D_{_{GC}}$ is the galactocentric distance in kpc,

$$\left[\frac{^{12}{\rm CO}}{{\rm C}^{18}{\rm O}}\right] = (58.8 \pm 11.8) D_{_{GC}} + (37.1 \pm 82.6), \tag{4.5}$$

giving a value of $\left[\frac{^{12}{\rm CO}}{{\rm C}^{18}{\rm O}}\right] = 478$ for AFGL 2591 for a galactocentric distance of 7.5 kpc.

It should be noted that the shape of the C^{18}O line profile, which is slightly asymmetric, may be showing the presence of outflow emission, or is instead indicating that this line is partially optically thick. In the latter case, the estimates of the outflow properties depending on the derived mass in Table 4.5 will be lower limits. In addition, as the C^{18}O emission only traces the densest inner parts of the flow, it only represents a small fraction of the mass and momentum from the entire large-scale outflow.

To find the momentum $M_{\rm outflow} V$ and kinetic energy $\frac{1}{2} M_{\rm outflow} V^2$ in the flow, the final term of equation 4.4 was replaced by $\int S_\nu (\nu - \nu_{_{\rm LSR}})/\sin i \; d\nu$ or $\frac{1}{2}\int S_\nu ((\nu - \nu_{_{\rm LSR}})/\sin i)^2 \; d\nu$ respectively, where ν is the velocity of each channel, $\nu_{_{\rm LSR}} = -5\,{\rm kms}^{-1}$ is the rest velocity of the cloud, and i is the inclination of the flow relative to the line of sight, taken to be 45° from the results of the SED modelling presented in Section 4.4.4.

The average velocity of the flow was calculated as the momentum over the mass in the flow: $\langle V \rangle = M_{\rm outflow} V / M_{\rm outflow}$, and the projected length of the flow was measured as the distance from the central source of AFGL 2591 to the furthest 3 σ contour from the source in

Table 4.5: Derived properties of the inner part of the blue-shifted outflow traced by the $C^{18}O$ emission

Parameter	Value
Velocity range (kms^{-1})	-8 to -5.3
Outflow length, l (AU)	22,600
Outflow mass, $M_{outflow}$ ($M_\odot$)	12.3
Outflow momentum, $M_{outflow}V$ ($M_\odot$ kms^{-1})	28.6
Outflow energy, $1/2\,M_{outflow}V^2$ ($M_\odot$ km^2s^{-2})	41.5
Outflow energy, $1/2\,M_{outflow}V^2$ (ergs)	8.3×10^{44}
Average velocity relative to v_{LSR}, $\langle V \rangle$ (kms^{-1})	-2.3
Dynamical timescale, t_{dyn} (yr)	4.6×10^4

the blue-shifted emission shown in Figure 4.11, which was found to be ∼16" or 16,000 AU at 1 kpc. Therefore the actual length of the flow l was calculated as $l = l_{proj}/\sin i$. The dynamical timescale of the flow was determined using the equation $t_{dyn} = l/\langle V \rangle$, however it should be noted that, as with any outflow, this value may not be an exact measure of the time taken to displace the gas, as the gas may have been set in motion at some distance from the central source. In addition, this assumes a constant outflow velocity, but the gas is observed to be accelerating away from the source. Nevertheless, this provides a characteristic timescale, which can be compared to other studies.

The -5 kms^{-1} central channel of the $C^{18}O$ emission shown in white contours in Figure 4.11 contains two emission peaks. The first is centred on AFGL 2591-VLA 3 and is elongated roughly perpendicular to the conical reflection nebula and blue-shifted $C^{18}O$ emission, with a length of ∼12" (12,000 AU) and a position angle of ∼150°. This emission is likely to be from a flattened envelope surrounding the massive (proto)star. Using observations of CS line emission, Yamashita et al. (1987) also found a large envelope elongated in the N-S direction towards AFGL 2591, with an extent of 80"×50", corresponding to a radius of 40,000 AU at 1 kpc, and a mass of 1000 $M_\odot$. This object was also observed to have a small velocity gradient across it in the N-S direction (0.4 kms^{-1} pc^{-1}). Figure 4.10 however does not show any velocity gradients in the $C^{18}O$ emission along a P.A. of ∼150°, yet there is a large amount of contamination from the outflow emission and from the peak to the south of the central source. Assuming that a velocity gradient due to rotation would be observable as a gradient in velocity across at least three channels (>1 kms^{-1}) along the axis of this flattened object, any rotation must be slower than 1 $kms^{-1}/\sin i$ at a radius of ∼6000 AU. Taking the inclination i to be 45° and assuming Keplerian rotation, an upper limit for the central mass of ∼14 $M_\odot$ was derived (if the rotation was instead not Keplerian, but influenced by accreting disk material within ∼6000 AU, the inferred central mass would be smaller). This

is consistent with high resolution observations of water and sulphur lines in the inner several hundred AU of AFGL 2591 (van der Tak et al., 2006), which show a velocity gradient of 4.6 kms^{-1} over a diameter of 0.3" or 300 AU. Assuming Keplerian rotation, these results imply a mass for the central object of $\sim 9\,\mathrm{M}_{\odot}$.

The secondary peak in the white contours shown in Figure 4.11 can also be seen in Figure 4.10, which shows a velocity gradient across it in roughly the NW-SE direction. There are no sources at this position in any of the images, limiting the possibility that this emission is from an outflow of a nearby object. Instead the velocity of the emission appears to decrease radially away from VLA 1, which is marked as a dashed circle in Figure 4.10. Indeed, Figure 4.6 indicates that VLA 1 is preferentially expanding towards the southeast, into possibly lower density gas. Hence the origin of this velocity gradient in Figure 4.10 may be due to the expansion of the gas around VLA 1 towards the observer, with a projected velocity of $\sim 1\,\mathrm{kms}^{-1}$ relative to the ambient cloud. Further, it is interesting to note that the lack of $\mathrm{C}^{18}\mathrm{O}$ emission at the position of VLA 1 again suggests that VLA 1 is at the same distance as AFGL 2591-VLA 3. The lack of $\mathrm{C}^{18}\mathrm{O}$ emission towards VLA 1 could be due to the fact it has swept-up the molecular cloud material around it, or the molecular gas has been dissociated by the high temperatures ($\sim 10^4$ K) in the HII region.

Figure 4.12 shows the continuum emission from the region at 106.7 and 110.5 GHz, in both of the wide 3 mm continuum bands observed. The morphology of the emission is similar to that seen in the millimetre continuum maps at various wavelengths presented by van der Tak et al. (1999) and van der Tak et al. (2006). The peak positions of VLA 1 to 3 are shown as crosses. The main two sources that are detected are VLA 1 and VLA 3, but there also is extended emission towards the position of VLA 2. Although the large uncertainties in the two measured 3 mm fluxes do not allow calculation of accurate spectral indices for VLA 1 and 2 using these values alone, the difference in the spectral index of the two sources can be seen from the difference in their relative brightnesses between the two images. The sources were fit with 2D Gaussians using the CASA task imfit to find the fluxes, which are given in Table 4.4.

However, the millimetre image appears to be systematically offset from the 3.6 cm peak positions (∼1.5" to the west), which may be due to an offset in the pointing of the millimetre observations. It is not possible to determine whether this offset is also present in the

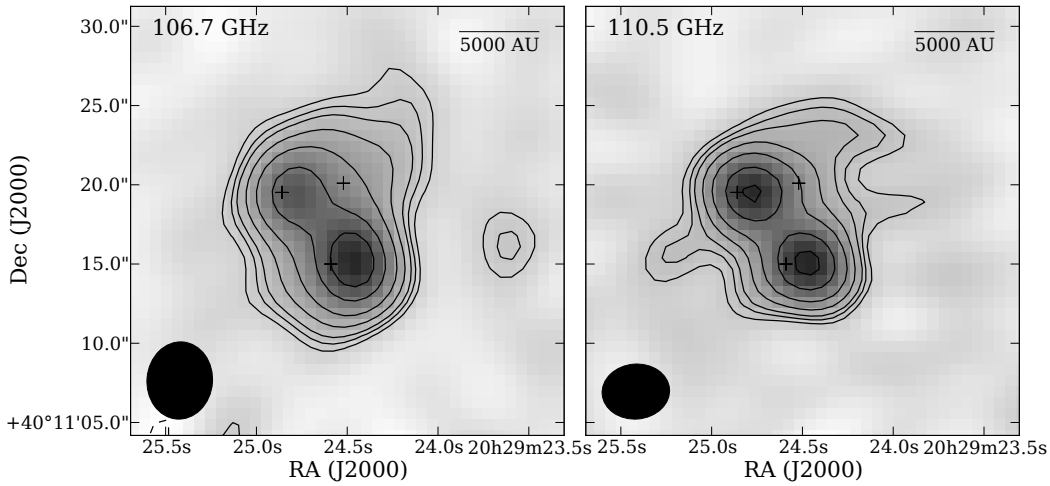

Figure 4.12: Continuum emission towards AFGL 2591 at 106.7 and 110.5 GHz (∼2.8 and 2.7 mm respectively), shown in both contours and greyscale. The rms noise in the images is σ =2.2 and 2.1 mJy beam^{-1} respectively. The greyscales extend from $-3\times\sigma$ to 65.5 and 54.0 mJy beam^{-1}. Contours are at $-3, 3, 4, 5, 7, 10, 15$ and $20\times\sigma$. The crosses show shows the positions of VLA 1 to 3. The synthesised beams are 4.9×4.1" P.A.= −4.8° and 4.3×3.5" P.A.= 94.7° respectively.

$C^{18}O$ maps, nevertheless, such an offset would change the above results minimally. In all cases, the positional coincidences mentioned would still hold. Another minimal change in the results due to this offset is that the projected length of the blue-shifted inner flow would be 1.5" shorter, giving a projected length of 14,500 AU instead of 16,000 AU (corresponding to deprojected lengths of 20,500 and 22,600 AU respectively) and hence decreasing the calculated dynamical timescale by ∼10%.

4.4 SED and Near-IR Image Modelling

4.4.1 2-D Radiation Transfer Dust Code

The SED of AFGL 2591 was modelled between near-IR and sub-mm wavelengths using the same 2D Monte Carlo dust radiation transfer code and genetic search algorithm used to model IRAS 20126+4104 in Chapter 3. The model set-up, and the details of the genetic search algorithm are given in Sections 3.2 and 3.3.3 of that Chapter respectively. Several small alterations to the model set-up are described below.

The fraction of the stellar surface covered with accretion spots was assumed to be 5%, as opposed to the entire stellar surface, in keeping with observations of T Tauri stars (Calvet & Gullbring, 1998). The spot emission was randomly distributed over the surface of the star

to provide the spot coverage $f_{\rm spot}$. The effective temperature of the accretion spots due to accretion is then:

$$T_{\star,\rm acc} = T_\star \left(\frac{f_{\rm spot} L_\star + L_{\rm heat}}{f_{\rm spot} L_\star} \right)^{1/4}, \tag{4.6}$$

where $L_\star$ is the luminosity of the star, and $L_{\rm heat}$ is the luminosity due to heating via accretion shocks. Therefore, most of the star has a temperature of $T_\star$, while only the spots have the temperature $T_{\star,\rm acc}$. Hence, the effective temperature of the star $T_{\rm eff}$ used to calculate the dust sublimation radius $R_{\rm sub}$ is

$$T_{\rm eff} = [(1 - f_{\rm spot}) T_\star^4 + f_{\rm spot} T_{\star,acc}^4]^{1/4}. \tag{4.7}$$

However, it was found that, as the source was deeply embedded, the emergent SED changed minimally at wavelengths longer than 1 μm compared to the case with $f_{\rm spot} = 1$ (as was used for IRAS 20126+4014).

In addition, as it was found that the luminosity from X-rays could not be ignored in the code for embedded sources (see Chapter 3), the luminosity from the shock which goes into X-rays was added. This luminosity is half of that liberated by accretion shocks on the star, the other half of which goes into heating the stellar surface, given by $L_{\rm heat}$. Therefore $L_{\rm x-ray} = L_{\rm heat}$. This X-ray emission was added to the code as photons sampled uniformly in energy between 15 and 60 nm.

For the genetic code, the size of the first generation N was set to 500, and the size of subsequent generations M was set to be 100. These values were increased compared to those used in Chapter 3, because the code was run on an 80 core cluster, and therefore to maximize their use, each generation had to contain > 80 models. The code was taken to be converged when the χ^2 value of the best fitting model decreased less than 5% in 15 generations.

4.4.2 Input Assumptions: Model Parameters

A set of plausible ranges for parameters describing the model, in which the genetic algorithm searched for the best fit, is given in Table 4.6. Ranges for the first six parameters - stellar mass, envelope outer radius, cavity half-opening angle, inclination, disk mass and disk radius - were chosen to accommodate results from the literature, specifically Yamashita et al. (1987); Minchin et al. (1991); van der Tak et al. (1999); Trinidad et al. (2003); Preibisch

et al. (2003); Hutawarakorn & Cohen (2005) and van der Tak & Menten (2005). The following three parameters in Table 4.6 - the envelope and disk accretion rates and cavity ambient density - were given large but physically plausible ranges.

The final two parameters, the stellar radius and temperature, were determined from the sampled stellar mass for that model in a similar manner to that outlined in Chapter 3, using the $\dot{M} \propto M^2$ evolutionary track presented in Figure 1 of Keto & Wood (2006). The stellar temperature $T_\star$ and the calculated stellar surface gravity were then used to select a model from the stellar atmosphere grid of Castelli & Kurucz (2004), or to calculate a blackbody spectrum for stars hotter than 50,000 K.

4.4.3 Model Fitting

As part of the genetic algorithm used here and described in Chapter 3, the models were fit to the data using the fitting tool of Robitaille et al. (2007), where A_V, the external extinction, was a free parameter in the fit. The distance was set to be 1 kpc, in keeping with the adopted distance to AFGL 2591, and the extinction A_V was allowed to vary between 0 and 40 magnitudes.

The errors on each data point were not modified, however each data point was weighted by the distance in wavelength between its two adjacent data points. This was done to allow the algorithm to search for a model which reproduced the shape of the entire SED, not only the sections with a high density of data.

The models were also simultaneously fit to the six flux profiles shown in Figure 4.3, measured from the 2MASS images. The model flux profiles were found in the same way as the observed profiles, by summing the flux in the model images within 24.6 and 104" wide strips aligned with and perpendicular to the outflow axis, and normalising them to the total flux. To produce the convolved model J,H and K_s band images, the model images were convolved with the FWHM of the 2MASS point-spread functions (PSF) for each band: 3.15", 3.23" and 3.42" for J, H and K_s bands respectively, which were determined by fitting Gaussian PSFs to stars in the observed images. The model images shown in Figure 4.2 are high signal-to-noise versions of the 1 million photon images used for fitting, produced by 10 million photon runs of the best-fitting models.

As in Chapter 3, the combined reduced χ^2 for each model given as input to the genetic

Table 4.6: Assumed ranges for model parameters as input to genetic search algorithm.

Parameter	Description	Value/Range	Sampling
$M_\star$	Stellar mass ($M_\odot$)	2 – 40	logarithmic
$R_{\rm env}^{\rm max}$	Envelope outer radius (AU)	10,000 – 200,000	logarithmic
$\theta_{\rm cav}$	Cavity half-opening angle at 10^4 AU (degrees)	10 – 40	linear
i	Inclination w. r. t. the line of sight (degrees)	20 – 70	linear
$M_{\rm disk}$	Disk mass ($M_\odot$)	0.1 – 20	logarithmic
$R_{\rm disk}$	Disk or centrifugal radius (AU)	100 – 50,000	logarithmic
$\dot{M}_{\rm disk}$	Disk accretion rate ($M_\odot$ yr^{-1})	10^{-7} – 10^{-3}	logarithmic
$\dot{M}_{\rm env}$	Envelope accretion rate ($M_\odot$ yr^{-1})	10^{-7} – 10^{-3}	logarithmic
$\rho_{\rm cav}$	Cavity ambient density (g cm^{-3})	10^{-21} – 10^{-16}	logarithmic
$R_\star$	Stellar radius	Determined from stellar mass	
$T_\star$	Stellar temperature	Determined from stellar mass	

algorithm was calculated as

$$\chi^2_{\rm combined} = \chi^2_{\rm SED} + \chi^2_{\rm profiles} \tag{4.8}$$

where $\chi^2_{\rm SED}$ is the best-fitting reduced χ^2 value for the SED alone, and $\chi^2_{\rm profiles}$ is the overall reduced χ^2 for the profile fits.

4.4.4 Results of SED and Image Modelling

The genetic code was run twice - firstly with the model parameter ranges given in Table 4.6 as input for all parameters, which will be referred to as the 'envelope plus disk' model, and secondly with the parameter ranges given in Table 4.6 for all parameters except the disk mass and disk accretion rate, $M_{\rm disk}$ and $\dot{M}_{\rm disk}$, which were set to zero and were therefore not treated as model parameters. This second run will be referred to as the 'envelope without disk' model. The envelope without disk model was run to ascertain whether the SED and images could be adequately produced without a disk, i.e. a simpler model which had two fewer parameters. For the envelope without disk model, $R_{\rm disk}$ will instead be referred to as the centrifugal radius of the envelope, $R_{\rm c}$, as these two parameters are interchangeable in the models.

The genetic search algorithm codes were stopped after 31 and 38 generations for the envelope plus disk and without disk models respectively, when the convergence criteria were reached. This corresponds to 3500 models or 7080 CPU hours for the envelope plus disk model, and 4200 models or 685 CPU hours for the envelope without disk model, which on average took a shorter time to run each model.

The resulting SEDs and profiles of these models are shown against the data in Figures 4.1 and 4.3, and the model images are compared to the observed images in Figure 4.2. The parameters of the best-fitting models are also given in Table 4.7, along with estimates of

Table 4.7: Parameters of the genetic algorithm best-fitting models

Parameter	Description	Value for envelope † plus disk model	Value for envelope † without disk model
$M_\star$	Stellar mass ($M_\odot$)	$6.5^{+0.9}_{-1.1}$	15^{+1}_{-0}
$R_{\rm env}^{\rm max}$	Envelope outer radius (AU)	$89{,}000^{+65{,}000}_{-37{,}000}$◇	$150{,}000^{+44{,}000}_{-59{,}000}$◇
$\theta_{\rm cav}$	Cavity half-opening angle at 10^4 AU (degrees)	28±3	11±1
i	Inclination w. r. t. the line of sight (degrees)	45^{+1}_{-2}	28±2
$M_{\rm disk}$	Disk mass ($M_\odot$)	14^{+6}_{-12}	...
$R_{\rm disk}$ or $R_{\rm c}$	Disk or centrifugal radius (AU)	270^{+180}_{-140}	$1400^{+43{,}000}_{-1300}$
$\dot{M}_{\rm disk}$	Disk accretion rate ($M_\odot$ yr^{-1})	$3.8\ ^{+0.2}_{-0.3} \times 10^{-4}$	...
$\dot{M}_{\rm env}$	Envelope accretion rate ($M_\odot$ yr^{-1})	$1.8\ ^{+0.1}_{-0.2} \times 10^{-4}$	$1.8 \pm 0.2 \times 10^{-4}$
$\rho_{\rm cav}$	Cavity ambient density (g cm^{-3})	$4.2\ ^{+3.9}_{-4.1} \times 10^{-20}$	$1.9\ ^{+3.6}_{-1.8} \times 10^{-20}$
$R_\star$	Stellar radius ($R_\odot$)	3.1	5.0
$T_\star$	Stellar temperature (K)	20,000	31,000

† The uncertainties shown are not formal errors, but instead the values for models with a $\Delta\chi^2 = (\chi^2 - \chi^2_{\rm best}) < 3$, which provide an indication of how well each parameter is constrained (see text).
◇ The values for the envelope outer radius should be viewed as lower limits (see text).

their uncertainties (which are not formal errors, see below). It should be noted that the envelope outer radii given in Table 4.7 are in actuality lower limits, due to the same effects as discussed in Section 3.4.1. The minimum reduced χ^2 for the best-fitting envelope plus disk model is 17.2, and the corresponding value for the best-fitting without disk model is 28.2. Therefore the model with a disk provides a better fit to the SED and profiles.

Comparing the model SEDs to the data shown in Figure 4.1, it can be seen that the model SEDs are very similar. The main difference between these is in the mid-IR regime, where the without disk model significantly overestimates the flux. However, it is interesting to note that although the emergent SEDs are similar, some of the physical parameters for the two models are very different, as can be seen in Table 4.7. For instance, for the without disk model, the central stellar mass is 15 $M_\odot$, however for the envelope plus disk model the central mass is 6.5 $M_\odot$. Here a large portion of the luminosity is instead being provided by accretion luminosity in the disk and in accretion shocks, allowing the stellar luminosity to be much less. Therefore an important result, although possibly not expected, is that the SED of AFGL 2591 can be fitted better by a B4 star with a high disk accretion rate. In fact, the accretion rate of the best-fitting envelope plus disk model is $3.8\times10^{-4}\,M_\odot$ yr^{-1}, almost twice that of the determined envelope accretion rate. Hence if AFGL 2591 is an intermediate to high-mass star, it must be undergoing an active accretion phase, and may be an example of an FU Orionis object. As an outflow and small scale ionized jet are observed towards AFGL 2591, which are thought to be sign posts of accretion, it seems likely that the

luminosity of AFGL 2591 is partially provided by accretion luminosity, and therefore is less massive than the 15 $M_\odot$ suggested by the without disk model.

In addition, both the inclination and cavity half-opening angle for the envelope plus disk model are higher than that found for the without disk model. The lower inclination is required by the model without a disk to reproduce the shape of the SED at near to mid-IR wavelengths, and the lower half-opening angle is required to produce a deep silicate feature at 10 μm. If the cavity half-opening angle is too large, the observer looks down the cavity instead of through the envelope, and the depth of the silicate feature is reduced. In the case of the envelope plus disk model however, more flux is provided by accretion in the disk at 1-10 μm, shortward of the silicate feature, and hence it can have a combination of inclination and cavity half-opening angle which better-reproduces the observed 2MASS images (see Figure 4.2). Although the model image profiles in Figure 4.3 provide a similar quality of fit to the data, the without disk model in red produces a profile perpendicular to the outflow axis which is too narrow and centrally peaked in comparison to the profile which was observed.

Although the best-fitting models differ in several regards, they find the same envelope accretion rate (1.8×10^{-4} $M_\odot$ yr^{-1}) and similar cavity ambient densities. For the envelope accretion rate, the far-IR and sub-mm fluxes determine the mass of the envelope and hence the envelope accretion rate, and therefore depend on the colder material in the outer regions of the envelope, and not on the presence of a disk.

To understand how well the parameters of AFGL 2591 were determined, the reduced χ^2-values of all the models run were plotted against each parameter for $\chi^2 < 200$, shown in Figures 4.13 and 4.14. As the first generation of the genetic code was sampled uniformly throughout the chosen ranges, it was therefore possible to adequately sample parameter space and recover an approximation of the minimum χ^2 surface. Therefore, in addition, the solid lines in Figures 4.13 and 4.14 also show histograms of the minimum χ^2 model in each bin.

For the envelope plus disk model, Figure 4.13 shows that the parameters best determined within the chosen ranges are the stellar mass, envelope accretion rate, inclination and cavity ambient density. The envelope outer radius and disk radius appear to be biased to higher and lower values respectively. Also, the cavity half-opening angle has a wide minimum centred on 25-30°. The disk accretion rate has a flat χ^2 surface except between 10^{-4} and 10^{-3} $M_\odot$ yr^{-1},

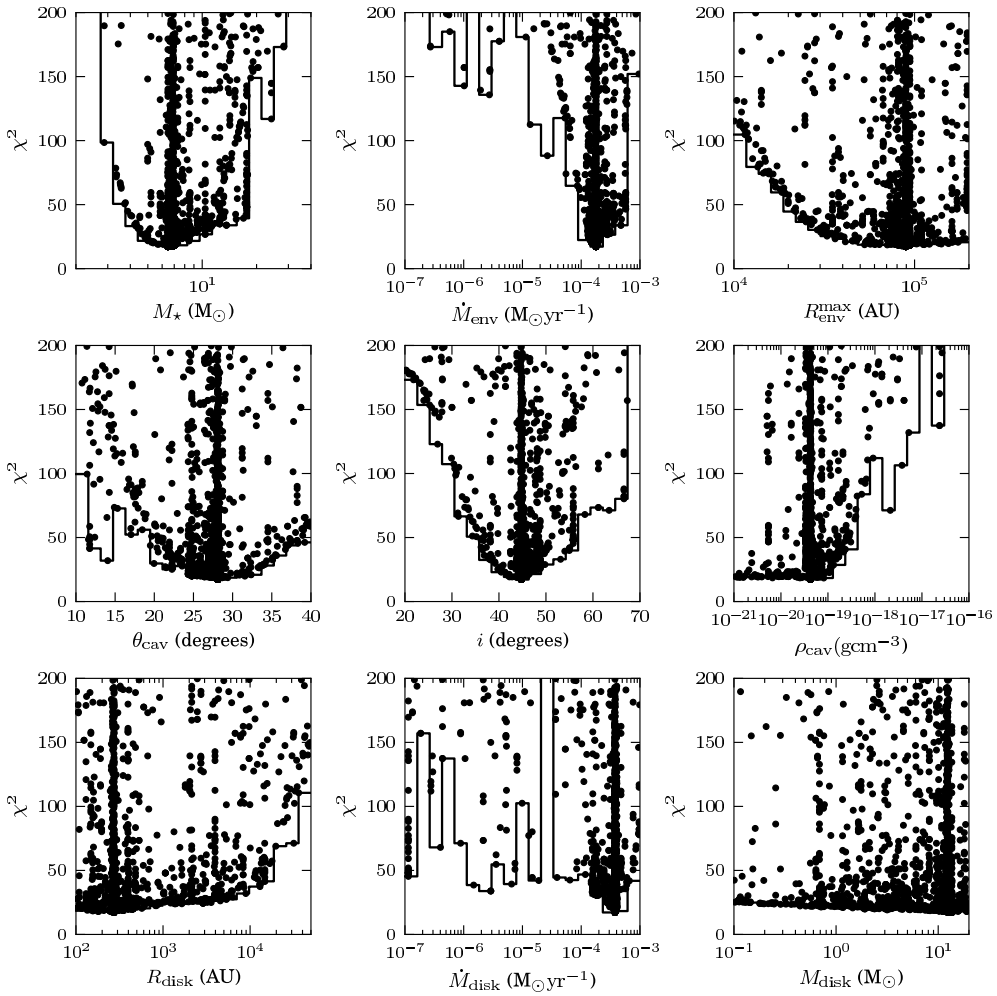

Figure 4.13: Plots of the χ^2-value for models with reduced $\chi^2 < 200$ against the nine varied model parameters for the envelope plus disk model. The solid line shows a histogram of the minimum χ^2-value in each bin, which provides a rough outline of the minimum χ^2 surface.

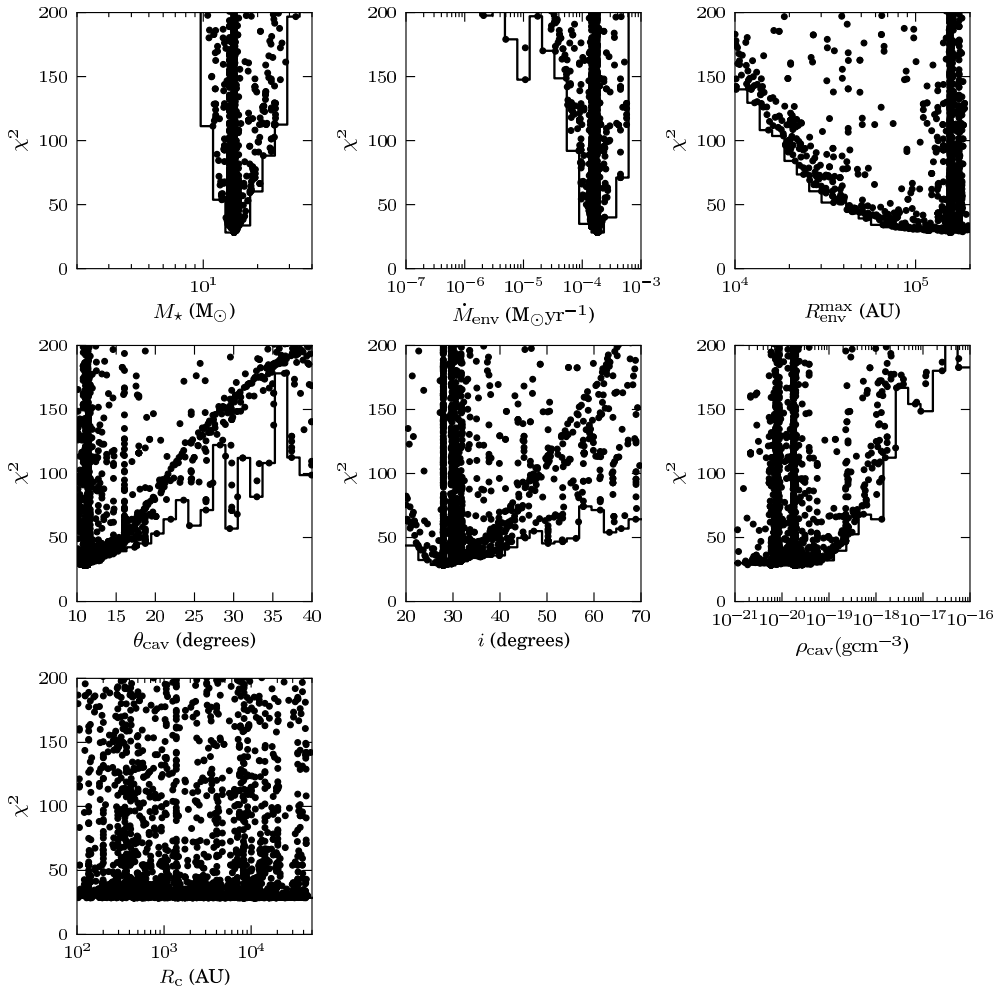

Figure 4.14: Plots of the χ^2-value for models with reduced $\chi^2 < 200$ against the seven varied model parameters for the envelope without disk model. The solid line shows a histogram of the minimum χ^2-value in each bin, which provides a rough outline of the minimum χ^2 surface.

where there is a sharp trough. The disk mass is the least constrained parameter, being slightly biased to higher values, hence the best fitting disk mass of 14 $M_\odot$ given in Table 4.7 is highly uncertain.

For the envelope without disk model, Figure 4.14 shows that the stellar mass and envelope accretion rate are very well determined, having steep minima. The envelope outer radius and cavity ambient density are constrained similarly to the envelope with disk model, however the inclination and cavity half-opening angle both have better fits towards lower values, as mentioned above. Finally, the centrifugal radius of the envelope is completely unconstrained by the data, and hence its best fitting value (1400 AU) should be taken with caution.

Although an estimate of the formal 1-sigma uncertainties can be found using the parameter values corresponding to a non-reduced delta chi-squared value of $\Delta\chi^2 = (\chi^2 - \chi^2_{\rm best}) = 1$, when calculated for the χ^2 surfaces shown in Figures 4.13 and 4.14, these values were found to be unrealistically small, and usually did not encompass more than the best fitting model (due to the coarse sampling of the models in parameter space). However, it is very unlikely that the models exactly reproduce the real geometry of AFGL 2591, which in reality is not axisymmetric or completely smooth in density. In addition, many YSOs are found to be variable, which is not included in the photometric errors. Therefore, as it is likely the parameters are actually more uncertain than given by formal errors, the parameter values for models with a *reduced* $\Delta\chi^2 = (\chi^2 - \chi^2_{\rm best}) < 3$ were used to indicate how uncertain each parameter was, and are given in Table 4.7. It was possible to quantify the uncertainties in this manner because the original pool of models in the genetic code contained 500 models instead of the 100 used in Chapter 3, where the sampling was still too coarse to determine accurately the $\Delta\chi^2 = 3$ parameter values.

In conclusion, the envelope plus disk model appears to reproduce the SED, profiles and images of AFGL 2591 more accurately than the without disk model. This model gives a best-fit mass for the central object of 6.5 $M_\odot$, which is much smaller than previous estimates which did not account for accretion luminosity (e.g. van der Tak & Menten, 2005, 16 $M_\odot$). Thus if this model is correct, AFGL 2591 is less massive than previously thought, being on the borderline of what is considered to be a massive star, with a spectral type of B4. Therefore, when required, the parameters for the envelope with disk model have been assumed

throughout the other Sections in this Chapter.

Comparing the results from modelling AFGL 2591 and IRAS 20126+4104 from Chapter 3, it can be seen that IRAS 20126+4104 has a much higher central stellar mass: 13 $M_\odot$ compared to 6.5 $M_\odot$. In addition, comparing the properties of their outflow cavities, it can be seen that the half-opening angles are almost equal, with values just below 30°, however the ambient density in the cavity is more than 10 times larger for IRAS 20126+4104. The disk properties for both sources are very different; while AFGL 2591 has a best-fitting disk radius of 270 AU, more than 10 times smaller than the 9200 AU best fitting disk radius of IRAS 20126+4104, its disk mass is more than twice as large: 14 $M_\odot$ compared to 5.9 $M_\odot$. Therefore AFGL 2591 has a dense, small disk and IRAS 20126+4104 a extended diffuse one. The envelope accretion rates are similar for both sources, with values of 1.8×10^{-4} and 3.9×10^{-4} $M_\odot$ yr^{-1} for AFGL 2591 and IRAS 20126+4104 respectively, however while AFGL 2591 has a similar and therefore high disk accretion rate, IRAS 20126+4104 has a disk accretion rate of $<2.6\times10^{-5}$ $M_\odot$ yr^{-1}. Therefore although both sources are fit better by a model with a disk, the properties of these disks are very different. This could be due to IRAS 20126+4104 being less evolved than AFGL 2591, or that the disk of AFGL 2591 is currently undergoing an burst of accretion after building up significantly in mass. As the envelope accretion rates of both sources are similar, this would suggest that they are in similar stages of evolution, favouring the latter scenario. Further studies of the disk properties of other young embedded sources with similar masses and envelope accretion rates may therefore lead to a deeper understanding of the possible range of disk properties and also whether this is caused by episodic disk accretion.

4.5 Modelling the Ionized Gas Emission

To determine whether the observed centimetre continuum emission from AFGL 2591-VLA 3 could be explained by photoionization of the surrounding circumstellar material, a simple photoionization code was used to ionize the circumstellar geometry established by the modelling of the dust geometry carried out in Section 4.4. The best-fitting envelope plus disk model was taken as the density structure to be ionized, and an initial estimate of the ionizing photon flux was taken to be $N_{\rm total} = 1.36 \times 10^{44}\,{\rm s}^{-1}$, determined from the 3.6 cm flux of VLA 3 via equation 2.8.

Photoionization of the circumstellar material was initially carried out using the code of Wood et al. (2004), which models ionization through an evenly spaced Cartesian density grid. This modelling showed that the material within the cavity was ionized out to an equilibrium radius, as well as a very small layer of the envelope at the boundary between the envelope and cavity, which will be referred to as the cavity walls. Due to the higher density within the cavity walls, these were found to dominate the overall emission. However, the maximum resolution of the code (128^3 cells) could not adequately resolve the cavity walls, which had a thickness of less than an AU, and simultaneously cover the entire ionized region (approximately 500 AU). Therefore a simple photoionization code was developed to allow images of the ionized gas to be created which both resolved the cavity walls and covered the entire region. This custom-written code is described in the following paragraphs.

Firstly, the depth of the cavity wall at different heights above the midplane $L_{\rm wall}$ was calculated by equating ionizations with recombinations in the cavity and envelope. The total number of ionizing photons per second through an infinitesimal solid angle $d\Omega$, emanating from the star, can be expressed as

$$\frac{d\Omega}{4\pi}N_{\rm total} = dN_{\rm cavity} + dN_{\rm wall}, \tag{4.9}$$

where $dN_{\rm cavity}$ is the number of ionizing photons which recombine in the cavity in $d\Omega$, given by

$$dN_{\rm cavity} = \frac{d\Omega}{3} n_{e,{\rm cav}}^2 \alpha_B \left(R_{\rm cavity}^3 - R_{\rm inner}^3 \right), \tag{4.10}$$

and $dN_{\rm wall}$ is the number of ionizing photons which recombine in the cavity wall in $d\Omega$,

$$dN_{\rm wall} = \frac{d\Omega}{3} n_{e,{\rm wall}}^2 \alpha_B \left((R_{\rm cavity} + L_{\rm wall})^3 - R_{\rm cavity}^3 \right). \tag{4.11}$$

Here $n_{e,{\rm cav}}$ and $n_{e,{\rm wall}}$ are the electron densities in the cavity and wall respectively, α_B is the case B recombination coefficient for hyrodgen, $R_{\rm cavity}$ is the distance of the inner surface of the cavity at a height z from the central source, and $R_{\rm inner}$ is the inner radius of the ionized gas, which was taken to be $R_{\rm gas}$ from the geometry in the dust code. Thus equation 4.9 was rearranged to determine $L_{\rm wall}$ for each height z above (and below for the mirrored cavity) the midplane.

For use in equations 4.10 and 4.11, the electron density in the cavity $n_{e,{\rm cav}}$ was calculated

by dividing the cavity density found from the SED and image modelling $\rho_{\rm cav}$ by the mass of gas per electron, $1.333\,m_H$, assuming canonical abundances of H and He, and assuming that only H was ionized. Similarly, $n_{e,\rm wall}$ for each height z was determined by finding the density in the determined circumstellar geometry at a small cylindrical distance (0.001 AU) within the envelope from the surface of the cavity at that height.

Having found the radius out to which the ionized gas extended in the cavity ($\sim$500 AU), and the depth of the cavity walls, an image of the ionized gas at a given frequency could be created. To do this, $N_{\rm points}$ random positions were generated in a volume V large enough to contain the HII region. If these were found to be in either the cavity or cavity wall, the corresponding electron density was used to calculate the emission coefficient j_ν at that point, using

$$j_\nu = \frac{1}{4\pi}\frac{32e^4hn_e^2}{3m^2c^3}\left(\frac{\pi h\nu_0}{3kT}\right)^{1/2}\exp(-h\nu/kT)\;g_{\rm ff}(T,\nu). \tag{4.12}$$

(equation 4.22 of Osterbrock & Ferland, 2006) where e is the charge of an electron, h is Planck's constant, m is the mass of an electron, c is the speed of light, ν_0 is the frequency above which photons can ionize hydrogen, k is the Boltzmann constant, T is the temperature of the gas, ν is the frequency of the emission, and $g_{\rm ff}(T,\nu)$ is the Gaunt factor, which can be approximated as (equation 4.30 of Osterbrock & Ferland, 2006):

$$g_{\rm ff}(T,\nu) = \frac{\sqrt{3}}{\pi}\left(\frac{\ln T^{3/2}}{\nu} + 17.7\right), \tag{4.13}$$

Each point was then projected on to an image via a chosen source inclination and rotation angle in the plane of the sky, and added to the image at the projected position. The luminosity from each point can be found by considering the luminosity emitted by an infinitesimal element dV:

$$dL = 4\pi j_\nu dV. \tag{4.14}$$

Since the number of points are uniformly sampled in the total volume V, the number of points dN which fall in dV can be expressed as $dN = N/V\,dV$. Thus, the luminosity emitted per point is $dL/dN = 4\pi j_\nu V/N$. Hence, when summed into the image, each point was weighted by its flux, $j_\nu V/(Nd^2)$, where d is the distance to the source from Earth. Since j_ν is a function of position, the flux from each point depends on the position of the point in the cavity or cavity walls.

In addition, optical depth effects were included in the model. To find the optical depth of the path of the "photon" (luminosity/energy packet) from each point, the total emission measure EM (the integral of n_e^2 along a line-of-sight from the generated point to the edge of the source) was found, and used to calculate the optical depth τ of the ionized gas via equation 2.3 in Chapter 2. This was added as a multiplicative weight $e^{-\tau}$ to each point when summed into the image. Determination of different path lengths through the various components of the source, i.e. the cavity surface and the cavity grid in z, was carried out by finding the points of intersection of a ray directed towards the observer with these surfaces.

Finally, the image was also convolved with the Gaussian synthesised beam of the 3.6 cm or 7 mm observations for comparison with the observed images. The initial estimate of the number of ionizing photons N_{phot} was also varied until the model integrated 3.6 cm flux matched that observed (1.52 mJy, corresponding to 2 mJy without optical depth effects), giving $N_{phot} = 1.7 \times 10^{44}\,\mathrm{s}^{-1}$, which produced an HII region of maximum radius 506 AU. The integrated model flux at 7 mm was 1.3 mJy (1.6 mJy without optical depth effects). The resulting spectral index between these two wavelengths was found to be approximately -0.1, consistent with optically thin emission. This is because the reduction of emission from the model HII region due to optical depth effects occurred in the high density cavity walls, which dominated the image morphology, however the emission from the cavity, which dominated the total flux, was unchanged, and therefore the spectral index of the model integrated flux corresponded to optically thin emission.

Figure 4.15 shows two model images of the ionized gas emission at 3.6 cm with no optical depth effects applied; firstly for an edge-on view of the source, so that the geometry of the cavity and cavity walls can be seen more clearly, and secondly for a viewing angle of 45° determined for the best-fitting envelope with disk model from Section 4.4. In addition, Figure 4.16 presents the unconvolved model images for both wavelengths, viewed at 45°, including optical depth effects. The flux correct model images, which are convolved with the 0.43×0.40" P.A. 43° beam of the 3.6 cm observations, and the 0.11×0.11" P.A. 43° of the 7 mm observations are also shown, along with the observed images at these wavelengths for comparison.

The effects of optical depth can be seen by comparing the right panel of Figure 4.15 with the top left panel of Figure 4.16. There is a dark band in the unconvolved model images

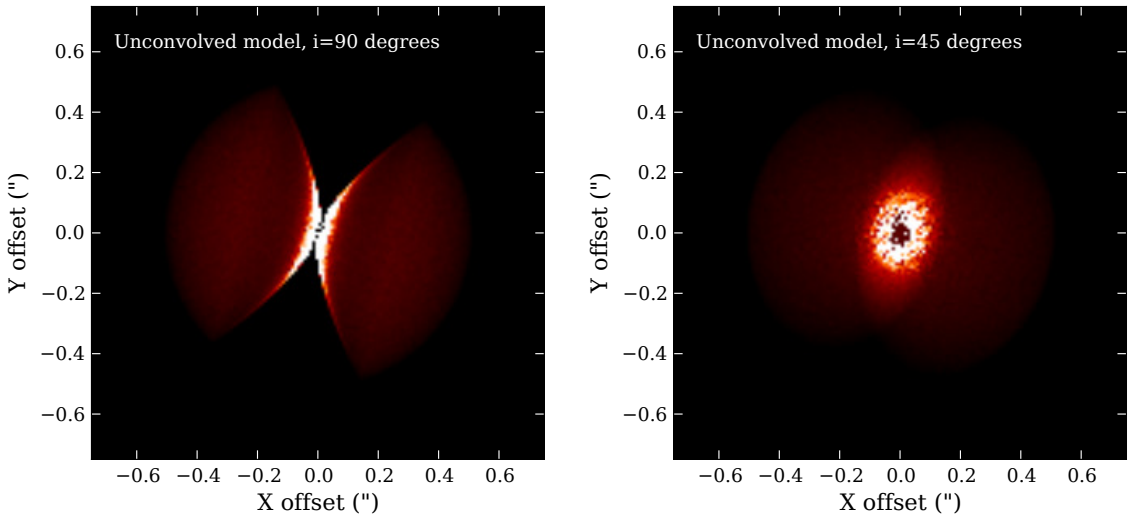

Figure 4.15: *Left:* Edge-on ($i = 90°$) view of the ionized envelope plus disk geometry. *Right:* The same ionized gas geometry but viewed at $i = 45°$, the inclination determined from the results of the genetic algorithm in Section 4.4. These two model images do not include optical depth effects.

shown in Figure 4.16, caused by absorption of continuum photons in the dense cavity walls. In addition, the flux is strongly reduced within a central radius of ∼200 AU.

Comparing the model 3.6 cm image to the VLA observations, it can be seen that although the morphology of the model is a bipolar HII region, it does not reproduce the jet-like extensions to the emission from VLA 3. However, it appears to reproduce the emission from the central 'core' of this source. In Section 4.3.1, it was found that it was unlikely that the ionized gas emission at 3.6 cm could be explained solely by shocks in a neutral wind or outflow. Therefore, a possible compromise would be that the 3.6 cm emission is caused partially by a hypercompact HII region similar to that modelled here (producing the compact component), and partially by an ionized jet (producing the extended jet-like morphology).

Much of model 7 mm emission (dominated by the cavity) is more extended than observed. Therefore although the total flux at 7 mm is within a factor of 2 of that observed (1.3 mJy compared to 2.5 mJy), the morphology of the peak emission in the 7 mm model image is too faint in comparison. The emission in the model image in Figure 4.16 has therefore been increased by a factor of 7 so that the morphology of the emission can be seen. This deficit in the 7 mm emission could possibly be explained by a larger fraction of compact dust emission than estimated in Section 4.3.1 (<0.5 mJy) contributing to the emission at this wavelength. Alternatively, ionization of a different geometry which has a denser central

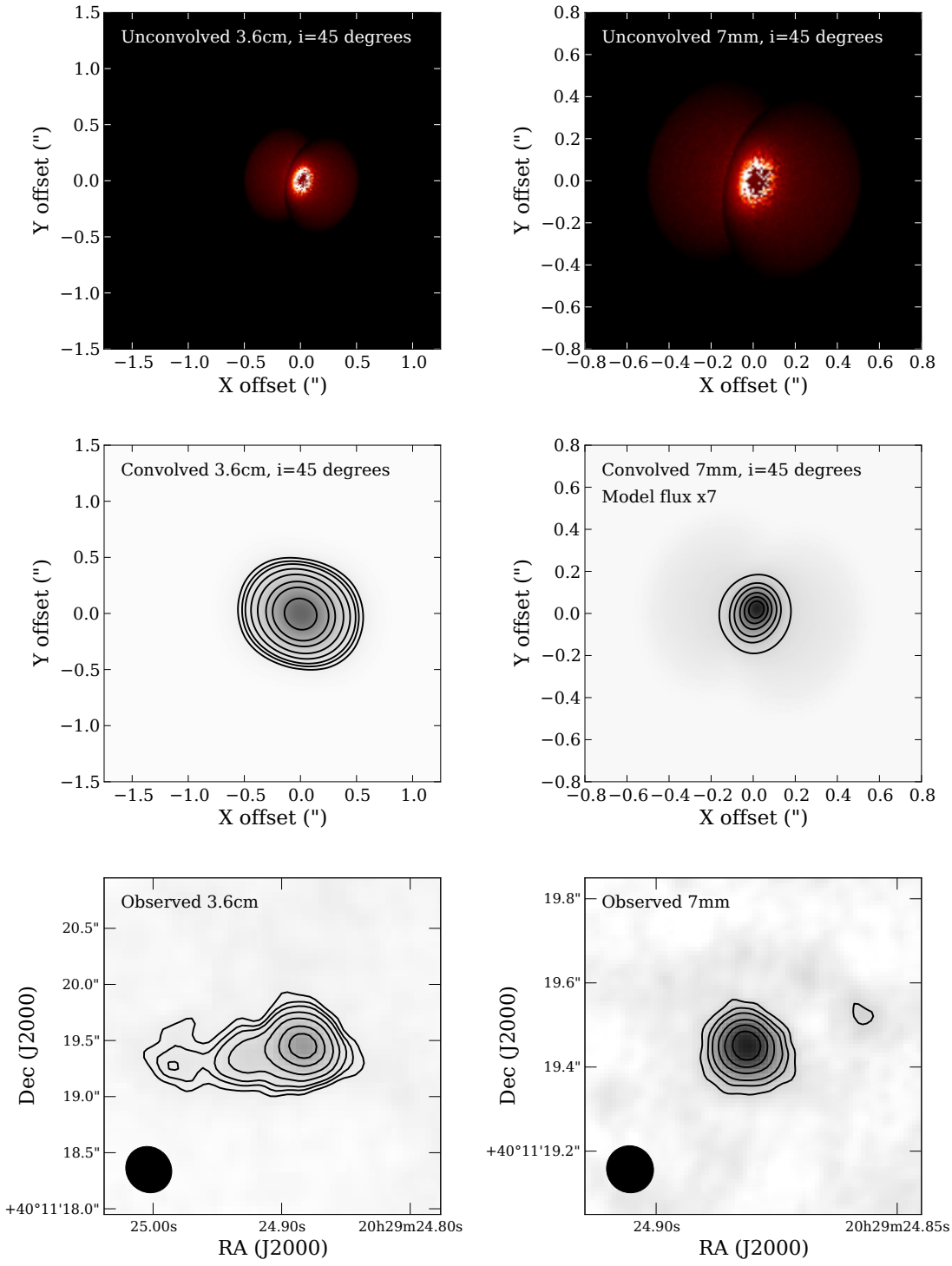

Figure 4.16: *Top panels:* Unconvolved model images of the ionized gas emission from AFGL 2591, at both 3.6 cm and 7 mm, including optical depth effects. *Middle panels:* Model 3.6 cm and 7 mm images (with same morphology as top panels) convolved by the observed 0.43×0.40" P.A.= 43° and 0.11×0.11" P.A.= 43° beams (at 3.6 cm and 7 mm respectively). *Bottom panels:* Observed 3.6 cm and 7 mm images as in Figures 4.4 and 4.5 respectively. The same contours are shown for both the model and observed images, however the flux in the model 7 mm image has been increased by a factor of 7.

component would also produce more centrally condensed emission from a more optically thick HII region.

A caveat of the model above is that it assumes that the presence of ionized gas does not affect the dust and vice versa. However, assuming an opacity of $1.3\times10^{-22}\,\mathrm{cm^2\,H^{-1}}$ for silicate dust at Lyman continuum wavelengths (Wood et al., 2010), the optical depth due to dust was found to be negligible through both the cavity and the cavity walls. Therefore the presence of dust should not significantly effect the ionization structure of the model.

In summary, ionization of the centrally condensed accreting model geometry determined from the SED and image modelling carried out in Section 4.4 cannot fully reproduce the observed images. However, these results show that emission from both a hypercompact HII region and ionized jet may be the best explanation of the 3.6 cm emission. At 7 mm, the flux predicted by the model falls short of that observed, suggesting that emission from dust is a larger component of the observed emission than estimated in Section 4.3.1, or that ionization of a more centrally condensed geometry than assumed may be able to reproduce the observed flux. In future, simultaneous modelling of both the SED, infrared and cm continuum images should be able to better determine a consistent dust and ionized gas geometry.

4.6 Chapter Conclusions

In this chapter, a study of the emission from the luminous forming star AFGL 2591 from near-IR through to cm wavelengths was carried out, to determine whether the properties of the source can be explained by the same processes thought to govern the formation of low-mass stars. The observed 3.6 cm images presented in Section 4.3.1 detect and more finely resolve the central powering source of AFGL 2591, VLA 3, which has a collimated jet morphology. The east component of the jet extends 1200 AU from the central source, with an opening angle of $< 10^\circ$ at this radius. This jet is also roughly parallel to the outflow seen at larger scales by Hasegawa & Mitchell (1995), confirming that VLA 3 is the powering source of the outflow from AFGL 2591. The multi-configuration 7 mm image detects both VLA 1 and VLA 3. At this wavelength, VLA 3 does not show a jet morphology, but instead presents compact (< 150 AU) emission, a fraction ($<$0.5 mJy or 20%) of which is estimated to be due to dust emission.

In addition to the four previously known radio continuum sources towards AFGL 2591, a fifth source to the south west, VLA 5, was also detected. Comparison with ancillary 0.3-0.4" Gemini near-IR images show that VLA 3 is coincident with the illuminating source of AFGL 2591, at the apex of the observed near-IR reflection nebula. Further, VLA 2 is coincident with the close binary first seen by Preibisch et al. (2003), and VLA 4 and VLA 5 are coincident with near-IR sources. However, VLA 1 is anti-correlated with the diffuse near-IR emission, showing that it is probably at the same distance as AFGL 2591-VLA 3, and is interacting with and displacing the surrounding ambient cloud. Therefore, the bright rim of near-IR emission at the edge of VLA 1 is likely to be swept-up material, and not a edge-on disk as suggested by Preibisch et al. (2003).

By fitting greybodies to the SEDs of VLA 1 and VLA 3 at wavelengths shorter than 1 mm, temperatures of 111 ± 14 K and 30 ± 1 K, were derived for each source respectively. For VLA 1, this derived temperature probably represents heated dust in the HII region, and for VLA 3 this represents cool dust in the outer layers of its circumstellar envelope. In addition, the contribution of VLA 1 to the total SED from AFGL 2591 was determined to be $< 30\%$ at wavelengths between 8 and 100μm, and to be negligible at other wavelengths. Therefore contamination by VLA 1, or fainter sources in the region (e.g. VLA 2), should not significantly change the emergent SED of the central powering object which dominates the luminosity from the region, AFGL 2591-VLA 3.

At radio wavelengths, the fitted spectral index of VLA 1 was found to be 0.00 ± 0.04, similar to that of an optically thin HII region, and the spectral index of VLA 3 was calculated (between 3.6 cm and 7 mm only) to be $< 0.56 \pm 0.02$, similar to that of an ionized wind, however the spectral index of VLA 3 is an upper limit, as a fraction of the 7 mm integrated flux may be due to dust.

The nature of the emission from VLA3 was also investigated. In Section 4.3.1, the 3.6 cm emission was modelled as an ionized jet, from which an upper limit for the mass loss rate in the jet was determined to be $2.0 \times 10^{-6}\,M_{\odot}yr^{-1}$. Assuming the eastern lobe of the ionized jet is entraining the small-scale red-shifted outflow observed by Hasegawa & Mitchell (1995), which has a mass loss rate of $6 \times 10^{-5}\,M_{\odot}yr^{-1}$ (Hasegawa & Mitchell, 1995), it was found that at least 96% of the mass in the outflow must be entrained by the jet. In addition, it was found that the jet may also have enough momentum to drive the larger-scale flow.

Alternatively, the jet was also modelled as shocks in a neutral wind or outflow. However, unless the shock efficiency is close to 1, it is unlikely that the observed 3.6 cm emission can be explained solely by shocks in the outflow.

In Section 4.3.2, the observed $C^{18}O$ emission towards the source was found to be tracing the densest accelerated or entrained material within the outflow. The blue-shifted emission shows an increasing velocity gradient westward away from the source, becoming more collimated at higher velocities, and is coincident with the inner part of the blue-shifted outflow observed by Hasegawa & Mitchell (1995). Therefore it is likely that this emission is tracing the densest parts of the entrained gas in the outflow which are being accelerated away from AFGL 2591-VLA 3. In addition, the dense red-shifted gas traced by $C^{18}O$ lies along the position angle of the ionized jet seen at 3.6 cm, directly between the jet and bow shocks seen in the near-IR Gemini image. Therefore it is likely this emission also traces a small, dense, segment of the red-shifted flow. The emission in the central channel at the rest velocity of the cloud (-5 kms^{-1}) is elongated perpendicular to the outflow, and therefore probably traces part of a flattened envelope around AFGL 2591-VLA 3. However, no velocity gradient was detected along it. Finally, the $C^{18}O$ gas appears to be anti-correlated with the position of VLA 1, again supporting the idea that this source lies at the same distance as VLA 3. In addition, there is a red-shifted velocity gradient in the gas surrounding VLA 1, suggesting that the gas around it is expanding outward as the HII region interacts with the ambient cloud material.

In Section 4.4, a Monte Carlo radiation transfer dust code was used to model the continuum absorption, emission and scattering through two scaled-up azimuthally symmetric dust geometries, the first consisting of a rotationally flattened envelope with outflow cavities, and the second which also includes a flared disk. The results of the genetic algorithm show that the envelope plus disk model reproduces the observed SED and images better than the envelope without disk model. The best-fitting values of the parameters for both models are given in Table 4.7. In contrast to the envelope only model, which has a derived stellar mass of 15 $M_{\odot}$, a significant fraction of the luminosity of the envelope with disk model is derived from accretion luminosity in the disk, and the stellar mass is instead 6.5 $M_{\odot}$ solar masses (spectral type B4), lying on the borderline of what is considered a massive star. The disk accretion rate in the best-fitting envelope plus disk model is almost twice that of the determined envelope accretion rate, which would make it an FU Orionis-type object. Hence if this

is the case, and AFGL 2591 is currently undergoing an accretion outburst, the luminosity of AFGL 2591 should drop dramatically once this phase ends.

Finally, in Section 4.5, the cm continuum emission was modelled by photoionization of the envelope plus disk geometry determined in Section 4.4. It was found that although this model could not fully reproduce the observed 3.6 cm and 7 mm images, the results suggest that a combination of hypercompact HII region and jet emission may be able to do so. The 7 mm model images also suggest that either the dust is contributing a larger fraction of the emission at this wavelength than estimated (<0.5 mJy or <20%), or that a more centrally condensed geometry is required. In future, simultaneous modelling of both the SED, infrared and cm continuum images should be able to better determine a consistent dust and ionized gas geometry.

The above results show that many of the properties of this forming star resemble those of low-mass protostars. For example, the outflow of AFGL 2591 comprises of both a collimated ionized jet, and a wide angle wind, a property seen in the outflow phenomena of many low-mass sources (e.g. Arce et al., 2007). The geometry of AFGL 2591 determined from modelling the SED and near-IR images of the source is also consistent with that of a rotationally flattened envelope plus flared disk. However, although the emission at 3.6 cm from AFGL 2591-VLA has the morphology of a jet, it is unlikely that it can be explained solely by shocks in a neutral wind or outflow. Therefore some part of the compact emission from the star may instead be provided by a hypercompact HII region. Yet if this is the case, its presence has not disrupted the accretion or outflow processes of AFGL 2591. Thus the formation of the embedded young B-type star AFGL 2591 does not appear to be significantly different to that of low-mass protostars.

Chapter Acknowledgments

This work makes use of observations obtained at the Gemini Observatory, which is operated by the Association of Universities for Research in Astronomy, Inc., under a cooperative agreement with the NSF on behalf of the Gemini partnership: the National Science Foundation (United States), the Science and Technology Facilities Council (United Kingdom), the National Research Council (Canada), CONICYT (Chile), the Australian Research Council (Australia), Ministério da Ciência e Tecnologia (Brazil) and Ministerio de Ciencia, Tecnología e Innovación Productiva (Argentina).

5

Conclusions

The first Chapter of this thesis outlined in two parts our current understanding of both low- and high-mass star formation. Comparing these two regimes, it is possible to see many similarities in the processes that form stars across the mass spectrum, including most prominently the presence of jets, outflows and disks. In addition, the effects of radiation pressure and ionization may not present such strong barriers against the formation of massive stars as previously thought, due to the fact the circumstellar material is likely to accrete non-spherically onto the star, and in some cases this material can accrete through an HII region. Therefore, although there is still some ambiguity as to whether the material which forms a massive star is sourced solely from a massive core surrounding it, or instead from the entire nearby cluster environment, once this material reaches the vicinity of the accreting object, there is little to stop it becoming a star.

The work in this thesis presents observations of the cluster-scale environments in which massive stars form, including how the properties of the ionized gas they create relates to the molecular material in which they form, as well as in-depth studies of two luminous forming stars, IRAS 20126+4104 and AFGL 2591, to determine whether they are forming similarly to their low-mass counterparts.

In Chapter 2, a survey of ionized gas at 3.6 cm, using the VLA, towards 31 Galactic intermediate- and high-mass clumps detected in previous millimetre continuum observations, was presented. In the 10 observed fields, 35 HII regions were identified, of which 20 are newly discovered. There is a large range in the properties of the observed HII regions; their physical sizes extend from <0.05 pc to 7.88 pc, and their spectral types cover B2 to O5. In addition, many of the HII regions are multiply peaked indicating the presence of a cluster of massive stars. The detected ionized gas was found to be preferentially associated towards the millimetre clumps: of the 31 millimetre clumps observed, 9 of these appear to be physically related to ionized gas, and a further 6 have ionized gas emission within 1'. For clumps with associated ionized gas, the combined mass of the ionizing massive stars was compared to the clump masses to provide an estimate of the instantaneous massive star formation efficiency. These values range from a few percent to 25%, and have an average of 7 ± 8%.

A correlation was also found between the clump mass and the mass of the ionizing massive stars within it, which is consistent with a power law, suggesting that the final mass of a massive star is determined by the mass of the clump in which it forms. It was shown that this relation is intrinsically related to the upper protostellar mass function, and therefore may in future be a powerful tool to distinguish between different theories of massive star formation.

Comparing the observations of the observed clumps at mm, cm, and mid-IR wavelengths allowed further insight into the nature of the clumps. Several "types" of millimetre clump were inferred from this comparison: more evolved star-forming clusters containing multiple sources of ionized gas and mid-IR emission, single massive stars or compact clusters associated with singly peaked HII regions, and the youngest or quiescent sources without associated ionized gas. These clumps were selected so that their declinations allowed future study with the EVLA and ALMA at higher resolution, to study the disks, outflows, and ionized gas around the young sources in these regions, and also to investigate the dynamics of the accreting gas on cluster scales.

In Chapters 3 and 4, the near-IR to sub-millimetre SEDs and infrared images of two luminous forming stars, IRAS 20126+4104 and AFGL 2591, were modelled successfully using a Monte Carlo dust code which performed radiation transfer through the standard envelope plus disk geometry commonly used to describe low-mass protostars. Two azimuthally sym-

metric dust geometries were fitted to the data, the first consisting of a rotationally flattened envelope with outflow cavities, and the second which also includes a flared disk. The results for both sources show that the envelope plus disk model generally reproduces the observed SED and images more accurately than the model without a disk. In both cases, some of the luminosity of the best-fitting envelope plus disk models is provided by disk accretion, with the remaining luminosity supplied by a 12.7 $M_\odot$ star for IRAS 20126+4104, and a 6.5 $M_\odot$ star for AFGL 2591, much less than mass estimates of AFGL 2591 without accretion luminosity (15 $M_\odot$). If this is the case, the high disk accretion rate inferred for AFGL 2591 would suggest that it is a rapidly accreting FU Orionis-type object.

In the case of IRAS 20126+4104, although in general the envelope plus disk model better-reproduces the SED and images, the envelope without disk model more closely reproduces the morphology of the mid-IR emission within a radius of 1.1" or ∼1800 AU. Several possible causes of this discontinuity were discussed in Chapter 3, including inner truncation of the disk due to stellar irradiation, or precession of the outflow cavity. The best fitting envelope plus disk model has a disk radius of 9200 AU, and therefore it is unlikely that the outer regions of such a disk would be in hydrostatic or centrifugal equilibrium. However, by calculating the Toomre parameter throughout the disk, it was found that the temperatures within the disk around IRAS 20126+4104 would keep it stable to fragmentation.

In addition, Chapter 4 presented new high sensitivity VLA 3.6 cm observations towards AFGL 2591, which uncovered a collimated jet towards VLA 3, the source coincident with its central illuminating object at infrared wavelengths. The jet extends roughly parallel to the large-scale flow, out to 1200 AU from the central source, with an opening angle of $<10^\circ$ at this radius. It was found that the momentum rate observed for the large-scale red-shifted outflow (in the direction in which the ionized jet emission was dominant) was unlikely to be sufficient to reproduce the observed 3.6 cm emission entirely via shocks in a neutral wind or outflow. In addition, the observed 7 mm images also uncovered compact emission (with a radius of <150 AU) which is likely to have a contribution from both dust and ionized gas. It was estimated that <20% or 0.5 mJy of the emission at 7 mm is due to dust, however the results of Section 4.5 suggest this value may be higher. $C^{18}O$(1-0) was observed at 3 mm, and was found to trace the densest parts of the outflow from AFGL 2591, as well as a flattened structure perpendicular to the outflow direction at the rest velocity of the cloud. The blue-shifted $C^{18}O$(1-0) emission shows a Hubble law relationship, with the dense gas increasing

in velocity away from the source, as well as higher collimation at higher velocities, hence showing many similarities to the properties of outflows around low-mass protostars. Finally, a photoionization code was developed to ionize the envelope plus disk geometry determined from the SED and image modelling of AFGL 2591, and also to produce images at 3.6 cm and 7 mm. The results showed that convolved images of the hypercompact HII region produced by ionization of this geometry could not reproduce the jet-like morphology seen in the 3.6 cm images, although they did reproduce the central compact component. Therefore, as it was unlikely that ionization from shocks could reproduce the 3.6 cm emission alone, it may be that this emission is due to both a hypercompact HII region and a shock-ionized jet.

The above results show that a scaled-up version of low-mass star formation is able to describe the forming B-type stars IRAS 20126+4104 and AFGL 2591, with their geometries consistent with rotationally flattened envelopes plus disks. Standing back to compare the properties of forming stars in both low- and high-mass regimes, it can be seen that the properties of jets, outflows and disks of B-type stars provide an upper continuation of those at lower masses. For instance, it was mentioned in Chapter 1 that disks around low-mass stars have radii of $\sim$200 AU (Andrews & Williams, 2007), but that disks around early B-type stars usually have radii $\gtrsim$500 AU (Cesaroni et al., 2007). The disk sizes of IRAS 20126+4104 and AFGL 2591 are both larger than 200 AU (9200 AU and 270 AU respectively), however the difference between these two disk radii is large. The smaller disk radius for AFGL 2591 may be due to the lower best-fitting central stellar mass (6.5 $M_{\odot}$), almost half that of IRAS 20126+4104 (12.7 $M_{\odot}$).

The masses of the disks around massive stars are generally several solar masses, while disks around low-mass stars have masses of 0.001 to 0.1 $M_{\odot}$ (Cesaroni et al., 2007 and Andrews & Williams, 2007 respectively). IRAS 20126+4104 and AFGL 2591 also follow this pattern, with disk masses of 5.9 and 14 $M_{\odot}$ respectively. Typical disk accretion rates for low-mass stars are $\sim 10^{-8}$ to $10^{-6}\,M_{\odot}\,yr^{-1}$ (Robitaille et al., 2007), whereas both disk accretion rates found for IRAS 20126+4104 and AFGL 2591 were above $10^{-5}\,M_{\odot}\,yr^{-1}$. It is interesting to note however, that AFGL 2591 has a marginally higher best-fitting disk accretion rate than envelope accretion rate. This suggests that the disk of AFGL 2591 is currently in an accretion outburst phase, which is corroborated by the fact it is smaller, more massive, and therefore much denser than the disk around IRAS 20126+4104.

The envelope accretion rates and therefore the envelope densities of forming massive stars are found to be larger than those of low-mass stars. For instance, Robitaille et al. (2007) found envelope accretion rates for nearby low-mass protostars of $\sim 9\times10^{-7}$ to $6\times10^{-5}\,M_\odot\,yr^{-1}$, while Osorio et al. (1999) found accretion rates of $\gtrsim 6\times10^{-4}\,M_\odot\,yr^{-1}$ for embedded massive stars. In agreement with this trend, the envelope accretion rates found in Chapters 3 and 4 for IRAS 20126+4104 and AFGL 2591 are $3.9\times10^{-4}\,M_\odot\,yr^{-1}$ and $1.8\times10^{-4}\,M_\odot\,yr^{-1}$ respectively.

In a similar vein, the properties of outflows and jets towards forming massive stars are also "scaled up" from those of low-mass protostars. Low mass outflows usually extend between 0.1 to 1 pc (Arce et al., 2005), whereas in comparison the large-scale flows of IRAS 20126+4104 and AFGL 2591 extend approximately 1 pc and 1.5 pc (from end to end) respectively (Shepherd et al., 2000; Hasegawa & Mitchell, 1995). One of the largest flows in the Galaxy, created by the early B-type star G192.16-3.82, measures 10 pc across (Devine et al., 1999). Hence it appears that the sizes of outflows increase with mass of the central source. This scaling up also occurs for the outflow energetics, such as momentum transport rate and outflow mass, which scale with the luminosity of the source over several decades of luminosity ($\sim$1 - $10^5 L_\odot$, e.g. Wu et al., 2004), suggesting that outflows from stars of all masses share a similar launching mechanism. However, one difference between outflows towards low- and high-mass (proto)stars is that massive star outflows are in general less collimated than their low-mass counterparts (see Arce et al., 2005, and references therein), yet there are several examples of outflows from high-mass stars which are highly collimated (e.g. Beuther et al., 2002a).

The ionized jets which are associated with actively accreting stars also appear to scale with the mass of the source. For example, Anglada (1996) found that the lengths of these microjets are in general larger for higher luminosity objects. Similarly, the one-sided ionized jet towards AFGL 2591 reported in Chapter 4 has a length of 1200 AU, which is significantly larger than the average length of $\sim$200 AU for sources with luminosities less than $10^4\,L_\odot$ (Anglada, 1996). The jet towards AFGL 2591 is also highly collimated, with an opening angle of $<10^\circ$ at 1200 AU from the driving source, similar to those from lower-mass objects. The upper limit for the mass loss rate for the jet from AFGL 2591 ($2.0\times10^{-6}\,M_\odot\,yr^{-1}$) is much higher than the mass loss rates determined for low mass stars ($5\times10^{-8}\,M_\odot\,yr^{-1}$, Ray et al., 2007), and the momentum transfer rate for the jet also lies at the upper end of the

range of those observed across the luminosity spectrum (Anglada, 1996).

As to the effects of photoionization on the formation of massive stars, the ionized jet observed towards the central source of AFGL 2591 appears not to have been disrupted by the presence of a hypercompact HII region. However, it may be that ionized gas or radiation pressure is the cause of the discontinuity observed in the central ∼1800 AU of IRAS 20126+4104. Therefore, although it does not halt accretion onto the star, radiation pressure or ionization may work to alter the physics of the accreting or outflowing material. This is in agreement with evidence showing that the formation of HII regions around massive stars appear to widen their outflows (Section 1.2.4). Future observations of radio recombination lines with ALMA will be able to resolve and therefore separate the ionized gas emission from jets and HII regions towards massive stars, as well as study their dynamics, which will allow further insight into how accretion and outflow is affected by the ionizing radiation of massive stars.

This is not the only question ALMA promises to answer. As well as resolving molecular line emission from disks and outflows down to resolutions of tens of AU at a distance of 1 kpc, ALMA will also allow much more detailed observations towards the majority of massive stars, which lie at much farther distances. Therefore observations with ALMA, using the vast array of molecular tracers available, may finally uncover disks around the most massive stars, which could exist within the flattened structures currently observed. A further question on which imaging with ALMA will shed light is whether disks around massive stars are stable, or whether they fragment or exhibit spiral density waves caused by instability of the disk. With the current paradigms in hand, the next decade of ALMA is set to revolutionise our view of high-mass star formation.

Bibliography

Adams, F. C., Lada, C. J., & Shu, F. H. 1987, ApJ, 312, 788

Adams, F. C., & Shu, F. H. 1986, ApJ, 308, 836

Afflerbach, A., Churchwell, E., Acord, J. M., Hofner, P., Kurtz, S., & Depree, C. G. 1996, ApJS, 106, 423

Akeson, R. L. et al. 2005, ApJ, 622, 440, arXiv:astro-ph/0412438

Alcalá, J. M. et al. 2008, ApJ, 676, 427, 0802.1424

Allen, L. E. et al. 2004, ApJS, 154, 363

Altenhoff, W. J., Mezger, P. G., Wendker, H., & Westerhout, G. 1960, Veroff. Sternwarte, Bonn, No. 59, 48

André, P., Ward-Thompson, D., & Barsony, M. 1993, ApJ, 406, 122

——. 2000, Protostars and Planets IV, 59, arXiv:astro-ph/9903284

Andrews, S. M., & Williams, J. P. 2007, ApJ, 659, 705, arXiv:astro-ph/0610813

Anglada, G. 1996, in Astronomical Society of the Pacific Conference Series, Vol. 93, Radio Emission from the Stars and the Sun, ed. A. R. Taylor & J. M. Paredes, 3–7

Anglada, G., Villuendas, E., Estalella, R., Beltrán, M. T., Rodríguez, L. F., Torrelles, J. M., & Curiel, S. 1998, AJ, 116, 2953

Appenzeller, I., Oestreicher, R., & Jankovics, I. 1984, A&A, 141, 108

Arce, H., Shepherd, D. S., Gueth, F., C., L., Bachiller, R., A., R., & Beuther, H. 2005

Arce, H. G., & Sargent, A. I. 2006, ApJ, 646, 1070, arXiv:astro-ph/0605139

Arce, H. G., Shepherd, D., Gueth, F., Lee, C., Bachiller, R., Rosen, A., & Beuther, H. 2007, Protostars and Planets V, 245, arXiv:astro-ph/0603071

Avalos, M., Lizano, S., Rodríguez, L. F., Franco-Hernández, R., & Moran, J. M. 2006, ApJ, 641, 406

Bacciotti, F., & Eislöffel, J. 1999, A&A, 342, 717

Bacciotti, F., Mundt, R., Ray, T. P., Eislöffel, J., Solf, J., & Camezind, M. 2000, ApJ, 537, L49, arXiv:astro-ph/0005463

Balbus, S. A., & Hawley, J. F. 1991, ApJ, 376, 214

Ballesteros-Paredes, J., Gómez, G. C., Loinard, L., Torres, R. M., & Pichardo, B. 2009, MNRAS, 395, L81, 0903.0603

Bally, J., & Lada, C. J. 1983, ApJ, 265, 824

Bally, J., & Zinnecker, H. 2005, AJ, 129, 2281, arXiv:astro-ph/0502485

Baudry, A., Desmurs, J. F., Wilson, T. L., & Cohen, R. J. 1997, A&A, 325, 255

Becker, R. H., White, R. L., Helfand, D. J., & Zoonematkermani, S. 1994, ApJS, 91, 347

Beltrán, M. T., Brand, J., Cesaroni, R., Fontani, F., Pezzuto, S., Testi, L., & Molinari, S. 2006, A&A, 447, 221, arXiv:astro-ph/0510422

Benjamin, R. A. et al. 2003, PASP, 115, 953, arXiv:astro-ph/0306274

Beuther, H., Schilke, P., & Gueth, F. 2004, ApJ, 608, 330, arXiv:astro-ph/0402563

Beuther, H., Schilke, P., Gueth, F., McCaughrean, M., Andersen, M., Sridharan, T. K., & Menten, K. M. 2002a, A&A, 387, 931, arXiv:astro-ph/0203010

Beuther, H., Schilke, P., Menten, K. M., Motte, F., Sridharan, T. K., & Wyrowski, F. 2002b, ApJ, 566, 945, arXiv:astro-ph/0110370

Beuther, H., & Shepherd, D. 2005, in Cores to Clusters: Star Formation with Next Generation Telescopes, ed. M. S. N. Kumar, M. Tafalla, & P. Caselli, 105–119

Beuther, H., Walsh, A., Schilke, P., Sridharan, T. K., Menten, K. M., & Wyrowski, F. 2002c, A&A, 390, 289, arXiv:astro-ph/0205348

Bjorkman, J. E., & Wood, K. 2001, ApJ, 554, 615, arXiv:astro-ph/0103249

Bonnell, I. A. 2005, in IAU Symposium, Vol. 227, Massive Star Birth: A Crossroads of Astrophysics, ed. R. Cesaroni, M. Felli, E. Churchwell, & M. Walmsley, 266–275

Bonnell, I. A., & Bate, M. R. 2002, MNRAS, 336, 659

Bonnell, I. A., Bate, M. R., & Zinnecker, H. 1998, MNRAS, 298, 93, arXiv:astro-ph/9802332

Bonnell, I. A., Clarke, C. J., Bate, M. R., & Pringle, J. E. 2001, MNRAS, 324, 573, arXiv:astro-ph/0102121

Bonnell, I. A., & Davies, M. B. 1998, MNRAS, 295, 691

Bontemps, S., Andre, P., Terebey, S., & Cabrit, S. 1996, A&A, 311, 858

Bronfman, L., Nyman, L.-A., & May, J. 1996, A&AS, 115, 81

Burrows, C. J. et al. 1996, ApJ, 473, 437

Cabrit, S., & Bertout, C. 1992, A&A, 261, 274

Calvet, N., & Gullbring, E. 1998, ApJ, 509, 802

Campbell, B. 1984a, ApJ, 287, 334

——. 1984b, ApJ, 282, L27

Cardelli, J. A., Clayton, G. C., & Mathis, J. S. 1989, ApJ, 345, 245

Cassen, P., & Moosman, A. 1981, Icarus, 48, 353

Castelli, F., & Kurucz, R. L. 2004, ArXiv Astrophysics e-prints, arXiv:astro-ph/0405087

Caswell, J. L., Murray, J. D., Roger, R. S., Cole, D. J., & Cooke, D. J. 1975, A&A, 45, 239

Cesaroni, R. 2005, Ap&SS, 295, 5

Cesaroni, R., Felli, M., Jenness, T., Neri, R., Olmi, L., Robberto, M., Testi, L., & Walmsley, C. M. 1999a, A&A, 345, 949

Cesaroni, R., Felli, M., Testi, L., Walmsley, C. M., & Olmi, L. 1997, A&A, 325, 725

Cesaroni, R., Felli, M., & Walmsley, C. M. 1999b, A&AS, 136, 333

Cesaroni, R., Galli, D., Lodato, G., Walmsley, C. M., & Zhang, Q. 2007, in Protostars and Planets V, ed. B. Reipurth, D. Jewitt, & K. Keil, 197–212

Cesaroni, R., Neri, R., Olmi, L., Testi, L., Walmsley, C. M., & Hofner, P. 2005, A&A, 434, 1039

Chiang, E. I., & Goldreich, P. 1997, ApJ, 490, 368, arXiv:astro-ph/9706042

Chieffi, A., & Straniero, O. 1989, ApJS, 71, 47

Churchwell, E. 1999, in NATO ASIC Proc. 540: The Origin of Stars and Planetary Systems, ed. C. J. Lada & N. D. Kylafis, 515–+

Churchwell, E. 2002, ARA&A, 40, 27

Churchwell, E. et al. 2006, ApJ, 649, 759

Churchwell, E., Walmsley, C. M., & Cesaroni, R. 1990, A&AS, 83, 119

Churchwell, E. et al. 2004, ApJS, 154, 322

Clark, P. C., Bonnell, I. A., & Klessen, R. S. 2008, MNRAS, 386, 3, 0803.4053

Codella, C., Lorenzani, A., Gallego, A. T., Cesaroni, R., & Moscadelli, L. 2004, A&A, 417, 615

Coffey, D., Bacciotti, F., Podio, L., & Nisini, B. 2010, ApJ, 719, 505, 1006.5400

Coffey, D., Bacciotti, F., Ray, T. P., Eislöffel, J., & Woitas, J. 2007, ApJ, 663, 350, arXiv:astro-ph/0703271

Cohen, M., & Schwartz, R. D. 1983, ApJ, 265, 877

Condon, J. J., Griffith, M. R., & Wright, A. E. 1993, AJ, 106, 1095

Cotera, A. S. et al. 2001, ApJ, 556, 958, arXiv:astro-ph/0104066

Crutcher, R. M. 1999, ApJ, 520, 706

Curiel, S., Rodriguez, L. F., Bohigas, J., Roth, M., Canto, J., & Torrelles, J. M. 1989, Astrophysical Letters Communications, 27, 299

Cyganowski, C. J. et al. 2008, AJ, 136, 2391, 0810.0530

D'Alessio, P., Canto, J., Calvet, N., & Lizano, S. 1998, ApJ, 500, 411, arXiv:astro-ph/9806060

De Buizer, J. M. 2007, ApJ, 654, L147, arXiv:astro-ph/0611559

De Buizer, J. M., Radomski, J. T., Telesco, C. M., & Piña, R. K. 2005, ApJS, 156, 179, arXiv:astro-ph/0410630

de Pree, C., Geballe, T., Goss, W. M., Mehringer, D., & Cecil, G. 1994, in Bulletin of the American Astronomical Society, Vol. 26, Bulletin of the American Astronomical Society, 1459–+

De Pree, C. G., Wilner, D. J., Deblasio, J., Mercer, A. J., & Davis, L. E. 2005, ApJ, 624, L101, arXiv:astro-ph/0504230

de Wit, W. J. et al. 2009, A&A, 494, 157, 0811.4050

Devine, D., Bally, J., Reipurth, B., Shepherd, D., & Watson, A. 1999, AJ, 117, 2919

Dobbs, C. L., Bonnell, I. A., & Clark, P. C. 2005, MNRAS, 360, 2, arXiv:astro-ph/0502479

Downes, D., Wilson, T. L., Bieging, J., & Wink, J. 1980, A&AS, 40, 379

Draine, B. T. et al. 2007, ApJ, 663, 866, arXiv:astro-ph/0703213

Dullemond, C. P., Hollenbach, D., Kamp, I., & D'Alessio, P. 2007, Protostars and Planets V, 555, arXiv:astro-ph/0602619

Dunham, M. M., Evans, N. J., Terebey, S., Dullemond, C. P., & Young, C. H. 2010, ApJ, 710, 470, 0912.5229

Edris, K. A., Fuller, G. A., & Cohen, R. J. 2007, A&A, 465, 865, arXiv:astro-ph/0701652

Edris, K. A., Fuller, G. A., Cohen, R. J., & Etoka, S. 2005, A&A, 434, 213

Egan, M. P., Shipman, R. F., Price, S. D., Carey, S. J., Clark, F. O., & Cohen, M. 1998, ApJ, 494, L199+

Eisner, J. A., Hillenbrand, L. A., Carpenter, J. M., & Wolf, S. 2005a, ApJ, 635, 396, arXiv:astro-ph/0508380

Eisner, J. A., Hillenbrand, L. A., White, R. J., Akeson, R. L., & Sargent, A. I. 2005b, ApJ, 623, 952, arXiv:astro-ph/0501308

Elia, D. et al. 2010, A&A, 518, L97+, 1005.1783

Enoch, M. L., Corder, S., Dunham, M. M., & Duchêne, G. 2009, ApJ, 707, 103, 0910.2715

Enoch, M. L. et al. 2006, ApJ, 638, 293, arXiv:astro-ph/0510202

Evans, I. N., Primini, F. A., Glotfelty, K. J., Anderson, C. S., Bonaventura, N. R., Chen, J. C., Davis, J. E., & et al., D. 2010, ApJS, 189, 37, 1005.4665

Fazio, G. G. et al. 2004, ApJS, 154, 10, arXiv:astro-ph/0405616

Felli, M., Massi, M., & Churchwell, E. 1984, A&A, 136, 53

Forster, J. R., & Caswell, J. L. 1989, A&A, 213, 339

Franco-Hernández, R., & Rodríguez, L. F. 2004, ApJ, 604, L105, arXiv:astro-ph/0402467

Fuller, G. A., Williams, S. J., & Sridharan, T. K. 2005, A&A, 442, 949, arXiv:astro-ph/0508098

Garay, G., Faúndez, S., Mardones, D., Bronfman, L., Chini, R., & Nyman, L.-Å. 2004, ApJ, 610, 313

Garay, G., & Lizano, S. 1999, PASP, 111, 1049, astro-ph/9907293

Garay, G., Rodriguez, L. F., Moran, J. M., & Churchwell, E. 1993, ApJ, 418, 368

Goldberg, D. E. 1989, Genetic algorithms in search, optimization and machine learning, ed. Goldberg, D. E.

Güdel, M., Skinner, S. L., Audard, M., Briggs, K. R., & Cabrit, S. 2008, A&A, 478, 797, 0712.1330

Guertler, J., Henning, T., Kruegel, E., & Chini, R. 1991, A&A, 252, 801

Gullbring, E., Hartmann, L., Briceno, C., & Calvet, N. 1998, ApJ, 492, 323

Haisch, Jr., K. E., Lada, E. A., & Lada, C. J. 2001, ApJ, 553, L153, arXiv:astro-ph/0104347

Hartmann, L., Calvet, N., Gullbring, E., & D'Alessio, P. 1998, ApJ, 495, 385

Hasegawa, T. I., & Mitchell, G. F. 1995, ApJ, 451, 225

Heathcote, S., Reipurth, B., & Raga, A. C. 1998, AJ, 116, 1940

Herbig, G. 2002, in Physics of Star Formation in Galaxies, ed. F. Palla, H. Zinnecker, A. Maeder, & G. Meynet, 1–7

Hernández, J. et al. 2007, ApJ, 671, 1784, 0709.0912

Hetem, A., & Gregorio-Hetem, J. 2007, MNRAS, 382, 1707, 0709.1959

Hill, T., Burton, M. G., Minier, V., Thompson, M. A., Walsh, A. J., Hunt-Cunningham, M., & Garay, G. 2005, MNRAS, 363, 405, astro-ph/0506402

Hill, T., Pinte, C., Minier, V., Burton, M. G., & Cunningham, M. R. 2009, MNRAS, 392, 768, 0810.3158

Hillenbrand, L. A., & Hartmann, L. W. 1998, ApJ, 492, 540

Hirth, G. A., Mundt, R., & Solf, J. 1997, A&AS, 126, 437

Ho, P. T. P., Martin, R. N., & Barrett, A. H. 1981, ApJ, 246, 761

Hoare, M. G., Kurtz, S. E., Lizano, S., Keto, E., & Hofner, P. 2007, in Protostars and Planets V, ed. B. Reipurth, D. Jewitt, & K. Keil, 181–196

Hoare, M. G., Lumsden, S. L., Oudmaijer, R. D., Busfield, A. L., King, T. L., & Moore, T. L. J. 2004, in Astronomical Society of the Pacific Conference Series, Vol. 317, Milky Way Surveys: The Structure and Evolution of our Galaxy, ed. D. Clemens, R. Shah, & T. Brainerd, 156–+

Hoare, M. G., Roche, P. F., & Glencross, W. M. 1991, MNRAS, 251, 584

Hofner, P., Cesaroni, R., Olmi, L., Rodríguez, L. F., Martí, J., & Araya, E. 2007, A&A, 465, 197

Hofner, P., Cesaroni, R., Rodríguez, L. F., & Martí, J. 1999, A&A, 345, L43

Holland, J. H. 1975, Adaptation in natural and artificial systems. an introductory analysis with applications to biology, control and artificial intelligence, ed. Holland, J. H.

Hollenbach, D., Johnstone, D., Lizano, S., & Shu, F. 1994, ApJ, 428, 654

Hunter, C. 1977, ApJ, 218, 834

Hutawarakorn, B., & Cohen, R. J. 2005, MNRAS, 357, 338

Ignace, R., & Churchwell, E. 2004, ApJ, 610, 351, arXiv:astro-ph/0403689

Indebetouw, R., Whitney, B. A., Johnson, K. E., & Wood, K. 2006, ApJ, 636, 362, arXiv:astro-ph/0509073

Jackson, J. M. et al. 2006, ApJS, 163, 145, arXiv:astro-ph/0602160

Jarrett, T. H., Chester, T., Cutri, R., Schneider, S., Skrutskie, M., & Huchra, J. P. 2000, AJ, 119, 2498, arXiv:astro-ph/0004318

Jenness, T., Scott, P. F., & Padman, R. 1995, MNRAS, 276, 1024

Joint Iras Science, W. G. 1994, VizieR Online Data Catalog, 2125, 0

Jørgensen, J. K., Bourke, T. L., Myers, P. C., Schöier, F. L., van Dishoeck, E. F., & Wilner, D. J. 2005, ApJ, 632, 973, arXiv:astro-ph/0506671

Jørgensen, J. K., van Dishoeck, E. F., Visser, R., Bourke, T. L., Wilner, D. J., Lommen, D., Hogerheijde, M. R., & Myers, P. C. 2009, A&A, 507, 861, 0909.3386

Joy, A. H. 1945, ApJ, 102, 168

Kahn, F. D. 1974, A&A, 37, 149

Kenyon, S. J., Calvet, N., & Hartmann, L. 1993, ApJ, 414, 676

Kenyon, S. J., & Hartmann, L. 1987, ApJ, 323, 714

Kenyon, S. J., Hartmann, L. W., Strom, K. M., & Strom, S. E. 1990, AJ, 99, 869

Kerr, F. J., & Lynden-Bell, D. 1986, MNRAS, 221, 1023

Keto, E. 2002, ApJ, 580, 980

——. 2007, ApJ, 666, 976, arXiv:astro-ph/0603856

Keto, E., & Wood, K. 2006, ApJ, 637, 850, astro-ph/0510176

Keto, E., & Zhang, Q. 2010, MNRAS, 648

Keto, E., Zhang, Q., & Kurtz, S. 2008, ApJ, 672, 423, 0708.3388

Kim, S., Martin, P. G., & Hendry, P. D. 1994, ApJ, 422, 164

Kitamura, Y., Momose, M., Yokogawa, S., Kawabe, R., Tamura, M., & Ida, S. 2002, ApJ, 581, 357

Kleinmann, S. G., & Lebofsky, M. J. 1975, ApJ, 201, L91

Kratter, K. M., & Matzner, C. D. 2006, MNRAS, 373, 1563, arXiv:astro-ph/0609692

Krumholz, M. R. 2006, ApJ, 641, L45, arXiv:astro-ph/0603026

Krumholz, M. R., Klein, R. I., & McKee, C. F. 2007, ApJ, 656, 959, arXiv:astro-ph/0609798

Krumholz, M. R., McKee, C. F., & Klein, R. I. 2005a, ApJ, 618, 757, arXiv:astro-ph/0409454

——. 2005b, ApJ, 618, L33, arXiv:astro-ph/0411526

Kuchar, T. A., & Bania, T. M. 1994, ApJ, 436, 117

Kurtz, S., Cesaroni, R., Churchwell, E., Hofner, P., & Walmsley, C. M. 2000, Protostars and Planets IV, 299

Kurtz, S., Churchwell, E., & Wood, D. O. S. 1994, ApJS, 91, 659

Kurtz, S., & Hofner, P. 2005, AJ, 130, 711, arXiv:astro-ph/0507039

Kurtz, S. E., Watson, A. M., Hofner, P., & Otte, B. 1999, ApJ, 514, 232

Lada, C. J. 1987, in IAU Symp. 115: Star Forming Regions, ed. M. Peimbert & J. Jugaku, 1–17

Lada, C. J., & Lada, E. A. 2003, ARA&A, 41, 57, arXiv:astro-ph/0301540

Lada, C. J., Thronson, Jr., H. A., Smith, H. A., Schwartz, P. R., & Glaccum, W. 1984, ApJ, 286, 302

Larson, R. B. 1969, MNRAS, 145, 271

——. 1981, MNRAS, 194, 809

——. 1982, MNRAS, 200, 159

——. 2003, Reports of Progress in Physics, 66, 1651, astro-ph/0306595

Larson, R. B., & Starrfield, S. 1971, A&A, 13, 190

Lebrón, M., Beuther, H., Schilke, P., & Stanke, T. 2006, A&A, 448, 1037

Looney, L. W., Mundy, L. G., & Welch, W. J. 2003, ApJ, 592, 255, arXiv:astro-ph/0303640

Marengo, M., Jayawardhana, R., Fazio, G. G., Hoffmann, W. F., Hora, J. L., Dayal, A., & Deutsch, L. K. 2000, ApJ, 541, L63, astro-ph/0008052

Martí, J., Rodriguez, L. F., & Reipurth, B. 1993, ApJ, 416, 208

Maschberger, T., Clarke, C. J., Bonnell, I. A., & Kroupa, P. 2010, MNRAS, 404, 1061, 1002.4401

Massey, P., Johnson, K. E., & Degioia-Eastwood, K. 1995, ApJ, 454, 151

Massey, P., & Thompson, A. B. 1991, AJ, 101, 1408

Masunaga, H., & Inutsuka, S. 2000, ApJ, 531, 350

Masunaga, H., Miyama, S. M., & Inutsuka, S. 1998, ApJ, 495, 346

Mathis, J. S., Rumpl, W., & Nordsieck, K. H. 1977, ApJ, 217, 425

Matthews, H. et al. 2009, AJ, 138, 1380

Matthews, H. E., Shaver, P. A., Goss, W. M., & Habing, H. J. 1978, A&A, 63, 307

McKee, C. F., & Offner, S. S. R. 2010, ApJ, 716, 167, 1004.3788

McKee, C. F., & Tan, J. C. 2003, ApJ, 585, 850, astro-ph/0206037

Mezger, P. G., & Henderson, A. P. 1967, ApJ, 147, 471

Minchin, N. R., Hough, J. H., McCall, A., Aspin, C., Hayashi, S. S., Yamashita, T., & Burton, M. G. 1991, MNRAS, 251, 508

Molinari, S., Brand, J., Cesaroni, R., & Palla, F. 1996, A&A, 308, 573

Molinari, S., Brand, J., Cesaroni, R., Palla, F., & Palumbo, G. G. C. 1998, A&A, 336, 339

Molinari, S., Pezzuto, S., Cesaroni, R., Brand, J., Faustini, F., & Testi, L. 2008, A&A, 481, 345

Molinari, S. et al. 2010, A&A, 518, L100+, 1005.3317

Molinari, S., Testi, L., Rodríguez, L. F., & Zhang, Q. 2002, ApJ, 570, 758

Motte, F., Bontemps, S., Schilke, P., Schneider, N., Menten, K. M., & Broguière, D. 2007, A&A, 476, 1243, 0708.2774

Mueller, K. E., Shirley, Y. L., Evans, II, N. J., & Jacobson, H. R. 2002a, in Astronomical Society of the Pacific Conference Series, Vol. 267, Hot Star Workshop III: The Earliest Phases of Massive Star Birth, ed. P. Crowther, 395–+

Mueller, K. E., Shirley, Y. L., Evans, II, N. J., & Jacobson, H. R. 2002b, ApJS, 143, 469, arXiv:astro-ph/0207322

Myers, P. C., Dame, T. M., Thaddeus, P., Cohen, R. S., Silverberg, R. F., Dwek, E., & Hauser, M. G. 1986, ApJ, 301, 398

Najita, J. R., Carr, J. S., Glassgold, A. E., & Valenti, J. A. 2007, Protostars and Planets V, 507, 0704.1841

Nakamura, F., & Li, Z. 2007, ApJ, 662, 395, arXiv:astro-ph/0703152

Nakano, T. 1998, ApJ, 494, 587

Natta, A., & Panagia, N. 1976, A&A, 50, 191

Offner, S. S. R., Klein, R. I., & McKee, C. F. 2008, ApJ, 686, 1174, 0806.1045

Olmi, L., Cesaroni, R., Hofner, P., Kurtz, S., Churchwell, E., & Walmsley, C. M. 2003, A&A, 407, 225

Omukai, K., & Inutsuka, S. 2002, MNRAS, 332, 59, arXiv:astro-ph/0112345

Osorio, M., Anglada, G., Lizano, S., & D'Alessio, P. 2009, ApJ, 694, 29, 0811.4096

Osorio, M., Lizano, S., & D'Alessio, P. 1999, ApJ, 525, 808

Ossenkopf, V., & Henning, T. 1994, A&A, 291, 943

Oster, L. 1961, Reviews of Modern Physics, 33, 525

Osterbrock, D. E., & Ferland, G. J. 2006, Astrophysics of gaseous nebulae and active galactic nuclei (Astrophysics of gaseous nebulae and active galactic nuclei, 2nd. ed. by D.E. Osterbrock and G.J. Ferland. Sausalito, CA: University Science Books, 2006)

Panagia, N. 1973, AJ, 78, 929

Panagia, N., & Felli, M. 1975, A&A, 39, 1

Panagia, N., & Walmsley, C. M. 1978, A&A, 70, 411

Pandian, J. D., Goldsmith, P. F., & Deshpande, A. A. 2007, ApJ, 656, 255, arXiv:astro-ph/0702147

Penston, M. V. 1969, MNRAS, 144, 425

Peretto, N., André, P., & Belloche, A. 2006, A&A, 445, 979, arXiv:astro-ph/0508619

Pillai, T., Wyrowski, F., Carey, S. J., & Menten, K. M. 2006, A&A, 450, 569, arXiv:astro-ph/0601078

Pinte, C. et al. 2008, A&A, 489, 633, 0808.0619

Planesas, P., Gómez-González, J., Rodríguez, L. F., & Cantó, J. 1991, Revista Mexicana de Astronomia y Astrofisica, 22, 19

Plume, R., Jaffe, D. T., & Evans, II, N. J. 1992, ApJS, 78, 505

Podio, L., Bacciotti, F., Nisini, B., Eislöffel, J., Massi, F., Giannini, T., & Ray, T. P. 2006, A&A, 456, 189, arXiv:astro-ph/0606280

Poetzel, R., Mundt, R., & Ray, T. P. 1992, A&A, 262, 229

Preibisch, T., Balega, Y. Y., Schertl, D., & Weigelt, G. 2003, A&A, 412, 735

Price, D. J., & Bate, M. R. 2009, MNRAS, 398, 33, 0904.4071

Price, S. D., Egan, M. P., Carey, S. J., Mizuno, D. R., & Kuchar, T. A. 2001, AJ, 121, 2819

Pringle, J. E. 1981, ARA&A, 19, 137

Pudritz, R. E., Ouyed, R., Fendt, C., & Brandenburg, A. 2007, in Protostars and Planets V, ed. B. Reipurth, D. Jewitt, & K. Keil, 277–294

Pudritz, R. E., Wilson, C. D., Carlstrom, J. E., Lay, O. P., Hills, R. E., & Ward-Thompson, D. 1996, ApJ, 470, L123+, arXiv:astro-ph/9608087

Pyo, T., Hayashi, M., Naoto, K., Terada, H., & Tokunaga, A. T. 2005, Journal of Korean Astronomical Society, 38, 249

Qiu, K. et al. 2008, ApJ, 685, 1005, 0806.2488

Quanz, S. P., Beuther, H., Steinacker, J., Linz, H., Birkmann, S. M., Krause, O., Henning, T., & Zhang, Q. 2010, ApJ, 717, 693, 1005.1652

Quireza, C., Rood, R. T., Bania, T. M., Balser, D. S., & Maciel, W. J. 2006, ApJ, 653, 1226, arXiv:astro-ph/0609006

Rathborne, J. M., Jackson, J. M., Chambers, E. T., Simon, R., Shipman, R., & Frieswijk, W. 2005, ApJ, 630, L181, arXiv:astro-ph/0508458

Rathborne, J. M., Johnson, A. M., Jackson, J. M., Shah, R. Y., & Simon, R. 2009, ApJS, 182, 131, 0904.1217

Ray, T., Dougados, C., Bacciotti, F., Eislöffel, J., & Chrysostomou, A. 2007, in Protostars and Planets V, ed. B. Reipurth, D. Jewitt, & K. Keil, 231–244

Reid, M. A., & Matthews, B. C. 2008, ApJ, 675, 1343, 0712.0026

Reynolds, S. P. 1986, ApJ, 304, 713

Richling, S., & Yorke, H. W. 1997, A&A, 327, 317

Robitaille, T. P., Whitney, B. A., Indebetouw, R., & Wood, K. 2007, ApJS, 169, 328, arXiv:astro-ph/0612690

Robitaille, T. P., Whitney, B. A., Indebetouw, R., Wood, K., & Denzmore, P. 2006, ApJS, 167, 256, astro-ph/0608234

Rodríguez, L. F., Anglada, G., & Raga, A. 1995, ApJ, 454, L149+

Roman-Duval, J., Jackson, J. M., Heyer, M., Johnson, A., Rathborne, J., Shah, R., & Simon, R. 2009, ApJ, 699, 1153, 0905.0723

Rosolowsky, E. et al. 2010, ApJS, 188, 123, 0909.2871

Saigo, K., & Hanawa, T. 1998, ApJ, 493, 342

Schuller, F. et al. 2009, A&A, 504, 415, 0903.1369

Scoville, N. Z., Sargent, A. I., Sanders, D. B., Claussen, M. J., Masson, C. R., Lo, K. Y., & Phillips, T. G. 1986, ApJ, 303, 416

Sewilo, M., Churchwell, E., Kurtz, S., Goss, W. M., & Hofner, P. 2004, ApJ, 605, 285

Shakura, N. I., & Sunyaev, R. A. 1973, A&A, 24, 337

Shepherd, D. S., & Churchwell, E. 1996a, ApJ, 472, 225

——. 1996b, ApJ, 457, 267

Shepherd, D. S., & Kurtz, S. E. 1999, ApJ, 523, 690

Shepherd, D. S., Yu, K. C., Bally, J., & Testi, L. 2000, ApJ, 535, 833

Shirley, Y. L., Claussen, M. J., Bourke, T. L., Young, C. H., & Blake, G. A. 2007, ApJ, 667, 329, 0705.1747

Shirley, Y. L., Evans, II, N. J., Young, K. E., Knez, C., & Jaffe, D. T. 2003, ApJS, 149, 375, arXiv:astro-ph/0308310

Shu, F., Najita, J., Ostriker, E., Wilkin, F., Ruden, S., & Lizano, S. 1994, ApJ, 429, 781

Shu, F. H. 1977, ApJ, 214, 488

Shu, F. H., & Adams, F. C. 1987, in IAU Symposium, Vol. 122, Circumstellar Matter, ed. I. Appenzeller & C. Jordan, 7–22

Shu, F. H., Adams, F. C., & Lizano, S. 1987, ARA&A, 25, 23

Shu, F. H., Ruden, S. P., Lada, C. J., & Lizano, S. 1991, ApJ, 370, L31

Silverglate, P., & Terzian, Y. 1978, AJ, 83, 1412

Simon, M., Dutrey, A., & Guilloteau, S. 2000, ApJ, 545, 1034, arXiv:astro-ph/0008370

Skrutskie, M. F., Cutri, R. M., Stiening, R., Weinberg, M. D., Schneider, S., & Carpenter, J. M. e. a. 2006, AJ, 131, 1163

Sloan, G. C., Kraemer, K. E., Price, S. D., & Shipman, R. F. 2003, ApJS, 147, 379

Solomon, P. M., Rivolo, A. R., Barrett, J., & Yahil, A. 1987, ApJ, 319, 730

Sridharan, T. K., Beuther, H., Saito, M., Wyrowski, F., & Schilke, P. 2005, ApJ, 634, L57, arXiv:astro-ph/0508421

Sridharan, T. K., Beuther, H., Schilke, P., Menten, K. M., & Wyrowski, F. 2002, ApJ, 566, 931, arXiv:astro-ph/0110363

Steinacker, J., Chini, R., Nielbock, M., Nürnberger, D., Hoffmeister, V., Huré, J., & Semenov, D. 2006, A&A, 456, 1013

Stil, J. M. et al. 2006, AJ, 132, 1158, arXiv:astro-ph/0605422

Su, Y., Liu, S., Chen, H., Zhang, Q., & Cesaroni, R. 2007, ApJ, 671, 571

Tamura, M., & Yamashita, T. 1992, ApJ, 391, 710

Tan, J. C., & McKee, C. F. 2003, ArXiv Astrophysics e-prints, arXiv:astro-ph/0309139

Taylor, A. R., Goss, W. M., Coleman, P. H., van Leeuwen, J., & Wallace, B. J. 1996, ApJS, 107, 239

Te Lintel Hekkert, P., & Chapman, J. M. 1996, A&AS, 119, 459

Terebey, S., Shu, F. H., & Cassen, P. 1984, ApJ, 286, 529

Thomas, H. S., & Fuller, G. A. 2008, A&A, 479, 751, arXiv:0712.1512

Tofani, G., Felli, M., Taylor, G. B., & Hunter, T. R. 1995, A&AS, 112, 299

Toomre, A. 1964, ApJ, 139, 1217

Torrelles, J. M. et al. 2003, ApJ, 598, L115

Trinidad, M. A. et al. 2003, ApJ, 589, 386

Ulrich, R. K. 1976, ApJ, 210, 377

Urquhart, J. S. et al. 2009, A&A, 501, 539, 0905.1174

van der Tak, F. F. S., & Menten, K. M. 2005, A&A, 437, 947, astro-ph/0504026

van der Tak, F. F. S., van Dishoeck, E. F., Evans, II, N. J., Bakker, E. J., & Blake, G. A. 1999, ApJ, 522, 991, astro-ph/9905035

van der Tak, F. F. S., van Dishoeck, E. F., Evans, II, N. J., & Blake, G. A. 2000, ApJ, 537, 283, arXiv:astro-ph/0001527

van der Tak, F. F. S., Walmsley, C. M., Herpin, F., & Ceccarelli, C. 2006, A&A, 447, 1011, astro-ph/0510640

Vázquez-Semadeni, E., Kim, J., & Ballesteros-Paredes, J. 2005, ApJ, 630, L49, arXiv:astro-ph/0507637

Walmsley, M. 1995, in Revista Mexicana de Astronomia y Astrofisica Conference Series, Vol. 1, Revista Mexicana de Astronomia y Astrofisica Conference Series, ed. S. Lizano & J. M. Torrelles, 137–+

Walsh, A. J., Burton, M. G., Hyland, A. R., & Robinson, G. 1998, MNRAS, 301, 640

Watson, C., Araya, E., Sewilo, M., Churchwell, E., Hofner, P., & Kurtz, S. 2003, ApJ, 587, 714

Weidner, C., Kroupa, P., & Bonnell, I. A. D. 2010, MNRAS, 401, 275, 0909.1555

White, R. J., & Hillenbrand, L. A. 2004, ApJ, 616, 998, arXiv:astro-ph/0408244

Whitney, B. A., Indebetouw, R., Bjorkman, J. E., & Wood, K. 2004, ApJ, 617, 1177

Whitney, B. A., Wood, K., Bjorkman, J. E., & Wolff, M. J. 2003, ApJ, 591, 1049, arXiv:astro-ph/0303479

Wilking, B. A., Blackwell, J. H., & Mundy, L. G. 1990, AJ, 100, 758

Williams, S. J., Fuller, G. A., & Sridharan, T. K. 2004, A&A, 417, 115, arXiv:astro-ph/0401633

——. 2005, A&A, 434, 257

Wilson, T. L., Pankonin, V., & Dickey, J. 1978, A&A, 68, 303

Wilson, T. L., & Rood, R. 1994, ARA&A, 32, 191

Wolfire, M. G., & Cassinelli, J. P. 1987, ApJ, 319, 850

Wood, D. O. S., & Churchwell, E. 1989, ApJS, 69, 831

Wood, K., Hill, A. S., Joung, M. R., Mac Low, M., Benjamin, R. A., Haffner, L. M., Reynolds, R. J., & Madsen, G. J. 2010, ApJ, 721, 1397, 1007.5348

Wood, K., Lada, C. J., Bjorkman, J. E., Kenyon, S. J., Whitney, B., & Wolff, M. J. 2002a, ApJ, 567, 1183, arXiv:astro-ph/0111283

Wood, K., Mathis, J. S., & Ercolano, B. 2004, MNRAS, 348, 1337, arXiv:astro-ph/0311584

Wood, K., Wolff, M. J., Bjorkman, J. E., & Whitney, B. 2002b, ApJ, 564, 887, arXiv:astro-ph/0109048

Wu, J., & Evans, II, N. J. 2003, ApJ, 592, L79, arXiv:astro-ph/0306543

Wu, Y., Wei, Y., Zhao, M., Shi, Y., Yu, W., Qin, S., & Huang, M. 2004, A&A, 426, 503, arXiv:astro-ph/0410727

Yamashita, T. et al. 1987, PASJ, 39, 809

Yorke, H. W. 1977, A&A, 58, 423

Yorke, H. W. 2004, in IAU Symposium, Vol. 221, Star Formation at High Angular Resolution, ed. M. Burton, R. Jayawardhana, & T. Bourke, 141–+

Yorke, H. W., & Sonnhalter, C. 2002, ApJ, 569, 846, arXiv:astro-ph/0201041

Yorke, H. W., & Welz, A. 1996, A&A, 315, 555

Yusef-Zadeh, F., Morris, M., & White, R. L. 1984, ApJ, 278, 186

Zhang, Q., Hunter, T. R., Brand, J., Sridharan, T. K., Cesaroni, R., Molinari, S., Wang, J., & Kramer, M. 2005, ApJ, 625, 864

Zhang, Q., Hunter, T. R., & Sridharan, T. K. 1998, ApJ, 505, L151

Zinnecker, H., & Yorke, H. W. 2007, ARA&A, 45, 481, 0707.1279

Zoonematkermani, S., Helfand, D. J., Becker, R. H., White, R. L., & Perley, R. A. 1990, ApJS, 74, 181